Mapping the proton using J/ψ photoproduction with ALICE and development of a novel structure of gaseous particle detector

Aude Glaenzer

université
PARIS-SACLAY

Mapping the proton using J/ψ photoproduction with ALICE and development of a novel structure of gaseous particle detector

Cartographier le proton via la photoproduction du J/ψ avec ALICE et développement d'une nouvelle structure de détecteur de particules gazeux

Thèse de doctorat de l'Université Paris-Saclay

École doctorale n°576 Particules, Hadrons, Énergie, Noyau, Instrumentation, Imagerie, Cosmos et Simulation (PHENIICS)

Spécialité de doctorat: Physique Hadronique

Graduate School: Physique *Référent:* Faculté des sciences d'Orsay

Thèse préparée au **Département de Physique Nucléaire** (Université Paris-Saclay, CEA), sous la direction de **Javier CASTILLO CASTELLANOS**, Directeur de recherche, le co-encadrement de **Francesco BOSSÙ**, Ingénieur de recherche, et le co-encadrement de **Michael WINN**, Ingénieur de recherche

Thèse soutenue à Paris-Saclay, le 22 septembre 2022, par

AUDE GLAENZER

Composition du Jury

Franck SABATIÉ Directeur de recherche, Université Paris-Saclay, Irfu	Président
Bernhard KETZER Professeur, HISKP	Rapporteur & Examinateur
Gines MARTINEZ Directeur de recherche, CNRS, Subatech	Rapporteur & Examinateur
Cyrille MARQUET Chargé de recherche, Institut Polytechnique de Paris	Examinateur
Javier CASTILLO CASTELLANOS Directeur de recherche, Université Paris-Saclay, Irfu	Directeur de thèse

THESE DE DOCTORAT

NNT : 2022UPASP081

université PARIS-SACLAY

ÉCOLE DOCTORALE
Particules, hadrons, énergie et noyau : instrumentation, imagerie, cosmos et simulation (PHENIICS)

Titre : Cartographier le proton via la photoproduction du J/ψ avec ALICE et développement d'une nouvelle structure de détecteur de particules gazeux

Mots clés : Structure du proton, Saturation de gluons, Chambre à projection temporelle, GEM, Micromegas, Retour d'ions

Résumé : Ce doctorat est divisé en deux parties, dont chacune durera un an et demi. La première partie fait suite au stage de trois mois déjà effectué au CEA, en recherche et développement sur des détecteurs Micromegas. Les détecteurs Micromegas sont des détecteurs gazeux à plaques parallèles constituées de deux étages : (1) un étage de dérive et (2) un étage d'amplification situé entre le circuit imprimé qui collecte le signal et une micro-grille. Le champ électrique présent dans l'espace d'amplification est très élevé, donnant lieu à un phénomène d'avalanche lorsqu'y pénètre un électron. Les ions résultant de cette avalanche sont ceux responsables de possibles distorsions du champ électrique dans la zone de dérive. Les GEMs (Gas Electron Multiplier) sont des feuilles percées de trous auxquels on peut appliquer deux potentiel electriques, créant ainsi une amplification dans les trous de la GEM. Le travail consiste à étudier la possibilité d'ajouter dans un détecteur Micromegas une ou plusieurs micro-grilles / GEM au dessus de la micro-grille d'amplification de façon à capturer ces ions avant qu'ils n'entrent dans l'espace de dérive. Cela nécessitera de construire et caractériser plusieurs détecteurs prototypes de taille réduite, d'en simuler les propriétés précises, puis de tester ces détecteurs en laboratoire. Ces détecteurs présentent de nombreuses applications dans les expériences de physique des particules, en particulier ce type de détecteur est déjà utilisé au LHC au CERN (à Genève) ainsi qu'au RHIC (Brookhaven National Laboratory (NY state, USA). Le but est de construire un détecteur qui dépasse la précision spatiale de ceux qui existent déjà, qui pourra dans un second temps être utilisé dans des expériences de détection des particules. La seconde partie de mon doctorat est portée sur l'étude de la structure du proton et l'interaction des particules élémentaires qui le constituent : l'interaction forte. Ces particules élémentaires sont des quarks et des gluons. Les gluons sont des particules capables de créer d'autres gluons d'elles-mêmes, menant ainsi à une "saturation" de la structure du proton. Ce phénomène est étudié au LHC dans des collisions dites "ultra-périphériques" de proton et de plomb (les noyaux de proton et de plomb se croisent, et interagissent sans se toucher), ultra-relativistes (les noyaux sont accélérés à la vitesse de la lumière). Le noyau de Plomb agit comme une source de photons (particules de lumières) qui vont interagir avec le proton : de cette interaction est produite une troisième particule (J/ψ), signataire de la structure du proton. En effet, le photon peut interagir plus ou moins profondément dans le proton avec ses constituants (quarks ou gluons), en fonction de son énergie. En caractérisant la production du J/ψ, on mesure l'état du proton à différentes profondeurs (ou échelles d'énergie). Cette analyse permettra de contraindre les modèles théoriques qui existent déjà pour comprendre l'interaction forte, qui gouverne le comportement de la matière et la cohésion des atomes.

université PARIS-SACLAY

ÉCOLE DOCTORALE
Particules, hadrons, énergie et noyau : instrumentation, imagerie, cosmos et simulation (PHENIICS)

Title: Mapping the proton using J/ψ photoproduction with ALICE and development of a novel structure of gaseous particle detector

Keywords: Proton structure, Gluon saturation, Time projection chamber, GEM, Micromegas, Ion backflow

Abstract: This doctorate is divided into two parts, each of which will last a year and a half. The first part follows on from the three-month internship already carried out at the CEA, in research and development on Micromegas detectors. Micromegas detectors are gas detectors with parallel plates made up of two stages: (1) a drift stage and (2) an amplification stage located between the printed circuit which collects the signal and a micro-grid. The electric field present in the amplification space is very high, giving rise to an avalanche phenomenon when an electron enters it. The ions resulting from this avalanche are those responsible for possible distortions of the electric field in the drift zone. GEMs (Gas Electron Multiplier) are sheets pierced with holes to which two electrical potentials can be applied, thus creating an amplification in the holes of the GEM. The work consists of studying the possibility of adding in a Micromegas detector one or more micro-grids / GEM above the amplification micro-grid so as to capture these ions before they enter the space of derivative. This will require building and characterizing several small prototype detectors, simulating their precise properties, and then testing these detectors in the laboratory. These detectors have many applications in particle physics experiments, in particular this type of detector is already used at the LHC at CERN (in Geneva) as well as at the RHIC (Brookhaven National Laboratory (NY state, USA). The goal is to build a detector which exceeds the spatial precision of those which already exist, which can subsequently be used in particle detection experiments. The second part of my doctorate is focused on the study of the structure of the proton and the interaction of the elementary particles that constitute it: the strong interaction. These elementary particles are quarks and gluons. Gluons are particles capable of creating other gluons on their own, thus leading to a "saturation" of the structure of the proton. This phenomenon is studied at the LHC in so-called "ultra-peripheral" collisions of proton and lead (the proton and lead nuclei intersect, and interact without touching each other), ultra-relativistic (the nuclei are accelerated at the speed of the light). The lead nucleus acts as a source of photons (light particles) which will interact with the proton: from this interaction is produced a third particle (J/ψ), signatory of the structure of the proton. Indeed, the photon can interact more or less deeply in the proton with its constituents (quarks or gluons), depending on its energy. By characterizing the production of J/ψ, we measure the state of the proton at different depths (or energy scales). This analysis will make it possible to constrain the theoretical models that already exist to understand the strong interaction, which governs the behavior of matter and the cohesion of atoms.

Remerciements

Mener à bien ce doctorat n'a pas été une tâche solitaire, bien au contraire. Les nombreuses interactions avec les collègues ont nourri non seulement les questionnements de ces trois années, mais ont surtout fait de la thèse une activité épanouissante.

Tout d'abord, j'ai eu la chance d'être accompagnée de près par deux superviseurs pleins d'énergie, bienveillants et toujours disponibles, Michael Winn et Francesco Bossù. Et pourtant, tout n'était pas si évident : le Covid a causé la fermeture des portes du CEA, mais tous les deux ont su garder un contact très régulier grâce aux moyens modernes (ils connaissent maintenant très bien l'horloge de ma cuisine !). De plus, tous les deux sont devenus papas au cours de mon doctorat, et ont réussi à cumuler les tâches avec brio. Merci mille fois à vous deux.

Je remercie les membres de mon jury, Franck Sabatié qui a bien voulu présider le jury, Cyrille Marquet, et mes rapporteurs Gines Martinez et Bernhard Ketzer qui ont pris le temps de corriger avec soin mon manuscrit pendant un été particulièrement caniculaire. Merci à vous tous pour vos nombreux commentaires instructifs. Et bien évidemment, je suis très reconnaissante envers mon directeur de thèse Javier Castillo Castellanos, qui est venu à mon secours de nombreuses fois, en particulier dans les problèmes de compilation du logiciel d'ALICE. Merci Javier pour ta patience !

Je tiens également à remercier toutes les personnes du DPhN qui ont été présentes au quotidien, en particulier mes collègues du LQGP (Laboratoire de Plasma de Quarks et de Gluons). Je garde un très bon souvenir de toutes nos discussions du déjeuner sur l'actualité et tous les événements qui ont marqué ces trois ans (les gilets jaunes, le Covid, la guerre en Ukraine, les élections présidentielles...), mais aussi les sujets plus légers et réjouissants, et en particulier les pauses post-déjeuner dédiées aux mots fléchés. J'ai eu la chance de travailleur au sein d'un laboratoire avec plusieurs jeunes doctorants, et je remercie en particulier Robin, Maurice et Sébastien pour leur dynamisme et motivation dans la construction d'un escape game que nous avons élaboré ensemble en vue de vulgariser notre domaine de la physique. Je suis particulièrement reconnaissante envers Sébastien, qui a démarré et terminé sa thèse en même temps que moi, et avec qui j'ai partagé le bureau, alternativement utilisé comme cour des larmes ou karaoké pendant ces trois années. J'ai hâte de te voir dans "N'oubliez pas les paroles" !

Hormis le LQGP, d'autres membres du DPhN ont particulièrement marqué ma thèse. Je dis un grand merci à Marine Vandebrouck, de m'avoir initialement dirigée vers le LQGP et mon sujet de thèse, mais aussi pour sa bonne humeur constante et sa bienveillance. Merci à Isabelle Richard, notre précieuse secrétaire qui a grandement contribué à ce que notre escape game voie le jour. Et un grand merci à tous les jeunes du DPhN, pour nos échanges du vendredi et

les quelques bières savourées ensemble lorsque les bars étaient ouverts.

Bien évidemment, j'ai une immense gratitude envers les personnes avec lesquelles j'ai été directement amenée à travailler : Jesús Guillermo Contreras Nuño et Simone Ragoni pour l'analyse ALICE, ainsi que Maxence Vandenbroucke, Stephan Aune, et Esther Ferrer Ribas du DEDIP qui m'ont guidée dans les étapes de construction et de tests du détecteur. Merci infiniment pout tous les précieux conseils, et de m'avoir appris tant de choses du métier de chercheur en physique, aussi bien sur la compréhension théorique de la physique qu'au laboratoire.

Enfin, je voudrais exprimer mon immense gratitude à ma famille et à tous mes proches. Je remercie mes parents pour leur gentillesse quotidienne à la maison, et leur intérêt pour mon sujet malgré leur méconnaissance de la physique des particules (c'est d'ailleurs ainsi que Papa a rebaptisé le plasma de quarks-gluons en "plasma de quarks gluants"). Merci à tous mes amis, à Paris, Lyon ou à Londres : que ce soit nos sorties à l'escalade, en concert jazz, en festivals, tous nos rires, et toutes nos sorties m'ont toujours aidée à prendre du recul sur mon travail et à retrouver beaucoup de joie et de motivation lorsque plus rien de marchait. Vous avez toujours su recharger mes batteries ! Je souhaite dire un merci tout spécial à Pierre, ma pile électrique, qui a toujours su transformer instantanément les moments de doute en opportunité de progrès et en rire.

Contents

General introduction **5**

I Probing the proton structure using J/ψ photoproduction in ultra-relativistic collisions of protons and lead nuclei with the ALICE experiment at the LHC **7**

1 Introduction **9**
1.1 The standard model and the strong interaction of particle physics 10
1.2 Probing the proton structure in deep inelastic scattering 17
1.3 Description of parton evolution in perturbative QCD 23
1.4 Unveiling the proton structure in ultra-peripheral collisions 29
1.5 Summary 36
Bibliography 38

2 Description of the ALICE experiment **45**
2.1 The Large Hadron Collider 46
2.2 ALICE detection instruments 50
2.3 Data acquisition and processing in ALICE 60
2.4 Summary 64
Bibliography 65

3 Data sample and event selection **67**
3.1 Data sets 68
3.2 Event selection 70
3.3 Luminosity determination 76
3.4 Summary 81
Bibliography 82

4 Signal extraction, corrections and uncertainties **83**
4.1 Signal extraction of exclusive two-photon interactions 84
4.2 Signal extraction for J/ψ photoproduction 92
4.3 Correction for acceptance and reconstruction efficiency 101
4.4 Corrections affecting J/ψ signal extraction 105
4.5 Systematic uncertainties 108
4.6 Summary 112
Bibliography 113

5 Results and comparison of measurements with models **115**
5.1 Cross sections for the dimuon continuum in two-photon interactions 116
5.2 Cross sections for J/ψ photoproduction off protons 122
5.3 Summary 131
Bibliography 132

II Development and characterization of a novel structure of micro-pattern gaseous detector reducing ion backflow **137**

6 Micro-Pattern Gaseous Detectors as TPC readout systems **139**
6.1 Time Projection Chambers 140
6.2 MPGDs as TPC readout systems 144
6.3 Producing events in a MPGD structure 149
6.4 Summary 151
Bibliography 152

7 Simulation of Micro-Pattern Gaseous Detectors **155**
7.1 Numerical tools 156
7.2 Definition of the observables in the simulation 159
7.3 Models simulated 160
7.4 Simulation results on MMGEM detectors 164
7.5 Summary 168
Bibliography 169

8 Measurements **171**
8.1 Description of the setup 172
8.2 Measurements with the 660-µm-gap detector 176
8.3 Measurements with the 128-µm-gap detector 192
8.4 Contamination on the drift electrode 197
8.5 Summary 199
Bibliography 200

9 Comparison of measurements with simulations and other detector configurations **201**
9.1 Comparison of laboratory tests with simulations 202
9.2 Comparison of MMGEM models with other geometric configurations 211
9.3 Summary 213
Bibliography 215

III Appendices - ALICE **217**

A Computation of the center-of-mass energy in the γp system **219**

B Studies on V0C detector **221**
B.1 Traces of dissociative J/ψ photoproduction in V0C 221
B.2 V0C matching 223
Bibliography 226

C Pile-up correction **227**

D Empirical functions to describe the data **229**
D.1 Landau distribution . . . 229
D.2 Double-sided Crystal Ball function . . . 229

E Estimation of the number of J/ψ events in γPb interactions **231**
Bibliography . . . 233

F Contamination from ϕ production at low mass in the continuum **235**
Bibliography . . . 236

G Computation of the expected number of $\psi(2S) \to \mu^+\mu^-$ from the feed-down factor **237**
G.1 Numerical application . . . 238
Bibliography . . . 238

IV Appendices - MPGD 241

H Interaction of photons in the detector gas **243**
H.1 Pile-up events in the transfer and drift spaces . . . 244
H.2 Contamination induced by events taking place outside the drift region . . . 248
Bibliography . . . 249

I Study of the impact of using a collimated source **251**

J Comparison of two Penning transfer rates **253**

K Comparison of two gas mixtures with simulations **255**
Bibliography . . . 256

V Other appendices 257

Acronyms and glossary **259**
Acronyms . . . 259
Glossary . . . 261

Summary in French **263**

General introduction

The current understanding of particle physics is based on the standard model of particles which includes all elementary particles and their interactions, except gravity. The proton is the smallest nucleus that exists and is an ideal place to study one of the interactions: the strong interaction, so-called because of its strength at short range. The gluons, mediators of this interaction, bind the constituents of the proton together and their density grows explosively when the proton is probed in high energy collisions, i.e., collisions of nuclei traveling at speeds close to that of light. When they reach a critical density, a state of *saturated* gluons is expected to be created which brings into play phenomena interpreted as gluon recombinations. "Ultra-peripheral" collisions of lead nuclei and protons, in which lead nuclei act as sources of photons that probe the proton in the distance, make it possible to study the proton structure. The interaction of the photon with the target proton via the exchange of two gluons can produce a new particle, a J/ψ meson. Two mechanisms of J/ψ production are studied: one where the proton remains intact after this interaction and one where the proton dissociates. The measurements of these two mechanisms, performed in the ALICE experiment at the Large Hadron Collider (LHC) with data from Run 2, give complementary information about the gluonic structure of the proton. The energy reached is similar to other measurements already taken in the past, and the measurements are in agreement. For the moment, no clear evidence of gluon saturation has been observed. Furthermore, this is the first time that the dissociative process is measured in an LHC experiment, which is a starting point for future data analyses at higher energy with LHC Runs 3 and 4.

The first chapter presents a history and motivation for the research of gluon saturation and describes how it can be tested at the LHC. The second chapter gives an overview of the ALICE detector used for the measurements, emphasizing the instruments used in the analysis and how the data is acquired and processed. The third chapter describes the data sample, event selection, and the computation of luminosity, which is related to the size of the data sample. The fourth chapter presents the analysis of the two J/ψ production mechanisms and a complementary measurement of two-photon interactions in the same data sample. Finally, the fifth chapter presents the results and comparisons to previous measurements and theoretical models.

The second part of this thesis is dedicated to the development of a new type of gas detector designed to read out a Time Projection Chamber (TPC). A TPC is a detector aiming to reconstruct particle trajectories using electromagnetic fields. Charged particles created in particle collisions ionize the gas of the TPC along their path, and electrons resulting from these ionizations drift towards the anode. The initial particle trajectory is reconstructed via the de-

tection of the electrons in readout detectors. The new detector structure presented combines MicroMEGAS detectors and GEMs. These two technologies are based on the use of electrodes separated by a distance of the order of a hundred micrometers, where a strong electric field region is created by applying different potentials to the electrodes. Thus, when electrons reach this region, they are accelerated to the point of ionizing the surrounding gas, giving rise to an avalanche phenomenon that amplifies the signal. However, the ions from this avalanche are likely to go towards the drift space, causing electric field distortions. These distortions can be responsible for a degradation of the spatial resolution of the TPC. The development work consists of studying the possibility of adding a micro-grid a few micrometers above a GEM to capture these ions (the *ion backflow*) before they enter the drift space. Simulations were firstly carried out before performing laboratory tests.

The sixth chapter introduces TPCs and Mico-Pattern Gaseous Detectors as TPC readout systems. The seventh chapter shows the simulations performed of different structures combining MicroMEGAS and GEMs. The eighth chapter presents the tests in the laboratory of two detector prototypes using the new structure. Finally, the ninth chapter compares firstly different MPGD structures in terms of ion backflow performance, and secondly, the measurements in the laboratory with predictions from simulations.

Part I

Probing the proton structure using J/ψ photoproduction in ultra-relativistic collisions of protons and lead nuclei with the ALICE experiment at the LHC

Chapter 1

Introduction

Contents

1.1 The standard model and the strong interaction of particle physics . . . 10

1.1.1 Introduction to the standard model of particles . . . 10

1.1.2 The strong interaction and Quantum Chromodynamics (QCD) 13

1.2 Probing the proton structure in deep inelastic scattering . . 17

1.2.1 The discovery of partons in deep inelastic scattering . . . 17

1.2.2 Parton distribution functions . . . 20

1.3 Description of parton evolution in perturbative QCD 23

1.3.1 Linear perturbative equations of parton evolution in QCD . . . 23

1.3.2 Gluon saturation in the color glass condensate framework . . . 26

1.4 Unveiling the proton structure in ultra-peripheral collisions 29

1.4.1 Ultra-peripheral collisions and photons from lead nuclei 30

1.4.2 Vector meson photoproduction in the color dipole model 31

1.4.3 Photoproduction of J/ψ mesons off protons in p–Pb UPCs . . . 32

1.5 Summary . . . 36

Bibliography . . . 38

The idea of breaking matter down into building blocks is central to our understanding of the physics of the Universe. A few microseconds after the Big Bang, it is thought that the Universe was bathing in a kind of extremely dense and hot soup called *quark gluon plasma* (QGP), in which point-like particles (the building blocks of matter) were "boiling". In such a medium, the point-like particles roam freely and cannot form bound states. The QGP is assumed to exist in the core of neutron stars, which are incredibly dense end-of-life stars. In ordinary matter, much less dense and much colder than in neutron stars or just after the Big Bang, these particles are assembled to form atoms and molecules.

The classification and hierarchy of building blocks that make up ordinary matter - the *elementary particles* - and their interactions are described by the field of physics called *particle physics* or *subatomic physics*. This designation comes from the fact that elementary particles have typical sizes smaller than the standard radius of an atom. The elementary particles and their interactions have been organized during the last century in a model, the *standard model of particle physics* [1, 2].

The first part of this chapter is dedicated to a description of the standard model and, in particular, of the characteristics of the strong interaction, which governs the behavior of *quarks* and *gluons* (the mediating fields of the strong interaction) on a length scale below the size of the proton. We then focus on past experimental measurements that provided insights into the proton structure, made up of quarks and gluons, thus giving constraints on the behavior of the gluons. The following section discusses perturbative models, which describe the behavior of quarks and gluons on a small length scale. These models predict a saturation of the density of gluons from a specific threshold length scale. The saturation can be tested experimentally at Large Hadron Collider (LHC) via so-called "ultra-peripheral" collisions, which are introduced in the last section. In particular, we describe the photoproduction of J/ψ off target protons in ultra-peripheral collisions and its production mechanisms.

1.1 The standard model and the strong interaction of particle physics

1.1.1 Introduction to the standard model of particles

Particle collision experiments carried out throughout the 1950s and 1960s led to the discovery of a very wide variety of particles: a "particle zoo" [3]. It was later understood that these were not elementary particles but combinations of a relatively small number of fundamental particles. The standard model of particles then appeared and was built throughout the twentieth century, in which the elementary particles are identified and by which the fundamental non-gravitational forces are described: strong, weak, and electromagnetic. Because of its success in explaining a wide variety of experimental results, the Standard Model is sometimes seen as a "theory of almost everything". Figure 1.1 presents all the elementary particles discovered so far.

There are two prominent families: the *fermions* which are characterized by a half-integer spin, and the *bosons* of integer spin.

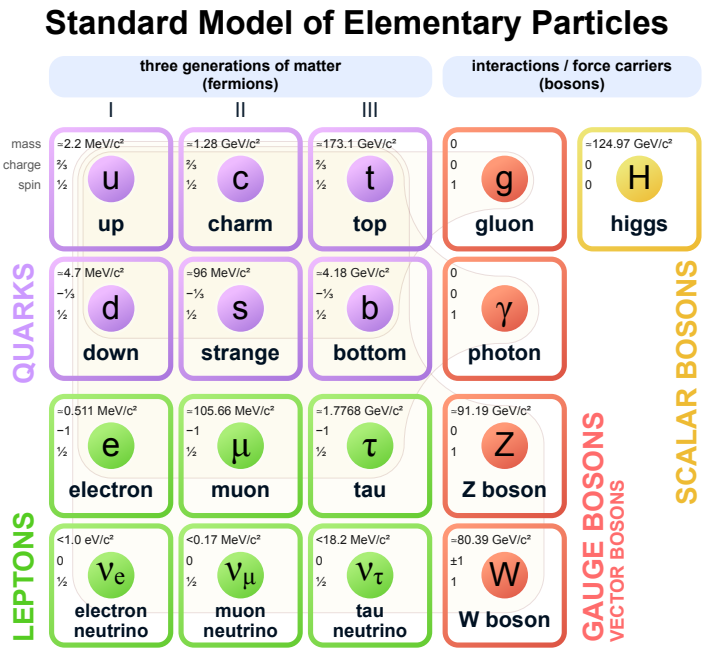

Figure 1.1: Table of elementary particles of the standard model. The fermions (quarks and leptons) are complemented with their anti-particle counterparts. Figure taken from reference [4].

The fermions

The family of fermions gathers the six elementary particles, which are the constituents of matter: quarks and leptons. Each of them is associated with different specific characteristics, such as their mass, their charge, or their spin[1] along with other quantum numbers. **Leptons** carry an integer charge and are subject to electromagnetic and weak interactions. Three generations of leptons are known, each including one negatively charged lepton (e^-, μ^-, and τ^-) and one neutral neutrino (ν_e, ν_μ, and ν_τ). **Quarks** are also grouped in three generations: the quarks up and down (u and d), charm and strange (c and s), and top and bottom (t and b), for a total of six so-called "flavors". Unlike leptons, quarks carry fractional electric charges. Each couple consists of a quark with charge $q = 2/3e$ (u, c, and t) and a quark with charge $q = -1/3e$ (d, s, and b) where e is the elementary charge. The generations of both leptons and quarks follow an increasing mass hierarchy. Ordinary matter consists only of first-generation particles. The higher mass particles are highly unstable and decay quickly into the stable states if produced.

All these particles are complemented with their analogous antiparticles, that is, particles of mass and spin equal to those of the corresponding particle but opposite-sign quantum numbers.

The bosons

Particles of integer spin correspond to the second family: the bosons. The Higgs-Englert-Broot boson, more commonly known as the Higgs boson [5, 6], is responsible for the mass of all elementary particles in the Standard Model. Besides the Higgs boson, which has spin 0, all

[1] Intrinsic quantum number of a particle often equated with angular momentum.

other bosons are spin 1 and are mediators of one of the interactions mentioned above: the gluon is the mediator of the strong interaction, the photon that of the electromagnetic interaction, and finally, the $W^{\pm}$ and Z^0 bosons are mediators of the weak interaction.

Each of the fundamental interactions is constructed in quantum field theory from symmetries. A characteristic of symmetries is that they are related to a conserved quantity. For example, for the electromagnetic interaction, the electric charge is conserved. Thus, the Lagrangian[2] which describes each interaction does not change (is invariant) under certain local transformations, called *gauge* transformations. The set of gauge transformations forms a symmetry group. For each group generator, there necessarily exists a corresponding field (usually a vector field, i.e., of spin 1). The generators of the symmetry group associated to an interaction (the gluon, the photon, and the $W^{\pm}$ and Z^0 bosons) are called *gauge bosons*. Some properties of gauge bosons are summarized in table 1.1 according to the interaction they mediate.

interaction	electromagnetic	weak	strong
mediator boson	photon	$W^{\pm}$ and Z^0 bosons	gluon
range	∞	10^{-18} m	10^{-15} m
mass (GeV/c^2)	0	80 ($W^{\pm}$) and 91 (Z^0)	0
fermions concerned	all charged particles (quarks, electrons, muons and tauons)	all particles (leptons and quarks)	quarks

Table 1.1: Properties of gauge bosons for the electromagnetic, weak, and strong interactions.

Although the standard model is tested with remarkable accuracy, it is not complete. Unlike the three other forces, gravity is not included. The Standard Model also does not contain the explanation for dark matter, responsible for the higher than expected speed of stars on the outskirts of galaxies, nor for dark energy, responsible for the expansion of the Universe. Without these contributions included, the Standard Model leaves 95% of the Universe unexplained.

The object of our interest will now be directed toward one of the interactions mentioned above, namely the strong interaction described by the theory of Quantum ChromoDynamics (QCD).

[2]The Lagrangian is a mathematical object that depends on dynamic variables and is used to write the system equations concisely.

1.1.2 The strong interaction and Quantum Chromodynamics (QCD)

Properties of Quantum Chromodynamics

The strong interaction rules the interactions of quarks (q), anti-quarks ($\bar{q}$), and gluons. It is described by the gauge theory of Quantum ChromoDynamics (QCD), where "chromodynamics" comes from the Greek word *chrôma* which means color. In this theory, a quantity called *color charge* is conserved. The color charge is an intrinsic characteristic of the particle and has nothing to do with visual perception. According to the theory of quantum chromodynamics, a quark carries a color charge which can take three values (color-triplet states): "blue" (B), "green" (V) or "red" (R), and the same logic applies on antiquarks which carry a charge "anti-blue" ($\bar{B}$), "anti-green" ($\bar{V}$), or "anti-red" ($\bar{R}$). The analogy with color conveniently allows us to notice that certain combinations of quarks and anti-quarks (therefore of colors and anti-colors) yield a neutral (or white) state. These neutral states, called hadrons, are the only ones allowed to exist in nature. They can be mesons, formed of a symmetric quark - anti-quark pair ($B\bar{B}$, $V\bar{V}$ or $R\bar{R}$), or baryons (from the Greek word *barus* which means heavy), formed of three quarks or anti-quarks (RGB or $\bar{R}\bar{G}\bar{B}$), as represented in figure 1.2.

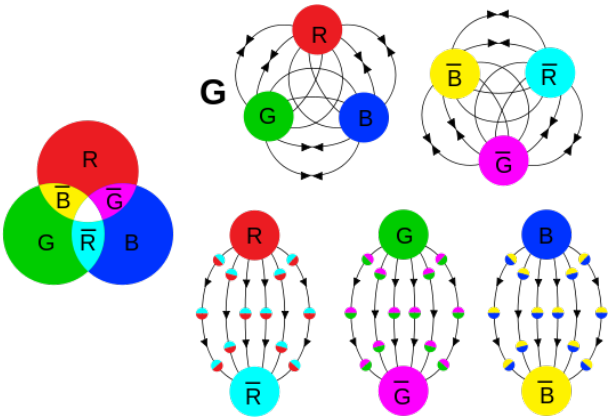

Figure 1.2: Representation of baryons (top) and mesons (bottom) in QCD. The black letter 'G' stands for gluon, which interconnects the quarks.

The gluons, mediators of the strong interaction, hold the quarks together within a hadron by making them exchange their colors. The color being always conserved, the gluons must carry a color and an anti-color, $C\bar{C}'$ where the colors C and C' are different. For example, a green quark will be able to emit a $G\bar{R}$ gluon while turning red. If this gluon is absorbed by its red neighbor, this latter quark will turn green. By this mechanism, the color charge of a given quark will change continuously by exchange of gluons with its neighbors, but the total charge of the hadron will be conserved over time.

In addition to mesons and baryons, other exotic colorless states are allowed to exist, as long as two (anti-)quarks do not carry the same quantum numbers according to Pauli's principle. These states are tetraquarks ($q\bar{q}q\bar{q}$) or pentaquarks ($qqqq\bar{q}$), for which evidence of their existence was recently observed [7, 8]. QCD also predicts the existence of glueballs - bound states of multiple gluons.

Since only colorless states are allowed to exist, and quarks are color charged, a quark alone cannot be observed: quarks are said to be "confined" in a hadron.

The symmetry group associated to the conservation of color charge is the SU(3) group, which is the Lie group of 3×3 unitary matrices with determinant 1. The generators of the SU(3) group are eight gluons (octet states): these form a basis from which all other color states can be constructed.

Since the strong interaction concerns all particles having a color charge, it acts on its own mediator particles, the gluons: the theory is said to be *non-abelian*. It is consequently possible for the gluon to interact with other gluons, which means that two gluons can merge into one, and a gluon can radiate other gluons. This property of the theory is a particularity of the strong interaction, unlike, for example, the electromagnetic interaction: the photon (mediator of the electromagnetic interaction), electrically neutral, is not subject to the electromagnetic interaction and therefore cannot interact with other photons.

For a full introduction to QCD, see reference [9].

The strong coupling constant α_s

What is a coupling constant?

All interactions are characterized by a coupling constant, which determines the relative strength of the interaction between particles and is unitless. In classical physics, in the case of linear theories with massless force carriers, a force coupling constant is a universal coefficient C_c that links two bodies, whose interaction strength is proportional to C_c/r^2 where r is the distance between them. The $1/r^2$ dependence is interpreted as the weakening of the force flux as it spreads uniformly through space. As an example, the further from Earth, the less intense gravity. In quantum field theory, instead of using a distance r, the interaction is defined as a function of the scaling Q^2, which corresponds to the square of the four-momentum[3] transferred in the interaction and is related to the distance r between the two objects by $r = \hbar c/\sqrt{Q^2}$. The possible interactions between two particles depend on the scale Q^2, and corrections must be applied to get the *effective* coupling between them. Therefore, the coupling constant in quantum field theory is, in fact, not necessarily a constant since it has a Q^2-dependence: the constant coupling is *running*.

Interactions between two particles

In quantum field theory, interactions between subatomic particles require complex calculations, challenging to apprehend intuitively. Feynman diagrams, invented by the American physicist of the same name, are a graphical representation of mathematical expressions describing the interactions of subatomic particles (see examples figure 1.3 or an introduction in reference [10]). Each connection point, called vertex, is associated with the square root of the coupling constant of the corresponding interaction. The processes which involve the coupling constant at the lowest order - they have the fewest vertices for a given process - are called Leading Order (LO) diagrams. Processes with higher numbers of vertices are called Next-to-Leading Order

[3] In special relativity, the four-moment is a four-vector of Minkowski space (space-time dimensions of special relativity), often denoted $P^\mu = (t, \vec{x})$ where t is the time of the particle considered, and $\vec{x}$ its position in three dimensions, or $P^\mu = (E, \vec{p})$ where E is the energy of the particle and $\vec{p}$ its momentum vector. This depends on the Lorentz frame (the four-coordinate system used in the special theory of relativity) in which it is defined.

(NLO), Next-to-Next-to-Leading Order (NNLO), and so on.

Let us consider two objects, quarks or gluons, subjected to the strong interaction, as shown in figure 1.3. These two objects are represented by the two horizontal lines. The process at LO simply involves the exchange of a gluon (figure a). If this were the end of the story, one would recover a universal coupling constant. However, other more complex diagrams are possible (figures b and c) and must be accounted for in the strength of the coupling in a renormalization procedure. The NLO diagrams b and c are due to *quantum vacuum fluctuations* which do not exist in classical physics and come from quantum field theory. The exchanged gluon fluctuates in a pair of *virtual* particles (a $q\bar{q}$ pair or a pair of gluons), allowed to exist for a very short time according to Heisenberg's uncertainty principle[4].

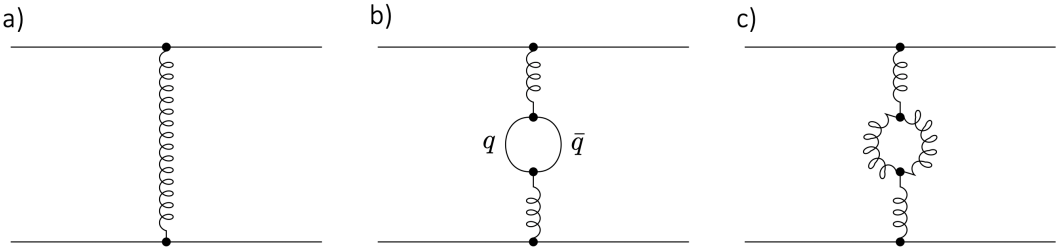

Figure 1.3: In each of these diagrams, the arrow of time goes from left to right. Diagram a) represents an interaction between two color charges (quarks or gluons) at leading order, while diagram b) represents a screening contribution of the interaction, and diagram c) the anti-screening one. By convention, quarks are represented by straight lines, while gluons are represented by curly lines. In this case, each of the horizontal line could have been a curly line instead. Vertices are indicated with a black dot.

In the case where the gluon fluctuates in a $q\bar{q}$ pair (diagram b in figure 1.3), the interaction is "screened": because of the presence of the $q\bar{q}$ pair, the perceived color charge by one or the other interacting object is reduced.

On the other hand, the vacuum will also be filled with virtual gluon pairs (diagram c in figure 1.3), which is allowed since QCD is non-abelian. Because the gluon cloud carries a color charge, it turns out that the effective color charge becomes more significant with a larger distance, i.e., with smaller Q^2. This effect is called "anti-screening".

Re-normalization of the strong coupling

Higher-order diagrams also contribute to the coupling, but these are neglected in the following. Considering the quark loops (diagram b) and the gluon loops (diagram c), the strong coupling constant is renormalized using a reference scale $Q^2 = \mu^2$ arbitrarily chosen and for which the strong coupling $\alpha_s(\mu^2)$ is known [11]:

$$\alpha_s(Q^2) = \frac{\alpha_s(\mu^2)}{1 + \beta_0 \alpha_s(\mu^2) \ln(Q^2/\mu^2)} \text{ with } \beta_0 = \frac{11N_c - 2N_f}{12\pi} \tag{1.1}$$

[4]According to Heisenberg's uncertainty principle, the energy and lifetime of a particle cannot be known exactly and simultaneously. This principle is written $E\Delta t \leq \hbar$, or equivalently $E \leq \hbar/\Delta t$. Given the relation $E = mc^2$, a particle may exist for a very brief moment.

where N_c is the number of colors, and N_f is the number of flavors. The value of $\alpha_s(Q^2)$ does not depend on the chosen renormalization scale μ^2. The factor $-2N_f/(12\pi)$ in β_0 comes from diagram b and causes screening, while the factor $+11N_c/(12\pi)$ comes from diagram c and causes anti-screening. Clearly with $N_c = 3$ and $N_f = 6$, the anti-screening wins over the screening, $\beta_0 > 0$, and α_s decreases with Q^2.

Measurements of the running coupling constant as a function of Q are shown in figure 1.4.

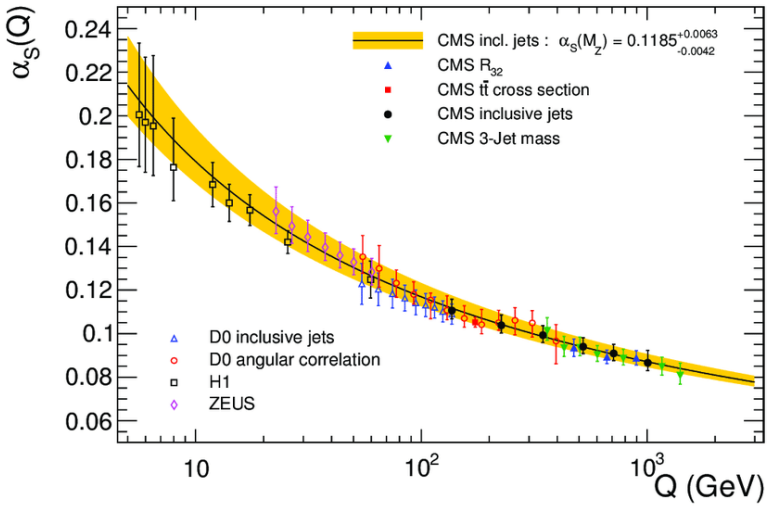

Figure 1.4: Measurements of the strong coupling constant α_s as a function of the energy scale $Q = \sqrt{Q^2}$. Figure taken from reference [12].

For high values of squared momentum transfer Q^2 - corresponding to very small distances between quarks - the strong coupling decreases, canceling out asymptotically. This causes the quarks inside hadrons to behave more or less as free particles. This phenomenon, called *asymptotic freedom*, was described by Gross, Wilczek and Politzer in 1973 [13]. In this domain, perturbation theory[5] can be used to predict hard scattering cross sections[6] in hadronic interactions. In this limit and to the first order [11], the expression 1.1 becomes

$$\alpha_s(Q^2) = \frac{12\pi}{(11N_c - 2N_f)\ln(Q^2/\Lambda^2_{\mathrm{QCD}})} \tag{1.2}$$

where Λ_{QCD} is defined as the scale at which α_s diverges, and was measured to be $\Lambda_{\mathrm{QCD}} \approx 200$ MeV.

Conversely at smaller Q^2 (larger distances between the interacting particles) the coupling becomes so strong that it is impossible to detach the individual quarks from the hadrons (it becomes cheaper to create a quark-antiquark pair which form a new hadron). This property is called *color confinement*, and explains why quarks cannot exist in a free state and are always *confined* in color-neutral particles (hadrons).

[5] In the perturbative regime of the QCD, theoretical predictions can be made starting from a known solution to which one applies a slight variation, which makes it possible to find the approximate solution of a problem, typically in the form of a series development of the powers of the parameter α_s where the inequality $\alpha_s \ll 1$ holds.

[6] The cross section, noted σ, is a physical quantity related to the probability of interaction of a particle for a given reaction. It has the dimension of a surface.

The behavior of quarks and gluons is studied by probing hadrons, typically protons which are the most stable hadrons.

1.2 Probing the proton structure in deep inelastic scattering

One of the simplest known hadrons is the proton, which is stable and abundant in the universe. Therefore it constitutes an ideal subject for studying its components, quarks and gluons, and testing their behavior in the high energy limit, i.e. in a frame of reference in which the proton is traveling at high speed and has its time dilated according to the principles of special relativity.

One way to know the structure of an object would be to break it by smashing it against another object and observe its components. Similarly, to understand the structure of the proton, particle accelerators have been built. Two types of interactions can take place. The first type of interaction is the elastic collision, in which the kinetic energy is conserved before and after the interaction, like two billiard balls bouncing on each other. In this type of process, each of the colliding particles interacts as a whole. The second type of interaction is the inelastic collision, in which the kinetic energy is not conserved. Part of the initial kinetic energy is converted into internal energy in at least one of the bodies, therefore the interaction takes place with one of the components of this body rather than with the whole. It is this type of interaction that has been brought into play to discover the internal structure of the proton, called Deep Inelastic Scattering (DIS), where the term "deep" refers to the fact that the target hadron is probed at small distances with respect to its size.

1.2.1 The discovery of partons in deep inelastic scattering

Since electrons and protons are abundant, stable and electricly charged particles, they can be easily accelerated to high energies via the application of electromagnetic fields. And as the electron is an elementary particle, it cannot dissociate and is considered point-like. Thus, electrons are ideal projectiles for probing the interior of protons in deep inelastic scattering. Though other collision systems are possible, only interactions of target protons and electrons are discussed in the following. A nice review of Deep Inelastic Scattering (DIS) with further details is presented in reference [14].

Kinematic description of deep inelastic scattering

The DIS process is illustrated in figure 1.5: a point-like electron with an incident quadri-momentum l collides with a proton. A virtual photon γ^* is emitted by the electron, and is then absorbed by the proton, transferring energy to one of its constituent quarks: instead of scattering off the proton, the point-like electron scatters off a quark inside the proton. The proton dissociates and the scattered quark is then eliminated from the proton. The final hadronic system, denoted X, is formed by the dissociated proton and new particles grouped in a jet and produced by the scattered quark in a process called hadronization.

The scattered electron is detected, and from the measurement of its final momentum l' one can deduce the momentum $q = l - l'$ transferred by the virtual photon to the proton.

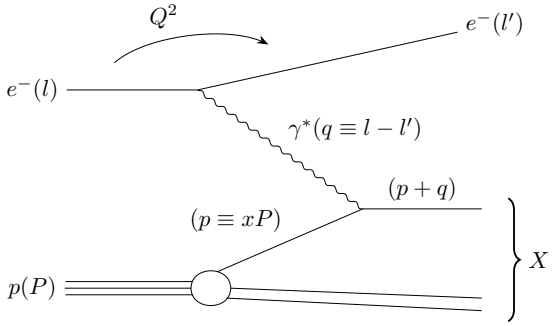

Figure 1.5: The electron probes the proton by emitting a virtual photon γ^*. Only one parton (quark or gluon) of the proton is involved in the interaction, represented by the line coming out of the blob. The quadri-moments are noted in parentheses.

The DIS process is described with two variables, arbitrarily chosen as the Bjorken-x scale and the virtuality[7] Q^2 of the virtual photon, defined as:

$$Q^2 = -q^2 = -(l - l')^2 \quad \text{and} \quad x \equiv \frac{Q^2}{2P \cdot q} = \frac{Q^2}{s + Q^2 - M_p^2}, \tag{1.3}$$

where P is the quadri-moment of the proton, $s \equiv (P + q)^2$ is the squared invariant energy of the system $\gamma^* p$, and M_p is the mass of the proton.

The Bjorken–x variable is the scale at which the proton is probed, and corresponds to the longitudinal momentum fraction x of the proton carried by the parton (quark or gluon) with which the virtual photon has interacted. Given equation 1.3, the higher the invariant energy of the system $\gamma^* p$, the lower the Bjorken–x scale at which the proton is probed.

On the other hand the virtuality Q^2 defines the scale of the interaction, as we have already seen in section 1.1.2. By analogy with a microscope, it defines the length fineness r with which the partons are probed, related to Q^2 by $r = \hbar c / \sqrt{Q^2}$. At low energy of the projectile and therefore low Q^2, a baryon only contains three quarks, and a meson only one quark-antiquark pair. These are called the valence quarks, and are present in the hadron throughout its existence. If the incident lepton arrives with sufficiently high energy, high virtuality photons can be produced. At high Q^2, it becomes possible to observe the virtual particles resulting from the quantum fluctuations of the states of the hadron (see figure 1.6). These virtual particles, called sea quarks, are explained in QCD as a cloud of quarks produced by gluons fluctuating to quark-antiquarks pairs, which recombine very quickly and are visible within a laps of time that is inversely proportional to $\sqrt{Q^2}$. Thus, the sea of partons gathers all the quark-antiquark pairs and gluons which appear and disappear permanently in the hadron.

Emergence of the parton model

In 1968, the new linear electron accelerator is commissioned at the Stanford Linear Accelerator Center (SLAC), and the SLAC-MIT experiment then studies inelastic electron-proton collisions. At that time, the theory of QCD had not even been developed yet, and the proton was thought

[7] When the particle under consideration is not "on-shell" (on one of the outer lines of the corresponding Feynman diagram), its virtuality Q^2 denotes the inverse of its four-moment (q) squared, $Q^2 = -q^2 > 0$.

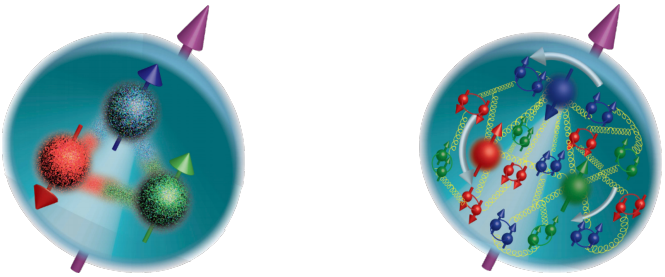

Figure 1.6: Representation of the proton with only its valence quarks probed at low Q^2 (left), or valence and sea quarks at high Q^2 (right). The sea quarks are represented by pairs of the same color. Image taken from reference [15].

to be a "soft" object with a relatively even internal distribution of its electrical charge [16]. They measured the differential cross section for electron scattering $\mathrm{d}^2\sigma/\mathrm{d}\Omega dE$ for a given scattering angle Ω and energy loss E of the scattered electron after the collision, as shown in figure 1.7, normalized with the cross section of electron scattering on a point-like particle [17, 18] calculated using the *Mott formula* [19]. The observed discrepancy of the measured cross section and the Mott formula at large Q^2 gives evidence that the proton is not a point-like particle.

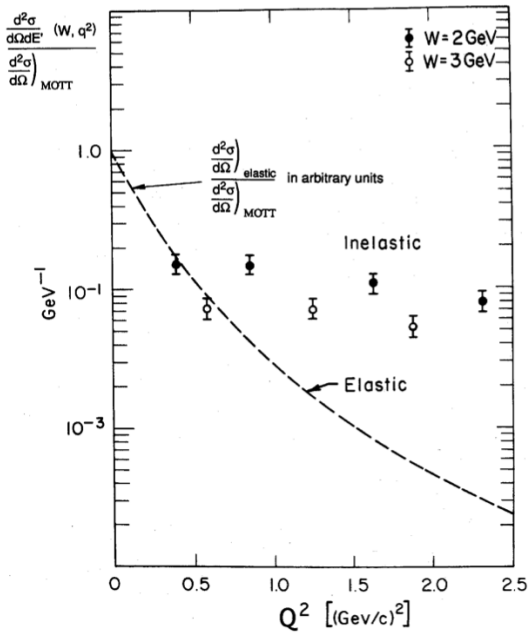

Figure 1.7: Electron scattering cross-sections from the first inelastic scattering experiments performed at SLAC by the SLAC-MIT collaboration, as a function of Q^2. The Q^2-dependence shows the striking difference between elastic and inelastic cross-sections for two values of invariant mass W of the recoiling hadronic final state.

Moreover, the cross section of DIS was found to decrease much more slowly with Q^2 than that for elastic scattering at large values of energy transferred by the electron and Q^2, as shown in figure 1.7. This property is called *scaling*, and was interpreted by the physicist R. P. Feynman during his visit at SLAC in August 1968 as scattering on point-like constituents within the target proton. The reasoning is the following: since Q^2 corresponds to a length scale, the

independence of the dynamics of DIS on Q^2 implies that the small and hard objects inside the proton are dimensionless somehow. The idea that protons were made up of a certain number of elementary constituents which behave like free particles was first suggested in 1966 by the physicist J. D. Bjorken [20, 21]. Based on Bjorken's idea and SLAC data, Feynman proposed in 1969 the "parton model", that assumes that the high-energy electrons were elastically scattered from point-like bits of charge in the protons [22, 23]. Subsequently, the partons described in this model were identified with quarks and gluons.

In the modern quark parton model (QPM), the proton is described as a composite object, made of valence quarks (two up and one down quarks), sea quarks (pairs of up, down, strange, charm and bottom quark-antiquarks) and gluons, which serve as the mediating carriers of the strong force binding the quarks within the proton. Subsequent experiments investigated how these objects are distributed in the proton, using mathematical objects called Parton Distribution Functions (PDFs).

1.2.2 Parton distribution functions

Measuring parton distribution functions in deep inelastic scattering

Let us consider anew DIS of electrons and protons. Since electrons (e) are subjected to the electromagnetic and weak interactions, they can interact with the proton (p) via the exchange of a photon γ, but also of Z and $W^{\pm}$ bosons (see figure 1.8). They are sorted in two types: neutral current (NC) reactions are mediated by a (uncharged) photon or a Z boson while in charged current (CC) scattering a (charged) $W^{\pm}$ boson is exchanged. These two types of reaction are easily distinguishable, since in the first case the electron is detected in the final state, whereas in the second case a neutrino is produced in the final state.

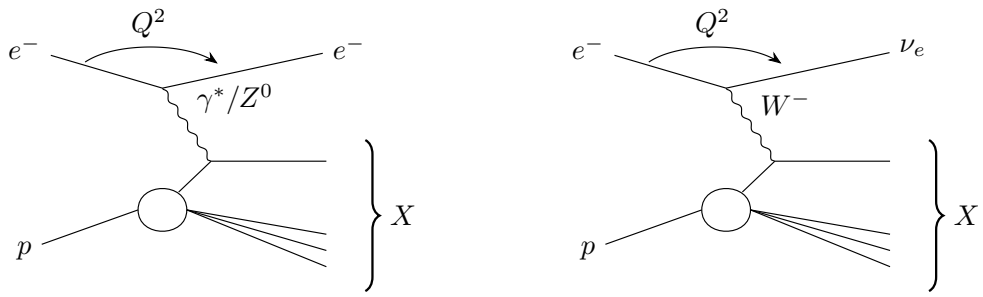

Figure 1.8: Representation at leading order of neutral current (left) and charged current (right) interactions.

In general terms within the QPM, the cross sections for ep-scattering are determined using the couplings of the point-like electrons, the properties of the exchanged bosons (γ, Z, W), and a set of inelastic proton structure functions F_i. These functions F_i are directly related to combinations of the so-called Parton Distribution Functions $xq_i(x)$, referred to as PDFs. PDFs are interpreted at LO as the probability[8] that a certain parton i carries a fraction x of the total proton momentum, and thus characterize the proton structure at the parton level. Within QCD theory, the PDFs $q_i(x, Q^2)$ depend on the x variable and the Q^2 scale.

[8] At NLO, PDFs can take negative values or values larger than 1, see for example reference [24].

As an example, the NC cross section can be expressed in terms of the F structure functions as [25]:

$$\frac{d^2\sigma_{NC}^{e^\pm p}}{dxdQ^2} = \frac{2\pi\alpha^2}{xQ^4}[Y_+\tilde{F}_2^\pm \mp Y_- x\tilde{F}_3^\pm - y^2\tilde{F}_L^\pm] \text{ with } Y_\pm = 1 \pm (1+y)^2 \text{ and } y = \frac{Q^2}{xs} \quad (1.4)$$

where α is the fine structure constant, y is the inelasticity and s the center-of-mass energy in the ep system. The structure function $\tilde{F}_2$ is the dominant contribution to the cross section, and is associated to pure photon exchange (see figure 1.8 on the left-hand-side with γ^*).

The Q^2-dependence of PDFs $q_i(x, Q^2)$ can be accurately described by perturbative evolution equations (see e.g. reference [26]). However, the x-dependence of the PDFs at low Q^2 cannot be obtained by analytical calculation. Given the size of the proton, the typical distance between the quarks at low Q^2 is such that the coupling constant is large and the usual calculation methods based on perturbative developments, successfully used in the case of a small coupling at high energies, are not applicable. Therefore the x-dependence of the PDFs can only be determined from the experimental data, as performed by various groups.

Herein, the individual PDFs as extracted by HERA (Hadron Elektron Ring Anlage) working groups based on HERA data only are discussed [27, 28]. Measurements from various other experiments, such as fixed-target, proton-antiproton scattering, proton-proton $W^\pm/Z^0$ production, or neutrino experiments, can also contribute information on the PDFs. Reference [29] provides a complete review of PDF measurements.

Parton distribution functions by HERA experiments

The HERA (Hadron Elektron Ring Anlage) collider, located at DESY (Deutsches Elektronen-Synchrotron) in Hamburg, was operated in the years 1992-2007. It was considered at that time the largest electron microscope in the world, where the DIS process in $e^\pm p$ was studied in collisions with energies in the center of mass $\sqrt{s}$ extending from 225 to 318 GeV. The kinematic region studied allowed to scan the quark and gluon PDFs in the proton down to $x \sim 10^{-4}$ with good precision, in a region never explored before. The attainable "spatial" resolution available δ to probe the composite proton, characterized by the scale Q^2 with $\delta \approx (\hbar c)/\sqrt{Q^2}$, reaches at HERA the level of 10^{-18} m. This means resolving details of a size 1000 times smaller than the size of the proton, measured already in the fifties to be around 10^{-15} m. Both neutral and charged currents reactions were analyzed by two experiments, H1 and ZEUS.

The combined H1 and ZEUS measurements of so-called reduced cross sections σ_r of the NC interactions are shown in figure 1.9 as a function of the scaling variable Q^2 for different x values. The reduced cross sections are directly proportional to the dominant structure function F_2 (see equation 1.4) associated to pure photon exchange. In the QPM picture, these data provide direct sensitivity to the valence quark content of the proton at high x, and to sea quarks and gluons at low x values.

Though the *scaling* is seen at high x, confirming the SLAC-MIT observation, the variation with Q^2 of the reduced cross sections of the NC interactions is increasingly violent for lower x. This phenomenon, called *scaling violation*, was not included in the QPM but was predicted by the QCD theory. In the QPM, only valence quarks were taken into account. However, developments of QCD theory led to the prediction that when x decreases, quark–gluon interactions become important and other processes can contribute. The two most important additional processes are related to the emission of gluons and of the "sea" of quark-antiquark pairs. The QCD calculations (red curves) describe remarkably well the precise data obtained at HERA over the

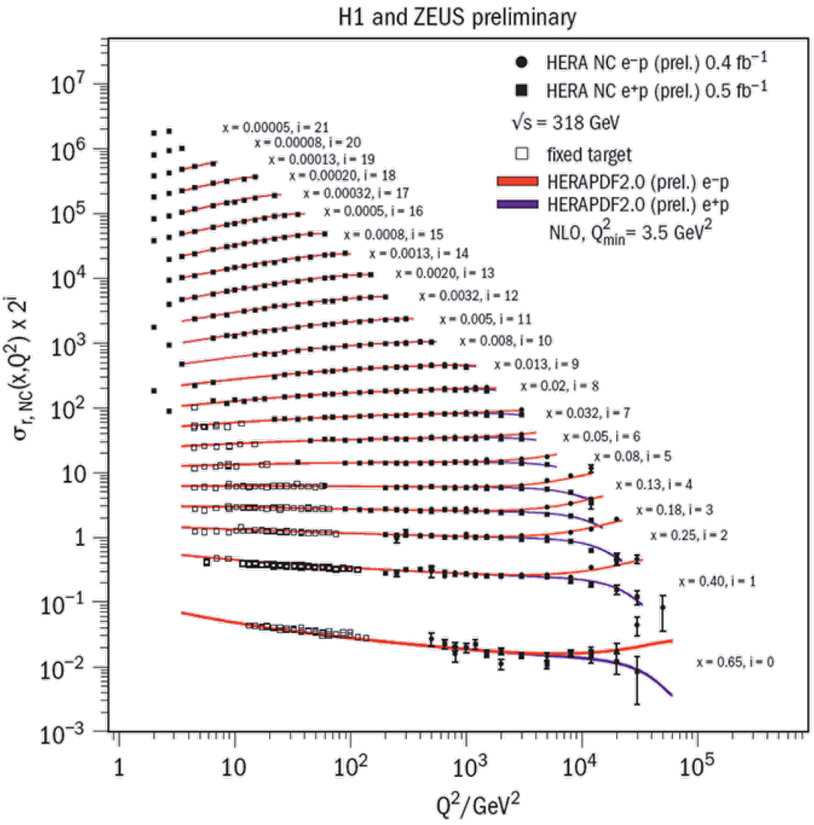

Figure 1.9: Reduced cross sections for neutral current processes measured by the H1 and ZEUS experiments, as a function of the scaling variable Q^2 for different values of x, the proton momentum fraction carried by the partons. The red curves represent the calculations based on the theory of strong interactions. Figure taken from reference [30].

very large kinematic range explored, and therefore this constitutes a great success of the QCD theory.

The analysis of the inclusive DIS data of the H1 and ZEUS experiments allowed the "HERA structure function working group" to extract the individual PDFs $xq_i(x)$ for the various partons of the proton [30, 31], referred to as HERAPDFs. These are represented in figure 1.10 at the scale $Q^2 = 10$ GeV^2. The valence quark contributions are prominently visible at high x, peaking around $x \approx 1/3$. The up quarks xu_v are twice as frequent as the down quark xd_v, which was interpreted as the proton having two up and one down valence quarks, corresponding to the naive expectations in which the total proton momentum is equally shared among the three valence quarks. When considering lower values of x, the sea quarks (x_S) and the gluons (x_g) (both scaled down by a factor of 20 for visibility in the figure) increase substantially and become completely dominant. Since sea quarks interact with the incoming electron within a laps of time that is inversely proportional to $\sqrt{Q^2}$, the amount of "visible" sea quarks at low x also increases with Q^2 : the higher Q^2, the shorter the time of interaction, increasing thereby the chances to reveal the gluon-to-quarks fluctuations. At low x, the proton appears to be filled with an explosive density of gluons.

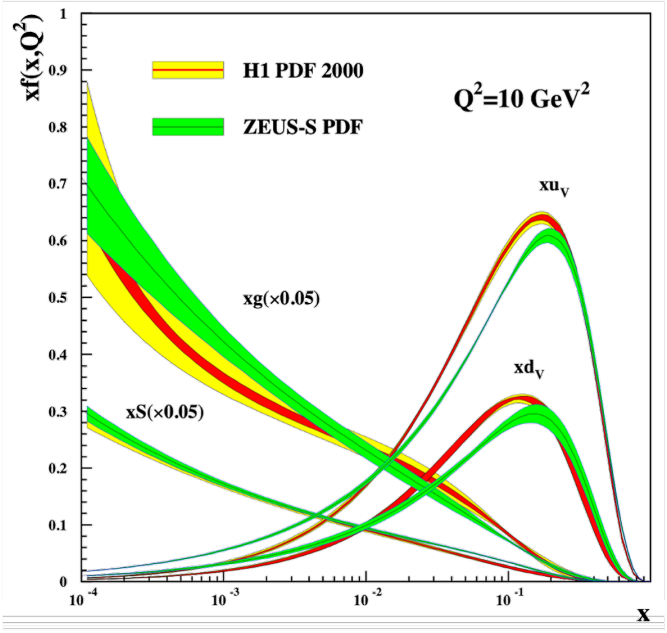

Figure 1.10: The valence quark (xu_v, xd_v), gluon (xg) and sea quark (x_S) distributions in a proton, as measured at HERA for $Q^2 = 10$ GeV^2. The gluon distribution is scaled down by a factor of 20. Figure taken from reference [30].

As already mentioned, even if the exact shape of the PDFs cannot be predicted, their evolution with Q^2 is calculable. The next section introduces the perturbative equations of QCD theory which describe the parton evolution.

1.3 Description of parton evolution in perturbative QCD

The QCD theory has proven itself successful in describing the available data where the perturbative equations are applicable. Two linear equations which describe the evolution of partons with the proton momentum fraction carried by the partons x and the scale Q^2 are herein introduced. The behavior of gluons at small x is discussed via the introduction of a new QCD framework, which includes corrections to the actual QCD that would tame the fast growth of gluon densities towards smaller x in the proton, as observed at HERA.

1.3.1 Linear perturbative equations of parton evolution in QCD

At LO, perturbative evolution equations are obtained by assuming that the variation of the parton density at x is given by the convolution of the parton density at $x' > x$ times the probability of emitting a gluon with fraction x/x' of the quark momentum. Let us start with a single fast-moving parton of momentum p within a hadron (quark or gluon). The probability of emitting a gluon, called gluon *bremsstrahlung*, with longitudinal momentum $k_z = xp$ and relative transverse momentum $k_\perp \ll k_z$ is, for small values of x,

$$dP \sim \alpha_s \frac{d^2\vec{k}_\perp}{\vec{k}_\perp^2} \frac{dx}{x} \tag{1.5}$$

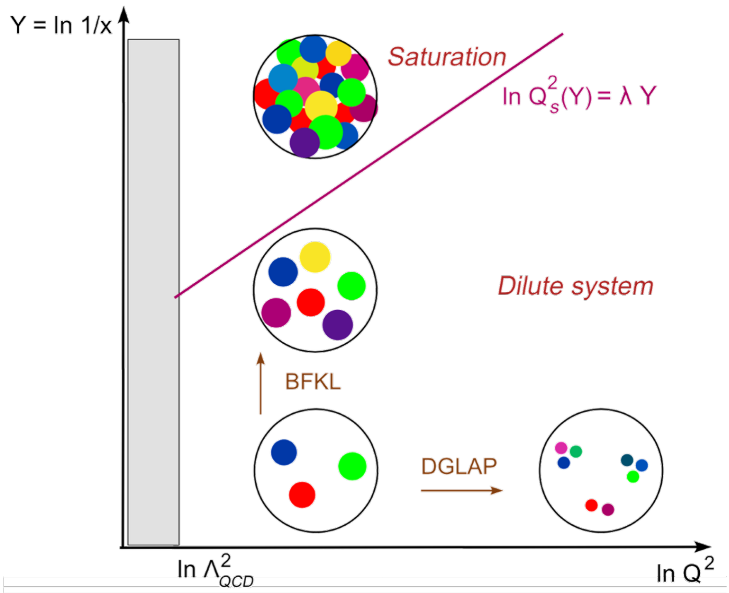

Figure 1.11: A cartoon of the QCD evolution in the kinematical plane for deep inelastic scattering.

This equation is the starting point to describing the evolution of partons in QCD at high energy. It exhibits singularities, i.e, it diverges for $k_\perp \to 0$ or $x \to 0$. Two QCD perturbative equations provide a compact tool to resum the radiative corrections to all orders in the form of differential equations in x or in Q^2.

The DGLAP equation

The DGLAP equation, named after the physicists who developed it (Y. Dokshitzer, V. Gribov, L. Lipatov, G. Altarelli and G. Parisi) [32–38], describes the evolution of the parton distributions with the resolution scale at which they are probed - i.e. with increasing virtuality Q^2, as illustrated in figure 1.11.

Considering x fixed, at the lowest order in the QCD coupling α_s, the integrated probability for gluon bremsstrahlung is obtained from equation 1.5 as:

$$P_{1-\text{emission}} \sim \alpha_s \ln(Q^2) \tag{1.6}$$

and the probability for n gluon emission is given by:

$$P_{n-\text{emission}} \sim (\alpha_s \ln(Q^2))^n \tag{1.7}$$

At the lowest order in the QCD coupling α_s, the DGLAP equation is a renormalization group equation for parton distribution functions that takes into account the radiative corrections enhanced by factors of $(\alpha_s \ln(Q^2))^n$ for all $n \geq 1$. According to the DGLAP equation, the number of gluons rises logarithmically with Q^2 while the surface occupied by each gluon decreases like $1/Q^2$. Considering the overall proton size fixed, the gluons in the proton become more and more **dilute**.

The predictions of the DGLAP equation - including its later refinements to NLO and NNLO - are very well confirmed by high Q^2 experimental data from HERA for the DIS structure functions [27, 39, 40].

The BFKL equation

The BFKL equation [41–43], named after the four physicists Yanko Balitsky, Viktor Fadine, Eduard Kuraiev and Lev Lipatov, describes the evolution of the parton density at fixed Q^2 and increasing energy (i.e. decreasing x), as illustrated in figure 1.11.

At the lowest order in the QCD coupling α_s and fixed Q^2, the integrated probability for gluon bremsstrahlung at small values of x is obtained from equation 1.5 and evolves according to

$$P_{1-\text{emission}} \sim \alpha_s \ln(1/x) \tag{1.8}$$

Even when the coupling α_s is small enough to ensure the applicability of perturbation theory, for sufficiently low values of x the large logarithm $\ln(1/x)$ compensates the smallness of the strong coupling and the probability for gluon bremsstrahlung becomes close to one. This suggests that successive gluon emissions with even smaller longitudinal moments $1 \gg x_1 \gg ... \gg x_n \gg x$ are also likely to occur (see figure 1.12). Considering that the new gluons live long enough to act coherently as sources of new gluon emissions, the probability of n-gluon emission is

$$P_{n-\text{emission}} \sim \alpha_s^n \int_x^1 \frac{dx_1}{x_1} ... \int_{x_{n-1}}^1 \frac{dx_n}{x_n} = \frac{1}{n!}(\alpha_s \ln(1/x))^n \tag{1.9}$$

which is also of order one. These contributions are re-summed in the BFKL evolution equation. With the precision of LO in $\alpha_s \ln(1/x)$, the BFKL equation predicts that the gluon distribution grows as a power of $1/x$, namely as

$$xg(x) \sim (1/x)^\lambda \text{ with } \lambda = (12 \ln 2/\pi)\alpha_s. \tag{1.10}$$

This fast growth of the gluon distribution towards smaller x is due to the successive gluon emissions in a chain reaction, leading to a so-called gluon shower as shown on the right-hand side of figure 1.12. The total surface occupied by gluons, $\sim xg(x, Q^2)/Q^2$, then increases much faster than the transverse area of the proton, which increases at most logarithmically with the energy, therefore with $1/x$. The gluons are brought to overlap in the transverse plane when their total number becomes sufficiently large: a **high density** regime is reached.

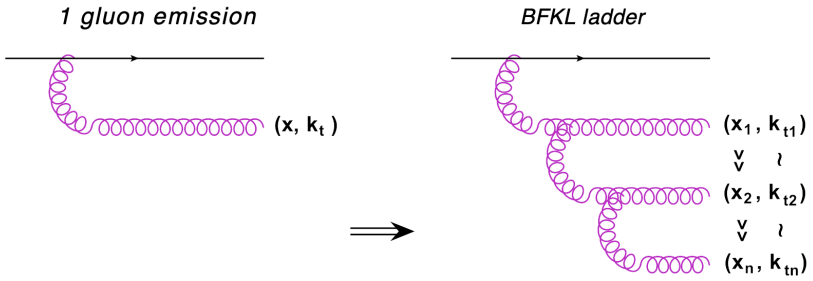

Figure 1.12: Schematic representation of diagrams relevant for small-x evolution: one gluon emission (left), and a BFKL ladder (right). Figure taken from reference [44].

The BFKL equation and its NLO corrections [45, 46] are very successful in modeling the DIS data taken at HERA, in a domain where Q^2 is large enough to ensure the applicability of perturbative calculations. The power-like growth of gluon densities in hadrons with decreasing x [44] predicted by the BFKL equation is observed in measurements of DIS at HERA, as shown

in figure 1.10. However, when the gluon distribution given in equation 1.10 is extrapolated to the high energy limit, i.e. $x \to 0$, this behavior predicts a divergence of the gluon density, which violates the unitarity[9] [47, 48] of the QCD theory, as well as the Froissart-Martin bound [49], as asserted in several reviews [44, 50, 51]. The Froissart-Martin bound states that in QCD, the total cross-section of a process cannot grow faster than the logarithm of the squared energy $\ln^2(s)$. As a consequence, it has been proposed that a new non-linear dynamics would emerge at sufficiently small x: the color fields (the gluons) could exert a retroaction on each other, taming the avalanche of gluons towards the small x domain (known as "soft") and restoring the unitarity of the theory. This domain is described by the effective field theory called the Color Glass Condensate (CGC), which includes the non-linear retroaction terms of this high-density environment on the evolution itself.

1.3.2 Gluon saturation in the color glass condensate framework

The BFKL and DGLAP equations are based on the implicit starting assumption that the considered hadron remains a dilute parton system at each stage of the evolution. Thus, each emitter (the gluons) acts independently and without any interference. However, this hypothesis can no longer be valid for sufficiently large gluon densities. Instead, the emission process of other gluons is expected to be coherent, i.e., gluon bremsstrahlung comes from all the emitters and no longer from individual emitters, causing destructive interference terms to appear. These non-linear terms would thus depend on the pre-existing color charge density. They can be interpreted as the feedback of this high-density environment on the evolution itself, such as gluon recombination processes (figure 1.13). Such processes would oppose an additional growth of the gluon distribution, giving rise to the **saturation**. This phenomenon was first hypothesized by L. Gribov, Levin and Ryskin [52].

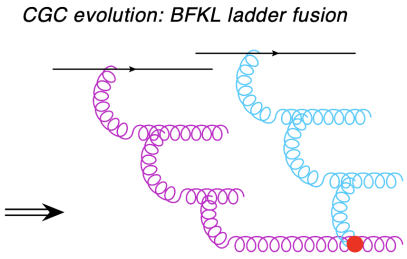

Figure 1.13: Schematic representation of the BFKL ladder fusion in color glass condensate non-linear evolution for small-x evolution. Figure taken from reference [44].

Domain of applicability of the Color Glass Condensate

Let us consider the proton as a homogeneous disk of radius R. The cross section corresponding to the probability that the respective gluon will be absorbed by any other gluon in the hadron,

[9] In quantum mechanics, unitarity designates the fact that the evolution of the wave function over time must be compatible with the probabilistic interpretation associated with it: $\iiiint \psi(X) d^4X$.

$gg \to g$, can be estimated by [53]:

$$\sigma_{gg\to g}(x, Q^2) \sim \frac{\alpha_s N_c}{N_c^2 - 1} \frac{xg(x, Q^2)}{Q^2} \tag{1.11}$$

where N_c is the number of colors. The recombination probability for a gluon $\Gamma(x, Q^2)$ is then obtained by dividing the cross section by the transverse area of the proton πR^2:

$$\Gamma(x, Q^2) \sim \frac{\alpha_s N_c}{Q^2} \frac{xg(x, Q^2)}{(N_c^2 - 1)\pi R^2} \tag{1.12}$$

Saturation is reached when the recombination probability becomes of order one. This condition defines a critical line relative to Q^2 and x, namely $Q^2 = Q_s^2$ with Q_s the saturation momentum [52, 54]:

$$\Gamma(x, Q^2) \sim 1 \Leftrightarrow Q_s^2(x) \sim \frac{\alpha_s N_c}{N_c^2 - 1} \frac{xg(x, Q_s^2)}{\pi R^2} \tag{1.13}$$

As established in the previous section (equation 1.10), as long as the saturation regime is not reached (domain of validity of the equation BFKL for x low enough), the gluon distribution increases as a power-law with $1/x$. According to the equation 1.13, the same behavior is expected for the saturation momentum squared $Q_s^2(x)$:

$$xg(x, Q_s^2) \propto (1/x)^\lambda \Rightarrow Q_s^2(x) \propto (1/x)^\lambda \Leftrightarrow \ln Q_s^2(Y) = \lambda Y + K \tag{1.14}$$

where $Y \equiv \ln 1/x$ and K is a constant. Therefore Q_s^2 grows as a power of $1/x$, so $\ln Q_s^2(Y)$ grows linearly along Y, as shown in figure 1.11. It separates a dilute regime at $Q^2 > Q_s^2$ in which the gluons act as independent emitters and linear equations are applicable, and a high-density regime at $Q^2 < Q_s^2$, where the gluons act coherently and interference terms appear. This latter regime is described by the Color Glass Condensate (CGC), which designates matter consisting of saturated gluons in which recombination processes compensate for radiative processes (bremsstrahlung). In this description, the gluons arrange themselves in the transverse plane so as to mutually shield their color charges, and color neutrality is achieved over a distance of order $r \sim (\hbar c)/\sqrt{Q_s^2}$ [55, 56]. Thus, the saturation momentum $Q_s \equiv \sqrt{Q_s^2}$ can be interpreted as a color neutrality scale. The condition $Q_s(x) \gg \Lambda_{\text{QCD}}$, obtained if x is low enough according to equation 1.14, guarantees that the CGC is weakly coupled ($\alpha_s \ll 1$). As a result, the physics of CGC is constantly perturbative, especially as the energy is high.

Description of the Color Glass Condensate

The theory of Color Glass Condensate (CGC) was named in references [57, 58] because of its physical properties.

- **Color**: The theory deals with the gluons which carry the "color" charge of QCD.
- **Glass**: Color fields (gluons) are disordered since they are weakly coupled, and they have very long lifetimes compared to natural time scales for high energy $\sim \ln(1/x)$ scattering. Its internal dynamics is then considered frozen.

- **Condensate**: High-density matter consisting of saturated gluons is a Bose-Einstein condensate[10] and gluons can be considered as classical fields, which allows calculations with classical techniques.

The CGC model was proposed based on Balitsky-Kovchegov (BK) non-linear evolution equation [59–61]. The BK equation describes the evolution of the amplitude of the scattering of a photon fluctuating to a color dipole $q\bar{q}$ on a hadronic target with rapidity[11]. This process is characterized by the exchange of one or several *pomerons*, a colorless object which in its simplest form is assumed to be formed of two gluons. In the BFKL equation, this process is described considering only single dipole-parton interactions: it is implicitly assumed that the color dipole "sees" only one parton, which is an acceptable approximation if Q^2 is high and x is not too small (partons are in a *dilute* regime). However, when the partons within the hadron overlap, the $q\bar{q}$ pair no longer sees a single parton. In this case, processes are represented by *fan graphs*, where Feynman diagrams are resummed by the probability that a gluon of momentum fraction x_0 evolves to a collection of n gluons with momentum fractions $x_0 \gg x_i \gg x_n$ through all the possible intermediate emissions of gluons. In the BK equation, the corrections due to the re-summing of the fan diagrams in the leading-logarithmic approximation are added to the standard BFKL evolution process. These situations are represented in figure 1.14. On the left, the color dipole scatters off only one parton, leading to the usual BFKL equation, while on the right, multiple scatterings - neglected by the BFKL evolution - occur.

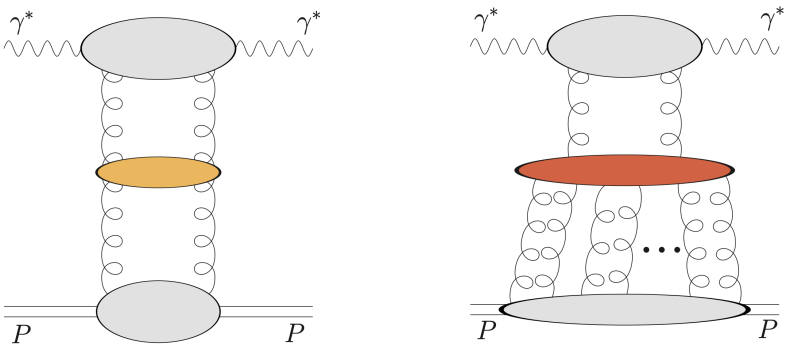

Figure 1.14: BFKL ladder (left) and fan graphs (right).

A subsequent phenomenological approach superseded the BK evolution equation to describe the CGC: the JIMWLK equation [58, 62–66], named after J. Jalilian-Marian, E. Iancu, L. McLerran, H. Weigert, A. Leonidov, and A. Kovner, or its NLO version [67, 68]. This renormalization group generates an effective Lagrangian for low x fields by integrating out all quantum fluctuations around the classical "background" gluon field. The low x gluon fields then are determined by solving classical equations that follow from this effective Lagrangian. This integrating out procedure changes the color charge density distribution in the effective Lagrangian. While in the BK equation, the quantum corrections from re-summing multiple rescatterings are

[10] A Bose-Einstein condensate is a state of matter apparent at the macroscopic level, formed of identical bosons, such that a large number of these particles occupy a single quantum state at the lowest energy level, the ground state.

[11] In special relativity, the rapidity, denoted y, is a measure of a particle motion. At low speed, the rapidity tends towards 0, while at speeds close to the celerity of light, the rapidity tends towards infinity. It is a dimensionless quantity.

implemented for the dipole-target scattering amplitude, the quantum fluctuations are added to the evolution for the strong gluon field at small-x in the JIMWLK equation.

The BK equation is regarded as the mean-field approximation of JIMWLK equation. The non-saturating regime and the saturating regime are well connected by both equations, and the unitarization of the high energy hadron scattering can be restored. The BK and JIMWLK evolution equations are based on parametrizations determined from existing data.

Both BK and JIMWLK equations are hallmarked by geometric scaling. For large values of Q^2 such that the target is dilute, typically $Q^2 > Q_s^2(x)$, non-linear terms can be neglected and the BFKL equation is recovered. However in the saturated regime $Q^2 < Q_s^2(x)$, their solutions noticeably differ from the BFKL solution and provide some interesting insights on the non-linear corrections to the BFKL evolution at high energy hadron scattering.

Detailed reviews on the technical aspects of the CGC formalism can be found for example in the references [69, 70].

Finding evidence of the Color Glass Condensate

The CGC is expected to be observable both in protons and in larger nuclei, at least indirectly, in collisions of high-energy protons and nuclei (p-A) or simply high-energy nuclei (A-A) in accelerators, at the Relativistic Heavy Ion Collider (RHIC) (Brookhaven, USA) and at the LHC (CERN). In such collisions, the CGC is expected to be formed at early stages of the interaction, and thus to determine the properties of the resulting parton system. The CGC theory can also be tested in *ultra-peripheral* collisions where the nuclei (p-A or A-A) intersect without nuclear overlap, but interact via the emission of photons, which is equivalent to photon-nucleus collisions. Thus the structure of nuclei - or protons depending on the collision system studied - can be probed by a photon at small x, revealing the behavior of small-x partons.

1.4 Unveiling the proton structure in ultra-peripheral collisions

As discussed in the previous section, perturbative Quantum ChromoDynamics (pQCD) predicts that the gluon density in hadrons increases with energy, or equivalently with decreasing Bjorken-x, to a point where non-linear effects are expected to tame this growth. This phenomenon is known as gluon saturation. The explosive growth of gluon density has been measured using the DIS process at HERA down to Bjorken-$x \sim 10^{-4}$ (see section 1.2.2). However, the analysis of HERA data is inconclusive regarding the gluon saturation issue, as the data can be described without (see e.g. reference [28]), or with (e.g. reference [71]) saturation effects. Gluon saturation can be investigated in ultra-peripheral collisions of nuclei, and in particular, in collisions of lead (Pb) nuclei and protons which is the subject of study in the following chapters. In such collisions, interactions between photons emitted by Pb nuclei and protons can result in the production of a J/ψ meson (bound state of the charmed quark and antiquark $c\bar{c}$ with a mass close to 3 GeV/c^2), final carriers of information on the structure of the proton. This section introduces ultra-peripheral collisions and describes the production mechanisms of vector mesons, particularly the J/ψ photoproduction off protons.

1.4.1 Ultra-peripheral collisions and photons from lead nuclei

An Ultra-Peripheral Collision (UPC) is a collision of two nuclei radiating a strong electromagnetic field, which intersect with a distance in the transverse plane - also called impact parameter and denoted b - larger than the sum of their two radii, as shown in figure 1.15. When nuclei travel at speeds close to the speed of light (*ultra-relativistic* speed), the two nuclei are contracted in the longitudinal direction - they are said to be *Lorentz-contracted*. The electromagnetic field

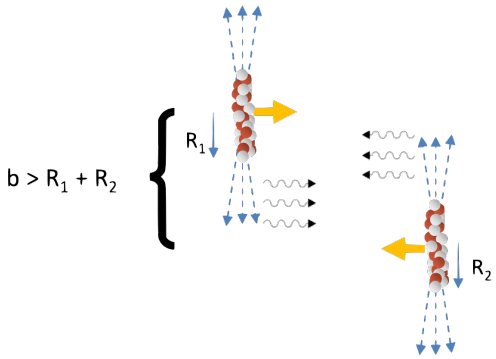

Figure 1.15: Schematic view of an ultra-peripheral collision of relativistic nuclei.

surrounding them is concentrated in the direction perpendicular to the direction of motion and can be considered as a flux of virtual photons [72–75]. The intensity of the electromagnetic field, and therefore the number of photons in the cloud surrounding the nucleus, is proportional to the square of the electric charge of the hadron, $(Ze)^2$ where Z is the number of protons in the nucleus and e is the elementary charge. Since the strong interaction has a short range, hadronic processes (mediated by gluons directly) are suppressed and the long-range electromagnetic force becomes dominant over the strong interaction.

Two scenarios can arise. In the first case, a virtual photon from one of the two nuclei probes the structure of the other nucleus, analogously to DIS. In the second case, two photons from the two nuclei interact, and these two-photon interactions can lead to the production of lepton pairs driven by quantum electrodynamics, of η_c or χ_{c0} particles, or pairs of bosons $W^{\pm}$. Thus, the domain of UPC physics is very broad, and particles in a wide mass range can be studied. Excellent reviews of UPC physics are given in references [76–78].

Photon - proton interactions resulting in the production of J/ψ vector mesons[12] are hereunder studied [78]. UPCs of protons and Pb nuclei ($Z = 82$) are ideal for studying this process. The J/ψ can be photoproduced either off protons ($\gamma\mathrm{p}$) where the photon is emitted from a Pb nucleus, or off Pb nuclei where the photon comes from a proton. However, since event rates in UPCs of nuclei depend on the photon flux $\mathrm{d}N_\gamma/\mathrm{d}k$ which scales as Z^2 in photoproduction, in p–Pb collisions J/ψ mesons are photoproduced 95% of the time off protons via the emission of a photon from the Pb ion.

Photons are produced coherently by the nucleus, i.e. they are produced by all its constituents and not by a single proton of the nucleus. Thus, their wavelength λ is limited by the

[12] A vector meson is a hadronic particle composed of two quarks with parallel spins. The vector meson has spin 1.

nucleus size. In ultra-relativistic collisions, since the nucleus is Lorentz-contracted, its longitudinal size is R_A/γ_L, where R_A is the nuclear radius and γ_L the Lorentz factor of the nucleus, hence the relation

$$\lambda > R_A/\gamma_L \text{ with } R_A \approx 1.2A^{1/3} \text{ [fm]} \tag{1.15}$$

where A is the number of nucleons. Consequently, the energy of coherently emitted photons is limited by a maximum given by:

$$E_\gamma = \frac{\hbar c}{\lambda} < \frac{\gamma_L \hbar c}{R_A} \tag{1.16}$$

At the highest-available LHC nuclear beam energies and for Pb beams, the maximum energy is $E_\gamma \sim 100$ GeV, corresponding to a Lorentz boost of $\gamma_L = 2595$.

Moreover, the virtuality of photons Q^2 is limited by the nuclear radius,

$$Q^2 < \left(\frac{\hbar c}{R_A}\right)^2 \approx 10^{-3} \text{ GeV}^2 \text{ with } R_A = 7 \text{ fm (size of a Pb ion)}, \tag{1.17}$$

and is negligible in UPCs. Photons can be treated as real and as such are often referred to as "quasi-real" in the Weizsäcker-Williams equivalent photon approximation (EPA) [74, 75].

1.4.2 Vector meson photoproduction in the color dipole model

In p–Pb UPCs, the photon emitted by the Pb nucleus may fluctuate into a quark–anti-quark pair and, since the photon has spin 1 and negative parity[13], the fluctuation will most likely be to a vector meson (*Vector Meson Dominance*). Thus the interaction of a quasi-real photon with a proton can produce a vector meson in a process called diffractive[14] photoproduction:

$$\gamma^* + \mathrm{p} \to V + \mathrm{p}/X$$

where the proton can either remain intact after the interaction or dissociate in a state denoted X, and V refers to a vector meson ($V = \rho, \phi, \mathrm{J}/\psi, \Upsilon, ...$), in our study $V = \mathrm{J}/\psi$.

To describe the diffractive production of vector mesons, we use the rest frame of the proton, or more precisely the "dipole picture" [79]. Given the energy of the photon E_γ and its virtuality Q^2, the dipole picture is defined such that $E_\gamma \gg Q$ but $\alpha_s \ln(E_\gamma/Q) \ll 1$ (leading twist approximation), and the photon decomposes according to the QCD Fock states in a 'bare' photon plus hadronic fluctuations:

$$|\gamma^*\rangle = c_0|\gamma\rangle + c_1|q\bar{q}\rangle + c_2|q\bar{q}g\rangle + ... \tag{1.18}$$

with $c_0 \sim 1$, $c_1 \sim \alpha_{\text{em}}$, $c_2 \sim \alpha_{\text{em}} \times \alpha_S \ln(E_\gamma/Q)$, and α_{em} is the fine structure constant. In the rest frame of the proton, the energy of the photon E_γ is greater than the virtuality Q. At high energies, the condition $E_\gamma \gg Q$ ensures that the lifetime of the quark-antiquark fluctuation ($\sim \hbar/(E_{q\bar{q}} - E_\gamma)$ where $E_{q\bar{q}}$ is the energy of the fluctuation) is much longer than the time scale of the dipole-target interaction ($\sim R_A/c\gamma_L$). Consequently, the transverse coordinates of the quark and of the antiquark which make up the dipole are considered to be "frozen" during the interaction with the hadron.

[13] In quantum mechanics, the parity transformation is the change in the sign of a spatial coordinate.

[14] Diffraction was first defined in optics to describe the behavior of waves when they encounter an obstacle or a hole. The image resulting from the scattering of light off a target provides insight on the properties of the target. Similarly in high energy particle collisions, diffraction provides information on the target depending on the impact parameter of the collision.

On the other hand, the condition $\alpha_s \ln(E_\gamma/Q) \ll 1$ guarantees that one can ignore Fock states at higher order in α_s like $|q\bar{q}g\rangle$: the dipole is a 'naked' pair with no extra gluons.

Thus, at the lowest order in $\alpha_{\rm em}$, the diffractive production of vector mesons can then be described by a process in which the photon fluctuates in a $q\bar{q}$ pair (or color dipole) at a large distance from the proton target.

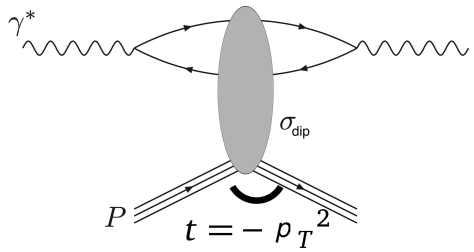

Figure 1.16: The dipole picture of deep inelastic scattering. Figure taken from reference [80].

This dipole interacts with the proton target via a color singlet exchange, which in the lowest order in QCD corresponds to a colorless pair of gluons [81, 82] (see figure 1.16). This interaction is characterized by the cross section of the color dipole $\sigma_{\rm dip}$. Finally, long after the interaction, the dipole forms a vector meson.

The structure of the proton is probed at the longitudinal momentum fraction

$$x_{\mathbb{P}} = \frac{M_V^2 + Q^2 - t}{W_{\gamma\rm p}^2 + Q^2 - M_p^2} \tag{1.19}$$

which is analogous to DIS Bjorken-x. Here $W_{\gamma\rm p}$ is the center-of-mass energy for the photon-proton scattering, M_V the mass of the produced vector meson, Q^2 the virtuality of the photon and M_p the mass of the proton. The energy of the photon-proton center of mass $W_{\gamma\rm p}$ is given by:

$$W_{\gamma\rm p}^2 = 2E_p M_V \exp(-y), \tag{1.20}$$

where E_p is the energy of the proton beam and y the rapidity of the produced vector meson. A derivation of this formula is given in appendix A. The rapidity is an experimentally measured quantity given by:

$$y = \frac{1}{2}\ln((p_0 + p_z)/(p_0 - p_z)) \tag{1.21}$$

where p_μ is the quadri-momentum of the produced vector meson. According to the equation 1.19, and in the limit where $Q^2 \sim 0$ and $t \to 0$, the proton is then probed at a Bjorken-x scale directly dependent on the $W_{\gamma\rm p}$ energy of the γp center-of mass energy:

$$x_{\mathbb{P}} = \left(\frac{M_V}{W_{\gamma\rm p}}\right)^2 \tag{1.22}$$

In the following, the vector meson considered is a J/ψ particle.

1.4.3 Photoproduction of J/ψ mesons off protons in p–Pb UPCs

The J/ψ photoproduction on a proton target can leave the proton intact in an elastic interaction, or the proton can dissociate. This section deals with these two processes and their physical interpretation.

Exclusive J/ψ photoproduction off protons

Let us consider first the exclusive J/ψ photoproduction off protons. This diffraction is said to be coherent, and the target proton remains in the same quantum state after the interaction, as shown in figure 1.17.

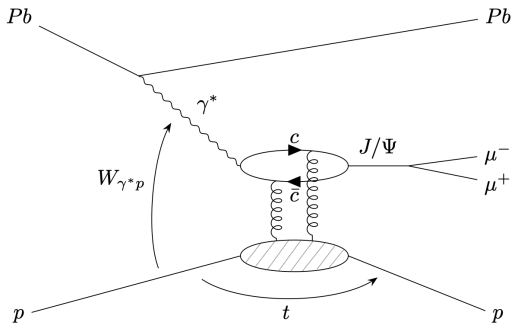

Figure 1.17: Feynman diagram for the exclusive J/ψ photoproduction at LO.

Using the Good-Walker formalism [83], the cross section of the coherent process is determined by the average interaction of the states $|i\rangle$, which correspond at LO to the fluctuation $q\bar{q}$ of the photon. One obtains [84]:

$$\frac{\mathrm{d}\sigma}{\mathrm{d}t}(\gamma \mathrm{p} \to \mathrm{J}/\psi \mathrm{p}) = \frac{1}{16\pi} \sum_i \left| \langle i | \mathcal{A}^{\mathrm{coh}} | i \rangle \right|^2 \tag{1.23}$$

$$= \frac{1}{16\pi} \left| \left\langle \mathcal{A}^{\mathrm{coh}} \right\rangle \right|^2 \tag{1.24}$$

where t is the square of the momentum transfer at the target vertex (at high energies $t \approx -p_{\mathrm{T}}^2$ with p_{T} the transverse momentum of the J/ψ) and $\mathcal{A}^{\mathrm{coh}}$ is the amplitude of the diffractive scattering[15]. The target proton is probed on all its possible configurations. Consequently, the scattering amplitude is sensitive to the average interaction of the $q\bar{q}$ dipole with the target from event to event. Since the dominant contribution at small x in the target proton are gluons, this interaction is mostly controlled by their average distribution. More precisely, the cross section of the exclusive J/ψ photoproduction in the LO approximation, with zero momentum transfer $t \to 0$ and negligible photon virtuality ($Q^2 \sim 0$) is given by the Ryskin result [81, 85, 86]:

$$\left.\frac{\mathrm{d}\sigma}{\mathrm{d}t}(\gamma \mathrm{p} \to \mathrm{J}/\psi \mathrm{p})\right|_{t=0} = \frac{\Gamma_{ee} M_{\mathrm{J}/\psi}^3 \pi^3}{48\alpha} \left[\frac{\alpha_s(\bar{Q}^2)}{\bar{Q}^4} (x g(x, \bar{Q}^2) \right]^2 \left(1 + \frac{Q^2}{M_{\mathrm{J}/\psi}} \right) \tag{1.25}$$

with

$$\bar{Q}^2 = (Q^2 + M_{\mathrm{J}/\psi}^2)/4 \approx M_{\mathrm{J}/\psi}^2/4 \tag{1.26}$$

$$\text{and } x = (Q^2 + M_{\mathrm{J}/\psi}^2)/(W_{\gamma \mathrm{p}}^2 + Q^2) \approx (M_{\mathrm{J}/\psi}/W_{\gamma \mathrm{p}})^2 \tag{1.27}$$

where Γ_{ee} is the width of the dielectron decay, $M_{\mathrm{J}/\psi}$ is the rest mass of the J/ψ, and $x g(x, Q^2)$ is the gluon PDF. The J/ψ being a heavy meson ($M_{\mathrm{J}/\psi} \sim 3$ GeV/c^2), $\bar{Q}^2$ is large enough to

[15] In quantum mechanics, the scattering amplitude $\mathcal{A}^{\mathrm{coh}}$ is the probability amplitude of a process. The probability $\mathcal{P}$ itself is obtained through the relation $\mathcal{P} = |\mathcal{A}|^2$.

guarantee a weak coupling α_s for the strong interaction and it is possible to describe the process in pQCD.

Equation 1.25, however, assumes that the two interacting gluons carry the same fraction x of the proton longitudinal momentum. In fact, the two exchanged gluons carry different fractions $x - \xi$ and $x + \xi$ where ξ is the *skewness* parameter. This asymmetry can be corrected for using Generalized Parton Distribution functions (GPDs) in the equation instead of the usual PDFs, which are conjectured to be connected at high energy via the Shuavev transform [87]. GPDs are functions of three variables, x, ξ and t, and thus make it possible to take into account the difference in longitudinal moment carried by the two interacting gluons and hence better describe the structure of hadrons. They are a recent theoretical approach that provide information about the spin and orbital angular momentum of the quarks and gluons in the nucleon, and are determined experimentally from exclusive processes [88, 89].

Nevertheless, the equation 1.25 remains valid in very good approximation for this process at LO, with $t \to 0$ and $Q^2 \sim 0$. Clearly in this form the cross section is sensitive to the small x gluon distribution. The dependence of the cross section on the squared gluon PDF implies that the cross section has a power law dependence on x in the domain where saturation effects are negligible[16], assuming that $xg(x, Q^2) \propto (1/x)^\lambda$ as predicted by the BFKL evolution (equation 1.10). Given the expression 1.27, the cross section is expected to increase like a power law with $W_{\gamma\mathrm{p}}$,

$$\sigma(\gamma\mathrm{p} \to \mathrm{J}/\psi\mathrm{p}) \propto W_{\gamma\mathrm{p}}^{\delta} \tag{1.28}$$

where δ is an experimentally measured number.

The exclusive cross section $\sigma(\gamma\mathrm{p} \to \mathrm{J}/\psi\mathrm{p})$ has been measured at HERA in DIS as previously discussed, but also at CERN with ALICE in Run 1 and with the LHCb experiment in Runs 1 and 2. These measurements are shown in figure 1.18 as a function of $W_{\gamma\mathrm{p}}$. By combining data from HERA and ALICE in Run 1, the power in $W_{\gamma\mathrm{p}}$ was determined to be $\delta = 0.65 \pm 0.02$. The measurement of ALICE data during Run 2 is the subject of this thesis.

Furthermore, the cross section for diffractive J/ψ photoproduction as a function of the $\gamma\mathrm{p}$ center-of-mass energy $W_{\gamma\mathrm{p}}$ is computed in reference [85] as:

$$\sigma(\gamma\mathrm{p} \to \mathrm{J}/\psi\mathrm{p}) = \frac{1}{b_{\mathrm{exc}}} \frac{d\sigma}{dt}(\gamma\mathrm{p} \to \mathrm{J}/\psi\mathrm{p})\Big|_{t\to 0} \tag{1.29}$$

where the slope parameter b_{exc} is measured experimentally and is related to the transverse[17] proton radius R_p via $R_p \sim \sqrt{2b_{\mathrm{exc}}}$. Hence the t-dependence of the cross section follows the exponential proportionality

$$\sigma(\gamma\mathrm{p} \to \mathrm{J}/\psi\mathrm{p}) \propto \exp(-b_{\mathrm{exc}} t) \tag{1.30}$$

From this equation, b_{exc} is interpreted as the Fourier conjugate of the squared transverse momentum transfer t, and the t slope directly measures the size of the proton.

Therefore, the exclusive J/ψ photoproduction not only probes the density of partons (essentially gluons), but is also sensitive to their spatial distribution in the plane of impact parameters.

[16] Recent studies presented in reference [90] show however that the scaling on the cross section with x may change from LO to NLO.

[17] The transverse plane corresponds to the plane of impact parameters.

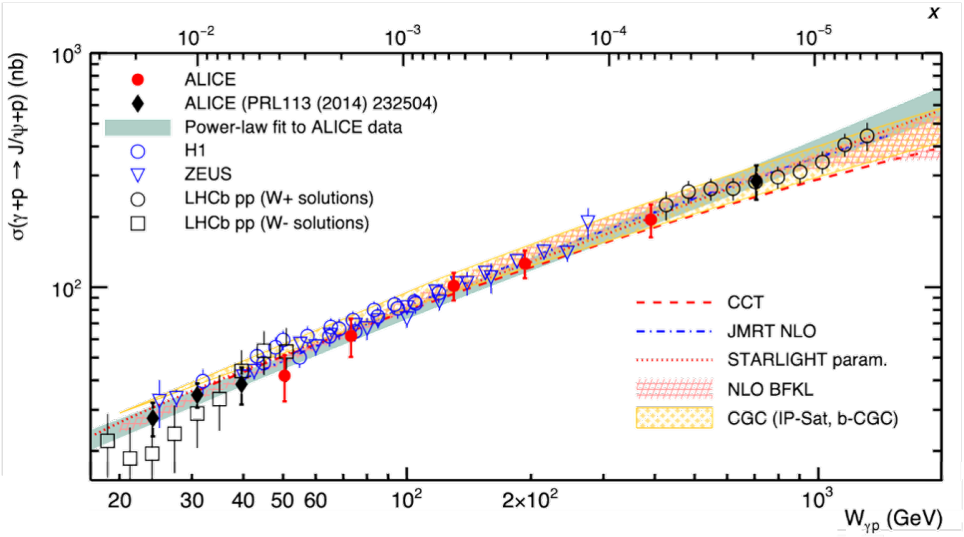

Figure 1.18: Measurements of the exclusive photoproduction of J/ψ off protons as a function of the center-of-mass energy of the photon–proton system $W_{\gamma p}$. The Bjorken-x value corresponding to $W_{\gamma p}$ is also displayed on the top of the figure. Figure taken from reference [91].

Dissociative J/ψ photoproduction off protons

Let us consider now the dissociative J/ψ photoproduction off protons. This diffraction is said

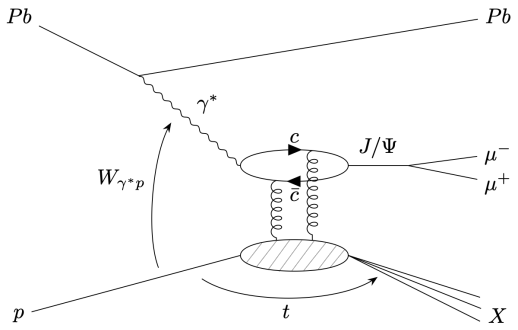

Figure 1.19: Feynman diagram for the dissociative J/ψ photoproduction at LO.

to be incoherent, and the target proton does not remain in the same quantum state after the interaction [92], as shown in figure 1.19. Instead, it dissociates into a low-mass system $M_X > M_p$ where M_X denotes the mass of the dissociated system (proton remnants) and M_p denotes the mass of the proton. The dissociative process is characterized by a rapidity gap between the J/ψ and the proton remnants, which experimentally manifests itself as a large region in a detector which do not show any activity.

Analogously to the calculation of the coherent cross section in the equation 1.23, the cross section of the incoherent process is determined by the interaction of the initial states $|i\rangle$ that exit in a different final state $|f\rangle$. Thus, the squared scattering amplitude $\mathcal{A}$ reads

$$\sum_{f\neq i} |\langle f|\mathcal{A}|i\rangle|^2 = \sum_f \langle i|\mathcal{A}^*|f\rangle\langle f|\mathcal{A}|i\rangle - \langle i|\mathcal{A}^*|i\rangle\langle i|\mathcal{A}|i\rangle = \langle i|\mathcal{A}^*\mathcal{A}|i\rangle - |\langle i|\mathcal{A}|i\rangle|^2 \tag{1.31}$$

The cross section is given by the squared amplitude $\mathcal{A}^{\text{incoh}}$ averaged over all possible initial states $|i\rangle$ [93].

$$\frac{d\sigma}{dt}(\gamma p \to \mathrm{J}/\psi X) = \frac{1}{16\pi}\sum_i \sum_{f\neq i} |\langle f|\mathcal{A}^{\text{incoh}}|i\rangle|^2 \tag{1.32}$$

$$= \frac{1}{16\pi}\sum_i \langle i|(\mathcal{A}^{\text{incoh}})^* \mathcal{A}^{\text{incoh}}|i\rangle - |\langle i|\mathcal{A}^{\text{incoh}}|i\rangle|^2 \tag{1.33}$$

$$= \frac{1}{16\pi}\left(\left\langle \left|\mathcal{A}^{\text{incoh}}\right|^2 \right\rangle - \left|\left\langle \mathcal{A}^{\text{incoh}} \right\rangle\right|^2\right) \tag{1.34}$$

Thus, the incoherent cross section is directly proportional to the variance[18] of $\mathcal{A}^{\text{incoh}}$ and it measures the fluctuations between the different possible initial state configurations of the target proton.

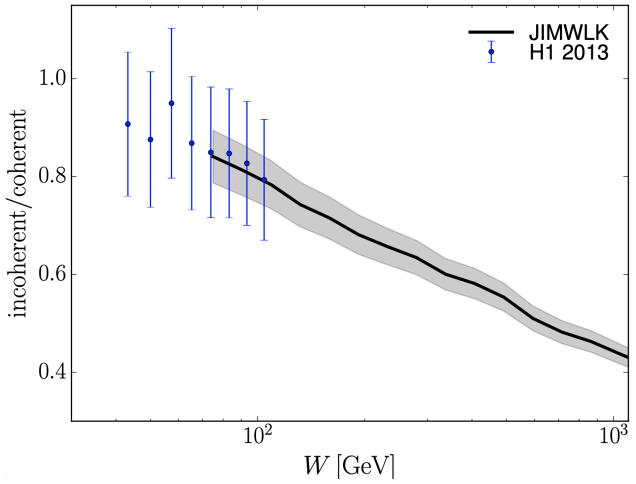

Figure 1.20: JIMWLK evolution of the ratio of incoherent and coherent cross sections with $W_{\gamma p}$, adapted to fit H1 data. Figure taken from reference [93].

Figure 1.20 shows the calculated incoherent and coherent cross sections ratio as a function of the energy $W_{\gamma p}$ using the JIMWLK parametrization (described in section 1.3.2). At high energy, the incoherent cross section is expected to vanish with respect to the coherent one [93]. This behavior, if observed experimentally, would demonstrate that the geometric fluctuations of the proton are suppressed at high energy, indicating a sign of saturation of the gluon PDF in the proton.

The LHC can explore a wide range of $W_{\gamma p}$ in p–Pb UPCs from a few tens of GeV to over a TeV, making it an ideal place to look for a clear signature of gluon saturation.

1.5 Summary

The data provided by the HERA collider brought a milestone in understanding the proton structure down to $x \sim 10^{-4}$. The proton PDFs are so far well described by linear perturbative

[18] In statistics and probability theory, the variance is a measure of the dispersion of values in a sample or a probability distribution. Be X a real random variable, its variance is given by $V(X) = \langle X^2\rangle - \langle X\rangle^2$ where $\langle\rangle$ designates the average.

equations, although non-linear effects are expected to tame the fast growth of gluons at low Bjorken-x values. This phenomenon, called gluon saturation, can be investigated in photon-proton interactions through heavy vector meson photoproduction. Ultra-peripheral collisions of protons and Pb nuclei are used to study this process.

The analysis work of this thesis focuses on the measurement of the exclusive (or coherent) and dissociative (or incoherent) cross sections of J/ψ photoproduction off protons at the LHC, which is the largest particle collider under operation. In the case of the exclusive process, the measurement is sensitive to the average distribution of gluons on different ranges in Bjorken-x. Moreover, it probes the structure of the proton in the transverse plane. The dissociative process on the other hand is a powerful tool to study gluon saturation in the proton at high energies, as it is controlled by the geometric fluctuations in the proton. Therefore, the ratio of incoherent to coherent cross sections is expected to vanish in the regime of gluon saturation.

The next chapter describes the measuring device used in this analysis: the ALICE experiment.

Bibliography

[1] Mary K. Gaillard, Paul D. Grannis, and Frank J. Sciulli. The Standard model of particle physics. *Rev. Mod. Phys.*, 71:S96–S111, 1999. doi: 10.1103/RevModPhys.71.S96.

[2] Michael E. Peskin. *Concepts of Elementary Particle Physics*. Oxford Master Series in Physics. Oxford University Press, 9 2019. ISBN 978-0-19-881218-0, 978-0-19-881219-7. doi: 10.1093/oso/9780198812180.001.0001.

[3] Peter Kalmus. Strange Beauty: Murray Gell-Mann and the Revolution in Twentieth Century Physics. *European Journal of Physics*, 21:275, 05 2000. doi: 10.1088/0143-0807/21/3/701.

[4] Wikipedia, the free encyclopedia, 2010. URL https://en.wikipedia.org/wiki/Standard_Model. [Online; accessed 28-May-2022].

[5] S. Chatrchyan et al. Observation of a new boson at a mass of 125 GeV with the CMS experiment at the LHC. *Physics Letters B*, 716(1):30–61, 2012. ISSN 0370-2693. doi: https://doi.org/10.1016/j.physletb.2012.08.021. URL https://www.sciencedirect.com/science/article/pii/S0370269312008581.

[6] G. A. et al. Observation of a new particle in the search for the Standard Model Higgs boson with the ATLAS detector at the LHC. *Physics Letters B*, 716(1):1–29, 2012. ISSN 0370-2693. doi: https://doi.org/10.1016/j.physletb.2012.08.020. URL https://www.sciencedirect.com/science/article/pii/S037026931200857X.

[7] S.-K. Choi et al. Observation of a Resonancelike Structure in the $\pi^{+-}\psi'$ Mass Distribution in Exclusive $B \to K\pi^{+-}\psi'$ Decays. *Phys. Rev. Lett.*, 100:142001, Apr 2008. doi: 10.1103/PhysRevLett.100.142001. URL https://link.aps.org/doi/10.1103/PhysRevLett.100.142001.

[8] Roel Aaij et al. Observation of $\mathrm{J}/\psi\mathrm{p}$ resonances consistent with pentaquark states in $\Lambda_b^0 \to J/\psi K^-\mathrm{p}$ decays. *Phys. Rev. Lett.*, 115:072001, 2015. doi: 10.1103/PhysRevLett.115.072001.

[9] F. Halzen and Alan D. Martin. *Quarks and leptons: an introductory course in modern particle physics*. 1984. ISBN 978-0-471-88741-6.

[10] M. J. G. Veltman. *Diagrammatica: The Path to Feynman rules*, volume 4. Cambridge University Press, 5 2012. ISBN 978-1-139-24339-1, 978-0-521-45692-0.

[11] Alexandre Deur, Stanley J. Brodsky, and Guy F. de Teramond. The QCD Running Coupling. *Nucl. Phys.*, 90:1, 2016. doi: 10.1016/j.ppnp.2016.04.003.

[12] David d'Enterria and Peter Z. Skands, editors. *Proceedings, High-Precision α_s Measurements from LHC to FCC-ee: Geneva, Switzerland, October 2-13, 2015*, Geneva, 12 2015. CERN.

[13] David J. Gross. The discovery of asymptotic freedom and the emergence of QCD. *Proceedings of the National Academy of Sciences*, 102(26):9099–9108, 2005. ISSN 0027-8424. doi: 10.1073/pnas.0503831102. URL https://www.pnas.org/content/102/26/9099.

[14] Gunther Piller and Wolfram Weise. Nuclear deep inelastic lepton scattering and coherence phenomena. *Phys. Rept.*, 330:1–94, 2000. doi: 10.1016/S0370-1573(99)00107-6.

[15] Engineering National Academies of Sciences and Medicine. *An Assessment of U.S.-Based Electron-Ion Collider Science*. The National Academies Press, Washington, DC, 2018. ISBN 978-0-309-47856-4. doi: 10.17226/25171. URL https://nap.nationalacademies.org/catalog/25171/an-assessment-of-us-based-electron-ion-collider-science.

[16] G. F. Chew, Murray Gell-Mann, and A. H. Rosenfeld. Strongly Interacting Particles. *Sci. Am.*, 210N2:74, 1964. doi: 10.1038/scientificamerican0264-74.

[17] E. D. Bloom, D. H. Coward, H. DeStaebler, J. Drees, G. Miller, L. W. Mo, R. E. Taylor, M. Breidenbach, J. I. Friedman, G. C. Hartmann, and H. W. Kendall. High-Energy Inelastic $e - p$ Scattering at 6° and 10°. *Phys. Rev. Lett.*, 23:930–934, Oct 1969. doi: 10.1103/PhysRevLett.23.930. URL https://link.aps.org/doi/10.1103/PhysRevLett.23.930.

[18] M. Breidenbach, J. I. Friedman, H. W. Kendall, E. D. Bloom, D. H. Coward, H. DeStaebler, J. Drees, L. W. Mo, and R. E. Taylor. Observed Behavior of Highly Inelastic Electron-Proton Scattering. *Phys. Rev. Lett.*, 23:935–939, Oct 1969. doi: 10.1103/PhysRevLett.23.935. URL https://link.aps.org/doi/10.1103/PhysRevLett.23.935.

[19] M.J. Boschini, C. Consolandi, M. Gervasi, S. Giani, D. Grandi, V. Ivanchenko, P. Nieminem, S. Pensotti, P.G. Rancoita, and M. Tacconi. An expression for the Mott cross section of electrons and positrons on nuclei with Z up to 118. *Radiation Physics and Chemistry*, 90:39–66, 2013. ISSN 0969-806X. doi: https://doi.org/10.1016/j.radphyschem.2013.04.020. URL https://www.sciencedirect.com/science/article/pii/S0969806X13002454.

[20] J. D. Bjorken. Density algebras and their saturation. *Conf. Proc. C*, 670828:490–502, 1967.

[21] J. D. Bjorken and E. A. Paschos. Inelastic electron-proton and γ-proton scattering and the structure of the nucleon. *Phys. Rev.*, 185:1975–1982, Sep 1969. doi: 10.1103/PhysRev.185.1975. URL https://link.aps.org/doi/10.1103/PhysRev.185.1975.

[22] R. Feynman. *Photon-hadron interactions*. 1972.

[23] J I Friedman and H W Kendall. Deep inelastic electron scattering. *Annual Review of Nuclear Science*, 22(1):203–254, 1972. doi: 10.1146/annurev.ns.22.120172.001223. URL https://doi.org/10.1146/annurev.ns.22.120172.001223.

[24] H. Hosseinkhani and M. Modarres. The LO and the NLO unintegrated parton distributions in the modified DGLAP formalism. *Physics Letters B*, 708(1):75–86, 2012. ISSN 0370-2693. doi: https://doi.org/10.1016/j.physletb.2012.01.020. URL https://www.sciencedirect.com/science/article/pii/S0370269312000330.

[25] R. Plačakytė. Structure Functions and PDF determination at HERA. In *48th Rencontres de Moriond on QCD and High Energy Interactions*, pages 349–352, 2013.

[26] R. Devenish and A. Cooper-Sarkar. *Deep inelastic scattering*. 2004. doi: 10.1093/acprof:oso/9780198506713.001.0001.

[27] F. D. Aaron et al. Combined Measurement and QCD Analysis of the Inclusive e+- p Scattering Cross Sections at HERA. *JHEP*, 01:109, 2010. doi: 10.1007/JHEP01(2010)109.

[28] H. Abramowicz et al. Combination of measurements of inclusive deep inelastic $e^{\pm}p$ scattering cross sections and QCD analysis of HERA data. *Eur. Phys. J. C*, 75(12):580, 2015. doi: 10.1140/epjc/s10052-015-3710-4.

[29] Jacob J. Ethier and Emanuele R. Nocera. Parton Distributions in Nucleons and Nuclei. *Ann. Rev. Nucl. Part. Sci.*, 70:43–76, 2020. doi: 10.1146/annurev-nucl-011720-042725.

[30] F. D. Aaron et al. Inclusive Deep Inelastic Scattering at High Q^2 with Longitudinally Polarised Lepton Beams at HERA. *JHEP*, 09:061, 2012. doi: 10.1007/JHEP09(2012)061.

[31] S. Chekanov et al. Measurement of neutral current cross sections at high Bjorken-x with the ZEUS detector at HERA. *Eur. Phys. J. C*, 49:523–544, 2007. doi: 10.1140/epjc/s10052-006-0164-8.

[32] V. N. Gribov and L. N. Lipatov. Deep inelastic e p scattering in perturbation theory. *Sov. J. Nucl. Phys.*, 15:438–450, 1972.

[33] Guido Altarelli and G. Parisi. Asymptotic Freedom in Parton Language. *Nucl. Phys. B*, 126:298–318, 1977. doi: 10.1016/0550-3213(77)90384-4.

[34] Yuri L. Dokshitzer. Calculation of the Structure Functions for Deep Inelastic Scattering and e+ e- Annihilation by Perturbation Theory in Quantum Chromodynamics. *Sov. Phys. JETP*, 46:641–653, 1977.

[35] G. Curci, W. Furmanski, and R. Petronzio. Evolution of Parton Densities Beyond Leading Order: The Nonsinglet Case. *Nucl. Phys. B*, 175:27–92, 1980. doi: 10.1016/0550-3213(80)90003-6.

[36] W. Furmanski and R. Petronzio. Singlet Parton Densities Beyond Leading Order. *Phys. Lett. B*, 97:437–442, 1980. doi: 10.1016/0370-2693(80)90636-X.

[37] S. Moch, J. A. M. Vermaseren, and A. Vogt. The Three loop splitting functions in QCD: The Nonsinglet case. *Nucl. Phys. B*, 688:101–134, 2004. doi: 10.1016/j.nuclphysb.2004.03.030.

[38] A. Vogt, S. Moch, and J. A. M. Vermaseren. The Three-loop splitting functions in QCD: The Singlet case. *Nucl. Phys. B*, 691:129–181, 2004. doi: 10.1016/j.nuclphysb.2004.04.024.

[39] S. Chekanov et al. Measurement of the neutral current cross-section and F(2) structure function for deep inelastic e + p scattering at HERA. *Eur. Phys. J. C*, 21:443–471, 2001. doi: 10.1007/s100520100749.

[40] C. Adloff et al. Deep inelastic inclusive e p scattering at low x and a determination of alpha(s). *Eur. Phys. J. C*, 21:33–61, 2001. doi: 10.1007/s100520100720.

[41] L. N. Lipatov. Reggeization of the Vector Meson and the Vacuum Singularity in Nonabelian Gauge Theories. *Sov. J. Nucl. Phys.*, 23:338–345, 1976.

[42] E. A. Kuraev, L. N. Lipatov, and Victor S. Fadin. The Pomeranchuk Singularity in Nonabelian Gauge Theories. *Sov. Phys. JETP*, 45:199–204, 1977.

[43] I. I. Balitsky and L. N. Lipatov. The Pomeranchuk Singularity in Quantum Chromodynamics. *Sov. J. Nucl. Phys.*, 28:822–829, 1978.

[44] Javier L. Albacete and Cyrille Marquet. Gluon saturation and initial conditions for relativistic heavy ion collisions. *Prog. Part. Nucl. Phys.*, 76:1–42, 2014. doi: 10.1016/j.ppnp.2014.01.004.

[45] Victor S. Fadin and L. N. Lipatov. BFKL pomeron in the next-to-leading approximation. *Phys. Lett. B*, 429:127–134, 1998. doi: 10.1016/S0370-2693(98)00473-0.

[46] Marcello Ciafaloni and Gianni Camici. Energy scale(s) and next-to-leading BFKL equation. *Phys. Lett. B*, 430:349–354, 1998. doi: 10.1016/S0370-2693(98)00551-6.

[47] Marcel Froissart. Asymptotic Behavior and Subtractions in the Mandelstam Representation. *Phys. Rev.*, 123:1053–1057, Aug 1961. doi: 10.1103/PhysRev.123.1053. URL https://link.aps.org/doi/10.1103/PhysRev.123.1053.

[48] A. Martin. Unitarity and High-Energy Behavior of Scattering Amplitudes. *Phys. Rev.*, 129:1432–1436, Feb 1963. doi: 10.1103/PhysRev.129.1432. URL https://link.aps.org/doi/10.1103/PhysRev.129.1432.

[49] Marcel Froissart. Asymptotic behavior and subtractions in the Mandelstam representation. *Phys. Rev.*, 123:1053–1057, 1961. doi: 10.1103/PhysRev.123.1053.

[50] Astrid Morreale and Farid Salazar. Mining for Gluon Saturation at Colliders. *Universe*, 7 (8):312, 2021. doi: 10.3390/universe7080312.

[51] Elena Ferreiro, Edmond Iancu, Kazunori Itakura, and Larry McLerran. Froissart bound from gluon saturation. *Nucl. Phys. A*, 710:373–414, 2002. doi: 10.1016/S0375-9474(02)01163-6.

[52] L. V. Gribov, E. M. Levin, and M. G. Ryskin. Semihard Processes in QCD. *Phys. Rept.*, 100:1–150, 1983. doi: 10.1016/0370-1573(83)90022-4.

[53] Edmond Iancu. *Physics of the Color Glass Condensate*. PhD thesis, IPhT, Saclay, 2005.

[54] Jamal Jalilian-Marian, Alex Kovner, Larry D. McLerran, and Heribert Weigert. The Intrinsic glue distribution at very small x. *Phys. Rev. D*, 55:5414–5428, 1997. doi: 10.1103/PhysRevD.55.5414.

[55] Alfred H. Mueller. Gluon distributions and color charge correlations in a saturated light cone wave function. *Nucl. Phys. B*, 643:501–513, 2002. doi: 10.1016/S0550-3213(02)00745-9.

[56] Edmond Iancu, Kazunori Itakura, and Larry McLerran. A Gaussian effective theory for gluon saturation. *Nucl. Phys. A*, 724:181–222, 2003. doi: 10.1016/S0375-9474(03)01477-5.

[57] Edmond Iancu, Andrei Leonidov, and Larry D. McLerran. Nonlinear gluon evolution in the color glass condensate. 1. *Nucl. Phys. A*, 692:583–645, 2001. doi: 10.1016/S0375-9474(01)00642-X.

[58] Heribert Weigert. Unitarity at small Bjorken x. *Nucl. Phys. A*, 703:823–860, 2002. doi: 10.1016/S0375-9474(01)01668-2.

[59] E. Iancu, K. Itakura, and S. Munier. Saturation and BFKL dynamics in the HERA data at small x. *Phys. Lett. B*, 590:199–208, 2004. doi: 10.1016/j.physletb.2004.02.040.

[60] G. Soyez. Saturation QCD predictions with heavy quarks at HERA. *Phys. Lett. B*, 655: 32–38, 2007. doi: 10.1016/j.physletb.2007.07.076.

[61] Mohammad Ahmady, Ruben Sandapen, and Neetika Sharma. Diffractive ρ and ϕ production at HERA using a holographic AdS/QCD light-front meson wave function. *Phys. Rev. D*, 94(7):074018, 2016. doi: 10.1103/PhysRevD.94.074018.

[62] Jamal Jalilian-Marian, Alex Kovner, Andrei Leonidov, and Heribert Weigert. Wilson renormalization group for low x physics: Towards the high density regime. *Phys. Rev. D*, 59: 014014, Nov 1998. doi: 10.1103/PhysRevD.59.014014. URL https://link.aps.org/doi/10.1103/PhysRevD.59.014014.

[63] Jamal Jalilian-Marian, Alex Kovner, and Heribert Weigert. The Wilson renormalization group for low x physics: Gluon evolution at finite parton density. *Phys. Rev. D*, 59:014015, 1998. doi: 10.1103/PhysRevD.59.014015.

[64] Elena Ferreiro, Edmond Iancu, Andrei Leonidov, and Larry McLerran. Nonlinear gluon evolution in the color glass condensate: II. *Nuclear Physics A*, 703(1):489–538, 2002. ISSN 0375-9474. doi: https://doi.org/10.1016/S0375-9474(01)01329-X. URL https://www.sciencedirect.com/science/article/pii/S037594740101329X.

[65] Jamal Jalilian-Marian, Alex Kovner, Andrei Leonidov, and Heribert Weigert. The Wilson renormalization group for low x physics: Towards the high density regime. *Phys. Rev. D*, 59:014014, 1998. doi: 10.1103/PhysRevD.59.014014.

[66] Edmond Iancu and Larry D. McLerran. Saturation and universality in QCD at small x. *Phys. Lett. B*, 510:145–154, 2001. doi: 10.1016/S0370-2693(01)00526-3.

[67] Ian Balitsky and Giovanni A. Chirilli. Rapidity evolution of Wilson lines at the next-to-leading order. *Phys. Rev. D*, 88:111501, 2013. doi: 10.1103/PhysRevD.88.111501.

[68] Alex Kovner, Michael Lublinsky, and Yair Mulian. Jalilian-Marian, Iancu, McLerran, Weigert, Leonidov, Kovner evolution at next to leading order. *Phys. Rev. D*, 89(6):061704, 2014. doi: 10.1103/PhysRevD.89.061704.

[69] Francois Gelis, Edmond Iancu, Jamal Jalilian-Marian, and Raju Venugopalan. The Color Glass Condensate. *Ann. Rev. Nucl. Part. Sci.*, 60:463–489, 2010. doi: 10.1146/annurev.nucl.010909.083629.

[70] Yuri V. Kovchegov and Eugene Levin. *Quantum Chromodynamics at High Energy*. Cambridge Monographs on Particle Physics, Nuclear Physics and Cosmology. Cambridge University Press, 2012. doi: 10.1017/CBO9781139022187.

[71] Javier L. Albacete, Nestor Armesto, Jose Guilherme Milhano, Paloma Quiroga-Arias, and Carlos A. Salgado. AAMQS: A non-linear QCD analysis of new HERA data at small-x including heavy quarks. *Eur. Phys. J. C*, 71:1705, 2011. doi: 10.1140/epjc/s10052-011-1705-3.

[72] E. Fermi. On the Theory of the impact between atoms and electrically charged particles. *Z. Phys.*, 29:315–327, 1924. doi: 10.1007/BF03184853.

[73] Stefano Frixione, Michelangelo L. Mangano, Paolo Nason, and Giovanni Ridolfi. Improving the Weizsacker-Williams approximation in electron - proton collisions. *Phys. Lett. B*, 319:339–345, 1993. doi: 10.1016/0370-2693(93)90823-Z.

[74] C. F. von Weizsacker. Radiation emitted in collisions of very fast electrons. *Z. Phys.*, 88: 612–625, 1934. doi: 10.1007/BF01333110.

[75] E. J. Williams. Correlation of certain collision problems with radiation theory. *Kong. Dan. Vid. Sel. Mat. Fys. Med.*, 13N4(4):1–50, 1935.

[76] Carlos A. Bertulani, Spencer R. Klein, and Joakim Nystrand. Physics of ultra-peripheral nuclear collisions. *Ann. Rev. Nucl. Part. Sci.*, 55:271–310, 2005. doi: 10.1146/annurev.nucl.55.090704.151526.

[77] A. J. Baltz. The Physics of Ultraperipheral Collisions at the LHC. *Phys. Rept.*, 458:1–171, 2008. doi: 10.1016/j.physrep.2007.12.001.

[78] J. G. Contreras and J. D. Tapia Takaki. Ultra-peripheral heavy-ion collisions at the LHC. *Int. J. Mod. Phys. A*, 30:1542012, 2015. doi: 10.1142/S0217751X15420129.

[79] Alfred H. Mueller. Parton saturation: An Overview. In *Cargese Summer School on QCD Perspectives on Hot and Dense Matter*, pages 45–72, 11 2001.

[80] Tuomas Lappi. Ultraperipheral collisions and low-x physics. In *28th International Workshop on Deep Inelastic Scattering and Related Subjects*, 7 2021.

[81] M. G. Ryskin. Diffractive J / psi electroproduction in LLA QCD. *Z. Phys. C*, 57:89–92, 1993. doi: 10.1007/BF01555742.

[82] S. J. Brodsky, E. Chudakov, P. Hoyer, and J. M. Laget. Photoproduction of charm near threshold. *Phys. Lett. B*, 498:23–28, 2001. doi: 10.1016/S0370-2693(00)01373-3.

[83] M. L. Good and W. D. Walker. Diffraction Dissociation of Beam Particles. *Phys. Rev.*, 120: 1857–1860, Dec 1960. doi: 10.1103/PhysRev.120.1857. URL https://link.aps.org/doi/10.1103/PhysRev.120.1857.

[84] Hannu I. Miettinen and Jon Pumplin. Diffraction scattering and the parton structure of hadrons. *Phys. Rev. D*, 18:1696–1708, Sep 1978. doi: 10.1103/PhysRevD.18.1696. URL https://link.aps.org/doi/10.1103/PhysRevD.18.1696.

[85] M. G. Ryskin, R. G. Roberts, Alan D. Martin, and E. M. Levin. Diffractive J/ψ photoproduction as a probe of the gluon density. *Z. Phys. C*, 76:231–239, 1997. doi: 10.1007/s002880050547.

[86] Stanley J. Brodsky, L. Frankfurt, J. F. Gunion, A. H. Mueller, and M. Strikman. Diffractive leptoproduction of vector mesons in QCD. *Phys. Rev. D*, 50:3134–3144, Sep 1994. doi: 10.1103/PhysRevD.50.3134. URL https://link.aps.org/doi/10.1103/PhysRevD.50.3134.

[87] A. G. Shuvaev, Krzysztof J. Golec-Biernat, Alan D. Martin, and M. G. Ryskin. Off diagonal distributions fixed by diagonal partons at small x and xi. *Phys. Rev. D*, 60:014015, 1999. doi: 10.1103/PhysRevD.60.014015.

[88] R. Manohar, A. Mukherjee, and D. Chakrabarti. Generalized Parton Distributions for the Proton in Position Space : Non-Zero Skewness. *Phys. Rev. D*, 83:014004, 2011. doi: 10.1103/PhysRevD.83.014004.

[89] John P. Ralston and Bernard Pire. Femtophotography of protons to nuclei with deeply virtual Compton scattering. *Phys. Rev. D*, 66:111501, 2002. doi: 10.1103/PhysRevD.66.111501.

[90] Kari J. Eskola, Christopher A. Flett, Vadim Guzey, Topi Löytäinen, and Hannu Paukkunen. Exclusive J/ψ photoproduction in ultraperipheral Pb+Pb collisions at the LHC to next-to-leading order perturbative QCD. 3 2022.

[91] Shreyasi Acharya et al. Energy dependence of exclusive J/ψ photoproduction off protons in ultra-peripheral p–Pb collisions at $\sqrt{s_{\rm NN}} = 5.02$ TeV. *Eur. Phys. J. C*, 79(5):402, 2019. doi: 10.1140/epjc/s10052-019-6816-2.

[92] A. Caldwell and H. Kowalski. The J/psi Way to Nuclear Structure. In *13th International Conference on Elastic and Diffractive Scattering (Blois Workshop): Moving Forward into the LHC Era*, pages 190–192, 9 2009.

[93] Heikki Mäntysaari. Review of proton and nuclear shape fluctuations at high energy. *Rept. Prog. Phys.*, 83(8):082201, 2020. doi: 10.1088/1361-6633/aba347.

Chapter 2

Description of the ALICE experiment

Contents

2.1 The Large Hadron Collider 46

2.1.1 Presentation of the LHC at CERN 46

2.1.2 Beam production at the LHC 48

2.1.3 Beam luminosity 49

2.1.4 Data taking at the LHC 50

2.2 ALICE detection instruments 50

2.2.1 General presentation of the ALICE detector 50

2.2.2 Detectors used in the analysis 51

2.2.3 The ALICE muon spectrometer 56

2.3 Data acquisition and processing in ALICE 60

2.3.1 The trigger system and data recording 61

2.3.2 Data taking during LHC operation and data reconstruction . . 62

2.4 Summary 64

Bibliography 65

Ultra-peripheral collisions of protons and lead nuclei can make it possible to map the interior of the proton by the photoproduction of J/ψ mesons off protons, as explained in the first chapter. In such collisions, the production of J/ψ particles contains crucial information on the gluon behavior at small Bjorken-x scales. J/ψ particles are not detected directly, since they live for a very short time (10^{-20} s on average). Instead, their decay products are detected, which in the present analysis are pairs of muons. This process is studied in the detector of A Large Ion Collider Experiment (ALICE), which is one of the four large detector systems at the LHC.

After a presentation of the LHC, the ALICE detector, composed of numerous detection technologies positioned around the nominal interaction point, is described, with special attention to the muon spectrometer, a crucial element for the analysis. Finally, we explain how the data is recorded and processed until its transformation into files ready to be analyzed.

2.1 The Large Hadron Collider

2.1.1 Presentation of the LHC at CERN

The Large Hadron Collider (LHC) [1] is a large particle accelerator and collider built between 50 and 100 meters underground on the French-Swiss border. It is hosted at the European Center for Nuclear Research (CERN) and was first commissioned in 2008 [1]. The LHC ring contains two circular pipes placed in parallel, which intersect at four points. The nuclei circulating there at the speed of light are destined to make head-on collisions at each of these points, thus giving access to their components (quarks and gluons) as well as to other particles created during these collisions. Joseph Incadela, former spokesperson for the Compact Muon Solenoid (CMS) collaboration, one of the experiments at the LHC, compared this technological achievement to "firing two knitting needles across the Atlantic and getting them to meet halfway".

The experiments that reside around the underground ring are located in spaces so vast that one could fit a Gothic cathedral with its nave and its towers. Four of them are particularly notable for their large size: A Toroidal LHC ApparatuS (ATLAS) experiment [2], the Compact Muon Solenoid (CMS) experiment [3], A Large Ion Collider Experiment (ALICE) [4], and the Large Hadron Collider beauty (LHCb) experiment [5]. The physics studied in each experiment varies: ATLAS and CMS mainly aim to study the Higgs boson and beyond the standard model physics such as supersymmetric particles (SUSY) [6]. LHCb is devoted to the study of CP violation, driven by our lack of understanding of the Matter-Antimatter asymmetry in our Universe and the search for rare decays that may bring out new physics in the beauty flavor sector. ALICE aims above all to characterize the quark-gluon-plasma, a dense and hot medium that would correspond to the state of the Universe a few microseconds after the Big Bang. These experiments also cover many other study topics, some common or complementary among several experiments.

The LHC consists of two quasi-circular and concentric tubes with a circumference of 26.7 km. Each of these tubes is made up of four circular arcs and four straight segments at the places where the beams of particles circulating therein must cross to create collisions. The four experiments mentioned above are distributed at each of these collision points, as shown in figure 2.1.

The pressure in the tubes is of the order of 10^{-10} to 10^{-11} mbar in order to limit beam-gas interactions, which are collisions of nuclei with residual gas atoms in the tube. Ultrahigh vac-

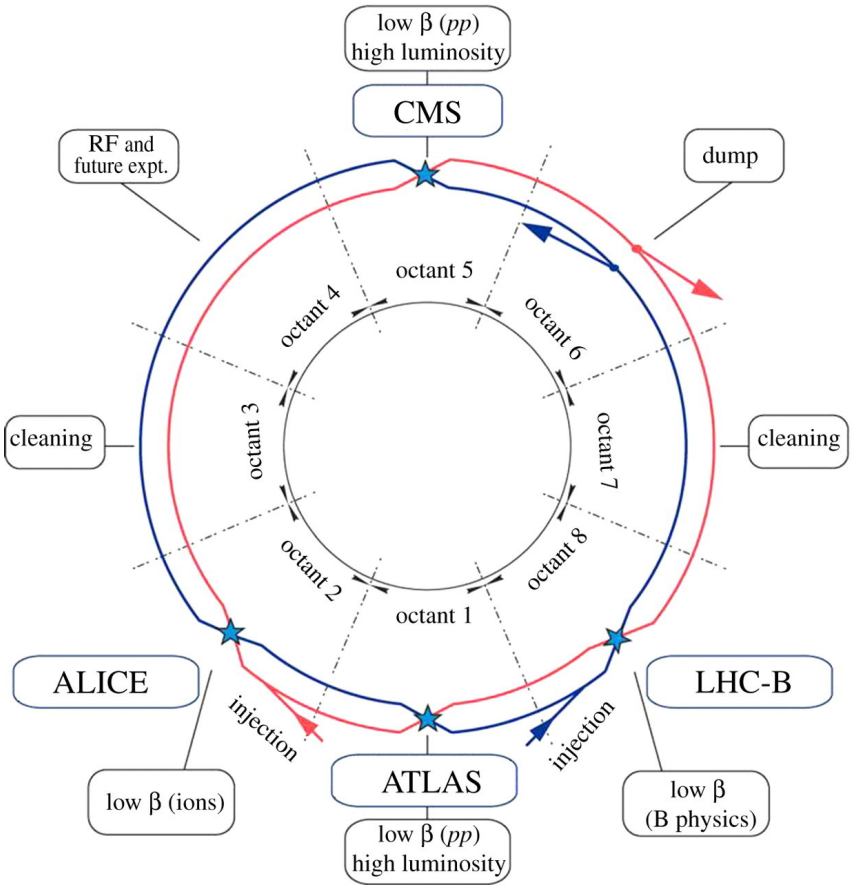

Figure 2.1: Schematic layout of the LHC, with Beam 1 (in blue) rotating clockwise, and Beam 2 (in red) anticlockwise [1].

uum is created and maintained in the tubes by cryogenic pumping. The beam tubes are cooled to extremely low temperatures, then the gases condense and adhere to the walls of the beam tube by adsorption. Almost two weeks of pumping are required to achieve the required ultra-high vacuum.

These particles are sent by bunches in the tubes in opposite directions via 2.5-km-long transfer lines. During LHC Runs[1] 1 and 2, three types of particles were injected into the tubes: protons (p), xenon (Xe) nuclei and lead (Pb) nuclei, thus allowing proton-proton (pp), proton-lead (p–Pb), lead-lead (Pb–Pb), and xenon-xenon (Xe–Xe) collisions. The maximum design energy to which protons can be accelerated is E_p = 7 TeV. In the case of lead $^{208}_{82}$Pb or xenon $^{129}_{54}$Xe ions, only the charged particles are accelerated and pull along the nucleus, i.e., Z protons among A nucleons. The maximum nominal energy per nucleon in Pb ions is then given by $E_{\mathrm{Pb}} = Z/A \cdot E_p = 2.75$ TeV.

[1] At the LHC, *Runs* with a capital letter denote periods of operation between two major upgrades of the experimental apparatus.

2.1.2 Beam production at the LHC

The acceleration of particles is based on the synchrotron principle: 1232 superconducting dipole magnets guide the beams by applying a magnetic field of 8.33 T oriented perpendicular to the circulation surface. Large currents are needed to obtain the large magnetic fields. Consequently, cryogenic techniques are used in order to make the material superconductive, and the structure must be maintained at a temperature of 1.9 K. In addition, 392 quadrupole, octupole, and decapole magnets are used to focus the beam. Before entering the LHC, the beam particles are pre-accelerated in other synchrotrons also hosted at CERN. The proton Synchro-Cyclotron (SC) was the first to exist, commissioned in 1957 and shut down in 1990. The Proton Synchrotron (PS), the Super Proton Synchrotron (SPS), and the Proton Synchrotron Booster (PSB) were built in 1960, 1971, and 1972, respectively. The preparation of protons and Pb nuclei and their pre-acceleration are two slightly different stories [1].

Producing proton beams

Protons are obtained initially with hydrogen[2] gas injected into a metal cylinder, to which an electric field is applied in order to break down the gas and separate protons and electrons. The protons leave the cylinder with an energy of up to 750 keV before being injected into the linear accelerator Linac 2, where they undergo a further acceleration, up to 50 MeV. The protons are bundled and accelerated in a new suite of serial injectors: the PSB, the PS, and the SPS. At last, the protons are injected into the LHC tubes, where they arrive with an energy of almost 450 GeV with a spacing of 25 ns between consecutive bunches. Protons reach the LHC maximum energy of 6.5 TeV[3] (nominal energy of protons in Run 2) after 20 minutes of circulation in the LHC tubes.

Producing lead ion beams

Lead nuclei are obtained initially from a piece of pure lead-208 placed in a vacuum cavity, immersed in a magnetic field. The first electrons are removed from the lead atoms by heating them with a 14.5 GHz microwave. The lead sample is then introduced into a chamber, where it is heated to about 800°C to vaporize a part of it. Electrons are excited by microwaves, and $(^{208}\mathrm{Pb})^{29+}$ ions are created. By the application of an electric field, they are then passed through a spectrometer which discards charge states other than 29+. A radiofrequency quadrupole arranges them into bunches, focuses them, and accelerates them to 250 keV per nucleon. They undergo another acceleration in the Linac 3, then pass through a 0.3-µm-thick carbon sheet which makes them lose electrons again and become 54+ lead ions. Some of them are selected by a magnetic field to be delivered to the Low Energy Ion Ring (LEIR), where they reach an energy of up to 72 MeV. As for the proton beam, the lead beam is injected into the PS and then into the SPS, which brings them to 177 GeV per nucleon. Between these two synchrotrons, they pass through a one-millimeter-thick aluminum sheet to eliminate their last electrons and become 82+ ions. Finally, the beam is accelerated in the LHC to 522 TeV (or 2.51 TeV per

[2] Hydrogen is only a proton with an electron orbiting around it.

[3] Although the maximum design energy of the proton beam is set at 7 TeV, significant constraints on the magnets would require their recycling to operate under these conditions, impinging on the time dedicated to physics research. A nice explanation can be found on the LHC website (https://home.cern/about/engineering/restarting-lhc-why-13-tev).

nucleon, which corresponds to the same acceleration per charge unit as for the proton) with a spacing of 152 ns between individual bunches.

The beams in the LHC

The beams are organized in bunches of accelerated particles located at regular time intervals around the orbit. The orbit is divided into 3564 slots with a time spacing of 25 ns, and each slot is subdivided into 10 buckets spaced by 2.5 ns. Thus, the beams are fully specified by different characteristics: the type of particle, their energy, the number of particles in each bunch, the number of bunches per beam, and the spacing in time between these bunches. In the case of beams of protons and Pb ions studied in the present thesis, some key figures are given in table 2.1.

Characteristic	**Protons**	**Lead ions**
Number of bunches per beam	702	548
Bunch spacing (ns)	100	200
Expected number of colliding bunch pairs at ALICE IP	216	
Number of particles per bunch (initially)	1.15×10^{11}	7×10^{7}
Number of revolutions per second	11245	
Beam lifetime	10h	$\sim$ 5h

Table 2.1: LHC figures for p–Pb collisions during Run 2, taken from the ALICE logbook [7].

The particle bunch must be in the central bucket of the slot. The particles delocalized from the center - outside the central bucket in the filled slot - are called satellites. Moreover, charges in slots that have not been intentionally filled are called ghost charges. These additional ghost and satellite charges must be taken into account in the analyses.

2.1.3 Beam luminosity

The beams are characterized by their luminosity $\mathcal{L}$. This variable is used to assess the quality of a collider to produce collisions, i.e., the number of particle crossings per unit area and time. It therefore depends directly on the intensity of the beams and is expressed in $\mathrm{cm}^{-2}\ \mathrm{s}^{-1}$. It is given by the formula:

$$\mathcal{L} = f_{\mathrm{coll}} \frac{n_1 n_2}{4\pi\sigma_x\sigma_y} \tag{2.1}$$

where f_{coll} is the accelerator revolution frequency, n_1 and n_2 the number of particles in each of the two crossing beams, σ_x and σ_y the horizontal and vertical widths of the beam, assuming a Gaussian profile.

When the particle beams are in circulation, the luminosity gradually decreases as collisions are produced and the numbers of surviving particles in each bunch n_1 and n_2 decrease. At the LHC, the luminosity is $10^{34}\ \mathrm{cm}^{-2}\mathrm{s}^{-1}$ for pp collisions and $6{\times}10^{27}\ \mathrm{cm}^{-2}\mathrm{s}^{-1}$ for Pb–Pb collisions in nominal regime [8]. However, the luminosity collected by the LHC detectors, although

related to the luminosity of the beam, is not the same. The latter depends greatly on the efficiencies and latencies of the detector triggers of the different experiments.

2.1.4 Data taking at the LHC

To this day, two *Runs* have been carried out at CERN. Run 1 took place from 2009 to 2013, Run 2 from 2015 to 2018, and Run 3 is planned to start this year (2022) and is foreseen to stop in 2026. A shutdown separates the Runs to install various upgrades in the detectors and on the LHC ring. During Run 1, the maximum energy reached by the protons was 4 TeV. The maximum energy was increased to 6.5 TeV for Run 2. With Run 3, the maximum energy could reach 7 TeV. Each Run includes several sets of data taking, each lasting a few weeks, using different particle beams, different energies, and different slot configurations.

The analysis work was carried out with p–Pb collisions data from Run 2 in ALICE, and next section gives a description of this detector during this period.

2.2 ALICE detection instruments

2.2.1 General presentation of the ALICE detector

A Large Ion Collider Experiment (ALICE) [4] is a detector installed on the LHC ring specialized in heavy-ion physics, typically collisions of Pb nuclei. The first proposal for a general-purpose heavy-ion detector was in 1990, the experiment was approved in 1997, and the first collisions were detected in 2009. The collaboration has over 1000 scientists representing more than 100 institutes from 31 countries, including the National Center of Scientific Research (CNRS) and the French Alternative Energies and Atomic Energy Commission (CEA).

The ALICE detector was designed to study the properties of the strong interaction, particularly at extreme energy densities at which a still little-known phase of matter, called quark-gluon plasma [9], is formed. In this state of matter, quarks are said to be "deconfined": quarks and gluons evolve freely. This plasma is expected to exist in the heart of neutron stars and would also correspond to the state of the Universe a few microseconds after the Big Bang. At the LHC, it is possible to recreate it for a very short time - less than 10^{-22} seconds - in central collisions[4] of lead nuclei, in which the energy densities are the highest.

Besides the operation with lead ions, the physics program also includes collisions with lighter ions (xenon ions) and dedicated proton-nucleus runs. This program thus makes it possible to cover a wide range of energy densities in collisions. In addition, ALICE also takes data with proton beams at the maximum energy of the LHC. These data serve as a reference to observe various nuclear effects in the heavy-ion program and to treat several QCD subjects for which ALICE is complementary to the other LHC detectors. Thus, the design of ALICE is guided by the physics requirements and the experimental conditions expected in nucleus-nucleus collisions at the LHC. The detector must make it possible to measure a wide dynamic range for the momentum of the particles produced, which can range from 100 MeV/c up to more than 100 GeV/c. It must also be able to reconstruct the several thousands of particle

[4]Central collisions are collisions for which the area of the overlapping nuclei is maximized.

trajectories per rapidity unit from central collisions of lead nuclei, and the detector has been optimized for charged particle densities typically up to $dN/d\eta$ = 4000 for a single event and to perform precise particle identification (PID). This allows a large safety margin since in Pb–Pb collisions, charged particle densities are expected to be of the order of $dN/d\eta$ = 2000 at $\sqrt{s_{\mathrm{NN}}}$ = 5 TeV. The ALICE detector performance has been checked in detailed simulations up to $dN/d\eta$ = 8000.

In order to meet these various physics requirements, the experiment incorporates 18 sub-detectors in Run 2. These sub-detectors, each using different technologies according to its own specifications, are classified according to their coverage in pseudorapidity[5]:

- Midrapidity detectors (covering in total $|\eta| < 1.5$). Also called Central Barrel detectors, they surround the point of interaction (IP) and are arranged inside a large solenoid magnet, which provides a 0.5 T solenoidal magnetic field. These are the Inner Tracking System (ITS), the Time Projection Chamber (TPC), the ALICE COsmic Ray DEtector (ACORDE), the Transition Radiative Detector (TRD), the Time Of Flight (TOF), the High Momentum Particle Identification Detector (HMPID), the PHoton Spectrometer (PHOS), ElectroMagnetic Calorimeter (EMCal) and Di-jet Calorimeter (DCal) detectors.
- Forward rapidity detectors (with an acceptance $|\eta| > 2.5$). These are the Zero Degree Calorimeter (ZDC), the Alice Diffractive detector (AD), the Photon Multiplicity Detector (PMD) and the Forward Multiplicity Detector (FMD), TZERO (T0) and VZERO (V0), and finally the muon arm detectors: the Muon CHambers (MCH) and the Muon TRigger (MTR).

An overview of the ALICE experiment during Run 2 is illustrated in figure 2.2. A complete review of these detectors and their recent update is given in reference [10].

In the analysis presented in the next chapters, only six of them are used to select the data of interest: the ITS, the ZDC, AD, V0, T0, and the muon spectrometer. In the following, we briefly describe only these six detectors, with a more important part dedicated to the muon spectrometer since it is dedicated to the reconstruction of the dimuons resulting for the J/ψ decay and thus, the J/ψ itself.

2.2.2 Detectors used in the analysis

The ALICE detector is divided into two sides on either side of the Interaction Point (IP): the side of the muon spectrometer is denoted C, and the opposite side is denoted A. Most of the forward rapidity detectors are arranged on both sides, and are therefore identified by the letters A and C depending on their position. Only one mid-rapidity detector is used in the analysis: the Inner Tracking System.

The Inner Tracking System (ITS)

The ITS is the most central detector, it surrounds and supports the beam pipe located in the central barrel of ALICE. It corresponds to the green object inside the TPC in figure 2.2. It is

[5]The pseudorapidity, denoted η, is a spatial coordinate commonly used to describe the angle of a particle's trajectory with respect to the beam axis. It is a dimensionless quantity. In ALICE convention, $\eta < 0$ designates the muon spectrometer side.

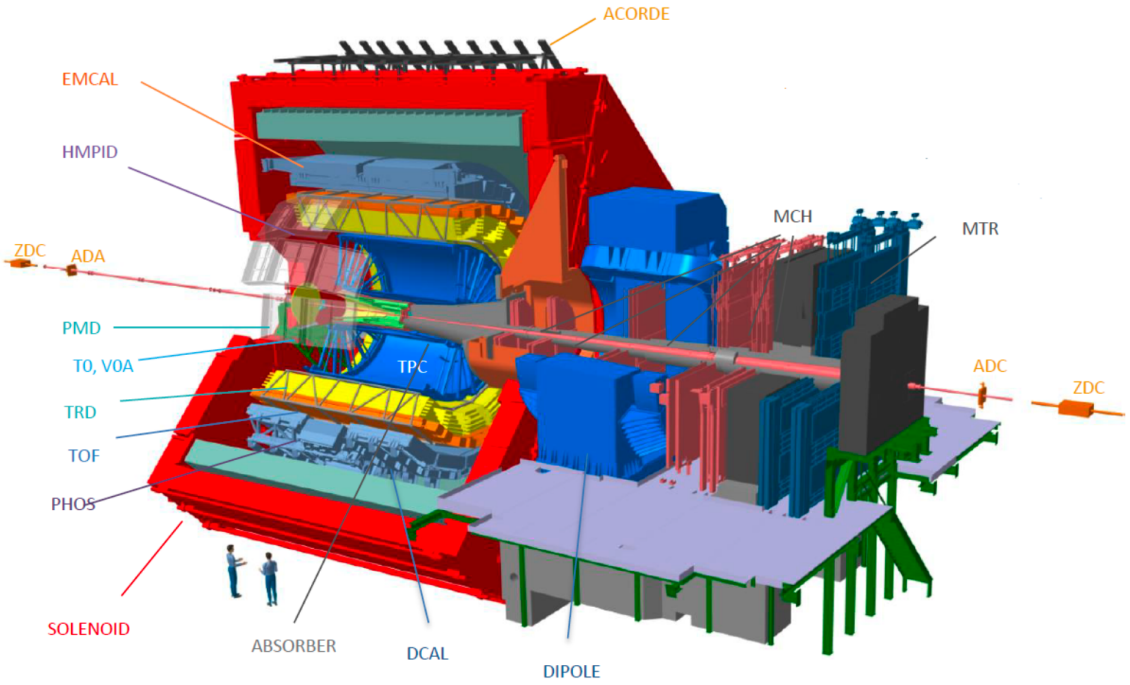

Figure 2.2: Layout of the ALICE experiment during Run 2. Figure taken from reference [11].

composed of six coaxial cylindrical layers of silicon detectors covering a total area of 6.28 m^2. In particular, it allows the identification of certain particles by measuring their energy loss and their trajectory. It is divided into three parts, each using a different technology.

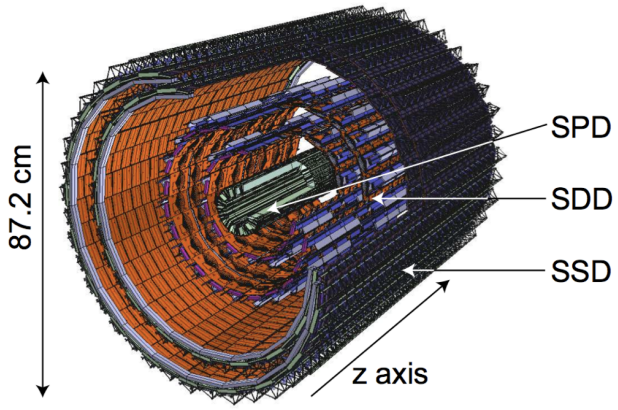

Figure 2.3: Layout of the ALICE ITS during Run 2. Taken from reference [12].

The first two layers, of 4 and 7 cm in radius, are called the Silicon Pixel Detector (SPD). The SPD notably allows locating the primary vertex with a resolution better than 100 µm, using the reconstruction of tracklets. Tracklets are track fragments created from two reconstructed points in the SPD, the first one in the inner layer and the second one in the outer layer. The number of tracklets is, therefore, a multiplicity estimator at mid-rapidity. The acceptance of SPD layers is $|\eta| < 1.4$.

The subsequent two layers compose the Silicon Drift Detector (SDD), and the two outermost layers are called the Silicon Strip Detector (SSD).

The pseudorapidy acceptance of the entire detector is $|\eta| < 0.9$.

In the analysis, the SPD will be useful in order to reject events for which tracklets have been reconstructed, which vetoes events in which particles are produced at mid-rapidity. This exclusivity criterion in the mid-rapidity region is necessary in UPC analyses.

The other detectors important for the analysis are all located at forward rapidity.

The Zero Degree Calorimeters (ZDC)

The ZDC consists of two identical sets of hadronic calorimeters located on either side of the IP, 112.5 m away from the IP. Each of the two sets consists of a neutron (ZN) and proton (ZP) calorimeter, shown in figure 2.4. At such a distance from the IP, each of the two beams circulates in its own tube, contrary to the position of the other detectors presented in this section, at which the two beams circulate in a single conduit. The ZDC measures the energy released by the spectator nucleons [6]: the neutrons for ZN and the protons for ZP.

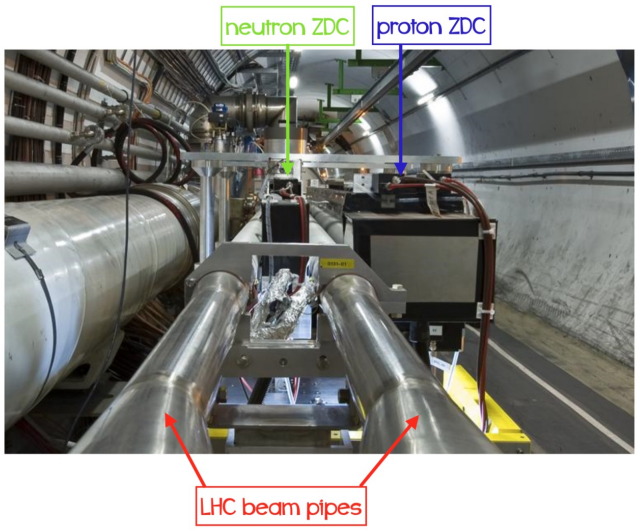

Figure 2.4: Picture of ZN and ZP in the cavern taken from reference [13].

In the magnetic field of the LHC, the spectator protons are deflected from the ion beam while the spectator neutrons fly at zero degrees with respect to the beam axis. Thus, the ZN is placed at zero degrees with respect to the LHC axis, between the two beam tubes, while the ZP is positioned on the exterior side of the outgoing beam tube. The principle of operation of the two calorimeters is based on the detection of cascades of particles, called showers. These showers are created by high-energy protons and neutrons passing through a dense tungsten (for ZN) or brass (for ZP) absorber. The particles from the shower emit Cherenkov radiation in quartz fibers. Quartz fibers emerge from the backside of the calorimeter, bringing light directly to PhotoMultiplier Tube (PMT).

[6] Unlike the participant nucleons in a collision, the spectators are located in the periphery of the collision center and do not interact.

The ZP cover an interval in pseudo-rapidity $6.5 < |\eta| < 7.5$ and ZN $|\eta| > 8.8$. On the opposite side to the muon spectrometer (side A), the hadronic calorimeters are complemented by two direct electromagnetic calorimeters (ZEM) placed about 7.35 m from the IP, covering the pseudorapidity range $4.8 < \eta < 5.7$.

The energy released by the spectator nucleons in ZN and ZP makes it possible to measure the number of participants and, therefore, the centrality of the collision. The ZDC also provides information on the reaction plane. The information obtained with ZN will be crucial for the analysis to ensure that the lead ion remains intact.

The ALICE Diffractive (AD)

The AD detector has been installed and commissioned for the second phase of operation (Run 2) of the LHC. It is made up of two main stations, ADA located 17 m from the IP, and ADC at 19.5 m. Each station comprises two detection layers, each made up of four plastic scintillator modules arranged around the LHC beam tube (eight pads per side).

Each plastic scintillator is coupled to a PMT via a wavelength shifter bar and an array of transparent optical fibers. This detector makes it possible to study diffractive physics, i.e. the processes in which at least one particle of the final state has dissociated. These processes are characterized by a rapidity gap between the final-state particles. For single diffractive processes and high masses of the dissociative system M_X, the average gap width is $\Delta y \approx \ln(s/M_X^2)$ where s is the center-of-mass energy in the collision system [14]. The AD detector, with its pseudorapidity coverage of $4.8 < \eta < 6.3$ (ADA) and $-7.0 < \eta < -4.9$ (ADC), allows with the central barrel and the forward detectors to increase considerably the pseudorapidity coverage, extending it from 8.8 to 12.1 units in η. This results in an increased sensitivity for diffractive

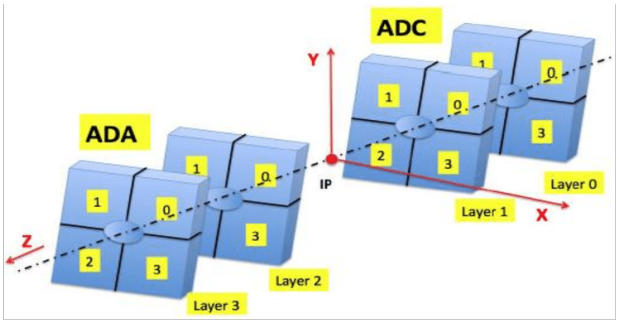

Figure 2.5: Representation of ADA and ADC sub-detectors. Figure taken from reference [15].

masses - the mass of all particles resulting from dissociation - close to the threshold, i.e. the sum of the masses of the proton and the pion ($m_p + m_\pi$). Thus, ALICE becomes sensitive to diffractive masses $M_X > 4$ GeV/c^2 (with 50 % efficiency), while the diffractive mass threshold was $M_X > 10$ GeV/c^2 in Run 1 (with 50 % efficiency).

The AD detector also provides a zero-level trigger signal and partially compensates for the loss of efficiency of an interaction (Minimum Bias (MB)) trigger which will be discussed later in this chapter.

The VZERO (V0)

The V0 detector consists of two arrays of organic scintillator counters placed on either side of the nominal interaction point, V0C (muon spectrometer side) and V0A (opposite side). The V0A is placed 330 cm from the IP and covers the pseudorapidity range $2.8 < \eta < 5.1$, while the V0C is placed 90 cm from the IP because of the presence of the muon spectrometer on the same side and covers $-3.7 < \eta < -1.7$.

Each of the two V0 detectors is segmented into thirty two elementary counters distributed over four concentric rings, thus forming eight sectors.

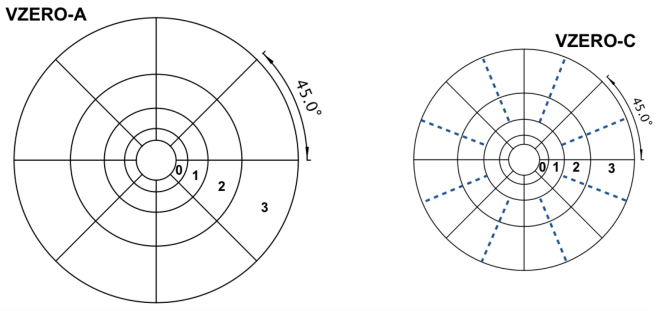

Figure 2.6: Representation of V0 detectors.

When a high-energy particle passes through the detector, organic scintillators emit light by the effect of excitation and de-excitation. This light is transported by optical fibers to photo-multipliers.

The V0 detector has many roles, in particular:

- It generates a MB trigger for the detectors in the central barrel.
- It makes it possible to discriminate beam–beam interactions from background events (such as beam-gas interactions). The time of arrival of the signal is used to discriminate the background events induced by the passage of the LHC beams.
- It provides the number of MB trigger events which is used to measure luminosity.
- It makes it possible to estimate the centrality of a Pb–Pb collision by summing the energy deposited in the two discs of V0. This observable evolves directly with the number of primary particles generated in the collision and therefore with the centrality.

In our analysis, the V0 allows to reject beam-beam interactions, it is thus used as a veto of the hadronic contamination in order to ensure that the selected events are only UPCs.

The TZERO (T0)

The T0 consists of two arrays of Cherenkov detectors on either side of the IP. Each array has 12 cylindrical quartz Cherenkov counters coupled to PMTs. The T0A is located at a distance of about 375 cm from the nominal IP, covering the pseudorapidity range $4.61 < \eta < 4.92$, on the opposite side from the muon spectrometer. On the other side, the T0C must be much closer due to the presence of the muon absorber, described in the next section. It is therefore at a distance of 72.7 cm from the nominal IP, within the pseudorapidity range $-3.28 < \eta < -2.97$. The

T0 provides a trigger signal to the various detectors, and makes it possible to deliver a measurement of the interaction time for the other detectors with great precision. It also separates beam-gas interactions from physics and provides minimum bias and multiplicity triggers. In the analysis, this detector will be used to count the events in order to measure the luminosity.

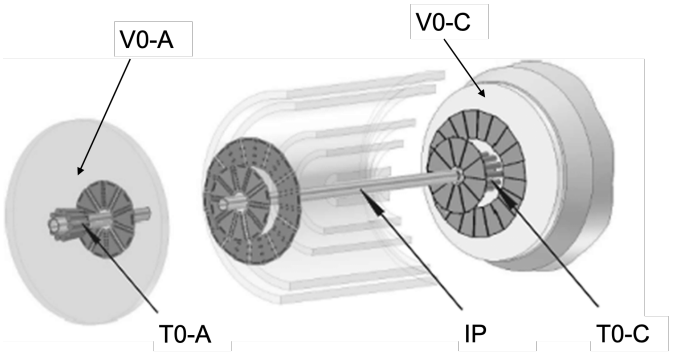

Figure 2.7: Location of T0 and V0 detectors in the central region of ALICE. T0A is on the extreme left, about 370 cm from IP, behind V0A and the fifth ring of FMD. T0-C is about 70 cm from IP, surrounded by two rings of FMD and V0-C. Both T0-C and V0-C are attached directly to the front of the absorber.

2.2.3 The ALICE muon spectrometer

The muon spectrometer measures the production of quarkonia (J/ψ, $\psi(2S)$, $\Upsilon(1s)$, $\Upsilon(2s)$, $\Upsilon(3s)$) which decay into dimuons, the production of heavy flavors via semi-lepton decays, and dimuon continuum production. Its coverage is $-4.0 < \eta < -2.5$ in pseudorapidity and full in azimuth.

The muon spectrometer provides information on the momentum, charge, pseudorapidity and radial position of the track at the entrance of the absorber. The invariant mass resolution of dimuons is of the order of 70 MeV/c at the J/ψ peak in central Pb–Pb collisions and about 100 MeV close to the Υ peak [16].

In the case of the analysis presented in the following chapters, the muon spectrometer is used to measure the dimuons resulting from the decay of a J/ψ.

The muon spectrometer and its various components are shown in figure 2.8. The element closest to the IP is the front absorber designed to absorb all particles from the interaction vertex except muons. Next is the tracking system, made up of ten detection planes structured in five tracking stations, denoted ST1 to ST5. Between stations 2 and 4, and around station 3, a 3 T·m integrated field dipole magnet is used to deflect the muon, allowing the measurement of its momentum. Finally, behind the tracking stations is a passive muon-filter wall and four trigger chamber planes.

We give in the following a more detailed description of these different elements.

The absorbers

The absorbers aim at protecting the muon chambers from the multitude of particles produced at the IP in the most central Pb–Pb collisions while degrading the signal quality as little as possible. A total of four absorbers are installed in the spectrometer.

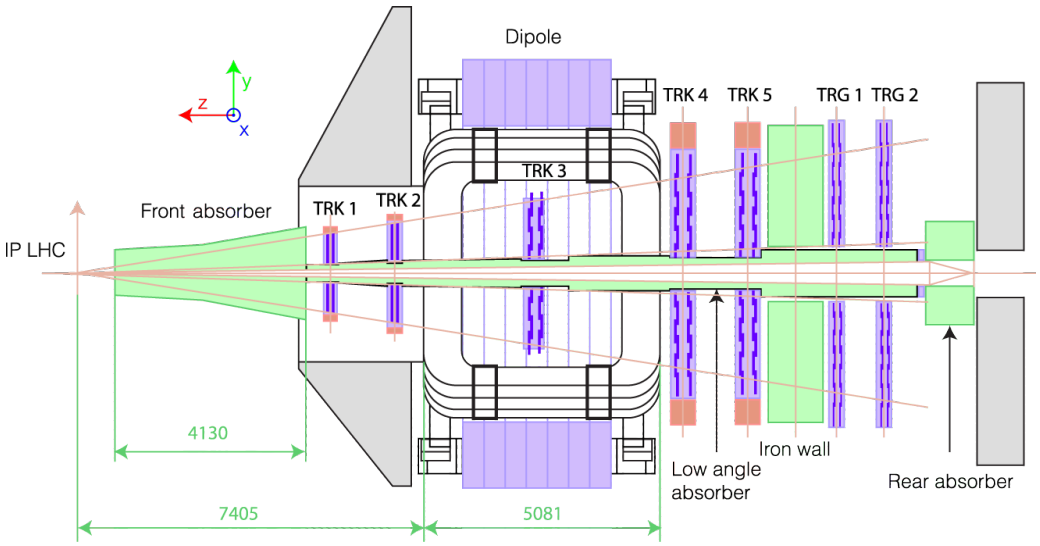

Figure 2.8: Schematic view of the muon spectrometer longitudinal section. According to the adopted numbering scheme station 1 (TRK1) is the closest to the interaction point. Figure taken from reference [4].

- **The front absorber**, located 90 cm from the IP, is designed to stop hadrons and photons coming from the interaction vertex and emitted in the acceptance of the muon spectrometer so that only muons can survive there to be detected behind in the tracking system. It is composed of carbon and concrete in order to limit multiple scattering and energy loss of the muons in the region close to the IP. The rear part, which is much denser, made of lead and borated polyethylene, absorbs low-energy photons and neutrons.
- A **concrete beam shield** protects the chambers from background events coming from particles at small angles with respect to the beam axis. It is made of tungsten, lead, and stainless steel. Together with the front absorber, it prevents high-energetic particles from reaching the MCH (denoted TRK in figure 2.8).
- The **Muon Filter** is a 1.2-meter-thick iron wall that aims to stop the last energetic hadrons that traversed the front absorber. The wall combined with the front absorber prevents muons with a momentum below $p_{\mathrm{T}} \simeq 4\,\mathrm{GeV}/c$ from reaching the MTR (denoted TRG in figure 2.8).
- The **Rear Absorber**, located behind the trigger elements, eliminates beam–gas interactions that could take place in the beam tube and produce tracks in the muon spectrometer, considered as a background.

The Dipole Magnet

The dipole magnet is located at about 7 m from the nominal IP, at the level of the third station of the tracking system which it surrounds. It is a resistive-type magnet made up of coils through which a direct current passes. It is water-cooled and operated at room temperature. This magnet generates a magnetic field oriented horizontally and perpendicular to the axis of the beam. Thus, the charged particles passing through the tracking system have a bent trajectory in the vertical plane, making it possible to measure their momentum. The requirements on

the mass resolution define the value of the magnetic field B_{dipole}. Thus, $B_{\text{dipole}} = 0.7$ T, which corresponds to a field integral of 3 T·m.

The tracking system

The tracking system, located between the front absorber and the iron wall, is made up of five stations (TRK1 to TRK5 in the figure 2.8), each being subdivided into two chambers. Its purpose is to measure the trajectory of muons, thus allowing to measure their kinematic characteristics. The first two stations, at 5.4 m and 6.8 m from the IP, are positioned before the dipole. The third station, 9.7 m from the IP, is located in the middle of the magnet. Finally, the last two stations, at 12.65 m and 14.25 m from the IP, are placed just before the muon filter.

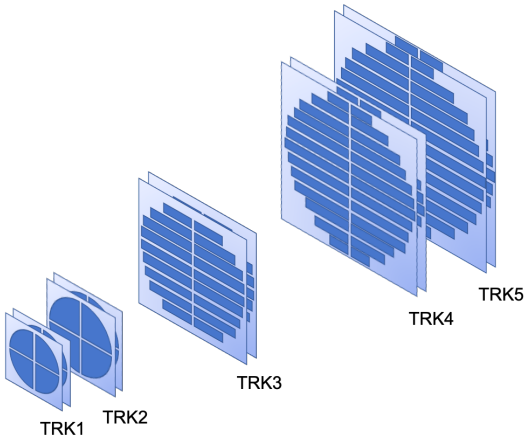

Figure 2.9: Layout of the five tracking chambers of the muon spectrometer.

Each tracking chamber is composed of several wire chambers arranged in different forms depending on their dimensions: the first two stations are made of quadrants whilst the largest chambers are made of modular detectors called "slats", as represented in figure 2.9. A wire chamber is a detector consisting of two cathode planes held at high voltage, which are in this case both read out to provide two-dimensional hit information. Between these two planes, an array of high voltage wires (anode) creates two regions of opposing electric fields. A representation is given in figure 2.10, and further details on the design of the tracking chambers are given in reference [4].

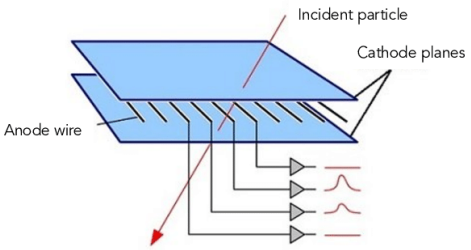

Figure 2.10: Representation of a multi-wire proportional chamber. Figure taken from reference [17].

The chambers are filled with a mixture of a noble gas and a *quencher*, here argon (80%) and CO_2 (20%). When a charged particle enters one chamber, it ionizes the gas, splitting the

atoms into negatively charged electrons and positively charged ions. The resulting ions and electrons are accelerated by the electric field through the chamber, causing a localized cascade of ionizations close to the anode wires when they have enough kinetic energy. During the ionization of argon (Ar) atoms, the excited Ar* atoms produced in the avalanche can de-excite via the emission of photons. The *quencher* (here CO_2) is used to absorb the photons emitted by the excited Ar* atoms, which could reach the cathode and ionize it, causing a new avalanche.

The cathodes are segmented in pads, and the charges induce an electrical signal of amplitude proportional to the ionization effect of the detected particle on the cathode pads. The distribution of the charge collected on the different pads thus indicates the trajectory of the particles. The segmentation of the pads on the two cathode planes are different, such that one is called bending plane because it has more granularity in the bending direction, and the other one non-bending plane. Each chamber of the tracking system has a spatial resolution of less than 100 µm (70 µm in the bending plane).

The Muon Trigger System (MTR)

The MTR is the furthest part of the muon spectrometer to the IP, at a distance of ~ 16 m, behind the Iron Wall. It is designed to provide a trigger signal for high-p_{T} muons emitted in the decay of heavy quarkonia. Low-p_{T} muons from pions and kaons decays are expected to be detected in the spectrometer in Pb–Pb collisions. In order to suppress these background signals, a p_{T} threshold is defined such that high-p_{T} muons only (emitted in the decay of heavy quarkonia) can induce a trigger signal. The values of the p_{T} thresholds vary from one data taking to another, in particular according to the collision system, and they can range from ~ 0.5 to ~ 2 GeV/c. Two programmable cuts (low-p_{T} and high-p_{T} cuts) are performed in parallel by the trigger electronics [18]. They represent a compromise between background rejection and signal detection efficiency in the mass regions of the J/ψ and Υ resonances, respectively. Thus, the MTR system provides a trigger signal for events in which at least one muon track has passed with a transverse moment p_{T} above threshold, or for events with two tracks of muons also satisfying the condition of p_{T} above threshold.

The MTR system consists of four detection chambers, grouped into two planes of Resistive Plate Chamber (RPC) spaced one meter apart from each other, which provide the transverse momentum p_{T} of each muon by estimating the deviation of a trace between the two stations assuming that it comes from the interaction vertex. Figure 2.11 shows the RPC design used in MTR.

Each RPC consists of two parallel low-resistivity Bakelite plates: an anode and a cathode, separated by a space of about 2 mm. The low resistivity Bakelite prevents the charge from spreading too much (thus allowing better localization) and allows fast reading. It allows operation at high particle flux to attain the needed rate capability (average measured value of about 4 Hz/cm^2 for Pb–Pb in Run 2 with a maximum of 7.5 Hz/cm^2). The two electrodes are covered with an insulating film connected to graphite sheets under high tension segmented into reading strips arranged in perpendicular directions to allow good spatial resolution. The strips are used to recover the electrical signal generated during the passage of a particle (in the form of a *cluster*). RPCs have a spatial resolution of less than 1 cm, needed to perform the p_{T} selection, and a temporal resolution of 2 ns, needed to identify bunch crossings. They thus constitute excellent muon trigger detectors for LHC experiments.

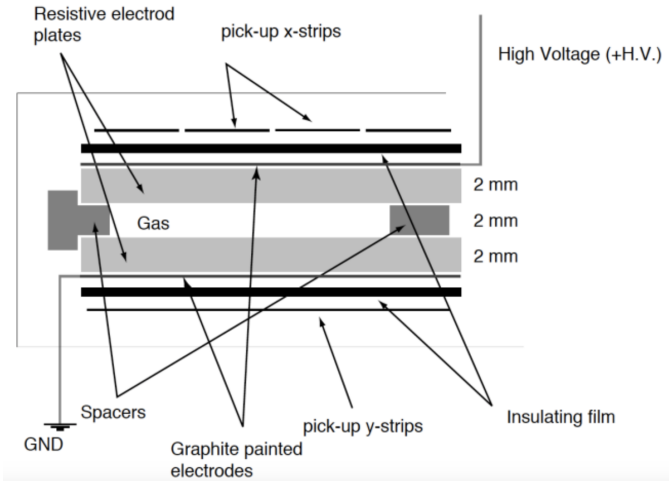

Figure 2.11: Structure of the RPC in Muon Trigger. Figure taken from reference [19].

Muon tracks reconstruction

The reconstruction of the muon tracks [20] is performed by the tracking algorithm, which uses the data from the tracking system and the muon trigger system. The tracking algorithm takes as input the coordinates of the cluster, obtained by the charge induced on the pads of the RPCs by the charged particles. It is based on the *Kalman filter* approach [21]. A Kalman filter is a probabilistic state estimation technique used to estimate the state of a dynamic system, where in this case, the state corresponds to the spatial coordinates of charges in each station. The Kalman filter recursively predicts the new state of a dynamic system, taking into account the inaccuracies of previous predictions when compared to observations. In the case of the reconstruction algorithm, the cluster information of stations 4 and 5 are used as first observations of the Kalman filter because they are furthest from the IP and are therefore exposed to tracks densities lower than that of stations 1 to 3. Then, all possible combinations of trajectories are obtained by linking cluster pairs on two stations and creating segments by joining the two clusters position by a straight line. Those segments are extrapolated in the magnetic field of the dipole to the vertex position. The reconstructed track is then matched with a trigger track, extrapolated to the vertex measured with the SPD, and corrected for energy loss and multiple scattering in the front absorber.

2.3 Data acquisition and processing in ALICE

ALICE must be able to record a large volume of data corresponding to pieces of information transmitted by several sets of detectors that will characterize an event. The data cannot be recorded continuously, and the information is stored when pre-defined trigger conditions are met. In addition, all relevant calibration information should be recorded and referenced. This calibration information is essential for data reconstruction. The performance of the experiment, such as momentum resolution and particle identification, depends on the calibration quality. We will now see in more detail how data is processed in ALICE.

2.3.1 The trigger system and data recording

The elements intervening in data recording are organized in three groups which are interconnected: the ALICE Central Trigger, Data AcQuisition system (DAQ), and High Level Trigger (HLT).

The Data Acquisition system (DAQ)

The DAQ handles the data flow from the detector to the permanent data storage in the CERN computing center. The DAQ procedure of ALICE [4] is organized in several steps, described here in a simplified way.

- First, the Local Trigger Unity (LTU) outputs the trigger signal from the Central Trigger Processor (CTP) to the detector. The signals recorded by the detectors are transmitted to the DAQ ReadOut Receiver Cards (D-RORC), via the Detector Data Link (DDL). D-RORCs are PCI-X modules hosted by Local Data Concentrator (LDC), which are simple PCs. Each LDC can manage more than one D-RORC. The task of the LDCs is to reconstruct the sub-events.
- The HLT receives all relevant data via the DDLs, and compresses it without physical loss. The output data then goes to the LDC dedicated to the HLT.
- Sub-events built within LDC are transported to the Global Data Collector (GDC), which are also basic PCs. GDCs assemble sub-events to create complete events. The data is then transported to the Transient Data Storage (TDS).
- Finally, the reconstructed data is stored in the Permanent Data Storage (PDS). Data from the PDS finally becomes available for reconstruction and physics analysis.

The Central Trigger Processor

After a collision in the ALICE detector, the final products of this interaction can be detected in the ALICE *trigger detectors*. The *trigger detectors* have the primary mission of alerting the CTP, which centralizes all the trigger signals, and combines them according to the desired trigger criteria. If the criteria are satisfied, then the CTP orders the recording of the event.

Data is recorded through the coordinated reading of a set of detectors. These groups of detectors are organized in *clusters*. The advantage of this reading by cluster makes it possible to overcome the dead times[7] of each detector.

There are different trigger configurations (or *trigger classes*). Each configuration is associated with a combination of trigger or veto signals in the trigger detectors and the detector cluster to be read. Trigger criteria are chosen depending on

- ALICE physics program,
- the performance of the detectors,

[7] The dead time of a detector corresponds to a period during which a detector can no longer record a signal, because it is still busy processing the previous signal, and its duration depends on the technology of the detectors.

- their readout electronics,
- the bandwidth of the DAQ
- and the raw data storage capacity.

The raw data are files containing encoded quantities such as particle hit positions, times stamps, or measured ionization.

The DAQ *bandwidth* is the amount of data transported through the DAQ per unit time, which needs to be minimized due to technical limitations, cost and storage capacity. To do this, the trigger rate can also be voluntarily reduced, for example by recording only one event out of ten among those that pass the selection criteria: this is called down-scaling. Allocation of DAQ bandwidth is also done by time sharing between different triggering criteria. Trigger classes are separated into two groups: *minimum bias (MB)* and *rare triggers*. The trigger rate of MB triggers can be reduced so that the DAQ is not saturated, and can allocate more bandwidth to rare triggers.

Trigger classes of the CTP are divided into four levels, depending on the time required for the signals of the detectors concerned to be produced and to reach it.

- Level Minus one (LM) introduced in Run 2 is the fastest trigger level (650 ns of latency). It was sent only to the TRD as a pre-trigger.
- Level 0 (L0) is the fastest trigger level (900 ns of latency). It is composed of V0, T0, SPD, EMCal and MTR. This is the one that applies to the classes in which we are interested. For the purposes of UPC triggers, the trigger classes are formed from the L0 inputs of SPD, TOF, V0, and the MTR. Current triggers for UPC processes only use trigger L0.
- Level 1 (L1) processes ZDC and TRD information, with a latency of 6.5 µs.
- Level 2 (L2) is the slowest level (88 µs of latency, which corresponds to the drift time of electrons in the TPC). This level makes the final decision to keep or reject an event.

In total there are 24 LM/L0 inputs, 24 L1 inputs, 12 L2 inputs and 100 trigger classes. Since the inputs are booleans, they can just as well be inverted in the trigger class (i.e. one requires its negation, e.g. no signal in a sub-detector). For each of the L0, L1 and L2 decision levels, counters called *scalers* record, for each trigger class, all the events, before (l0b) and after (l0a) the decision of the CTP to trigger the acquisition or not. For example, if an event is recorded only by passing trigger L2, the number of events for each trigger class is recorded for L0, L1, and L2. These numbers are essential for luminosity measurement for a given trigger class.

The High-Level Trigger

The HLT allows the implementation of more sophisticated trigger criteria than the CTP, via an online pre-reconstruction of the data. In doing so, the HLT allows filtering events of interest in order to optimize the use of the available DAQ bandwidth without physical loss.

2.3.2 Data taking during LHC operation and data reconstruction

For a single configuration (energy of the beams, collision system, magnetic field, etc.), the data sets are subdivided in *runs* with a lowercase letter as opposed to the *Runs* discussed in section 2.1.4. In the ALICE nomenclature, a run is a set of data collected within a start and a stop of

the data acquisition under stable detector and trigger configuration. For the considered data-taking period, the duration of the run spanned from a few tens of minutes to a few hours. At the LHC, runs are categorized into so-called *periods* of continuous data taking. Several aspects distinguish periods: the energy of the beams, the magnetic field, the configuration of the distribution of the bunches along the LHC, the particles which circulate in the beams, or the configuration of the detector (such as the trigger classes). A period is indicated by the last two digits of the year and a single letter incremented in alphabetical order.

Parameters for each run are collected and stored as objects in the Offline Condition Data Base (OCDB). The parameters are, for example, the geometric alignment of the detectors, the calibration of the detectors (typically pedestals), the magnetic field, dead and inactive channels, or the scalers. They are used in simulation as well as data reconstruction and analysis. These parameters are essential, for example, to reproduce the conditions of data acquisition in the simulations. In particular, dead and inactive channels are of great importance to evaluate the detector efficiency. Events are recorded in the form of *raw data* files containing encoded quantities such as particle hit positions, times stamps, or measured ionization. No physics analysis is possible using these data, and recorded events typically go through several cycles of reconstruction called *passes*. The results of each reconstruction pass are stored in Event Summary Data (ESD) files, from which the physics analysis can be performed. The ESDs contain the essential information for the analyses, such as particle momenta, coordinates of interaction, and decay vertices, as well as for specific calibrations and performance studies of the detectors. Events that come from Monte Carlo simulations are also stored in ESD files.

Finally, ESDs are again filtered into smaller files called Analysis Object Data (AOD), which contain reduced information. This is where the analysis can begin.

The GRID

ALICE uses a monitoring service called the GRID [4], which is available for the different CERN collaborations. This GRID is formed by a vast network of servers and computing centers worldwide. These are the servers on which the data is saved. They are accessible by CERN members via the AliEn middleware, within the limit of quotas concerning computing time and disk space to avoid excessive use per user. When a user sends a task to the GRID, which can be a simulation or a real data analysis, the latter divides it into several independent sub-tasks, called *jobs* and controlled using the Job Description Language (JDL). This drastically reduces the time needed for a simulation or analysis. The output files are then merged into one. Alternatively, analyses can be run on the GRID via *LEGO (Lightweight Environment for Grid Operators) trains*. This system combines analysis from different users which are then executed within the same Grid jobs thereby reducing the number of times the data needs to be read from the storage systems. This is done by collecting multiple analysis tasks which analyze the same dataset and by running them within the same analysis job. Following this procedure, the data is read once, and then it is used for multiple analysis tasks. A *train* can contain multiple instances of an analysis, and allows to run jobs in parallel.

ALIROOT framework

Data reconstruction and analysis in ALICE is done using the ALIROOT framework [22]. ALIROOT is based the ROOT software [23]. ROOT is written in C++ and was created in 1994 at CERN for high energy physics. It is still continuously under development, and contains a bank

of classes, methods and statistical tools for the analyses. ALIROOT uses many ROOT packages, and was developed by the collaboration to implement tools needed for event simulation, reconstruction and analysis. The complete geometry of the ALICE detector is described there using the ROOT geometry classes. The magnetic field is described by a detailed parametrization. Among the activities carried out by ALIROOT, an important task is Monte Carlo simulations.

Monte Carlo (MC) simulations[8] in ALICE are based on a Monte Carlo generator, which generates events of a given physical process, from inputs such as initial particles, their energy, their charge. The particles are transported through the detector, creating hits in the sensitive volumes of the detectors. These hits correspond to the energy deposition of a particle in these volumes. Particle transport in the construction material is managed using the GEANT 3 [25] package. Then, the response of the detectors is applied to the recorded hits. Finally, the reconstruction of the simulated data follows the same reconstruction chain as for the real data. All these steps are integrated into a single simulation job, which will be sent to the GRID for execution. The output file is then an ESD file, which also contains information on the generated particles.

The reconstruction procedures are the same for experimental or simulated data. In the case of simulations, an event corresponds to one iteration of the event generator producing the particles that belong to the simulated interaction, whereas in the case of real data, an event corresponds to a collision of the beams recorded by the ALICE detector during data taking. The physical analysis is performed by the analysis task, which runs on ESD or AOD files. The analysis consists of applying an algorithm to the event object, and generally processes the reconstructed tracks in the event and evaluates other event observables such as energy deposition in ZDCs, number of triggered cells in the V0 detectors, or the multiplicity in the SPD. Each analysis is sent to the GRID where it is divided into separate jobs, each job being assigned a set of data files. Finally, the outputs of all jobs belonging to the given analysis are merged into one single output file in ROOT format.

2.4 Summary

ALICE is a heavy-ion experiment supplied by LHC beams. The detector comprises numerous subsystems, of which six are used in the analysis, in particular, the muon spectrometer in the front region $-4 < \eta < -2.5$ that is used to reconstruct the muons resulting from the decay of J/ψ particles. We reviewed how data is processed and saved following a decision based on different trigger criteria until its conversion into AOD files. These files are the starting point for the analysis. However, a so-called "offline" selection must be made among the recorded events to sort out the events of interest and the background events. This selection is determined based on the expected signals in the ALICE detectors for the production of J/ψ particles in UPCs protons and lead ions, as discussed in the next chapter.

[8] A Monte Carlo method is an algorithmic method aimed at calculating an approximate numerical value using random processes. A more detailed explanation can be found for example in reference [24].

Bibliography

[1] Lyndon Evans and Philip Bryant. LHC Machine. *Journal of Instrumentation*, 3(08):S08001–S08001, aug 2008. doi: 10.1088/1748-0221/3/08/s08001. URL https://doi.org/10.1088/1748-0221/3/08/s08001.

[2] G. Aad et al. The ATLAS Experiment at the CERN Large Hadron Collider. *JINST*, 3: S08003, 2008. doi: 10.1088/1748-0221/3/08/S08003.

[3] S. Chatrchyan et al. The CMS Experiment at the CERN LHC. *JINST*, 3:S08004, 2008. doi: 10.1088/1748-0221/3/08/S08004.

[4] K. Aamodt et al. The ALICE experiment at the CERN LHC. *JINST*, 3:S08002, 2008. doi: 10.1088/1748-0221/3/08/S08002.

[5] A. Augusto Alves, Jr. et al. The LHCb Detector at the LHC. *JINST*, 3:S08005, 2008. doi: 10.1088/1748-0221/3/08/S08005.

[6] Pierre Fayet and S. Ferrara. Supersymmetry. *Phys. Rept.*, 32:249–334, 1977. doi: 10.1016/0370-1573(77)90066-7.

[7] V Altini, F Carena, W Carena, S Chapeland, V Chibante Barroso, F Costa, R Divia, U Fuchs, I Makhlyueva, F Roukoutakis, K Schossmaier, C Soos, P Vande Vyvre, and B Von Haller. The ALICE Electronic Logbook. *J. Phys.: Conf. Ser.*, 219:022027, 2010. doi: 10.1088/1742-6596/219/2/022027. URL https://cds.cern.ch/record/1269927.

[8] Roderik Bruce, Gianluigi Arduini, Hannes Bartosik, Riccardo De Maria, Massimo Giovannozzi, Giovanni Iadarola, John Jowett, Kevin Shing Bruce Li, Mike Lamont, Anton Lechner, Elias Metral, Daniele Mirarchi, Tatiana Pieloni, Stefano Redaelli, Giovanni Rumolo, Benoit Salvant, Rogelio Tomas Garcia, and Jorg Wenninger. LHC Run 2: Results and challenges. page MOAM5P50. 7 p, Jul 2016. doi: 10.18429/JACoW-HB2016-MOAM5P50. URL https://cds.cern.ch/record/2201447.

[9] Sourav Sarkar, Helmut Satz, and Bikash Sinha, editors. *The physics of the quark-gluon plasma*, volume 785. 2010. doi: 10.1007/978-3-642-02286-9.

[10] B Abelev et al. Upgrade of the ALICE Experiment: Letter Of Intent. *J. Phys. G*, 41:087001, 2014. doi: 10.1088/0954-3899/41/8/087001.

[11] L. Palomo. The ALICE experiment upgrades for LHC Run 3 and beyond: contributions from mexican groups. *Journal of Physics: Conference Series*, 912:012023, 10 2017. doi: 10.1088/1742-6596/912/1/012023.

[12] Domenico Colella. ALICE ITS: the Run 1 to Run 2 transition and recent operational experience. *PoS*, VERTEX2015:003, 2015. doi: 10.22323/1.254.0003. URL https://cds.cern.ch/record/2159190.

[13] Alice website. URL https://alice-collaboration.web.cern.ch/node/34995.

[14] B. Abelev et al. Measurement of inelastic, single- and double-diffraction cross sections in proton–proton collisions at the LHC with ALICE. *The European Physical Journal C*, 73(6), jun 2013. doi: 10.1140/epjc/s10052-013-2456-0. URL https://doi.org/10.1140%2Fepjc%2Fs10052-013-2456-0.

[15] J C Cabanillas, M I Martínez, and I León. ALICE Diffractive Detector Control System for RUN-II in the ALICE Experiment. *Journal of Physics: Conference Series*, 761:012025, oct 2016. doi: 10.1088/1742-6596/761/1/012025. URL https://doi.org/10.1088/1742-6596/761/1/012025.

[16] Betty Bezverkhny Abelev et al. Performance of the ALICE Experiment at the CERN LHC. *Int. J. Mod. Phys. A*, 29:1430044, 2014. doi: 10.1142/S0217751X14300440.

[17] Giacomo Mauri. Development and Characterization of Detectors for large Area Application in Neutron Scattering and small Area Application in Neutron Reflectometry. 05 2019.

[18] G. Blanchard, P. Crochet, and P. Dupieux. The Local Trigger Electronics of the ALICE dimuon trigger. Technical report, 2004. URL http://hal.in2p3.fr/in2p3-00020308.

[19] *ALICE dimuon forward spectrometer: Technical Design Report*. Technical design report. ALICE. CERN, Geneva, 8 1999. URL https://cds.cern.ch/record/401974.

[20] L. Aphecetche et al. Numerical Simulations and Offline Reconstruction of the Muon Spectrometer of ALICE. Aug 2009. URL https://edms.cern.ch/document/1054937/1.

[21] R. Frühwirth. Application of Kalman filtering to track and vertex fitting. *Nuclear Instruments and Methods in Physics Research Section A: Accelerators, Spectrometers, Detectors and Associated Equipment*, 262(2):444–450, 1987. ISSN 0168-9002. doi: https://doi.org/10.1016/0168-9002(87)90887-4. URL https://www.sciencedirect.com/science/article/pii/0168900287908874.

[22] F. Carminati and A. Morsch. Simulation in ALICE. *eConf*, C0303241:TUMT004, 2003.

[23] I. Antcheva et al. ROOT: A C++ framework for petabyte data storage, statistical analysis and visualization. *Comput. Phys. Commun.*, 180:2499–2512, 2009. doi: 10.1016/j.cpc.2009.08.005.

[24] Dirk P. Kroese, Tim J. Brereton, Thomas Taimre, and Zdravko I. Botev. Why the monte carlo method is so important today. *Wiley Interdisciplinary Reviews: Computational Statistics*, 6, 2014.

[25] R. Brun, F. Bruyant, M. Maire, A. C. McPherson, and P. Zanarini. GEANT3. 9 1987.

Chapter 3

Data sample and event selection

Contents

3.1 Data sets **68**
3.1.1 Signature of J/ψ events in the detector 68
3.1.2 Triggers 69
3.1.3 Monte Carlo samples 70
3.2 Event selection **70**
3.2.1 Muon cuts 70
3.2.2 Cuts in the SPD, ZDC, V0 and AD detectors 72
3.2.3 Exclusivity in the proton-going side 75
3.3 Luminosity determination **76**
3.3.1 Calculation method 77
3.3.2 Application to the data sample used in the analysis 79
3.4 Summary **81**
Bibliography **82**

As discussed in chapter 1, the interior of the proton can be probed by the photoproduction of J/ψ mesons off protons in ultra-peripheral collisions of protons and lead nuclei. Two measurements can achieve this goal: the measurement of the exclusive process, in which the two colliding nuclei stay intact, and the measurement of the dissociative process, in which the proton breaks up. To perform these measurements, the data taken with the ALICE detector presented in the chapter 2 must be analyzed, the goal being to measure the exclusive and dissociative cross sections of J/ψ photoproduction in UPCs. In this analysis, the J/ψ is measured in a particular configuration: the proton beam goes in the direction of the muon spectrometer, while the lead beam goes in the opposite direction. The J/ψ is measured in the muon spectrometer, i.e. in the same direction as the proton, via its decay into two muons. Of course not all the data taken by the ALICE detector are needed, and only a subsample of the data contains events of this type. So the first step, which is developed throughout this chapter, is to select the data to be used in the analysis. First, a description of the data taken in real conditions and resulting from simulations is given. Then, we focus on the so-called "offline" selection of the data using the information provided by different ALICE detectors. Finally, we compute the luminosity of the data sample used for the present analysis. This quantity is crucial to characterize the data sample since it is related to the number of collisions of interest - and therefore the size of the data sample - and is used as a normalization factor to deduce cross sections.

3.1 Data sets

3.1.1 Signature of J/ψ events in the detector

Events of J/ψ photoproduction are identified by their signature in the ALICE detectors. The J/ψ has a very short lifetime - of the order of 10^{-20} seconds - and decays mainly into lighter hadrons or lepton pairs. In particular the J/ψ decays into a pair $\mu^+\mu^-$ with a probability close to 6% [1]: this decay channel is the one used to measure the J/ψ in the present analysis. The muons are detected in the muon spectrometer described in the previous chapter (see section 2.2.3), and the information on their trajectory makes it possible to reconstruct the history of the original J/ψ, giving access for example to its rapidity y, to its energy, to its momentum, and to its mass.

Let us recall that the center-of-mass energy $W_{\gamma p}$ of the photon-proton system is given by:

$$W_{\gamma p}^2 = 2E_p M_{J/\psi} \exp(-y) \tag{3.1}$$

where the rapidity of the J/ψ is defined with respect to the proton beam direction (see section 1.4.2 for a definition of rapidity). Details of this computation are given in appendix A.

Given the position of the muon spectrometer with respect to the beams, two configurations are possible. Either the proton beam goes in the direction of the muon spectrometer, and so the muons are detected in the same direction as the proton. According to the equation 3.1, with $y > 0$, this gives access to the low energy configuration $W_{\gamma p}$. Conversely, if the proton beam goes in the reverse direction - that is, towards the opposite side of the spectrometer muon - then the rapidity of the J/ψ with respect to the proton is negative, $y < 0$. According to the equation 3.1, this corresponds to the high energy configuration. The accessible energies $W_{\gamma p}$ according to the beam configuration are given in the table 3.1.

In this analysis, only data in which the proton goes in the direction of the muon spectrometer is used. This configuration is denoted p–Pb, and it is presented in the figure 3.1.

Beams configuration	J/ψ rapidity	Energy range (GeV)	Bjorken-x scale
p–Pb	$2.5 < y < 4.0$	$27 < W_{\gamma p} < 57$	$5 \times 10^{-3} < x < 2 \times 10^{-2}$
Pb–p	$-4.0 < y < -2.5$	$702 < W_{\gamma p} < 1486$	$8 \times 10^{-6} < x < 3 \times 10^{-5}$

Table 3.1

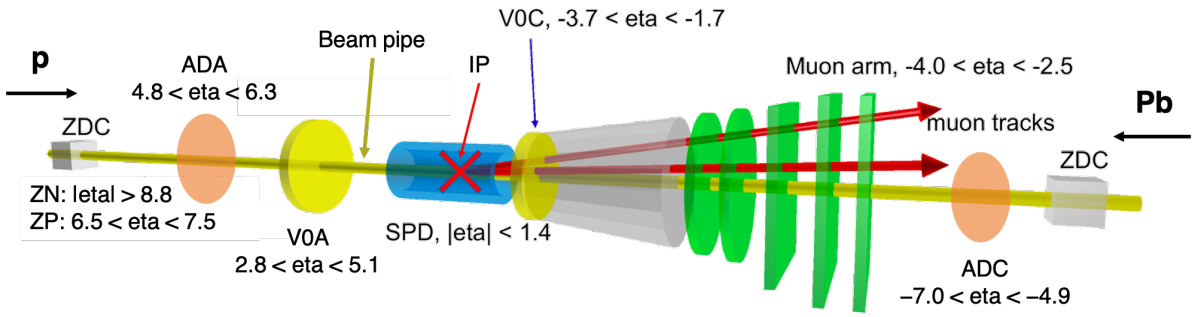

Figure 3.1: Schematic layout of the ALICE detector. The individual detectors are not in scale. Figure taken from reference [2].

In the case of exclusive J/ψ photoproduction in UPCs, no other particle production than the J/ψ meson is expected. In the case where the proton dissociates, debris of particles are produced in the direction of the proton with a rapidity gap between them and the J/ψ. The values of Q^2 and t are small and generally, the Pb ion (and the proton in the exclusive process) is (are) only very weakly deflected and therefore not detected by the experimental apparatus. Thus, the events studied to identify diffractive J/ψ photoproduction are characterized by two muons detected in the muon spectrometer and no activity in the detectors on the Pb-going side since the lead nucleus remains intact. If the proton does not dissociate (exclusive production), there should be no activity in the detectors on the p-going side as well. In the following, the "proton(Pb) side" means the proton(Pb)-going side.

3.1.2 Triggers

The data used in the analysis is recorded after the decision of a specific *online* trigger, appropriate to select UPCs with a potential J/ψ candidate and with as little activity as possible. The trigger can either require a signal in a detector or conversely require no signal in a detector, in which case it is used as a "veto". Veto names are represented with a '*' symbol. The trigger class used for the studied data is CMUP14-B-NOPF-MUFAST, where

- CMUP14 is the class name, where 'C' stands for class, 'M' for muon and 'UP' for ultra-peripheral
- B stands for "beam–beam" collisions

- NOPF stands for "no past-future protection", which means that no online timing vetoes around the time of the actual event were applied (no protection on other bunch crossings)
- MUFAST is the detector cluster used to read signals, which gathers in this case the AD, MCH, MTR, SPD, T0, V0, and ZDC detectors

and the trigger associated is 0MSL *0VBA *0UBA where

- 0MSL triggers on a single muon in the MTR (before track reconstruction in the MCH) with a low p_{T} (0.5 GeV/c) threshold,
- *0UBA is a veto on activity in the AD beam–beam time windows,
- *0VBA is a veto on activity in the V0A beam–beam time window.

Let us recall that the letter 'C' designates the detectors on the side of the muon spectrometer, while the letter 'A' designates the detectors on the opposite side. The two last criteria of this list ensure the suppression of events in which the lead nucleus dissociates.

As explained in section 2.3, the data are then stored in AOD files. The period used, LHC16r, includes 55 runs.

3.1.3 Monte Carlo samples

The Monte Carlo processes used for the analysis were produced with the STARlight 2.2.0 MC generator [3–5]. STARlight is a program that calculates the cross sections of many UPC processes within specific kinematic constraints, as a function of $W_{\gamma\mathrm{p}}$, the final-state rapidity and the final-state transverse momentum p_{T}. The produced processes for the analysis are exclusive J/ψ production in $\gamma\mathrm{p}$ interactions, production of J/ψ in $\gamma\mathrm{Pb}$ interactions, production of $\psi(2\mathrm{S})$ in $\gamma\mathrm{p}$ interactions decaying into J/ψ and anything, and exclusive dimuon production in two-photon interactions - these three last processes will be discussed in the next chapter. The decay muons are tracked in a model of the apparatus implemented in GEANT 3.21 [6], and events are folded with the detector response simulation to reproduce the 2016 p–Pb running conditions.

In order to account for time-varying conditions of the data taking in the simulations, the latter are done run by run. For each run, the conditions of the real data taking are loaded from the OCDB files, and a weight proportional to the number of events triggered by the CMUP14 trigger is applied to the generated events.

3.2 Event selection

The data selection is dictated by the expected signature of events in the various detection elements, as explained in section 3.1.1. This selection, firstly done with the trigger presented in section 3.1.2, is completed by the offline analysis applied on the AOD files directly.

3.2.1 Muon cuts

Each muon must meet the following requirements.

- Each muon track reconstructed by the MCH must be associated with a muon track in the MTR chambers and belong to an event triggered according to the description given in section 3.1.2, in order to guarantee that each track is real and that it comes from the IP.

Typically, this makes it possible to reduce the contribution of muons resulting from the decays of pions and kaons.

- Each muon track has to lie within the pseudorapidity η acceptance of the muon spectrometer, i.e. $-4.0 < \eta < -2.5$.
- The angle θ_{abs} from the interaction vertex between the position of the trace at the end of the front absorber and the axis of the beam must satisfy the condition $2° < \theta_{abs} < 10°$ (see figure 3.2). This makes it possible to reject traces passing through parts of the absorber of different compositions, whether they are emitted at small or large angles. Or equivalently, each muon track has to satisfy the requirement for the absorber: $17.5 < R_{\text{abs}} < 89.5$ cm where R_{abs} is the radial position of the muon at the end of the absorber.
- A cut is applied on the product $p\times$DCA, where p is the total track momentum, and DCA stands for Distance of Closest Approach. The DCA is the distance in the transverse plane between the extrapolated position of the reconstructed track in the MCH and the position of the nominal IP (see figure 3.2). The dispersion of the DCA around the interaction vertex is mainly due to the Coulomb scatterings of the muons in the front absorber materials. Thus to first order, this dispersion is of Gaussian nature with a standard deviation proportional to $1/p$. The $p\times$DCA cutoff, independent of the particle's momentum, selects particles for which the $p\times$DCA is within 6 σ where σ is the dispersion of the $p\times$DCA distribution. Thus, it makes it possible to ensure that the selected muons indeed come from the interaction vertex with no loss. It rejects non-primary particles reconstructed by the tracking algorithm, typically background events coming from beam–gas interaction (interaction of beam particles with the residual gas inside the beam pipe) or secondary particles produced in the front absorber.

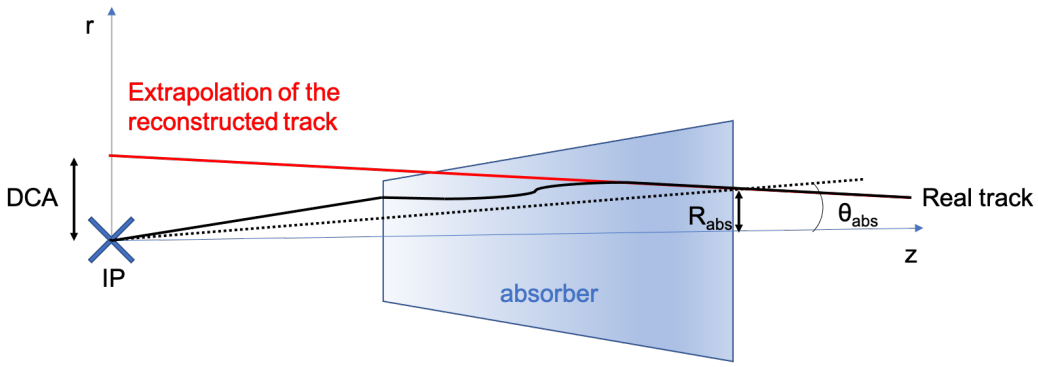

Figure 3.2: Geometric view of the front asborber and a muon track.

Moreover, two muons of opposite signs are expected in the muon spectrometer - two muons *only*. Thus, in addition to these selections applied to single muons, each event is filtered according to the following criteria.

- There must be exactly two muons.
- The two muons carry opposite electric charges.
- The dimuon rapidity, reconstructed from the addition of the two Lorentz vectors that describe each muon, has to satisfy the requirement $2.5 < y < 4.0$.

The effect of this muon-based selection on the number of events is shown in table 3.2.

Selection	Number of events
Events analyzed	14687514
Triggered	12227445
Two good tracks	20439
Opposite electric charge	16482

Table 3.2: Effect of each muon cut on the data sample.

The reconstructed dimuon invariant mass after the muon cuts is shown in figure 3.3 within the range $1.0 < M_{\mu\mu} < 3.5$ GeV/c^2. The J/ψ peak around 3.1 GeV/c^2 is clearly visible, above a so-called dimuon background continuum.

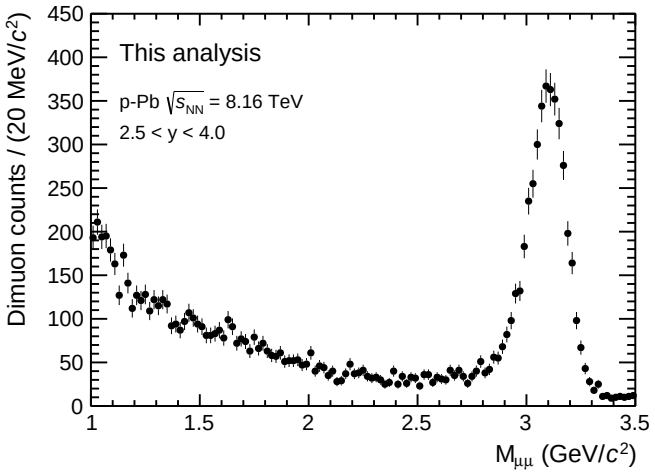

Figure 3.3: Dimuon invariant mass in the data after applying muon filters.

The muons being selected with the MCH and MTR information, selections on the other detectors have to be applied to ensure that the lead nucleus remains intact and that the collisions studied indeed correspond to exclusive and dissociative J/ψ photoproduction in UPCs.

3.2.2 Cuts in the SPD, ZDC, V0 and AD detectors

In order to avoid hadronic collisions, which could result in the emission of particles at mid-rapidity, the SPD detector is used. The SPD identifies tracklets, which are track fragments created from two reconstructed points in the SPD, the first in the inner layer and the second in the outer layer. The number of tracklets is, therefore, an estimator of charged particle multiplicity at mid-rapidity. Thus, at most two tracklets are required in the SPD. The tolerance of two tracklets makes it possible not to remove a significant quantity of events in which an event of interest is accompanied by another event in the same bunch crossing (pile-up), typically electromagnetic events where two photons coming from both a proton and a lead nucleus interact ($\gamma\gamma \to ee$), or beam–gas interactions, that would result in a signal in the SPD.

Moreover, as discussed in section 3.1.1, the lead nucleus is expected to remain intact after the interaction. Its break-up could induce signals in the forward detectors on the A side. The forward detectors used for this analysis are the neutron ZDC (ZN), the AD, and V0 detectors (see figure 3.1). These detectors should not show any activity related to the break-up of the Pb nucleus.

- Each quadrant of the ZN detector records timing information of possible collisions for each event with a time resolution of the order of 0.1 ns. They use the expected moment of bunch crossing as the reference time, and they save a default value of -999 ns if no signal was detected. None of these instants in the four quadrants of ZNA must be within the window [-2 ns, $+2$ ns], which concentrates all the events which were not stored at the default value.

- The V0 and AD detectors also record the times of the collected signals. Their temporal resolution is better than 1 ns, thus making it possible to discriminate "beam–gas" events, in which the beam particles interact with the residual gas inside the beam pipe, from "beam–beam" interactions. If these signals are within a time window of about 4 ns around the expected bunch crossing time, then they are classified as coming from "beam–beam" interactions. All these events classified as "beam–beam" interactions are rejected by V0A and by ADA.

One last criterion is applied on the proton-going side to discard background events such as hadronic collisions in V0C. This cutoff assumes that events with a dissociative proton do not leave a signal there, given the Lorentz boost of the proton. This assumption is confirmed by studies presented in appendix B.1. As the V0C detector is positioned in front of the muon spectrometer, the latter can then detect the passage of muons, even if its acceptance coverage is smaller ($-3.7 < \eta < -1.7$ for V0C and $-4.0 < \eta < -2.5$ for the muon spectrometer). Each muon is identified by its (η, φ) coordinates, and the same goes for each cell of V0C. Then, it becomes possible to match the fired cells of V0C with the muons that have crossed them: the cells are said to be matched to a muon. Thus, the V0C cut restricts the number of fired cells to the sum of the number of matched cells plus two. This tolerance of two additional fired cells, discussed in appendix B.2, is necessary because of pile-up events and electronic background signals that can occur in V0C cells, thus inducing an inefficiency of the detector.

The effect of these cuts on the number of events over the whole invariant mass and p_{T} ranges after the preselection is presented in table 3.3.

Selection	Number of events
Events after preselection	16482
No beam-beam activity in ZN Pb-side	15336
No beam-beam activity in AD Pb-side	15321
No beam-beam activity in V0 Pb-side	14221
No extra beam-beam activity in V0 p-side	7582
Less than three tracklets in SPD	7059

Table 3.3: Effect of requirements on the ZDC, V0, AD and SPD detectors on the data sample.

Pile-up correction

The fact of using vetoes in the data selection may suppress events of interest. This typically happens when collisions produce events of interest and another interaction, a phenomenon known as pile-up. When this happens, this other interaction may leave signals in the vetoes, which will reject the event of interest at the same time. Therefore, the number of counts in the selected data has to be corrected for this pile-up probability. Details on the computation of this correction factor are presented in appendix C.

Mass distribution of the selected data

Finally, the data is selected within the dimuon transverse momentum p_{T} range $p_{\mathrm{T}} < 3$ GeV/c. This selection using the SPD, ZN, AD, V0 detectors and the p_{T} cut is the selection used to extract the number of J/ψ (in next chapter). In what follows, this selection is called the **standard selection**. The dimuon invariant mass spectrum of the data resulting from the standard selection are shown in figure 3.4. Clearly, a large amount of background events are suppressed when compared to figure 3.3.

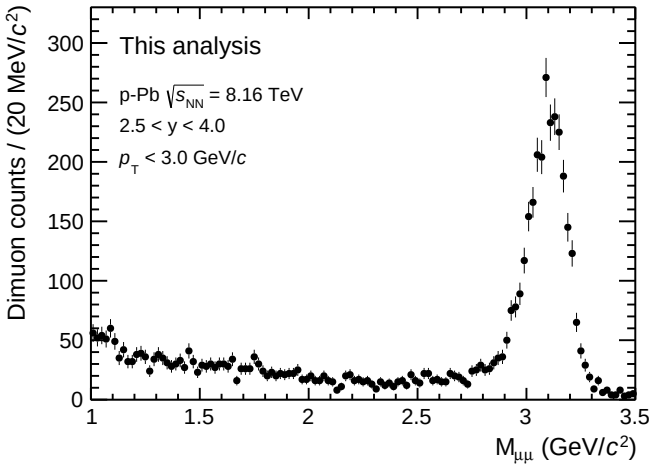

Figure 3.4: Dimuon invariant mass in the data, after the standard selection.

3.2.3 Exclusivity in the proton-going side

The analysis also uses a more restricted event selection in order to constrain the p_{T} shapes of exclusive processes, for which only two muons are produced in the final state and both p and Pb nuclei stay intact. This pure exclusive sample is obtained by applying additional vetoes on the proton side.

- None of the four times stored in ZNC is within ± 6 ns with respect to the expected time of bunch crossing. This more restrictive cut compared to the one on the Pb-going side is due to a broader time distribution of events in ZNC. A possible explanation is that the energy deposition of particles produced in the proton direction is weaker than is the Pb side, hence a worse resolution.

- Analogously to the cut on V0A and ADA, all events classified as "beam–beam" interactions are rejected in V0C and ADC.

- Since the photons are emitted coherently by an object of size R, and since there is no boost - like in the longitudinal direction - that increases their momentum component, the transverse momentum of the photons goes as $\hbar c/R$. As a consequence of momentum conservation, the p_{T} of the produced dimuon also behaves as $O(\hbar c/R)$. For inclusive production, there is no such condition on the photon being emitted coherently, limiting the size of its wavelength. Therefore the photon p_{T} is not driven by the size of the emitting object, and inclusive production is usually characterized by larger transverse dimuon momenta p_{T}. Therefore, exclusive events in which the nucleus stays intact are expected to peak at lower p_{T} than inclusive events where the target dissociates in either a photo-induced interaction or a hadronic interaction. Consequently, the transverse momentum p_{T} of the dimuon pair has to lie within the restricted range $p_{\mathrm{T}} < 1.2$ GeV/c.

The effect of these additional cuts on the number of events is presented in the table 3.3. In the following this selection will be referred to as the **exclusive selection**.

Selection	Number of events
Selection on intact Pb ions	7059
No beam-beam activity in AD p-side	5158
No beam-beam activity in ZN p-side (± 6 ns)	3972

Table 3.4: Effect of requirements for exclusivity on the proton side.

The data resulting from this exclusive selection are shown in figure 3.5. Then again, one can see the J/ψ peak and a continuum mostly present at lower invariant masses, which survives the exclusive selection and therefore must leave in the detectors the same signature as exclusive J/ψ photoproduction. These events are mostly dimuon production in two-photon interactions, $\gamma\gamma \to \mu^+\mu^-$, shown in figure 3.6. In this process, the proton and the lead nucleus interact via the emission of two quasi-real photons, which in turn produce a pair of muons. Thus the two nuclei remain intact, and only two muons are produced in the final state.

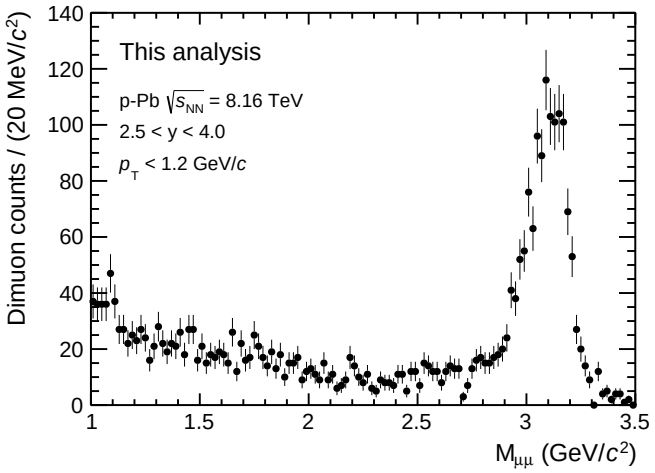

Figure 3.5: Dimuon invariant mass in the data, after the exclusive selection.

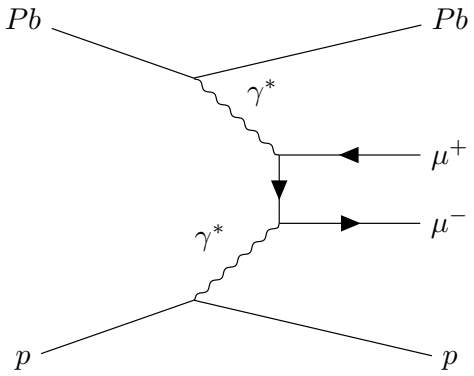

Figure 3.6: Feynman diagram at LO for dimuon production in two-photon interactions, in p–Pb UPCs.

3.3 Luminosity determination

As explained in section 2.1.3, the data are characterized by the *instantaneous* luminosity $\mathcal{L}$ which assesses the quality of a collider to produce collisions for each run. It is expressed in cm^2s^{-1}, as opposed to the *integrated* luminosity, which corresponds to the instantaneous luminosity integrated over time and which is expressed in $[\text{nb}^{-1}]$[1]. The measurements presented using this data must be normalized to the integrated luminosity of the trigger class used $\mathcal{L}_{\text{class}}$ for each one of the runs considered (as defined in section 2.3.2). The latter depends on the delivered luminosity in the LHC machine and is reduced due to the inefficiencies and latencies of the detectors used in the trigger class for a given data set.

This section presents the method for calculating the integrated luminosity over the entire duration of the data taking, then we apply it to the data set used in the present analysis.

[1]The barn (symbol b) is a unit of area used especially in nuclear and particle physics to express cross sections. Its value is 10^{-24} cm^2, and one nanobarn corresponds to 10^{-33} cm^2.

3.3.1 Calculation method

In its simplest formulation, the integrated luminosity for a given trigger class is defined by:

$$\mathcal{L}_{\text{class}} = \frac{N_{\text{class}}}{\sigma_{\text{class}}} \tag{3.2}$$

where N_{class} is the number of inputs of the trigger used in the analysis, and σ_{class} is the cross section of the trigger signature that is used to count N_{class}. In practice, the cross section σ_{class} is not known. Thus, we will instead use a reference process, i.e. a class of inelastic events satisfying a given trigger condition, based only on the V0 or T0 detector (MB trigger), and for which the inelastic cross section σ_{REF} is measured as explained in the following (see Luminosity determination for the reference process).

The luminosity integrated over the duration of the data taking for the analysis trigger class can then be defined from the luminosity of the reference process:

$$\mathcal{L}_{\text{class}} = \mathcal{L}_{\text{REF}} \cdot \epsilon_{\text{class}} \tag{3.3}$$

where ϵ_{class} is a normalization factor to reduce the number of counts to the one in the analysis trigger, and $\mathcal{L}_{\text{REF}}$ is the integrated luminosity for the MB trigger class considered. $\mathcal{L}_{\text{REF}}$ is defined analogously to the equation 3.2 such that

$$\mathcal{L}_{\text{REF}} = \frac{N_{\text{REF}}}{\sigma_{\text{REF}}} \tag{3.4}$$

where N_{REF} is the number of L0 entries of the MB trigger obtained from the OCDB files for the reference process.

All the details of the calculation are presented in reference [7] for the data sample used, and we will now see how the different terms of the equations 3.3 and 3.4 are obtained.

Luminosity determination for the reference process

Let us consider the terms of equation 3.4.

The reference cross section σ_{REF} seen by a given detector is in our case the cross section of inelastic events that satisfy a given trigger condition. The cross sections were directly measured for two reference processes: one is based on the V0 detector, the other on the T0 detector (see section 2.2.2 for a description of the V0 and T0 detectors). In our analysis, the reference process based on the T0 detector is used.

The trigger condition based on T0 requires at least one hit in each of the two sub-detectors of the T0, i.e. on both sides of the IP. Also, the longitudinal coordinate of the interaction vertex must be in the range $|z| < 30$ cm where $z = 0$ is the position of the nominal IP. This cut aims to reject the background of beam–gas and beam–satellite interactions[2] (more details are given in references [8, 9]).

The reference cross section is defined by

$$\sigma_{\text{REF}} = R/\mathcal{L} \text{ with } \mathcal{L} = N_1 N_2 f_{\text{rev}}/(h_x h_y) \tag{3.5}$$

where R is the measured head-on collision rate of the collision process, $\mathcal{L}$ is luminosity for head-on collisions of a pair of bunches, N_1 and N_2 are the numbers of particles in each of the

[2]Satellite charges are charges which are located within a filled bunch slot but outside the central 2.5 ns radio-frequency bucket of this slot.

colliding bunches, f_{rev} is the accelerator revolution frequency and h_x and h_y are the effective convolved beam widths in the two transverse directions.

The cross section σ_{REF} is firstly evaluated from MC estimates, and then from a method called Van der Meer (VdM) scan [10, 11]. The VdM scan analysis procedure is described in detail in documents [8, 9]. It allows to measure the beam widths h_x and h_y, while the other parameters, N_1, N_2, and f_{rev}, are well known. The method consists in slightly displacing one of the two beams with respect to the other in the transverse directions x (horizontal) and y (vertical). The variation of the reaction rate allows a direct quantification of the transverse distribution of the particles in each one of the two beams. By observing the rate of a particularly well-known reaction (called a standard candle), the VdM scan method makes it possible to establish the absolute scale for calibrating the luminosity measurement.

The second term of the equation 3.4 is the number of L0 inputs of the MB trigger based on T0 or V0, N_{REF}. This number is determined from the raw trigger rates taking into account the background noise contamination of the beam, stacking effects and the time dependence of the burst intensities. It is then written to the OCDB files for the corresponding reference process.

Fraction of inelastic events that satisfy the trigger condition

Let us now consider the terms of equation 3.3. The term $\mathcal{L}_{\text{REF}}$ has just been explained above. The term ϵ_{class} corresponds to the fraction of events triggered by the analysis trigger and by the reference trigger. Moreover, a small contamination by multiple interactions in the same bunch crossing can also affect the ϵ_{class} factor. Thus, the factor ϵ_{class} is defined by:

$$\epsilon_{\text{class}} = \frac{N_{\text{class}}}{N_{\text{REF}}} C_{\text{pu}}(\mu_{\text{REF}}) \cdot C_{\text{ds}} \tag{3.6}$$

where N_{class} is the number of events containing a trigger signal of the trigger class used for the analysis, $C_{\text{pu}}(\mu_{\text{REF}})$ is the correction factor for pile-up with μ_{REF} the average number of collisions per bunch crossing, and C_{ds} is the correction factor related to the possible downscaling of triggers.

Now let us look at the calculation of the correction factor for the pile-up. The probability P of having k collisions in a bunch crossing follows a Poisson law with mean μ_{REF}:

$$P(X = k) = \frac{\mu_{\text{REF}}^k}{k!} e^{-\mu_{\text{REF}}} \tag{3.7}$$

where X is the random variable corresponding to the number of collisions in a bunch crossing, and the average number of collisions in a bunch crossing μ_{REF} is given by:

$$\mu_{\text{REF}} = -\log\left(1 - \frac{L^B_{\text{REF}}}{N_{bc}}\right) \tag{3.8}$$

where $N_{bc} = N_{\text{coll}} \times f_{\text{LHC}} \times \Delta t_{\text{run}}$ is the number of bunch crossings per run, N_{coll} is the number of colliding beam bunches, f_{LHC} is the revolution frequency of the LHC, and Δt_{run} is the duration of the run.

The probability of a collision with no pile-up is given by

$$P(\text{no pile-up}) = \frac{P(X=1)}{P(X>0)} \tag{3.9}$$

$$= \frac{P(X=1)}{1-P(X=0)} \tag{3.10}$$

$$= \frac{\mu_{\text{REF}}\ e^{-\mu_{\text{REF}}}}{1-e^{-\mu_{\text{REF}}}} \tag{3.11}$$

$$P(\text{no pile-up}) \sim e^{-\mu_{\text{REF}}} \text{ under the assumption that } \mu_{\text{REF}} \ll 1 \tag{3.12}$$

Thus, the correction factor for the pile-up is given for each run by:

$$C_{\text{pu}}(\mu_{\text{REF}}) = e^{-\mu_{\text{REF}}} \tag{3.13}$$

Now let us look at the correction factor C_{ds}. In some cases, the trigger rate of a process can be intentionally reduced, as explained in section 2.3: this practice is called down-scaling. Thus the counts must be normalized according to the down-scaling factor associated with them, and the factor C_{ds} simply corresponds to

$$C_{\text{ds}} = \frac{\text{DS}_{\text{REF}}}{\text{DS}_{\text{class}}} \tag{3.14}$$

where DS_{REF} and DS_{class} are the down-scaling factors of the MB trigger and of the class used by the analysis, respectively, taken from the OCDB files.

In the case where no down-scaling has been performed, one simply has $C_{\text{ds}} = 1$.

3.3.2 Application to the data sample used in the analysis

The reference process used for the calculation of the luminosity of the data sample is C0TVX-B-NOPF-CENTNOTRD where

- 'C0TVX' means that the T0 detector was used as MB trigger
- 'B' stands for "beam–beam" collisions
- 'NOPF' stands for no past-future protection, which indicates that there was no protection on other bunch crossings
- 'CENT' means that the detector cluster used to read the data gathers the AD, ACORDE, SDD, SPD, SSD, T0, TPC, V0, and ZDC detectors, and other detectors which have not been described so far, namely the ElectroMagnetic Calorimeter (EMC), the Forward Multiplicity Detector (FMD), the High-Momentum Particle Identification Detector (HMPID), the PHOton Spectrometer (PHOS), and the Time-Of-Flight (TOF) detectors. 'NOTRD' means that the Transition Radiation Detector (TRD), which was not necessarily available, is not needed by the trigger. Details on these detectors can be found in references [12, 13].

The time-integrated luminosity for each run is shown in figure 3.7. The reference luminosity, represented by the blue histogram, was corrected in each run for

- the fraction of the events that were analyzed, $N_{\text{CMUP14}}/N_{\text{REF}}$ where N_{CMUP14} is the number of dimuon events triggered by the CMUP14 trigger class,

- the correction factor for the C0TVX triggers that were lost due to pile-up, $C_{\mathrm{pu}} = e^{-\mu_{\mathrm{REF}}}$, where μ_{REF} is the average number of hadronic collisions per bunch crossing.

Since no down-scaling was performed, the down-scaling correction factor C_{ds} is equal to 1 and therefore does not enter into the calculation of the luminosity in the present analysis. Using the reference cross section evaluated with MC estimates, the integrated analyzed luminosity was found to be

$$\mathcal{L}^{\mathrm{MC}}_{\mathrm{CMUP14}} = 7.357\ \mathrm{nb}^{-1}. \tag{3.15}$$

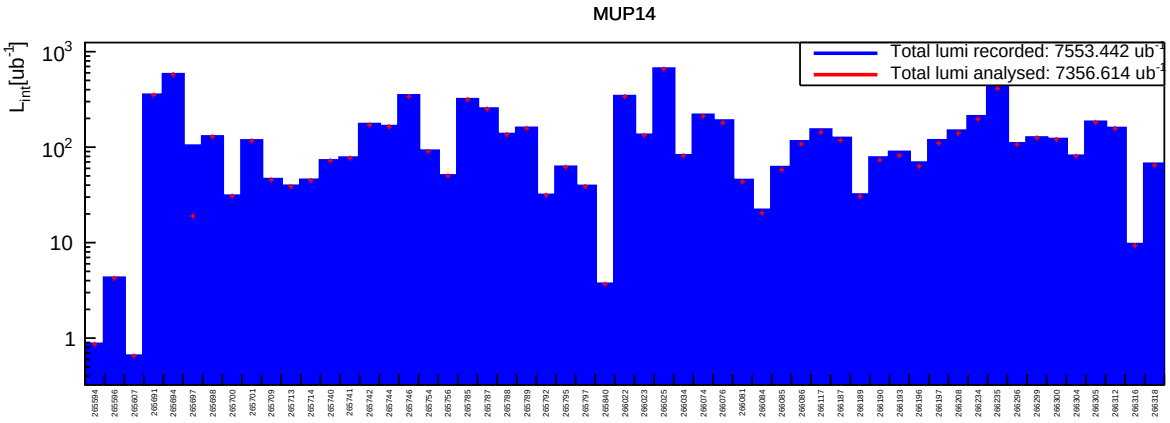

Figure 3.7: Integrated luminosity for each run included in the data set. The recorded luminosity corresponds to the luminosity computed with the reference trigger, while the analyzed luminosity corresponds to the luminosity of the trigger used in the analysis with correction factors.

Correction with VdM scans

The reference cross section for all the analyzed runs σ_{REF} was firstly evaluated at $\sigma^{\mathrm{MC}}_{\mathrm{REF}} = 1.715$ b with the MC estimates, and later evaluated at $\sigma^{\mathrm{VdM}}_{\mathrm{REF}} = 1.655 \pm 0.030$ b (syst.) with VdM scans measurements, based on the T0 detector. Thus, the analyzed luminosity which uses the reference cross section given by the MC estimates must be corrected by this correction factor due to the error on σ_{REF}. Thereby,

$$\mathcal{L}_{\mathrm{CMUP14}} = \mathcal{L}^{\mathrm{MC}}_{\mathrm{CMUP14}} \times \frac{\sigma^{\mathrm{VdM}}_{\mathrm{REF}}}{\sigma^{\mathrm{MC}}_{\mathrm{REF}}} \tag{3.16}$$

$$\mathcal{L}_{\mathrm{CMUP14}} = 7.357 \times \frac{1.715}{1.655}\ \mathrm{nb}^{-1} \tag{3.17}$$

$$\mathcal{L}_{\mathrm{CMUP14}} = 7.624\ \mathrm{nb}^{-1} \tag{3.18}$$

The only uncertainty taken into account in the luminosity calculation is the systematic uncertainty on $\mathcal{L}_{\mathrm{REF}}$. This uncertainty, taken from [7], is 1.8% according to the VdM scan measurement, considering parameters such as the stability of luminosity counters, or the luminosity decay with time. Statistical uncertainties are negligible compared to systematic uncertainties. Finally, the luminosity used in the analysis is

$$\mathcal{L}_{\mathrm{CMUP14}} = 7.62 \pm 0.14\ (\mathrm{syst.})\ \mathrm{nb}^{-1}. \tag{3.19}$$

3.4 Summary

In this chapter, we presented the data sample used for the analysis, determined by the appropriate online trigger to record the signals corresponding to the following criteria:

- at least one muon with a low (~ 0.5 GeV/c) p_{T} threshold is detected in the MTR,
- the lead nucleus remains intact, which is ensured by the use of vetoes in the forward detectors V0A and ADA in the Pb-going side.

The data then undergoes an offline selection in order to retain only dimuons coming from the decay of a J/ψ, while removing as much background as possible.

Moreover, the calculation of the luminosity gives the size of the data sample containing the events of interest, that is to say triggered by the analysis trigger. This element is essential for normalizing event counting, as is pile-up correction.

However, other background processes that leave the same signature in the detectors as J/ψ photoproduction events survive in the data. This is the case of, for example, two-photon interactions resulting in the production of dimuons. Thus a simple count of events is not enough to obtain the number of events corresponding to the J/ψ photoproduction. Instead, the event counts are obtained by a method in which a model function is fitted to the data, taking into account both the signal components - the exclusive production and the dissociative production of J/ψ that we want to measure, and background components - such as two-photon interactions. The signal extraction method is covered in the next chapter.

Bibliography

[1] P. A. Zyla et al. Review of Particle Physics. *PTEP*, 2020(8):083C01, 2020. doi: 10.1093/ptep/ptaa104.

[2] Jaroslav Adam. *Photoproduction of J/ψ in ultra-peripheral p-Pb and Pb-Pb collisions with the ALICE detector at the LHC*. PhD thesis, Prague, Tech. U., 5 2016.

[3] Spencer Klein and Joakim Nystrand. Exclusive vector meson production in relativistic heavy ion collisions. *Phys. Rev.*, C60:014903, 1999. doi: 10.1103/PhysRevC.60.014903.

[4] Spencer R. Klein, Joakim Nystrand, Janet Seger, Yuri Gorbunov, and Joey Butterworth. STARlight: A Monte Carlo simulation program for ultra-peripheral collisions of relativistic ions. *Comput. Phys. Commun.*, 212:258–268, 2017. doi: 10.1016/j.cpc.2016.10.016.

[5] STARLIGHT website. http://starlight.hepforge.org/.

[6] René Brun, F. Bruyant, Federico Carminati, Simone Giani, M. Maire, A. McPherson, G. Patrick, and L. Urban. GEANT Detector Description and Simulation Tool. 10 1994. doi: 10.17181/CERN.MUHF.DMJ1.

[7] ALICE luminosity determination for p-Pb collisions at $\sqrt{s_{\mathrm{NN}}} = 8.16$ TeV. Apr 2018. URL https://cds.cern.ch/record/2314660.

[8] Betty Bezverkhny Abelev et al. Measurement of visible cross sections in proton-lead collisions at $\sqrt{s_{\mathrm{NN}}}$ = 5.02 TeV in van der Meer scans with the ALICE detector. *JINST*, 9(11): P11003, 2014. doi: 10.1088/1748-0221/9/11/P11003.

[9] ALICE luminosity determination for pp collisions at $\sqrt{s} = 13$ TeV. Jun 2016. URL https://cds.cern.ch/record/2160174.

[10] S van der Meer. Calibration of the effective beam height in the ISR. Technical report, CERN, Geneva, 1968. URL https://cds.cern.ch/record/296752.

[11] Vladislav Balagura. Notes on van der Meer Scan for Absolute Luminosity Measurement. *Nucl. Instrum. Meth. A*, 654:634–638, 2011. doi: 10.1016/j.nima.2011.06.007.

[12] K. Aamodt et al. The ALICE experiment at the CERN LHC. *JINST*, 3:S08002, 2008. doi: 10.1088/1748-0221/3/08/S08002.

[13] B Abelev et al. Upgrade of the ALICE Experiment: Letter Of Intent. *J. Phys. G*, 41:087001, 2014. doi: 10.1088/0954-3899/41/8/087001.

Chapter 4

Signal extraction, corrections and uncertainties

Contents

4.1 Signal extraction of exclusive two-photon interactions 84

4.1.1 Characterization of the exclusive dimuon production 84

4.1.2 Signal extraction from the data 87

4.1.3 Systematic uncertainty on signal extraction 89

4.2 Signal extraction for J/ψ photoproduction 92

4.2.1 Mass distribution of the different processes 93

4.2.2 Characterization of the p_{T} distribution of dimuons from two-photon interactions 94

4.2.3 Characterization of the p_{T} distribution of J/ψ events 97

4.2.4 Signal extraction with the standard selection sample 99

4.2.5 Systematic uncertainty on signal extraction 100

4.3 Correction for acceptance and reconstruction efficiency . . . 101

4.3.1 Computation method of acceptance and reconstruction efficiency 103

4.3.2 Results of $A \times E$ computation 104

4.4 Corrections affecting J/ψ signal extraction 105

4.4.1 Feed-down from $\psi(2S)$ 105

4.4.2 Photon flux 106

4.5 Systematic uncertainties 108

4.5.1 Common uncertainties 108

4.5.2 Uncertainties affecting $\gamma\gamma \to \mu^+\mu^-$ signal only 110

4.5.3 Uncertainties affecting J/ψ signal only 110

4.6 Summary 112

Bibliography 113

As we have just seen in the previous chapter, the data selection makes it possible to significantly reduce the number of background events in the sample, that is, events that do not correspond to the exclusive or dissociative J/ψ photoproduction. However, some of them survive in the data after the selection because they have the same signature in the detectors as J/ψ photoproduction events: this is the case in particular for the production of dimuons in two-photon interactions, $\gamma\gamma \to \mu^+\mu^-$, where the two photons are not real (just nearly, since their virtuality is very small). The production of dileptons in two-photon interactions is called Breit-Wheeler process, after the names of the physicists who first described it [1].

The extraction of the Breit-Wheeler process is attractive because it allows testing directly Quantum ElectroDynamics (QED) computations and the nuclei form factors. Since it is the main process competing with J/ψ photoproduction, it ensures better control of the background during the extraction of the signal from J/ψ mesons. Thus this measurement is made to complement the J/ψ production measurement, which is the primary object of this analysis.

This chapter deals with the extraction of signals, first from $\gamma\gamma \to \mu^+\mu^-$ in the invariant mass range $1.0 < M_{\mu\mu} < 2.5$ GeV/c^2 where J/ψ events are absent, and then from J/ψ events around the J/ψ mass peak in the range $2.5 < M_{\mu\mu} < 3.5$ GeV/c^2, produced either exclusively or in a dissociative process. Then the chapter presents the corrections that need to be applied to the extracted signal yields. Finally, the systematic uncertainties associated with these measurements are discussed.

4.1 Signal extraction of exclusive two-photon interactions

The dimuons produced in two-photon interactions have a continuous distribution in the mass spectrum as discussed in section 3.2.3, unlike the dimuons resulting from the decay of the J/ψ-they are said to be a *resonance peak* in the mass spectrum. The non-resonant dimuons are part of the *dimuon continuum*. They are measured in the invariant mass range $1.0 < M_{\mu\mu} < 2.5$ GeV/c^2, where the absence of J/ψ production offers a clean sample of this process.

The measurements are performed by dividing the sample into three mass bins:

- $1.0 < M_{\mu\mu} < 1.5$ GeV/c^2,
- $1.5 < M_{\mu\mu} < 2.0$ GeV/c^2,
- $2.0 < M_{\mu\mu} < 2.5$ GeV/c^2,

for the full rapidity coverage, and in two rapidity bins:

- $2.50 < y < 4.00$,
- $2.50 < y < 3.25$,
- $3.25 < y < 4.00$.

4.1.1 Characterization of the exclusive dimuon production

Event selection

In exclusive $\gamma\gamma \to \mu^+\mu^-$ events, neither the proton nor the Pb nucleus dissociates. Therefore the Breit-Wheeler signal can be studied using the standard selection, presented in section 3.2.2, or the exclusive selection, presented in section 3.2.3. The exclusive selection is used initially to characterize the signals in the detector. The standard selection, which allows the proton to dissociate, contains inclusive events, which should be substantially suppressed in the exclusive

selection. Both selections are used to count $\gamma\gamma \to \mu^+\mu^-$ events in order to ensure that there is no bias between the two selections. However, since this analysis mainly deals with exclusive and dissociative J/ψ photoproduction and uses the standard selection, the final numbers are taken from the standard selection for consistency.

Transverse momentum distribution

As just said earlier, the exclusive production of muons has a continuous mass distribution. Nothing in its spectrum distinguishes it from the inclusive production of dimuons, in which other particles are produced. The dimuon transverse momentum p_{T} is the variable that makes it possible to discriminate between these two processes. As discussed in section 3.2.3, the p_{T} distribution of the dimuons produced exclusively behaves as $O(\hbar c/R)$, and inclusive dimuon production is usually characterized by larger dimuon p_{T}.

The dimuon p_{T} distribution is represented in figure 4.1 for data contained within the invariant mass range $1.0 < M_{\mu\mu} < 2.5$ GeV/c^2, before the application of the vetoes (but after applying the muon filters described in section 3.2.1), with the standard selection (see section 3.2.2) and with the exclusive selection (see section 3.2.3). It is clearly noticeable that the events before the veto cuts contain much larger p_{T} dimuons, which are effectively suppressed in the standard and exclusive selections.

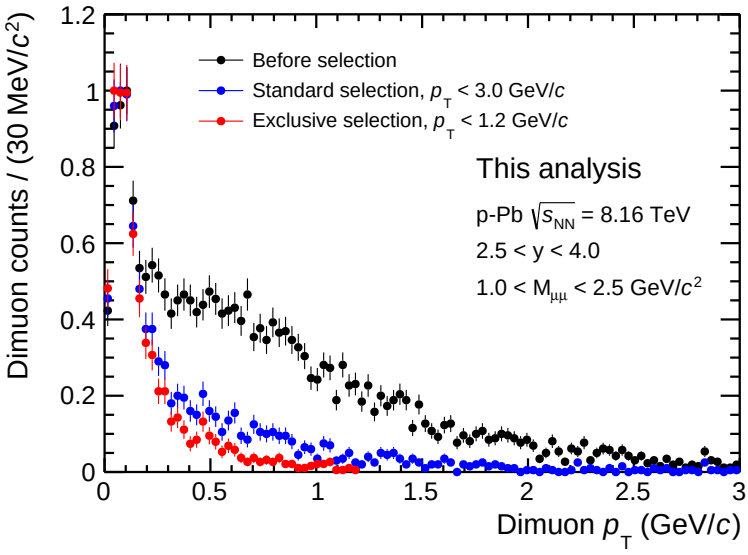

Figure 4.1: Distribution of dimuons transverse momentum p_{T} using different selections. All these distributions are normalized in order to emphasize their shape differences.

The goal consists of modeling the exclusive production of $\gamma\gamma \to \mu^+\mu^-$ to extract the number of corresponding events by taking the integral of the model and, finally, to evaluate the systematic uncertainty in counting the number of events induced by the choice of the model function.

Choosing a model to describe the $\gamma\gamma \to \mu^+\mu^-$ p_{T} distribution

The first step is finding an empirical function that best describes the exclusive $\gamma\gamma \to \mu^+\mu^-$ production. The exclusive selection described in section 3.2.3 is applied to the data to select a pure sample of $\gamma\gamma \to \mu^+\mu^-$ events.

First, the MC data reconstructed in the rapidity range $2.5 < y < 4.0$ and mass range $1.0 < M_{\mu\mu} < 2.5$ GeV/c^2 are considered to model the signal. The obtained histogram template is used as a model to fit to the data by a method of binned maximum likelihood[1], and the result is shown in figure 4.2. The result of the fit is evaluated by its χ^2/ndf within the range $p_{\mathrm{T}} <$

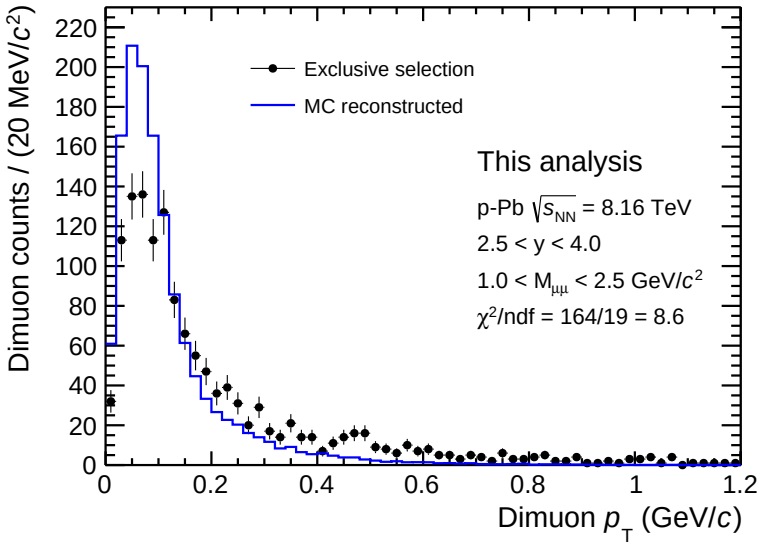

Figure 4.2: Binned likelihood fit to the data using the reconstructed MC sample corresponding to the $\gamma\gamma \to \mu^+\mu^-$ process. The χ^2 is computed within the range $p_{\mathrm{T}} < 0.4$ GeV/c.

0.4 GeV/c to ensure that each bin contains more than 5 counts. The value found, $\chi^2/\mathrm{ndf} = 164/19 = 8.6 \gg 1$, testifies that the reconstructed MC data exhibit essential differences with the data that passed the exclusive selection, notably the fact that the p_{T} distribution of MC events peaks at lower values of p_{T} than the real data. These differences may be due to several effects. For instance, the simulation of the experimental resolution induced by the track propagation through the thick muon absorber might not be sufficiently well modeled in the GEANT-based simulation at the low momentum edge of muons. In addition, the generator level simulation is based on the STARlight event generator, which implements LO QED and does not take into account more recent theoretical developments concerning the p_{T} distribution of the initial state photons in UPC, e.g., reference [3]. The fact that this shape is not well reproduced by full simulations based on STARlight has also been observed in Pb–Pb collisions [4, 5].

As a consequence, a Landau distribution, whose functional form is given in appendix D.1, is chosen to model the data. As advocated by the ATLAS collaboration in Pb–Pb collisions [5], sizeable effects from NLO corrections are expected, which the Landau distribution could properly model because of its high-p_{T} tail. This function has the advantages of having a small

[1]For a review of the different fitting methods in high energy physics, see the review [2].

number of parameters - the location and scale parameters μ and σ, and it has the flexibility to move the peak to lower values. It remains compatible with the template of reconstructed STARlight events, as shown in figure 4.3, where an unbinned likelihood fit is carried out with a Landau distribution. The parameters μ and σ are left free to vary during this step. However,

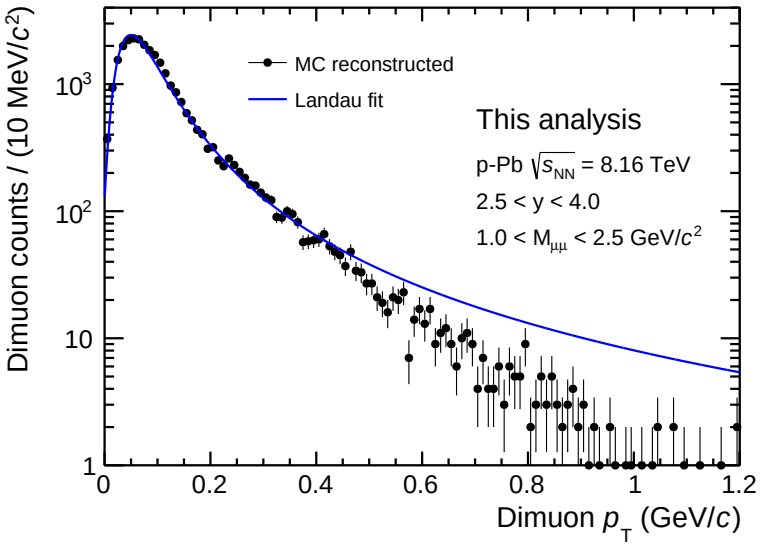

Figure 4.3: Unbinned likelihood fit of a Landau distribution to reconstructed Monte Carlo events.

a deviation of the model from the MC data is observed from a certain p_{T} threshold. This p_{T} threshold is estimated at 0.38 GeV/c, and 97% of the reconstructed MC events are located below this limit. Since the final fit result is the integral of the model, the result is not expected to be affected by the deviation of the model from the data at higher p_{T}.

4.1.2 Signal extraction from the data

Fixing the Landau distribution with the exclusive selection

In each bin of mass and rapidity studied, the Landau distribution is fitted to the data resulting from the exclusive selection, up to $p_{\mathrm{T}} = 0.38$ GeV/c, with free μ and σ parameters. Figure 4.4 shows an example of fit in the mass range $1.5 < M_{\mu\mu} < 2.0$ GeV/c^2 and rapidity range $2.5 < y < 4.0$. Restricting the fit range is justified by the fact that on the one hand the Landau distribution describes well the MC sample within this range only, indicating that LO processes are properly described at low p_{T}, and on the other hand because the fit could be biased by possible inclusive events at higher p_{T} which would survive in the selection. According to the MC simulations and as mentioned previously, 97% for events are taken into account when restricting the fit. The numbers of $\gamma\gamma \to \mu^+\mu^-$ events extracted are equal to the integral of the model over the full p_{T} range, and they are given in table 4.1.

Then, the μ and σ parameters are extracted from the fit, to be used in the next step.

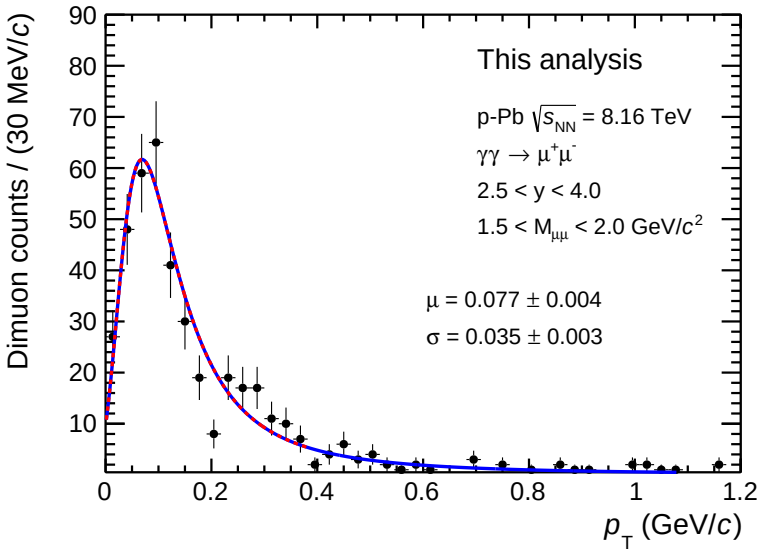

Figure 4.4: Unbinned likelihood fit of a Landau distribution to real data, where the dashed red curve represents the model in the fit range only, and the blue curve is its extension to higher p_{T} values. Unbinned likelihood fit up to $p_{\mathrm{T}} = 0.38$ GeV/c of a Landau distribution on the sample that passed the exclusive selection. The dashed red curve represents the model in the fit range only, and the blue curve is extended to higher p_{T} values.

Yield extraction with the standard selection sample

In the previous step, the model for describing the p_{T} distribution of $\gamma\gamma \rightarrow \mu^+\mu^-$ events has been fixed by assigning to the μ and σ parameters of the Landau distribution the values extracted using the exclusive selection. The next step consists in extracting the number of $\gamma\gamma \rightarrow \mu^+\mu^-$ events using the standard selection described in section 3.2.2. As we can see in figure 4.1, the standard selection sample contains events at higher p_{T} which are absent in the exclusive selection sample and are assumed to be a mixture of dissociative and inclusive events. This last component is parameterized according to the H1 parametrization for dissociative events [6]:

$$\frac{\mathrm{d}N^{\mathrm{inc}}_{\gamma\gamma}}{\mathrm{d}p_{\mathrm{T}}} = N^{\mathrm{inc}}_{\gamma\gamma} \cdot C_1 \frac{p_{\mathrm{T}}}{\left(1 + (b_{\mathrm{inc}}/n_{\mathrm{inc}}) \cdot p^2_{\mathrm{T}}\right)^{n_{\mathrm{inc}}}} \tag{4.1}$$

where $N^{\mathrm{inc}}_{\gamma\gamma}$ is the number of dissociative and inclusive two-photon interaction events, C_1 is the normalisation coefficient of the fraction, b_{inc} and n_{inc} are two free parameters. The two sources of background, inclusive and dissociative events, are not separated due to very limited statistics. Depending on the mass and rapidity bin, this number ranges between 40 and 200. The function in the formula 4.1 has the advantage of having a tail that spans large p_{T} values.

Thus the data is modeled by a two-component function:

- a Landau distribution whose μ and σ parameters are fixed according to the first step and whose yield is free, to model the exclusive $\gamma\gamma \rightarrow \mu^+\mu^-$
- and a function as defined in the equation 4.1 with free b_{inc} and n_{inc} parameters and whose yield is left free, to model inclusive two-photon interactions.

Finally, an unbinned likelihood fit of the model to the data is performed up to $p_{\mathrm{T}} = 3$ GeV/c. An example of fit on the standard selection sample is presented in figure 4.5, corresponding to the same mass and rapidity region as presented in figure 4.4.

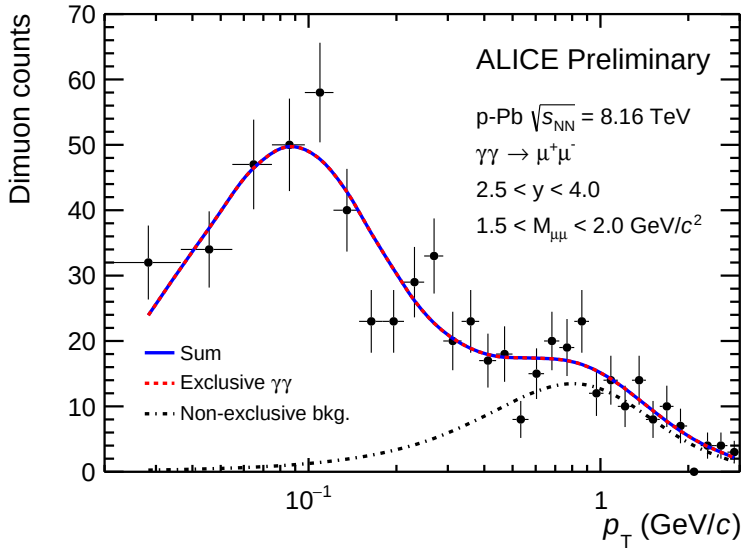

Figure 4.5: Unbinned likelihood fit up to $p_{\mathrm{T}} = 3.0$ GeV/c of the two-component model on the standard selection sample. For visibility purposes of the peak at low p_{T}, the data is shown with variable-sized bins.

Results

To summarize, the following steps are repeated for each rapidity and mass bin studied:

1. The μ and σ parameters of a single-component model using a Landau distribution are extracted from fitting the data that passed the exclusive selection. The yields are also extracted.
2. The data that passed the standard selection are fitted with a two-component model, which includes a Landau distribution with fixed μ and σ parameters - obtained from step 1 - and from which the raw $\gamma\gamma \rightarrow \mu^+\mu^-$ yield is obtained, to be compared with the yields obtained in step 1.

The extracted numbers of exclusive two-photon interactions $N_{\gamma\gamma}^{\mathrm{exc}}$ are given in table 4.1 for all rapidity and mass bins with their statistical uncertainties. The numbers extracted with both selections are similar, assessing that background events are under control. In the computation of the cross section, the numbers obtained with the standard selection are used, to be consistent with the J/ψ analysis which also uses the standard selection to extract the numbers of exclusive and dissociative J/ψ events.

4.1.3 Systematic uncertainty on signal extraction

Instead of using a Landau distribution to model the exclusive two-photon interactions, a function of the form of expression 4.1 has been used. Following the procedure described in the

Mass range	Rapidity range	$N_{\gamma\gamma}^{\text{exc}}$ (exclusive sel.)	$N_{\gamma\gamma}^{\text{exc}}$ (standard sel.)
$1.0 < M_{\mu\mu} < 1.5\ \text{GeV}/c^2$	$2.50 < y < 4.00$	637 ± 27	618 ± 33
	$2.50 < y < 3.25$	96 ± 10	99 ± 11
	$3.25 < y < 4.00$	542 ± 25	522 ± 31
$1.5 < M_{\mu\mu} < 2.0\ \text{GeV}/c^2$	$2.50 < y < 4.00$	433 ± 23	437 ± 26
	$2.50 < y < 3.25$	150 ± 14	150 ± 14
	$3.25 < y < 4.00$	283 ± 19	283 ± 22
$2.0 < M_{\mu\mu} < 2.5\ \text{GeV}/c^2$	$2.50 < y < 4.0$	199 ± 16	191 ± 18
	$2.50 < y < 3.25$	91 ± 11	85 ± 13
	$3.25 < y < 4.00$	107 ± 11	103 ± 13

Table 4.1: Number of exclusive $\gamma\gamma \to \mu^+\mu^-$ events extracted from the data that passed the exclusive and standard selections.

previous selection, a single-component fit is first performed on the data that passed the exclusive selection to extract the two free parameters of the function. Then, the data that passed the standard selection is fitted with a two-component function. During this step, the function modeling the exclusive component has a shape fixed to the one obtained with the exclusive selection. The numbers extracted $N_{\gamma\gamma}^{\text{exc}}$ are very similar to those found with the Landau distribution, and statistical uncertainties largely dominated the relative difference.

Therefore, the systematic uncertainty on the raw yield extraction of the exclusive $\gamma\gamma$ candidates mainly comes from fixing the μ and σ parameters of the Landau distribution that models the exclusive $\gamma\gamma$ component. This impact is hereunder studied, based on the values of μ and σ obtained in the step described in section 4.1.2, μ_{mean} and σ_{mean}, and their statistical uncertainties $\Delta\mu_{\text{mean}}$ and $\Delta\sigma_{\text{mean}}$ respectively.

The fitting procedure on the standard selection sample is repeated for values of μ varying from $\mu_{\text{mean}} - 3\Delta\mu_{\text{mean}}$ to $\mu_{\text{mean}} + 3\Delta\mu_{\text{mean}}$ with steps of $0.6 \times \Delta\mu_{\text{mean}}$ GeV/c. Similarly, for each one of these new μ values, the procedure is also repeated for values of σ varying from $\sigma_{\text{mean}} - 3\Delta\sigma_{\text{mean}}$ to $\sigma_{\text{mean}} + 3\Delta\sigma_{\text{mean}}$ with steps of $0.6 \times \sigma_\sigma$ GeV/c. The number of exclusive $\gamma\gamma$ events and their systematic uncertainty are obtained by performing a weighted average of the numbers obtained for each (μ, σ) values. Weights are distributed as a two-dimensional Gaussian function of μ and σ, taking into account their correlation coefficient r. Therefore, the weights $w_{i,j}$ for each μ_i, σ_j where i, j are the indices of the μ, σ parameters are given by:

$$w_{i,j} = \frac{1}{2\pi\Delta\mu_{\text{mean}}\Delta\sigma_{\text{mean}}\sqrt{1-r^2}} \exp\left(-\frac{1}{2}\left[\left(\frac{\mu_i - \mu_{\text{mean}}}{\Delta\mu_{\text{mean}}}\right)^2 + \left(\frac{\sigma_j - \sigma_{\text{mean}}}{\Delta\sigma_{\text{mean}}}\right)^2 - 2r\frac{(\mu_i - \mu_{\text{mean}})(\sigma_j - \sigma_{\text{mean}})}{\Delta\mu_{\text{mean}}\Delta\sigma_{\text{mean}}}\right]\frac{1}{1-r^2}\right) \tag{4.2}$$

Then the weighted average is given by:

$$N_{\gamma\gamma}^{\text{exc}} = \sum_{i,j}^{n} w_{i,j}(N_{\gamma\gamma}^{\text{exc}})_{i,j} \tag{4.3}$$

where n is the number of iterations it went through for each σ or μ.

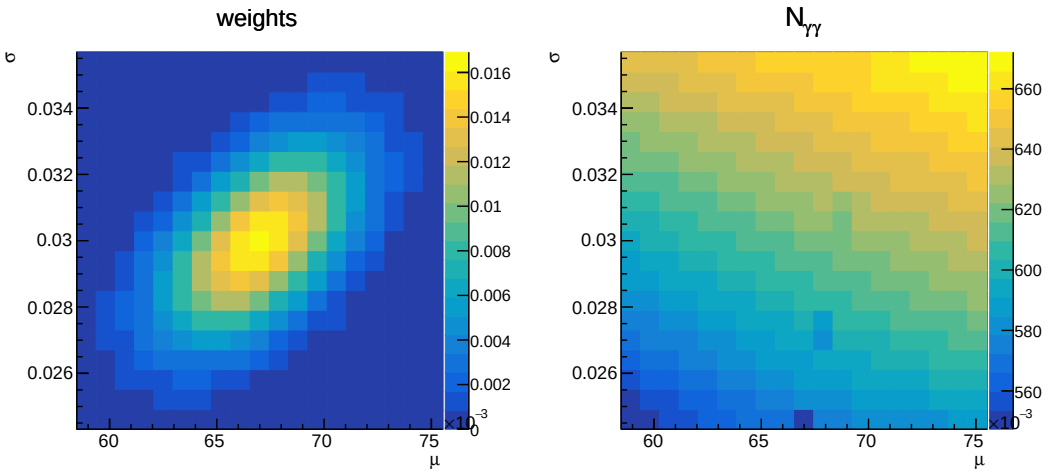

Figure 4.6: Left: distribution of weights $w_{i,j}$ as a function of μ, σ. Right: number of exclusive $\gamma\gamma$ events extracted as a function of μ, σ. In this example, data is selected within the rapidity $2.5 < y < 4.0$ and in the mass range $1.0 < M_{\mu\mu} < 1.5\,\text{GeV}/c^2$.

Figure 4.6 shows the weights and the extracted numbers $(N^{\text{exc}}_{\gamma\gamma})_{i,j}$ for each (μ_i, σ_j) combination. The related uncertainty is then computed as:

$$\Delta N^{\text{exc}}_{\gamma\gamma} = \sqrt{\frac{n^2}{n^2-1}\sum_{i,j} w_{i,j}(N^{\text{exc}}_{\gamma\gamma} - (N^{\text{exc}}_{\gamma\gamma})_{i,j})^2} \tag{4.4}$$

where n^2 corresponds to the total number of iterations.

The relative uncertainties $\Delta N^{\text{exc}}_{\gamma\gamma}/N^{\text{exc}}_{\gamma\gamma}$ obtained from this calculation are given in table 4.2.

Mass range	Rapidity range	$\frac{\Delta N^{\text{exc}}_{\gamma\gamma}}{N^{\text{exc}}_{\gamma\gamma}}$
$1.0 < M_{\mu\mu} < 1.5\,\text{GeV}/c^2$	$2.50 < y < 4.00$	3.2%
	$2.50 < y < 3.25$	3.9%
	$3.25 < y < 4.00$	3.2%
$1.5 < M_{\mu\mu} < 2.0\,\text{GeV}/c^2$	$2.50 < y < 4.00$	3.3%
	$2.50 < y < 3.25$	4.2%
	$3.25 < y < 4.00$	4.4%
$2.0 < M_{\mu\mu} < 2.5\,\text{GeV}/c^2$	$2.50 < y < 4.00$	4.9%
	$2.50 < y < 3.25$	7.6%
	$3.25 < y < 4.00$	6.1%

Table 4.2: Computation of the systematic uncertainty induced on signal extraction.

The analysis of $\gamma\gamma \to \mu^+\mu^-$ signal extraction presented in this section will be useful in the

following. As the process $\gamma\gamma \to \mu^+\mu^-$ is continuous in mass, it is also present in the data in the invariant mass $2.5 < M_{\mu\mu} < 3.5$ GeV/c^2 studied for the extraction of the J/ψ signal.

4.2 Signal extraction for J/ψ photoproduction

The extraction of the J/ψ signal is a little bit more complex since in the studied mass region, $2.5 < M_{\mu\mu} < 3.5$ GeV/c^2, and in the standard selection, five processes are present and must be differentiated. Among these, there are on the one hand events resulting from two-photon interactions:

- exclusive two-photon interactions, $\gamma\gamma \to \mu^+\mu^-$, and
- non-exclusive two-photon interactions,

and on the other hand dimuons from the J/ψ decay, where the latter can be produced:

- exclusively off protons,
- dissociatively off protons,
- exclusively off Pb nuclei.

The challenge of this section is to correctly describe all the signal components in the mass and transverse momentum spectra p_{T}, in order to extract the numbers of J/ψ produced exclusively and dissociatively off protons in the full rapidity coverage:

- $2.50 < y < 4.00$,

and in two rapidity bins:

- $2.50 < y < 3.25$,
- $3.25 < y < 4.00$.

This sections deals first with the characterization of the signals in the dimuon mass spectrum, then in p_{T}. Finally, we compute on the systematic uncertainty induced by the choice of the function to model the contribution of the exclusive J/ψ events produced off protons.

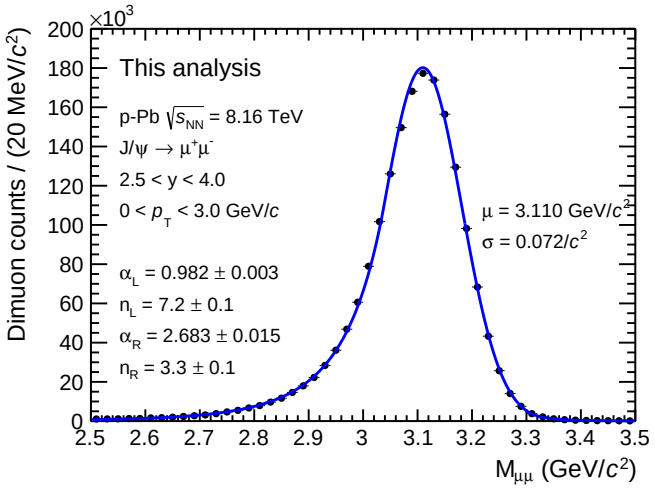

Figure 4.7: Binned likelihood fit of a double-sided crystal ball function with seven free parameters (the mean μ and the standard deviation σ, the tail parameters α_L, n_L, α_R, n_R, and the yield) on reconstructed Monte Carlo events.

4.2.1 Mass distribution of the different processes

In the dimuon invariant mass spectrum, the dimuon continuum and J/ψ decay signals have recognizable signatures. On the one hand, the continuum has in good approximation the shape of a decreasing exponential which has the advantage of displaying only one free parameter, except for the yield:

$$\frac{\mathrm{d}N_{\gamma\gamma}}{\mathrm{d}M_{\mu\mu}} = N_{\gamma\gamma} \cdot C_2 e^{-aM_{\mu\mu}}, \tag{4.5}$$

where $N_{\gamma\gamma}$ is the number of two-photon interaction events, C_2 is the normalization coefficient of the exponential function and $a > 0$ is a free parameter of the function. On the other hand, the J/ψ is modeled by a function that peaks around its mass, $M_{\mathrm{J}/\psi} = 3096.900 \pm 0.006\ \mathrm{MeV}/c^2$ [7]. The function used is the double-sided crystal-ball function (CB2), defined in appendix D.2, which has a Gaussian core with differently parameterized distribution tails. This asymmetry makes it possible to correctly model several effects. The final-state QED radiation of muons and non-gaussian multiple Coulomb scattering in the front absorber are reflected in the data as a loss of particle energy and therefore a shift of the dimuon invariant mass towards lower values. These effects are responsible for the non-Gaussian tails on the left side. The non-gaussian tails on the right-hand side are due to non-gaussian multiple scattering.

The CB2 function has a total of six free parameters, plus the distribution yield. A high number of free parameters in the final model function reduces the chances of convergence of the fitting algorithm. In order to reduce this number of free parameters, the tail parameters on both sides of the Gaussian are fixed to the values obtained by performing a binned likelihood fit of the CB2 on the MC data. The same cuts used for the data on the dimuon mass, transverse momentum ($p_{\mathrm{T}} < 3$ GeV/c) and rapidity ($2.5 < y < 4.0$) are applied to the reconstructed muons from the MC simulations. The result of fitting the CB2 on the selected MC data is shown in figure 4.7.

Since the continuum and the J/ψ peak in the mass spectrum are each made up of several components, their differentiation is made possible because of their p_{T} distribution. Let us start

with the characterization of the p_{T} distributions of the two-photon interactions.

Remark on the resolutions obtained in MC and real data

The mass resolution $\Delta M_{\mu\mu}$ is given by the width of the Gaussian core of the CB2 function fitted to the data. When fitting the MC sample, the mass resolution obtained is $\Delta M_{\mu\mu} = 0.072\ \mathrm{GeV}/c^2$ (see figure 4.7), while in real data using the strong selection, $\Delta M_{\mu\mu} = 0.079\ \mathrm{GeV}/c^2$, hence a relative difference of ~ 10 %.

The dimuon p_{T} resolution Δp_{T} is related to the mass resolution via the relation

$$\Delta p_{\mathrm{T}} = \Delta M_{\mu\mu}/\sqrt{2} \tag{4.6}$$

thus the same relative difference exists in p_{T} resolution. This resolution is computed for masses around the J/ψ peak. At lower masses where the number of background events is larger, it may be worse. This resolution difference between MC and real data may be one of the reasons why the MC p_{T} distribution fails at reproducing the real $\gamma\gamma \to \mu^+\mu^-$ p_{T} shape. Thus, this observation may hint that the issue in the $\gamma\gamma \to \mu^+\mu^-$ simulation description has a significant contribution from the detector simulation, which may be more important that the contribution from generator physics.

4.2.2 Characterization of the p_{T} distribution of dimuons from two-photon interactions

Analogously to the $\gamma\gamma \to \mu^+\mu^-$ signal extraction method described in section 4.1, the p_{T} shape of exclusive $\gamma\gamma \to \mu^+\mu^-$ events is described by a Landau distribution, whose definition is given in the appendix D.1, while the p_{T} shape of non-exclusive two-photon interactions is described by the equation 4.1, where b_{inc} and n_{inc} are two free parameters.

The objective here is to fix the parameters μ and σ of the Landau distribution. In order to do this, a p_{T} template of $\gamma\gamma \to \mu^+\mu^-$ events is extracted using the exclusive data selection described in section 3.2.3. In the invariant mass range $2.5 < M_{\mu\mu} < 3.5\ \mathrm{GeV}/c^2$, this sample contains only to good approximation the J/ψ produced exclusively off protons and Pb nuclei, and the exclusive $\gamma\gamma \to \mu^+\mu^-$ interactions. In order to separate in the p_{T} distribution J/ψ photoproduction and two-photon interactions, the sPlot tool is used [8]. From a two-component mass fit as described in section 4.2.1, this tool makes it possible to calculate for each event a weight (sWeight), which may have negative values. Consequently, the sPlot method assigns on an event-by-event basis each event to one of the processes under investigation. The fit of the mass distribution, used as the discriminating variable for sPlot, is shown in figure 4.8 in the full rapidity coverage.

Then, these sWeights are applied to the dimuon p_{T} distribution, which makes it possible to obtain on the one hand the p_{T} distribution of the J/ψ produced exclusively off protons and Pb nuclei (figure 4.9 on the left), and on the other hand, that of the exclusive $\gamma\gamma \to \mu^+\mu^-$ interactions (figure 4.9 on the right).

The p_{T} template of $\gamma\gamma \to \mu^+\mu^-$ thus extracted, a Landau distribution is fitted to the data in the range $0 < p_{\mathrm{T}} < 0.38\ \mathrm{GeV}/c$, following the same method as in section 4.1. The parameters μ and σ are then obtained to be used in the following.

However, the use of sPlot assumes that the discriminating observable, i.e., the invariant mass, should be statistically independent of the reconstructed variable, i.e., the transverse momentum p_{T}, for each type of signal. Yet the mass and p_{T} of the dimuons produced through the

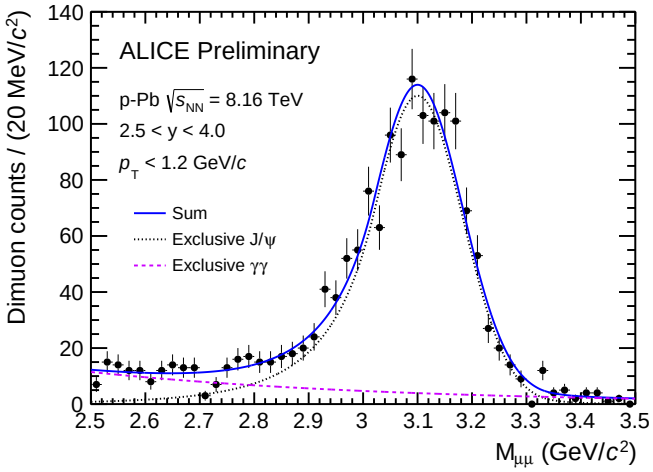

Figure 4.8: Unbinned likelihood fit of the dimuon invariant mass of the exclusive selection sample in order to assign sWeights to each event using the sPlot technique [8].

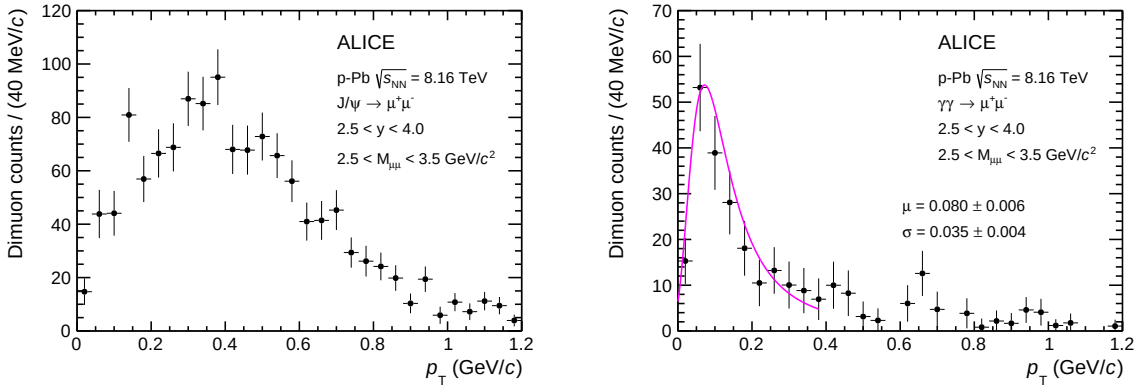

Figure 4.9: Reconstructed p_{T} distribution of $\mathrm{J}/\psi \to \mu^+\mu^-$ (left) and $\gamma\gamma \to \mu^+\mu^-$ (right) events with sPlot, using the exclusive selection sample. An unbinned likelihood fit of a Landau distribution on the extracted $\gamma\gamma \to \mu^+\mu^-$ p_{T} template is performed up to $p_{\mathrm{T}} = 0.38$ GeV/c.

$\gamma\gamma \to \mu^+\mu^-$ process are in principle correlated. In order to assess the bias that the sPlot technique introduces in reconstructing the signals due to this correlation, a cross check is performed using the MC sample for exclusive J/ψ photoproduction off protons and for the $\gamma\gamma \to \mu^+\mu^-$ process. The sample consists of a mixture of randomly chosen events of 1300 reconstructed J/ψ and 500 reconstructed $\gamma\gamma \to \mu^+\mu^-$ events, within the ranges $2.5 < y < 4.0$, $2.5 < M_{\mu\mu} < 3.5$ GeV/c^2 and $p_{\mathrm{T}} < 1.2$ GeV/c. Then, the sPlot technique is applied following the same steps as described above: by fitting the resulting mass distribution, sWeights are computed and finally the p_{T} shapes for each of the two contributions are obtained. The reconstructed distributions with sPlot are drawn on top of the original ones (before mixing the two samples) in figure 4.10.

Finally, a single component unbinned likelihood fit of a Landau distribution is performed both on original and reconstructed $\gamma\gamma \to \mu^+\mu^-$ distributions, up to $p_{\mathrm{T}} = 0.38$ GeV/c. The results of the fits are shown in figure 4.11, from which the obtained μ and σ parameters are

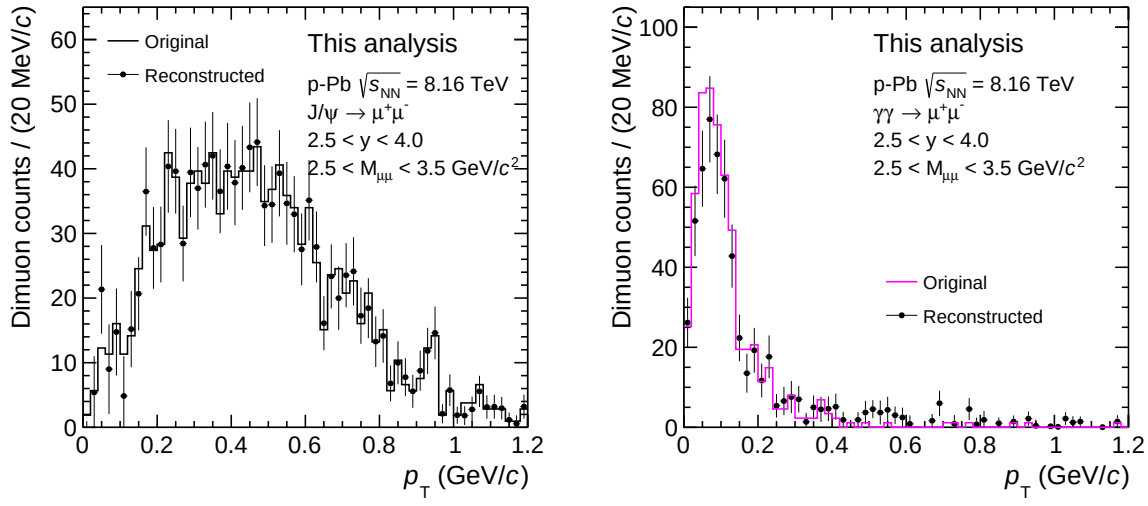

Figure 4.10: p_{T} distribution of the original and sPlot-reconstructed J/ψ events (left) and $\gamma\gamma \to \mu^+\mu^-$ events (right).

compared.

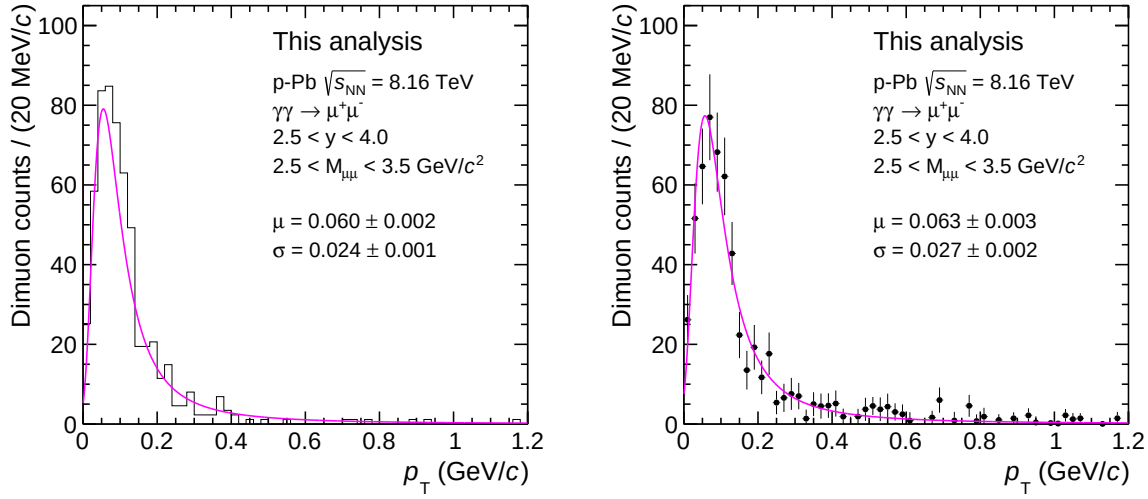

Figure 4.11: Landau distribution fits to the original Monte Carlo data sample injected in the mixture (left) and to the sPlot-reconstructed events (right), for the $\gamma\gamma \to \mu^+\mu^-$ process.

The test is repeated 50 times with a random choice of 1300 J/ψ and 500 $\gamma\gamma \to \mu^+\mu^-$ events. For each iteration, the subtraction of the parameters for the reconstructed and the initial samples is recovered, $\mu_{\mathrm{rec}} - \mu_{\mathrm{ini}}$ and $\sigma_{\mathrm{rec}} - \sigma_{\mathrm{ini}}$. The average difference $\mu_{\mathrm{rec}} - \mu_{\mathrm{ini}}$ of these 50 trials can be understood as the systematic uncertainty introduced by sPlot on the μ parameter, while the width of the distribution can be understood as the statistical uncertainty. The same reasoning is valid for σ instead of μ. The mean and standard deviation of the distributions of these differences are given in table 4.3, along with the statistical uncertainties obtained on the μ and

Distribution	Average value (GeV/c)	Standard deviation (GeV/c)	Statistical uncertainty on the reconstructed parameter (GeV/c)
$\mu_{\text{rec}} - \mu_{\text{ini}}$	-0.0011	0.0019	$\Delta\mu_{\text{rec}} = 0.0025$
$\sigma_{\text{rec}} - \sigma_{\text{ini}}$	-0.0004	0.0010	$\Delta\sigma_{\text{rec}} = 0.0015$

Table 4.3: Parameters obtained from the distributions $\mu_{\text{rec}} - \mu_{\text{ini}}$ and $\sigma_{\text{rec}} - \sigma_{\text{ini}}$ obtained from 50 trials with sPlot. The last column is the statistical uncertainty on the reconstructed parameters obtained from the fit (figure 4.11).

σ parameters obtained from fitting the reconstructed sample. The average value of the deviation of the μ and σ parameters introduced by sPlot (second column in table 4.3) is found to be negligible with respect to the statistical uncertainties obtained on the μ and σ parameters (last column), demonstrating that the μ and σ parameters are negligibly affected by the sPlot signal extraction method.

4.2.3 Characterization of the p_{T} distribution of J/ψ events

Let us recall that the J/ψ mass peak actually contains three processes:

- the exclusive J/ψ photoproduction off protons,
- the dissociative J/ψ photoproduction off protons,
- and the exclusive J/ψ photoproduction off Pb nuclei.

The process of exclusive J/ψ photoproduction off protons is modeled according to the H1 parametrization for exclusive J/ψ events [6] by a function of the form

$$\frac{\mathrm{d}N^{\text{exc}}_{\text{J}/\psi}}{\mathrm{d}p_{\text{T}}} = N^{\text{exc}}_{\text{J}/\psi} \cdot C_3 p_{\text{T}} \cdot \exp(-b_{\text{exc}} p^2_{\text{T}}), \tag{4.7}$$

where $N^{\text{exc}}_{\text{J}/\psi}$ is the number of exclusive J/ψ events, C_3 is the normalization coefficient of the function $p_{\text{T}} \cdot \exp(-b_{\text{exc}} p^2_{\text{T}})$, and $b_{\text{exc}} > 0$ is a parameter to be fixed in order to reduce as much as possible the number of free parameters in the final fit.

As already mentioned, dissociative processes result in the production of dimuons with larger p_{T}. For this reason, they are be modeled according to the H1 parametrization with equation 4.1 that is recalled here:

$$\frac{\mathrm{d}N^{\text{diss}}_{\text{J}/\psi}}{\mathrm{d}p_{\text{T}}} = N^{\text{diss}}_{\text{J}/\psi} \cdot C_4 \frac{p_{\text{T}}}{\left(1 + (b_{\text{diss}}/n_{\text{diss}}) \cdot p^2_{\text{T}}\right)^{n_{\text{diss}}}}, \tag{4.8}$$

where $N^{\text{diss}}_{\text{J}/\psi}$ is the number of dissociative J/ψ events, C_4 is the normalization coefficient of the fraction, and b_{diss} and n_{diss} are free parameters.

Finally, the exclusive (or coherent) J/ψ photoproduction off Pb nuclei is modeled with the p_{T} template obtained from the analysis of the corresponding reconstructed MC sample. Although the STARlight description of the $\gamma\gamma \to \mu^+\mu^-$ p_{T} template is not so accurate (see section

4.1.1), the generated MC data for J/ψ photoproduction based on STARlight uses inputs from HERA results that provide a precise description of J/ψ events.

The number of exclusive J/ψ photoproduction off Pb nuclei events is fixed to the expected value based on the ALICE measurement in Pb–Pb collisions [9] and details of this calculation are given in appendix E.

Fixing the exclusive J/ψ p_{T} shape

The goal here is to fix the p_{T} shape of exclusive J/ψ events, i.e., the b_{exc} parameter in equation 4.7. This is done using the exclusive selection described in section 3.2.3 which removes dissociative events from the data sample and selects events within the range $p_{\mathrm{T}} < 1.2$ GeV/c. The probability density functions of mass and transverse momentum of each component but the dissociative J/ψ one are multiplied to obtain a model describing the two-dimensional space ($M_{\mu\mu}$, p_{T}). These functions are summarized in table 4.5. Next, a fit of the model is made on the selected data, so as to simultaneously fit the dimuon mass and p_{T}. During this step, the b_{exc} parameter is left free. Figure 4.12 shows the result of the two-dimensional fit of the exclusive selection sample in the full rapidity coverage $2.5 < y < 4.0$. The procedure is repeated for the two rapidity sub-ranges, $2.50 < y < 3.25$ and $3.25 < y < 4.00$. The values of the b_{exc} parameters are extracted and given in the table 4.4 along with the numbers of exclusive J/ψ photoproduced off protons in the different rapidity ranges.

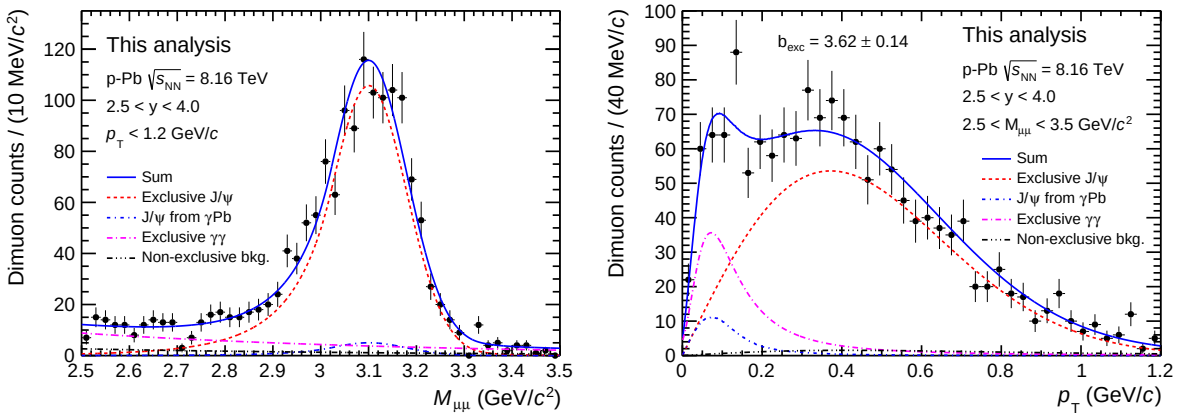

Figure 4.12: Projection of the two-dimensional fit for $2.5 < y < 4.0$ on the mass (left) and p_{T} (right), using the exclusive selection.

Rapidity range	Energy range $W_{\gamma\mathrm{p}}$ [GeV]	b_{exc} [GeV/c]$^{-2}$	$N^{\mathrm{exc}}_{\mathrm{J}/\psi}$
$2.50 < y < 4.00$	$27 - 57$	3.62 ± 0.14	1181 ± 41
$2.50 < y < 3.25$	$39 - 57$	3.86 ± 0.20	613 ± 29
$3.25 < y < 4.00$	$27 - 39$	3.38 ± 0.17	567 ± 28

Table 4.4: Values of the p_{T} slope for the exclusive J/ψ photoproduction and number of candidates.

4.2.4 Signal extraction with the standard selection sample

To summarize, let us recall that various components of the signal have been fixed or constrained with the use of the MC data, in particular:

- the J/ψ mass distribution
- the p_T distribution of exclusive J/ψ photoproduction off Pb nuclei

or via the use of data-driven methods, such as

- the use of sPlot and the exclusive selection to fix the p_T template of the $\gamma\gamma \to \mu^+\mu^-$ component
- the use of the exclusive selection to fix the p_T template of the exclusive J/ψ photoproduction off protons.

The complete list of the different components which intervene in the fit for signal extraction are summarized in table 4.5, with a color differentiation for the free and fixed parameters of the model.

Physical process	**Mass description**	**Transverse momentum description**
Exclusive two-photon interactions $\gamma\gamma \to \mu^+\mu^-$	$(N_{\gamma\gamma}^{\text{exc}} + N_{\gamma\gamma}^{\text{inc}}) \cdot C_2 e^{-aM_{\mu\mu}}$ (equation 4.5)	Landau distribution with fixed μ and σ, and free yield $N_{\gamma\gamma}^{\text{exc}}$
Non-exclusive two-photon interactions		$N_{\gamma\gamma}^{\text{inc}} \cdot C_1 \frac{p_T}{\left(1 + (b_{\text{inc}}/n_{\text{inc}}) \cdot p_T^2\right)^{n_{\text{inc}}}}$ (equation 4.1)
Exclusive J/ψ photoproduction off protons $\gamma + p \to J/\psi + p$	Double-sided crystal ball function with fixed α_L, n_L, α_R and n_R, free μ_{CB}, σ_{CB} and yield $(N_{J/\psi}^{\text{exc}} + N_{J/\psi}^{\text{diss}} + N_{J/\psi}^{\gamma\text{Pb}})$	$N_{J/\psi}^{\text{exc}} \cdot C_3 p_T \cdot \exp(-b_{\text{exc}} p_T^2)$ (equation 4.7)
Dissociative J/ψ photoproduction off protons $\gamma + p \to J/\psi + X$		$N_{J/\psi}^{\text{diss}} \cdot C_4 \frac{p_T}{\left(1 + (b_{\text{diss}}/n_{\text{diss}}) \cdot p_T^2\right)^{n_{\text{diss}}}}$ (equation 4.8)
Exclusive J/ψ photoproduction off Pb nuclei $\gamma + \text{Pb} \to J/\psi + \text{Pb}$		Monte Carlo template from reconstructed STARlight events with fixed yield $N_{J/\psi}^{\gamma\text{Pb}}$

Table 4.5: Summary of the different fit components used for the exclusive and dissociative J/ψ signal extraction The numbers in orange are free parameters of the fit, while the numbers in blue are fixed parameters.

The probability density functions, which describe the mass and transverse momentum p_T of these five components, are multiplied anew in the two-dimensional space formed by the dimuons mass and p_T. Thus, the two-dimensional model has a total of eleven free parameters: these are the parameters $N_{J/\psi}^{\text{exc}}$ and $N_{J/\psi}^{\text{diss}}$ which are the ones we want to extract, but also the parameters a, $N_{\gamma\gamma}^{\text{exc}}$, $N_{\gamma\gamma}^{\text{inc}}$, b_{inc}, n_{inc}, μ_{CB}, σ_{CB}, b_{diss}, and n_{diss}.

An unbinned likelihood fit of this model is performed on the data sample that passed standard selection. Figure 4.13 shows the result of the two-dimensional fit of the sample in the full rapidity coverage $2.5 < y < 4.0$. The procedure is repeated for the two rapidity sub-ranges, $2.50 < y < 3.25$ and $3.25 < y < 4.00$. The numbers of both exclusive and dissociative J/ψ events extracted from the fit are given in table 4.6 with their statistical uncertainties. One can note that the numbers of exclusive J/ψ events obtained here and with the exclusive selection sample given in the table 4.4 are very close. The differences range from 0.1 % to 2.6%, and these numbers are much smaller than relative statistical uncertainties. Hence, this gives confidence that the exclusive selection is quite efficient. Therefore, the p_{T} shape obtained from the exclusive selection is not expected to be biased by efficiency loss. However, the uncertainty induced by fixing the p_{T} shape for exclusive J/ψ events is studied subsequently. The ratio $R = N^{\mathrm{diss}}_{\mathrm{J}/\psi}/N^{\mathrm{exc}}_{\mathrm{J}/\psi}$ and its statistical uncertainty are also extracted from the fit. The statistical uncertainties take into account the correlation between the numbers of exclusive and dissociative J/ψ events, and are rather large due to anti-correlations between these two yields in the two-dimensional fit.

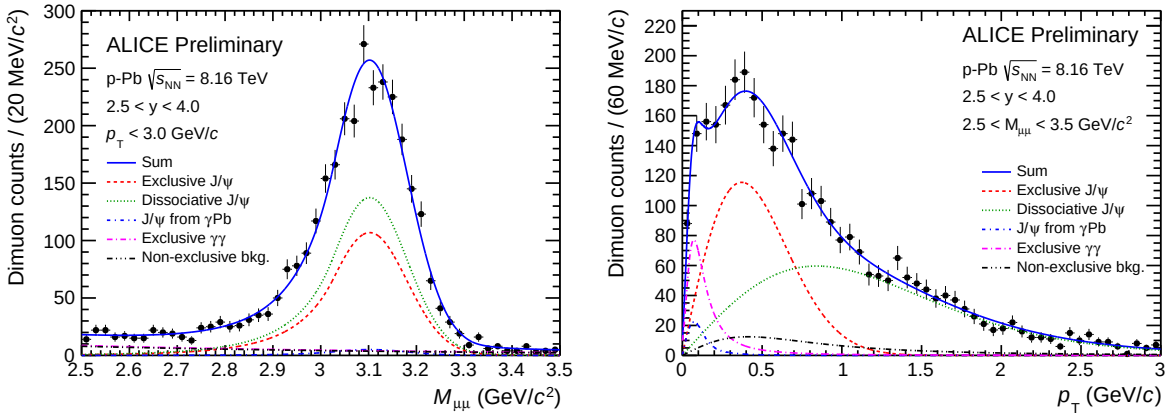

Figure 4.13: Projections of final two-dimensional fits on the mass (left) and p_{T} (right) using the mid-selection in the full rapidity coverage.

Rapidity range	$N^{\mathrm{exc}}_{\mathrm{J}/\psi}$	$N^{\mathrm{diss}}_{\mathrm{J}/\psi}$	$R = N^{\mathrm{diss}}_{\mathrm{J}/\psi}/N^{\mathrm{exc}}_{\mathrm{J}/\psi}$
$2.50 < y < 4.00$	1180 ± 84	1515 ± 83	1.28 ± 0.15
$2.50 < y < 3.25$	629 ± 54	768 ± 55	1.21 ± 0.18
$3.25 < y < 4.00$	564 ± 53	733 ± 52	1.29 ± 0.23

Table 4.6: Number of exclusive and dissociative J/ψ extracted from the two-dimensional model fitted to the data that passed the standard selection.

4.2.5 Systematic uncertainty on signal extraction

The numbers of exclusive and dissociative J/ψ events are correlated with the b_{exc} parameter value, and the impact of this value on the raw yield extraction of the exclusive and dissociative J/ψ candidates produced off protons is hereunder studied.

The fitting procedure described in section 4.2.4 is repeated for values of b_{exc} from $b_{\text{exc}}^{\text{mean}} - 3\Delta b_{\text{exc}}^{\text{mean}}$ to $b_{\text{exc}}^{\text{mean}} + 3\Delta b_{\text{exc}}^{\text{mean}}$ where $b_{\text{exc}}^{\text{mean}}$ is the value of b_{exc} obtained in table 4.4 and $\Delta b_{\text{exc}}^{\text{mean}}$ its statistical uncertainty, with steps of 0.04 [GeV/c]$^{-2}$. The number of exclusive and dissociative J/ψ and their systematic uncertainty are obtained by performing a weighted average of the numbers obtained for each b_{exc} value. Weights are distributed as a Gaussian function, represented in figure 4.14 at top left. Its width is given by the $\Delta b_{\text{exc}}^{\text{mean}}$, and its mean by the actual value $b_{\text{exc}}^{\text{mean}}$. The raw yields of exclusive and dissociative J/ψ ($N_{\text{J}/\psi,i}^{\text{exc/diss}}$) and their ratio are extracted in figure 4.14 as a function of the b_{exc} value used in the fit.

For each one of the two components, the weighted average is then given by:

$$N_{\text{J}/\psi}^{\text{exc/diss}} = \sum_{i}^{n} w_i N_{\text{J}/\psi,i}^{\text{exc/diss}} \,, \tag{4.9}$$

where n is the total number of iterations it went through, w_i are the weights associated with each b_{exc} value, and $N_{\text{J}/\psi,i}^{\text{exc/diss}}$ are the numbers of exclusive or dissociative J/ψ extracted for each b_{exc} value. The weights, numbers of exclusive or dissociative J/ψ extracted and their ratio are shown in figure 4.14 as a function of b_{exc}. The related uncertainty is then computed as:

$$\Delta N_{\text{J}/\psi}^{\text{exc/diss}} = \sqrt{\frac{n}{n-1}\sum_{i} w_i (N_{\text{J}/\psi}^{\text{exc/diss}} - N_{\text{J}/\psi,i}^{\text{exc/diss}})^2} \tag{4.10}$$

and similarly for the ratio of dissociative to exclusive J/ψ numbers $R = N_{\text{J}/\psi}^{\text{diss}}/N_{\text{J}/\psi}^{\text{exc}}$:

$$\Delta R = \sqrt{\frac{n}{n-1}\sum_{i} w_i (R - R_i)^2} \tag{4.11}$$

and finally, the relative uncertainties $\Delta N_{\text{J}/\psi}^{\text{exc}}/N_{\text{J}/\psi}^{\text{exc}}$, $\Delta N_{\text{J}/\psi}^{\text{diss}}/N_{\text{J}/\psi}^{\text{diss}}$ and $\Delta R/R$ are given in table 4.7.

Rapidity range	$\frac{\Delta N_{\text{J}/\psi}^{\text{exc}}}{N_{\text{J}/\psi}^{\text{exc}}}$	$\frac{\Delta N_{\text{J}/\psi}^{\text{diss}}}{N_{\text{J}/\psi}^{\text{diss}}}$	$\frac{\Delta R}{R} = \frac{\Delta(N_{\text{J}/\psi}^{\text{diss}}/N_{\text{J}/\psi}^{\text{exc}})}{(N_{\text{J}/\psi}^{\text{diss}}/N_{\text{J}/\psi}^{\text{exc}})}$
$2.50 < y < 4.00$	3.56%	2.90%	6.20%
$2.50 < y < 3.25$	3.97%	3.78%	7.31%
$3.25 < y < 4.00$	5.50%	4.37%	7.63%

Table 4.7: Relative uncertainties induced by the choice of the b_{exc} value in the two-dimensional fit on the raw yields of exclusive and dissociative J/ψ photoproduced off protons, and their ratio.

4.3 Correction for acceptance and reconstruction efficiency

The raw numbers extracted from signal extraction procedures for both $\gamma\gamma \to \mu^+\mu^-$ events (section 4.1) and J/ψ events (section 4.2) must be corrected by the response function of the detector. This function takes into account both the acceptance of the detector, since it does not

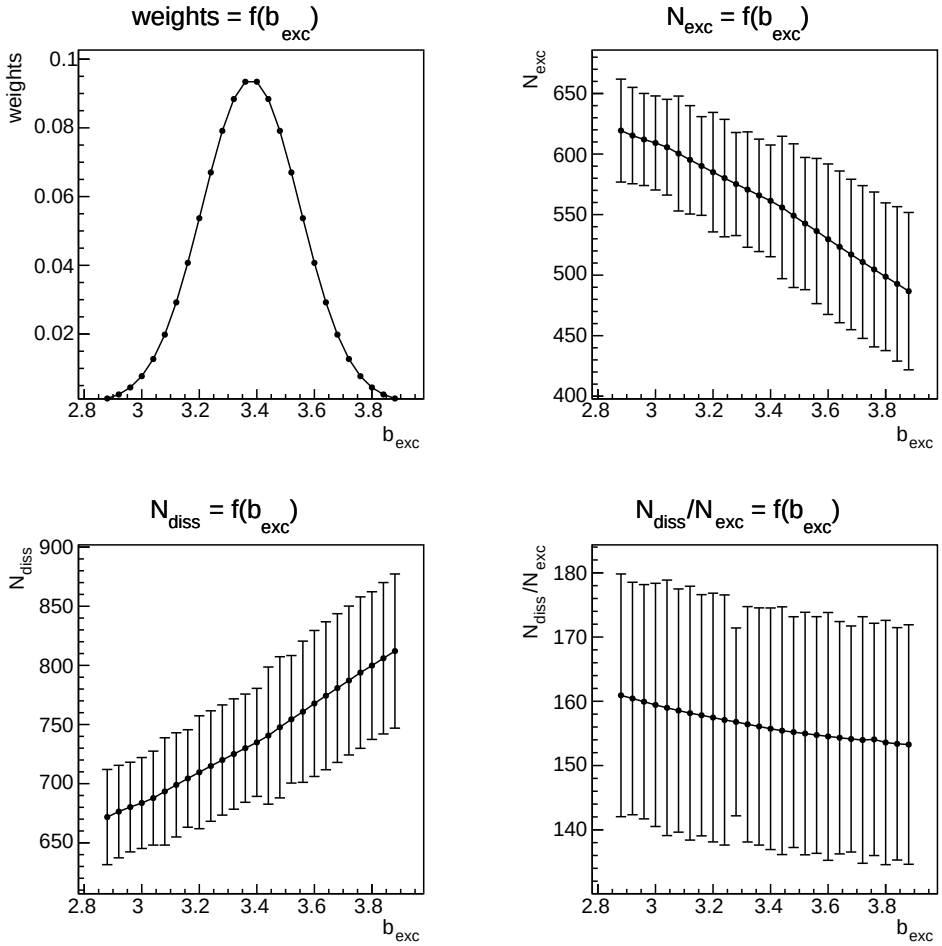

Figure 4.14: The impact of the uncertainty for b_{exc} is shown for the exclusive and dissociative J/ψ candidates, and for the number of exclusive dimuon events. This example is taken for $2.5 < y < 4.0$.

cover all directions in space, and its reconstruction efficiency. Therefore it is called acceptance - efficiency correction, denoted $A \times E$, and corresponds to the probability that the dimuons resulting from two-photon interactions or from the decay of J/ψ are successfully reconstructed in the detector. In order to estimate this probability, the MC simulations of the process in question are used (see section 3.1.3 for details). The analysis of the simulated data gives the number of reconstructed events $N^{\mathrm{rec}}_{\mathrm{J}/\psi/\gamma\gamma}$ for the process of interest, applying the same requirements as for the determination of the number of measured events. Given the number $N^{\mathrm{gen}}_{\mathrm{J}/\psi/\gamma\gamma}$ of events generated in a given rapidity range (and in a given mass range for the process $\gamma\gamma \to \mu^+\mu^-$), this correction factor is defined by the ratio:

$$(A \times E)_{\mathrm{J}/\psi/\gamma\gamma} = \frac{N^{\mathrm{rec}}_{\mathrm{J}/\psi/\gamma\gamma}}{N^{\mathrm{gen}}_{\mathrm{J}/\psi/\gamma\gamma}} \tag{4.12}$$

The number of generated and reconstructed MC events are given by the count of events that pass a given selection. They depend mainly on two variables: the dimuon rapidity y and the dimuon p_{T}. The events are generated in a wider range of rapidity for the dimuons $2.4 < y_{\mu\mu} < 4.1$ to account for rapidity migration effects caused by the reconstruction inside

the detector. The rapidity of generated and reconstructed MC events are shown in figure 4.15. In addition, the events are counted over the full p_{T} range $p_{\mathrm{T}} < 3$ GeV/c. Consequently, the

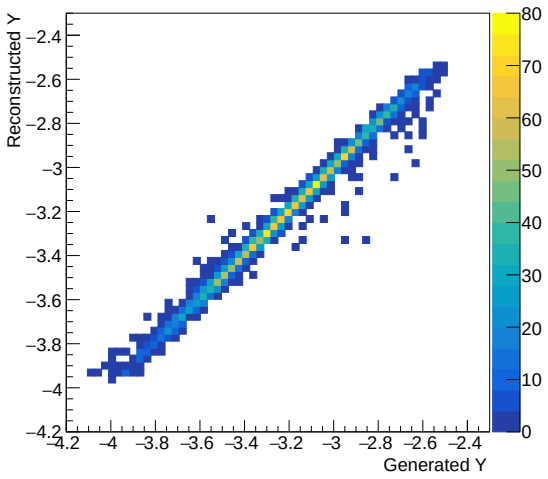

Figure 4.15: Comparison of rapidity at the generated and reconstructed levels.

rapidity and p_{T} resolutions have a minor impact on the computation of $A \times E$ factors.

4.3.1 Computation method of acceptance and reconstruction efficiency

Selection of generated Monte Carlo events

The events are generated in a wider dimuon rapidity range, namely $2.4 < y_{\mu\mu} < 4.1$, to account for rapidity migration effects caused by the reconstruction inside the detector. The generated events to be considered in the analysis must match the following requirements.

- The event has to belong to one of the good runs.
- It contains exactly two oppositely charged muon tracks.
- The rapidity of the dimuon pair lies within the range imposed to reconstructed dimuons. This also in turns, accounts for rapidity migration due to the reconstruction inside the muon spectrometer.
- In the case of exclusive dimuon production in two-photon interactions, the invariant mass of the dimuons has to be within the range imposed to reconstructed dimuons.

Selection of reconstructed Monte Carlo events

The selection of reconstructed events follows closely what is done for real data, which is described in section 3.2.2. The requirements on reconstructed MC events are hence the following.

- The event has to belong to one of the good runs.
- The event has to be triggered, using simulated L0 information since full trigger information is not available. The L0 inputs contain the information related to the muon tracks in the muon spectrometer. The trigger used in the real data analysis, CMUP14, includes the condition of having a single muon above a low p_{T} threshold. Simulated events must have this trigger input.

- It contains exactly two oppositely charged muon tracks.
- The invariant rapidity of the dimuon pair lies within the studied range.
- In the case of exclusive dimuon production in two-photon interactions, the invariant mass of the dimuons has to be within the studied range.
- There is no signal in the simulated V0A and ADA detectors.

ZDC calorimeters are not simulated in GEANT, and hence, the requirement on ZNA is not enforced in the reconstructed events from the simulations.

Uncertainty on $A \times E$

The number of reconstructed dimuons follows a binomial distribution where $p = A \times E$ is the probability of success, here defined by the probability for an event to have been reconstructed.

The standard deviation of the frequency of successes, which corresponds to $A \times E$, is given by the square root of its variance. Thus, the statistical uncertainty on $A \times E$ is given by

$$\Delta(A \times E) = \sqrt{\frac{p \cdot (1-p)}{N^{\text{gen}}}} = \sqrt{\frac{(A \times E) \times (1 - A \times E)}{N^{\text{gen}}}}. \tag{4.13}$$

where N^{gen} is the simplified notation of the number of generated dimuons.

4.3.2 Results of $A \times E$ computation

$A \times E$ for dimuon production in two-photon interactions

The factors of the detector acceptance and efficiency, calculated using the MC sample corresponding to the $\gamma\gamma \to \mu^+\mu^-$ process, are given in table 4.8 along with their statistical uncertainties.

Mass range	Rapidity range	$A \times E$
$1.0 < M_{\mu\mu} < 1.5\ \text{GeV}/c^2$	$2.50 < y < 4.00$	$(1.66 \pm 0.01)\%$
	$2.50 < y < 3.25$	$(0.45 \pm 0.01)\%$
	$3.25 < y < 4.00$	$(3.23 \pm 0.03)\%$
$1.5 < M_{\mu\mu} < 2.0\ \text{GeV}/c^2$	$2.50 < y < 4.00$	$(3.04 \pm 0.03)\%$
	$2.50 < y < 3.25$	$(1.82 \pm 0.03)\%$
	$3.25 < y < 4.00$	$(4.74 \pm 0.06)\%$
$2.0 < M_{\mu\mu} < 2.5\ \text{GeV}/c^2$	$2.50 < y < 4.00$	$(4.09 \pm 0.06)\%$
	$2.50 < y < 3.25$	$(3.25 \pm 0.07)\%$
	$3.25 < y < 4.00$	$(5.32 \pm 0.10)\%$

Table 4.8: Summary of the $A \times E$ values used for the exclusive $\gamma\gamma \to \mu^+\mu^-$ analysis and their statistical uncertainties.

$A \times E$ for exclusive and dissociative J/ψ

The factors of the detector acceptance and efficiency, calculated using the MC sample corresponding to the exclusive J/ψ photoproduction process, are given in table 4.9 along with their statistical uncertainties.

The factor $A \times E$ is affected by kinematics, and dissociative events have a higher p_{T} signature. In order to assess whether MC data of exclusive events can be used to compute $A \times E$ factors for dissociative events, the factors $A \times E$ are computed in ten p_{T} bins up to $p_{\mathrm{T}} = 3\,\mathrm{GeV}/c$ over the full rapidity bin. Then each value is weighted with the number of counts $\mathrm{d}N/\mathrm{d}p_{\mathrm{T}}$ obtained from the 2D fit. Using this method, the $A \times E$ factors found are 0.1932 using the weights extracted from exclusive events and 0.1937 from dissociative events. Thus the $A \times E$ factors obtained using the exclusive MC data sample are considered valid for the dissociative J/ψ photoproduction process.

Mass range	Rapidity range	$A \times E$
$2.5 < M_{\mu\mu} < 3.5\,\mathrm{GeV}/c^2$	$2.50 < y < 4.00$	$(19.34 \pm 0.03)\%$
	$2.50 < y < 3.25$	$(18.20 \pm 0.04)\%$
	$3.25 < y < 4.00$	$(20.93 \pm 0.05)\%$

Table 4.9: Summary of the $A \times E$ values used for the J/ψ analysis.

4.4 Corrections affecting J/ψ signal extraction

In order to compute the cross sections for exclusive and dissociative J/ψ photoproduction, $\sigma(\gamma + \mathrm{p} \to \mathrm{J}/\psi + \mathrm{p})$ and $\sigma(\gamma + X \to \mathrm{J}/\psi + X)$ respectively, the numbers extracted from the two-dimensional fit must be corrected for the number of J/ψ events that are not directly produced in γp interactions, but that are decay products of another more massive particle. This phenomenon is commonly called the feed-down, and is the first object of this section. Furthermore, in order to obtain the cross section of J/ψ production in γp interactions rather than in p–Pb interactions, the measurement must be normalized to the number of photons surrounding the Pb nuclei. This number of photons, or photon flux, is calculated using STARlight simulations and is presented in the second part.

4.4.1 Feed-down from ψ(2S)

Analogously to the J/ψ photoproduction, $\psi(2\mathrm{S})$ vector mesons are also produced in p–Pb UPCs. This particle is heavier (3.69 GeV/c^2) than the J/ψ and decays very quickly into lighter particles. In particular, it decays into a dimuon pair with a probability of $(0.8 \pm 0.06)\%$ [7]. In the studied data sample with the standard selection and over the full rapidity coverage of the muon spectrometer, there are about 99 candidates of this process, evaluated from the invariant mass distribution around the $\psi(2\mathrm{S})$ mass peak using a double-sided crystal ball function. This number is also computed based on the number of J/ψ candidates and $\psi(2\mathrm{S}) \to \mathrm{J}/\psi + X$ events, as presented in appendix G. The calculation predicts 51 $\psi(2\mathrm{S}) \to \mu^+\mu^-$ events using the mid-selection. This underestimation remains reasonable given the amount of statistics. The

favored decay channel of $\psi(2S)$ mesons instead is a J/ψ accompanied by at least one other particle, which corresponds to a branching ratio of $(61.4 \pm 0.6)\%$ [7]. The resulting J/ψ, in turn, decays in $(5.961 \pm 0.033)\%$ of the time into a muon pair [7] and the other particles produced may not be detected in the experimental apparatus, thus leaving in the detector the same signature as the J/ψ photoproduction. This contribution must be subtracted from the number of J/ψ candidates extracted from the two-dimensional fit.

Thus, we have

$$N^{\text{fit}}_{J/\psi} = N^{\gamma p}_{J/\psi} + N^{\text{FD}}_{J/\psi} \tag{4.14}$$

where $N^{\text{fit}}_{J/\psi}$ is the total number of J/ψ candidates extracted from the two-dimensional fit, $N^{\gamma p}_{J/\psi}$ is the number of measured J/ψ produced in γp interactions and $N^{\text{FD}}_{J/\psi}$ is the number of measured J/ψ resulting from the decay of a $\psi(2S)$ photoproduced in γp interactions.

We define the feed-down factor f_D as being the ratio between the number of J/ψ and $\psi(2S)$ produced in γp interactions, $f_D = N^{\text{FD}}_{J/\psi}/N^{\gamma p}_{J/\psi}$, so equation 4.14 becomes

$$N^{\text{fit}}_{J/\psi} = N^{\gamma p}_{J/\psi} + f_D \cdot N^{\gamma p}_{J/\psi} \tag{4.15}$$

and finally the real number of J/ψ produced in γp interactions is

$$N^{\gamma p}_{J/\psi} = \frac{N^{\text{fit}}_{J/\psi}}{(1 + f_D)}. \tag{4.16}$$

The objective is to find the feed-down fraction f_D, knowing that the true numbers $N^{\text{FD}}_{J/\psi}$ and $N^{\gamma p}_{J/\psi}$ are not known. The ratio of these numbers can be found by using the cross sections of these two processes, multiplied by their respective acceptance-efficiency factor and for the $\psi(2S)$ its branching ratio of decay in J/ψ. Thus, the feed-down fraction f_D can be expressed as follows:

$$f_D = \frac{\sigma_y\left(\psi(2S)\right) \cdot BR(\psi(2S) \to J/\psi + X) \cdot (A \times E)^{\text{FD}}_{J/\psi}}{\sigma_y(J/\psi) \cdot (A \times E)_{J/\psi}} \tag{4.17}$$

where σ_y is the cross section of a process at a given rapidity, $BR(\psi(2S) \to J/\psi + X) = (61.4 \pm 0.6)\%$ is the decay branching ratio of a $\psi(2S)$ to J/ψ and any other particle, and the terms $(A \times E)^{\text{FD}}_{J/\psi}$ and $(A \times E)_{J/\psi}$ denote acceptance - efficiency factors for the J/ψ resulting from the decay of a $\psi(2S)$ and produced in γp interactions, respectively. These latter factors and their uncertainties are obtained as described in section 4.3 using the corresponding MC samples for each process.

In the calculation of f_D, the ratio $\sigma_y\left(\psi(2S)\right)/\sigma_y(J/\psi)$ is taken from H1 measurements for $40 < W_{\gamma p} < 70$ GeV [10], regardless of the rapidity bin considered:

$$\frac{\sigma_y\left(\psi(2S)\right)}{\sigma_y(J/\psi)} = 0.150 \pm 0.013 \pm 0.011, \tag{4.18}$$

where the uncertainties are first statistical and then systematic. The obtained feed-down factors are given in table 4.10 for each rapidity bin. Their uncertainties are computed as the sum in quadrature of statistical and systematic uncertainties, and branching ratio uncertainty.

4.4.2 Photon flux

The cross section $d\sigma/dy(p + Pb \to p + Pb + J/\psi)$ is related to the γp cross section, $\sigma(\gamma + p \to J/\psi + p)$, through the photon flux, dn/dk:

$$\frac{d\sigma}{dy}(p + Pb \to p + Pb + J/\psi) = k\frac{dn}{dk}\sigma(\gamma + p \to J/\psi + p) \tag{4.19}$$

Rapidity range	$A \times E^{FD}_{\mathrm{J}/\psi}$	$A \times E_{\mathrm{J}/\psi}$	f_D
$2.50 < y < 4.00$	0.1923 ± 0.0001	0.1934 ± 0.0001	0.092 ± 0.012
$2.50 < y < 3.25$	0.1791 ± 0.0002	0.1820 ± 0.0002	0.091 ± 0.012
$3.25 < y < 4.00$	0.2121 ± 0.0002	0.2094 ± 0.0002	0.093 ± 0.012

Table 4.10: Feed-down f_{D} correction factors for J/ψ photoproduction in p–Pb.

where k is the photon energy, which is determined by the J/ψ mass and rapidity, $k = (1/2)M_{\mathrm{J}/\psi}\exp(-y)$. Thus, the number of J/ψ must be normalized to the photon flux to obtain the J/ψ photopro-

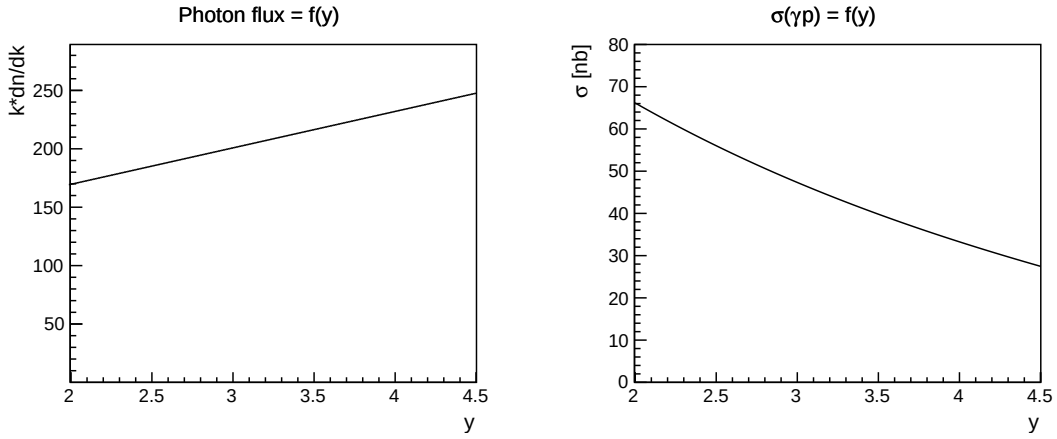

Figure 4.16: Photon flux from the Pb nucleus computed with STARlight as a function of the J/ψ rapidity, adapted for a Lorentz boost of the Pb nucleus γ_{Pb} = 2745.

duction cross section in $\gamma\mathrm{p}$ interactions. This quantity is calculated according to the standard procedure in ALICE analyses using the STARlight event generator, which is given as input parameters the Lorentz boost factors of each of the two colliding nuclei, their atomic number Z and their mass number A. The calculation of the photon flux is done in small rapidity bins, and the result of the simulation is given in figure 4.16 at the left-hand side. STARlight also calculates differential velocity or integrated cross sections (figure 4.16 on the right). The average photon flux values for the different rapidity intervals are listed in table 4.11. For each rapidity bin, the mean $\gamma\mathrm{p}$ energy, $\langle W_{\gamma\mathrm{p}}\rangle$, is calculated by weighting with the product of the photon flux and the cross section $\sigma(\gamma\mathrm{p})$ from STARlight. The derivation of photon flux uncertainties is described later in the chapter, in section 4.5.3.

Rapidity range	$k\frac{\mathrm{d}k}{\mathrm{d}n}$	Energy range $W_{\gamma\mathrm{p}}$ (GeV)	$\langle W_{\gamma\mathrm{p}}\rangle$ (GeV)
$2.50 < y < 4.00$	208.6	$(27, 57)$	39.9
$2.50 < y < 3.25$	196.9	$(39, 57)$	47.7
$3.25 < y < 4.00$	220.3	$(27, 39)$	32.8

Table 4.11: Photon flux values computed with the STARlight event generator with the energy range $W_{\gamma\mathrm{p}}$ and their mean value, weighted with the photon flux.

4.5 Systematic uncertainties

The signal extraction is affected by several sources of systematic uncertainties, many of which have already been explained previously. The purpose of this section is to summarize all the systematic uncertainties to take into account in the measurement. Among them, some affect all signals, such as the efficiency of the muon spectrometer in identifying tracks, while others only concern the extraction of dimuons coming from the $\gamma\gamma \to \mu^+\mu^-$ process or the J/ψ protoproduction in γp interactions. When measuring the ratio of dissociative to exclusive J/ψ photoproduction cross sections, many uncertainties cancel out, as discussed in the end of the section.

4.5.1 Common uncertainties

The uncertainties that affect the entire data sample come from:

- the luminosity, whose relative systematic uncertainty - already discussed in section 3.3 - is 1.8%
- the muon tracking efficiency, which refers to muon reconstruction in the MCH
- the muon trigger efficiency, since the data is recorded when a single muon with a transverse momentum above a low threshold ($p_T > 0.5$ GeV/c) is identified in the MTR
- the efficiency of matching a muon track identified in the MTR and in the MCH
- and pile-up correction due to vetoes in the detectors (not including V0C, for which the cut on the number of fired cells has a special treatment), discussed in appendix C and whose systematic uncertainty is estimated at 0.2%.

The uncertainty due to the V0C cutoff in the data selection, computed in appendix B.2, is also common to both measurements. However, this uncertainty is evaluated differently for each process and depends on the mass and rapidity ranges studied. Thus, these uncertainties are presented as affecting one or the other of the processes in tables 4.13 and 4.14. The calculation of these uncertainties are based on the variation of the number of allowed fired cells in V0C. When increasing this number, the yields of exclusive J/ψ events and exclusive $\gamma\gamma \to \mu^+\mu^-$ are found to be stable, while the yield of dissociative J/ψ events increases, as the sample can be contaminated with inclusive photoproduction or hadronic production of J/ψ events. The number of expected dissociative J/ψ events is computed as the product of the number of exclusive J/ψ events and the ratio of exclusive to dissociative J/ψ events when all fired cells in V0C are matched to a muon. The systematic uncertainty on the number of dissociative J/ψ events is computed as the relative difference between the number of expected and extracted dissociative J/ψ events, while the systematic uncertainty on the numbers of exclusive J/ψ and $\gamma\gamma \to \mu^+\mu^-$ events is obtained by varying the condition on V0C. It amounts to values ranging from 0.5% to 1.7% depending on the mass bin for $\gamma\gamma \to \mu^+\mu^-$ signal, and to 2.6% and 13% for exclusive and dissociative J/ψ events respectively.

The systematic uncertainties on tracking efficiency, muon trigger efficiency, and muon matching efficiency were already computed for the inclusive J/ψ production analysis using the same data sample [11]. These efficiencies are typically p_T-dependent, and the dimuons p_T distribution is similar in the inclusive and present analyses. Therefore, the same values can be safely used. They are now briefly presented.

Muon tracking efficiency

The uncertainty on the tracking efficiency corresponds to the muon track reconstruction efficiency in the MCH chambers. It is calculated by comparing the efficiencies evaluated in the data and MC simulations. The components taken into account are the efficiency of each tracking plane and the single muon tracking efficiency calculated according to the tracking algorithm. The systematic uncertainty on the dimuon tracking efficiency is estimated at 1% in this data sample.

Muon trigger efficiency

The efficiency of the single muon trigger is incorporated in the acceptance and efficiency calculations ($A \times E$) for the reconstruction of the dimuons.

Two sources affect the muon trigger efficiency: the intrinsic efficiency of the trigger chambers (MTR) and the efficiency of the trigger threshold cutoff. As for the muon tracking efficiency, the intrinsic efficiency of the MTR chambers is estimated by comparing the trigger efficiency in the data and the realistic MC simulations at the level of single muons and then is propagated at the level of J/ψ. Its systematic uncertainty is evaluated at 1%. The efficiency of the trigger threshold cutoff is obtained by studying the behavior of the trigger around the threshold, and its systematic uncertainty is evaluated as a discrepancy between the trigger response in the data and in MC simulations. The trigger response function varies with the muon p_{T} and is obtained for each p_{T} as the ratio of muon tracks matching the trigger to all muon tracks. The value of the total systematic uncertainty on the J/ψ level is about 2.4%, integrating over all the p_{T} in p–Pb collisions. Both contributions are summed in quadrature to obtain the total uncertainty of the dimuon trigger efficiency of 2.6%.

Muon matching efficiency

The muon matching efficiency corresponds to the efficiency of matching a muon track candidate in the MCH to a trigger track above the 0.5 GeV$/c$ p_{T}-threshold in the MTR. Its uncertainty is estimated by varying the cutoff χ^2 applied to the pairing of the reconstructed tracks in the muon tracking and triggering systems, and it is found to be 1%.

Summary

The systematic uncertainties affecting the entire data sample are presented in table 4.12. Un-

Source	Value (%)
Luminosity	1.8%
Tracking efficiency	1%
Muon trigger efficiency	2.6%
Matching efficiency	1%
Pile-up correction	0.2%
Total common	3.5%

Table 4.12: Summary of systematic uncertainties affecting all signals.

certainties on tracking, trigger and muon matching efficiencies are considered as uncorrelated over y. All other components are taken fully correlated across the rapidity y.

4.5.2 Uncertainties affecting $\gamma\gamma \to \mu^+\mu^-$ signal only

The sources of systematic uncertainties which affect the extraction of the $\gamma\gamma \to \mu^+\mu^-$ signal are the following:

- in the lowest mass bin studied, $1.0 < M_{\mu\mu} < 1.5$ GeV/c^2, the production of ϕ mesons decaying to dimuons which might contaminate the sample,
- and the choice of the p_{T} shape to model $\gamma\gamma \to \mu^+\mu^-$ signals in the data.

The systematic uncertainty induced by the first contribution is estimated by computing the expected number of $\phi \to \mu^+\mu^-$ events in the sample at low mass and then normalizing it to the number of $\gamma\gamma \to \mu^+\mu^-$ events extracted. This uncertainty amounts to 1.5%, and details of this calculation are presented in appendix F. The second contribution is obtained by varying both parameters of the Landau distribution, as discussed in section 4.1.3, and the induced relative uncertainties are given in table 4.2.

Finally, these uncertainties are summed in quadrature with the uncertainties given in table 4.12, and they are summarized in table 4.13. Uncertainties on signal extraction are considered as uncorrelated over y. All other components are taken fully correlated across the rapidity y.

Source	Mass range (GeV/c^2)	Value (%)
V0C veto	(1.0, 1.5)	1.2%
	(1.5, 2.0)	1.7%
	(2.0, 2.5)	0.5%
$\phi \to \mu^+\mu^-$ contamination	(1.0, 1.5)	1.5%
Signal extraction	(1.0, 1.5)	from 3.2% to 3.9%
	(1.5, 2.0)	from 3.3% to 4.4%
	(2.0, 2.5)	from 4.9% to 7.6%
Total	(1.0, 1.5)	**from 5.1% to 5.5%**
	(1.5, 2.0)	**from 4.8% to 5.6%**
	(2.0, 2.5)	**from 4.9% to 8.4%**

Table 4.13: Summary of systematic uncertainties on the calculation of $\gamma\gamma \to \mu^+\mu^-$ cross sections in different mass ranges. The ranges of values correspond to different rapidity bins.

4.5.3 Uncertainties affecting J/ψ signal only

The sources of systematic uncertainties which affect the extraction of the J/ψ signal are the following:

- the branching ratio of J/ψ decaying into dimuons, whose relative uncertainty is taken from reference [7], and amounts to 0.55%

- the choice of the p_{T} shape to model exclusive J/ψ photoproduction signals in the data, as discussed in section 4.2.5, and whose relative uncertainties are given in the table 4.7
- the feed-down, whose uncertainties are listed in table 4.10
- and the photon flux.

The photon flux systematic uncertainty

The uncertainty on the photon flux is obtained by modifying several parameters in the source code of the STARlight program.

1. The **nuclear radius** of the Pb is changed by ± 0.5 fm, corresponding to the nuclear skin thickness. Assuming that the **nuclear density** ρ_0 of the Pb nucleus has a cubic dependence on the radius, it is varied accordingly.

2. The **form factor** is normally taken from the equation (14) in reference [12], and is replaced instead by a Helm form factor, as presented in equation (12) of [13].

3. The **number of steps** in the calculation of the photon flux is doubled.

4. The **minimum value for impact parameter** is changed from $0.7 \times R_{\mathrm{Sum}}$ to $0.5 \times R_{\mathrm{Sum}}$ where R_{Sum} is the sum of the radii of the two colliding nuclei.

5. The **hadronic interaction probability**, which affects whether the J/ψ might be accompanied by a hadronic interaction, is usually calculated using equation (7) of the STARlight article [14]. The constant value σ_{NN} in this equation is changed from 7.0 mb to 6.0 mb.

Finally, the systematic uncertainty on the p–Pb beam configuration is obtained by computing the maximum deviation of the photon flux with respect to the central value when changing the parameters described above. The final relative uncertainty is estimated at 2%, where most of the deviation comes from changing the nuclear radius and density.

Uncertainties affecting the exclusive and dissociative J/ψ cross sections

The total systematic uncertainties are obtained by summing the common uncertainties given in table 4.12 and those presented in this section. They are given in table 4.14. Uncertainties on signal extraction are considered as uncorrelated over y. All other components are taken fully correlated across the rapidity y.

Uncertainties affecting the ratio of the numbers of dissociative and exclusive events

When computing the ratio of dissociative to exclusive cross sections, $\sigma^{\mathrm{diss}}/\sigma^{\mathrm{exc}}$, most of the systematic uncertainties presented above cancel out. The remaining sources of uncertainty are due to the variation of the b_{exc} parameter (see section 4.2.5), and the variation on the number of allowed fired V0C cells, presented in appendix B.2.2. The systematic uncertainties of the ratio are then computed as the quadratic sum of these two components only. They are given in table 4.15. Uncertainties on signal extraction are considered as uncorrelated over y, while uncertainties on V0C veto are taken fully correlated across the rapidity y.

Source	Value (%)
V0C veto	2.6% (excl.), 13% (diss.)
Branching ratio	0.55%
Photon flux	2%
$\delta(1 + f_{\mathrm{D}})$	1.1%
Signal extraction (excl.)	from 3.56% to 3.97%
Signal extraction (diss.)	from 2.90% to 4.37%
Total (excl.)	**from 6.1% to 7.4%**
Total (diss.)	**from 14.0% to 14.3%**

Table 4.14: Summary of systematic uncertainties on the calculation of exclusive and dissociative cross sections, computed in the mass range $2.5 < M_{\mu\mu} < 3.5$ GeV/c^2. The ranges of values correspond to different rapidity bins.

Source	Value (%)
V0C veto	4.3%
Signal extraction	from 7% to 8%
Total	**from 8% to 9%**

Table 4.15: Systematic uncertainties on the calculation of the cross section ratio $\sigma^{\mathrm{diss}}/\sigma^{\mathrm{exc}}$. The ranges of values correspond to different rapidity bins.

4.6 Summary

In this chapter, we have presented the different components that allow the calculation of cross sections. First, the method of signal extraction using a two-dimensional fit was presented with particular care to model each component of the signal in the dimuons mass and p_{T} spectra. Then, the corrections to be applied on the obtained yields were explained and computed. This chapter then presented the systematic uncertainties that come into play in the final result in addition to the statistical uncertainties. We can then move on to the computation of cross sections and connect them with the first chapter of this thesis.

Bibliography

[1] G. Breit and John A. Wheeler. Collision of Two Light Quanta. *Phys. Rev.*, 46:1087–1091, Dec 1934. doi: 10.1103/PhysRev.46.1087. URL https://link.aps.org/doi/10.1103/PhysRev.46.1087.

[2] Luca Lista. *Statistical Methods for Data Analysis in Particle Physics*, volume 941. Springer, 2017. doi: 10.1007/978-3-319-62840-0.

[3] Spencer Klein, A. H. Mueller, Bo-Wen Xiao, and Feng Yuan. Lepton pair production through two photon process in heavy ion collisions. *Phys. Rev. D*, 102:094013, Nov 2020. doi: 10.1103/PhysRevD.102.094013. URL https://link.aps.org/doi/10.1103/PhysRevD.102.094013.

[4] Dielectron production at midrapidity at low transverse momentum in peripheral and semi-peripheral Pb−Pb collisions at $\sqrt{s_{\mathrm{NN}}} = 5.02$ TeV. 4 2022.

[5] Georges Aad et al. Exclusive dimuon production in ultraperipheral Pb+Pb collisions at $\sqrt{s_{\mathrm{NN}}} = 5.02$ TeV with ATLAS. *Phys. Rev. C*, 104:024906, 2021. doi: 10.1103/PhysRevC.104.024906.

[6] C. Alexa et al. Elastic and Proton-Dissociative Photoproduction of J/ψ Mesons at HERA. *The European Physical Journal C*, 73(6):2466, 2013. doi: 10.1140/epjc/s10052-013-2466-y. URL https://doi.org/10.1140/epjc/s10052-013-2466-y.

[7] P. A. Zyla et al. Review of Particle Physics. *PTEP*, 2020(8):083C01, 2020. doi: 10.1093/ptep/ptaa104.

[8] sPlot website. http://arogozhnikov.github.io/2015/10/07/splot.html.

[9] Shreyasi Acharya et al. Coherent J/ψ photoproduction at forward rapidity in ultra-peripheral Pb-Pb collisions at $\sqrt{s_{\mathrm{NN}}} = 5.02$ TeV. *Phys. Lett. B*, 798:134926, 2019. doi: 10.1016/j.physletb.2019.134926.

[10] C. Adloff et al. Diffractive photoproduction of psi(2S) mesons at HERA. *Phys. Lett. B*, 541: 251–264, 2002. doi: 10.1016/S0370-2693(02)02275-X.

[11] Shreyasi Acharya et al. Inclusive J/ψ production at forward and backward rapidity in p-Pb collisions at $\sqrt{s_{\mathrm{NN}}}$ = 8.16 TeV. *JHEP*, 07:160, 2018. doi: 10.1007/JHEP07(2018)160.

[12] Spencer Klein and Joakim Nystrand. Exclusive vector meson production in relativistic heavy ion collisions. *Phys. Rev.*, C60:014903, 1999. doi: 10.1103/PhysRevC.60.014903.

[13] D.K. Papoulias, T.S. Kosmas, R. Sahu, V.K.B. Kota, and M. Hota. Constraining nuclear physics parameters with current and future COHERENT data. *Physics Letters B*, 800: 135133, 2020. ISSN 0370-2693. doi: https://doi.org/10.1016/j.physletb.2019.135133. URL https://www.sciencedirect.com/science/article/pii/S037026931930855X.

[14] Spencer R. Klein, Joakim Nystrand, Janet Seger, Yuri Gorbunov, and Joey Butterworth. STARlight: A Monte Carlo simulation program for ultra-peripheral collisions of relativistic ions. *Comput. Phys. Commun.*, 212:258–268, 2017. doi: 10.1016/j.cpc.2016.10.016.

Chapter 5

Results and comparison of measurements with models

Contents

5.1 Cross sections for the dimuon continuum in two-photon interactions . . . 116

5.1.1 Measurements and predictions of cross sections . . . 117

5.1.2 Results and discussion . . . 117

5.1.3 Outlook: measuring timelike Compton scattering at the LHC . 119

5.2 Cross sections for J/ψ photoproduction off protons . . . 122

5.2.1 Calculation of cross sections . . . 122

5.2.2 Previous measurements of J/ψ photoproduction . . . 123

5.2.3 Description of some theoretical models of J/ψ photoproduction 125

5.2.4 Discussion of the results . . . 127

5.2.5 Discussion and outlook . . . 129

5.3 Summary . . . 131

Bibliography . . . 132

In the previous chapter, we saw how the signal (Breit-Wheeler process or J/ψ photoproduction) is extracted from the data and the corrections to be applied to transform event counts into cross sections. It is now time to put all these ingredients together to present the cross sections measurements.

This chapter first focuses on the results concerning the exclusive production of the dimuon continuum in two-photon interactions. After the presentation of the calculation of the cross section, the measurements are then compared to STARlight, a theoretical model which incorporates the current understanding of the QED to LO. In a second step, this chapter deals with the main object, the J/ψ photoproduction off protons. The results are first presented and then compared to existing measurements on the one hand, and on the other hand to theoretical models which incorporate our understanding of the proton structure and QCD at high energy.

5.1 Cross sections for the dimuon continuum in two-photon interactions

Two-photon interactions can give rise to exclusive, non-resonant dimuon production, in a process referred to as the Breit-Wheeler process. Precise measurements of the Breit-Wheeler process offer the opportunity to test for the presence of higher-order QED effects [1]. Predictions exist where this effect is negligible in Au–Au, Ar–Ar, and Pb–Pb collisions [2]. However, other studies obtained a 16% reduction in the cross section from higher-order terms in Pb–Pb collisions at the LHC [3]. The use of asymmetric p–Pb collisions could also help separate higher-order corrections from multi-photon exchange with only one or with both ions [4]. Higher-order terms are expected to be important due to large $Z\alpha$ coupling. In particular, the Coulomb corrections, related to possible photon exchanges between final-state leptons and heavy ions, is a longly debated subject. Hencken et al. [2] argued that Coulomb corrections are strongly suppressed due to cancellations of diagrams involving positively and negatively charged leptons, however recent studies suggest that Coulomb corrections might be significant [1].

In addition, this process appears as a background signal when measuring other UPC processes, such as the photonuclear production of hadrons and jets [5] when studied at similar mass ranges. Therefore, precise measurements of the Breit-Wheeler process could allow for calibrating its rates, ensuring a better background control, and could be used as a constraint on the photon fluxes from Pb nuclei.

Dilepton production has been widely studied in the past in Pb–Pb collisions at the LHC [6–9] and in Au–Au collisions at RHIC [10–13]. Latest precision measurements by the ATLAS and ALICE collaboration at the LHC [14, 15] reveal significant discrepancies with STARlight, up to 20% at large dimuon rapidities and for $p_{\mathrm{T}} < 0.1$ GeV/c in the measurement of dielectron production presented by ALICE. According to reference [1], the higher-order correction to the lowest-order QED result could explain ATLAS results.

The past measurements focus either on mid-rapidity or high invariant masses. Therefore, the low invariant mass region at forward rapidity below 1.5 GeV/c^2 in heavy-ion collisions is unexplored.

We first present the calculation of cross sections, then we compare them to the STARlight model. Finally, we discuss possible studies at the LHC in the future using the Breit-Wheeler process.

5.1.1 Measurements and predictions of cross sections

Calculation of cross sections

As we saw in chapter 3, the data, once extracted, must be normalized by the luminosity of the beams $\mathcal{L}$ for the trigger class considered in the data and corrected by the pile-up due to detector vetoes with the factor ϵ_{veto}. The numbers extracted from the signal $N_{\gamma\gamma}$ in chapter 4 must also be corrected by the acceptance factor - efficiency $(A \times E)_{\gamma\gamma}$, which takes into account the efficiency of the detectors as well as the fact that muons are not detected in all directions in space.

Thereby, the cross section $\sigma(\gamma\gamma \to \mu\mu)$ is given by the formula:

$$\sigma(\gamma\gamma \to \mu\mu) = \frac{N_{\gamma\gamma}}{(A \times E) \cdot \mathcal{L} \cdot \epsilon_{\text{veto}}} \tag{5.1}$$

and the calculation is repeated in all mass and rapidity bins studied.

Cross sections given by the STARlight model

Additionally, cross sections $\sigma^{SL}(\gamma\gamma \to \mu\mu)$ are computed with STARlight using the kinematics of p–Pb beam at $\sqrt{s_{\text{NN}}} = 8.16$ TeV.

STARlight uses all primary physical mechanisms in its calculations, but it does not take into account dissociative processes, QED final-state radiations (FSRs) or other NLO effects. The FSR is an additional contribution from photon radiation off the final hadrons. In the case of lepton pair creation in two-photon interactions (Breit-Wheeler process), the calculations use the EPA, which is a semi-classical LO calculation, where the photons are treated as massless [16, 17]. Although the kinematic distributions are generally in good agreement with the data, the EPA approach finds a lower mean p_{T} than in the data. A full QED calculation, which includes photon virtuality, finds better agreement with the data [11]. Corrections to NLO are expected in the calculation of cross sections [3, 18].

5.1.2 Results and discussion

The cross section corresponding to the exclusive $\gamma\gamma \to \mu^+\mu^-$ process is drawn as a function of mass, hence it is computed in each mass bin as:

$$\frac{\mathrm{d}\sigma_{\gamma\gamma}}{\mathrm{d}M_{\mu\mu}}(\mathrm{p} + \mathrm{Pb} \to \mathrm{p} + \mathrm{Pb} + \mu^+ + \mu^-) = \frac{N_{\gamma\gamma}}{(A \times E)_{\gamma\gamma} \cdot \mathcal{L} \cdot \epsilon_{\text{veto}} \cdot \Delta M_{\mu\mu}}, \tag{5.2}$$

where $N_{\gamma\gamma}$ is the number of reconstructed $\gamma\gamma \to \mu^+\mu^-$ events, $(A \times E)_{\gamma\gamma}$ is the factor of acceptance and reconstruction efficiency in the corresponding mass and rapidity bin studied, ϵ_{veto} is the correction factor for veto inefficiency and $\Delta M_{\mu\mu}$ is the mass interval. The differential cross sections $d\sigma_{\gamma\gamma}/dM_{\mu\mu}$ are presented in table 5.1 in two rapidity bins and integrated over rapidity, along with the predictions from STARlight 2.2.0 for comparison, where the mass differential cross sections are simply computed as

$$\frac{\mathrm{d}\sigma^{\mathrm{SL}}_{\gamma\gamma}}{\mathrm{d}M_{\mu\mu}} = \frac{\sigma^{SL}(\gamma\gamma \to \mu\mu)}{\Delta M_{\mu\mu}} \tag{5.3}$$

Mass range (GeV/c^2)	Rapidity range	$\frac{\mathrm{d}\sigma_{\gamma\gamma}}{\mathrm{d}M_{\mu\mu}}$ (nb·GeV$^{-1}\cdot c^2$)	$\frac{\mathrm{d}\sigma^{\mathrm{SL}}_{\gamma\gamma}}{\mathrm{d}M_{\mu\mu}}$ (nb·GeV$^{-1}\cdot c^2$)
$1.0 < M_{\mu\mu} < 1.5$	$2.50 < y < 4.00$	$10 \pm 1 \pm 1$	8.4
	$3.25 < y < 4.00$	$4.4 \pm 0.3 \pm 0.3$	4.1
	$2.50 < y < 3.25$	$6.9 \pm 0.7 \pm 0.2$	4.4
$1.5 < M_{\mu\mu} < 2.0$	$2.50 < y < 4.00$	$3.9 \pm 0.2 \pm 0.5$	3.0
	$3.25 < y < 4.00$	$1.6 \pm 0.1 \pm 0.1$	1.4
	$2.50 < y < 3.25$	$2.2 \pm 0.2 \pm 0.1$	1.6
$2.0 < M_{\mu\mu} < 2.5$	$2.50 < y < 4.00$	$1.3 \pm 0.3 \pm 0.3$	1.4
	$3.25 < y < 4.00$	$0.53 \pm 0.01 \pm 0.03$	0.67
	$2.50 < y < 3.25$	$0.72 \pm 0.01 \pm 0.04$	0.74

Table 5.1: Mass differential cross sections for exclusive $\gamma\gamma \to \mu^+\mu^-$ production in ultra-peripheral p–Pb collisions at $\sqrt{s_{\mathrm{NN}}} = 8.16$ TeV.

In addition, the measurements and STARlight predictions are shown in figure 5.1 in the two sub-rapidity bins studied. Both agree within ranges varying from 0.2σ to 3.1σ depending on the mass and rapidity bin, where σ is the quadratic sum of statistical and systematic uncertainties of the measurements. In the two lowest mass bins, an excess of the cross sections is observed compared with STARlight, while the opposite behavior is seen in the highest mass bin. As the uncertainties on the photon flux were included in the systematics, they are unlikely to explain this discrepancy. A possible explanation could be higher-order effects which behave differently in mass.

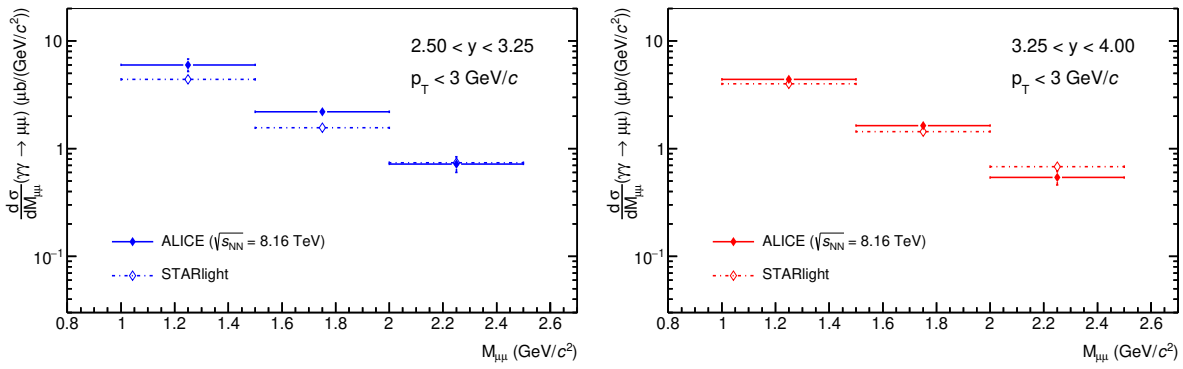

Figure 5.1: The differential cross sections for exclusive $\gamma\gamma \to \mu^+\mu^-$ production for p–Pb UPCs at $\sqrt{s_{\mathrm{NN}}} = 8.16$ TeV, as a function of $M_{\mu\mu}$, in two rapidity bins: $2.50 < y < 3.25$ (left) and $3.25 < y < 4.00$ (right). The vertical error bars represent the statistical and systematic uncertainties summed in quadrature. The results are compared with predictions from STARlight [19, 20].

As discussed in the beginning of this section, the main goals of a high-precision measurement of the $\gamma\gamma \to \mu^+\mu^-$ process are first to check our understanding of the QED, and also to

be able to fix the photon flux coming from the lead nucleus. If the models were confirmed, it would allow better control of background counts when measuring J/ψ photoproduction or other UPC processes. However, the uncertainties on the measurements vary from 7 to 17%. Given the 2% relative uncertainty on the photon flux provided by STARlight (see section 4.5.3), the current precision does not allow one to constrain the possible photon flux uncertainties from the Pb nucleus.

5.1.3 Outlook: measuring timelike Compton scattering at the LHC

Timelike Compton Scattering (TCS) produces the same final state as the Bethe-Heitler (BH) process. With a target proton, it corresponds to the reaction

$$\gamma(q)\mathrm{p}(p) \to \gamma^*(q')\mathrm{p}(p') \to l^-(k)l^+(k')\mathrm{p}(p') \tag{5.4}$$

where the lepton pair produced l^-l^+ can be either e^+e^-, either $\mu^+\mu^-$. This process is of great interest because its production mechanism reveal information on GPDs in the proton [21]. It is represented to LO in α_s by the two Feynman diagrams in figure 5.2.

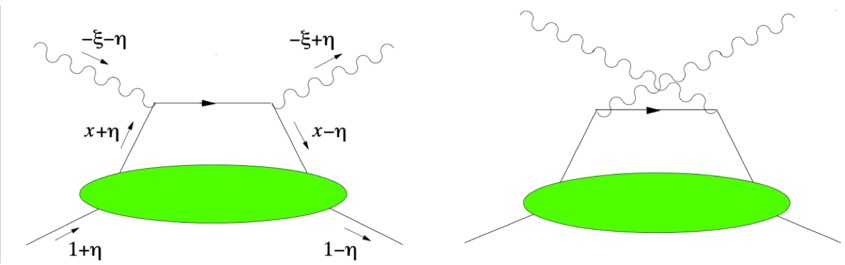

Figure 5.2: Timelike Compton scattering to leading order in α_s. Figure taken from reference [21].

The kinematics of the $\gamma(q)\mathrm{p}(p) \to l^+(k)l^-(k')\mathrm{p}(p')$ process are shown in figure 5.3, which introduces the polar and azimuthal angles θ and φ of the momentum of one of the leptons $\vec{k}$ in the l^+l^- center-of-mass system with respect to the outgoing proton momentum $\vec{p}'$.

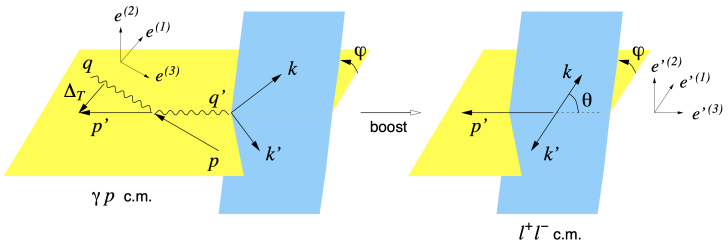

Figure 5.3: Kinematical variables and coordinate axes in the $\gamma\mathrm{p}$ and l^+l^- center-of-mass frames. Figure taken from reference [21].

Measuring TCS

In general terms, the cross section of the reaction $\gamma p \to p' l^+ l^-$ can be written as:

$$\sigma(\gamma p \to p' \mu^+ \mu^-) = \sigma_{BH} + \sigma_{TCS} + \sigma_{INT} \tag{5.5}$$

where σ_{BH}, σ_{TCS} and σ_{INT} are the cross sections of BH, TCS, and the TCS-BH interference respectively. At LO and leading twist in QCD, σ_{INT} can be expressed as a linear combination of GPD-related quantities [22].

TCS can be accessed in a kinematic domain where the two processes are of the same order of magnitude (although the BH process always dominates over TCS) following one or the other of the two following methods [21].

1. By subtracting the BH contribution. The BH amplitude is computed from the two Feynman diagrams in figure 5.4, and is completely calculable in QED.

2. By analyzing interference terms between the two processes.

The BH cross section σ_{BH} scales with $1/\sin^2(\theta)$ and is largely dominant over TCS in a region where the term $\sin^2(\theta)$ is small. As a consequence, a cutoff on the θ angle is necessary to ensure that the two processes are of the same order of magnitude. Nevertheless, since the BH process always dominates over TCS, analyzing interference terms is usually the preferred method.

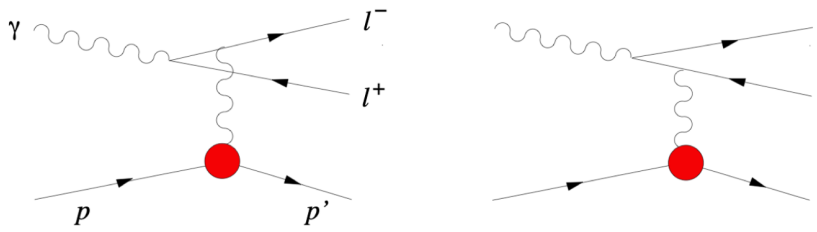

Figure 5.4: Feynman diagrams for the Bethe-Heitler process. Figure taken from reference [21].

A hallmark of the interference term between TCS and BH is that it is odd under exchange of the l^+ and l^- momenta (when $\varphi \to \pi + \varphi$ and $\theta \to \pi - \theta$) due to charge conjugation, whereas σ_{BH} and σ_{TCS} are even. As a consequence, the interference can be accessed through the angular distribution of the lepton pair [22], eliminating in particular the large BH contribution. The CLAS12 experiment, located at Jefferson Lab, measured the angular asymmetries in a complementary kinematic domain as accessible at the LHC [23].

Measuring TCS at the LHC

Reaching a kinematic domain where the BH and TCS processes are of the same order of magnitude should be possible at the LHC. The study presented in reference [21] predicts values for the BH cross section σ_{pp}^{BH} and the TCS cross section σ_{pp}^{TCS} in pp collisions at $\sqrt{s} = 7$ TeV

$$\sigma_{pp}^{BH} = 2.9 \text{ pb and } \sigma_{pp}^{TCS} = 1.9 \text{ pb} \tag{5.6}$$

where σ_{pp}^{BH} is integrated over $\theta = [\pi/4, 3\pi/4]$, $\varphi = [0, 2\pi]$, $t = [-0.05, -0.25]$ GeV^2, $Q'^2 = [4.5, 5.5]$ GeV^2, and photon energies $k = [20, 900]$ GeV. However, the GPDs presented in this

work are modeled to LO in α_s only, and NLO calculations such as the inclusion of gluon GPDs are not taken into account. In p–Pb, the photon flux from lead nuclei is enhanced by a factor Z^2 with respect to that of the proton in pp collisions, hence higher cross sections are expected.

However, applying a θ cutoff is necessary to ensure that the two processes are of the same order of magnitude, and the processes are currently measured integrated over θ where the BH contribution is largely dominant. Measuring the θ angle is not a trivial task. In ALICE, the main limitation of the apparatus is the angular resolution of the muons behind the absorber is a limitation of the apparatus. For the same reason, the measurement of angular asymmetry between the two muons is limited.

Moreover, measuring the proton momentum with sufficient precision is challenging because of the dispersion of the angle of incoming protons in a bunch at the IP. When protons are accelerated using electric fields fed into Radio-Frequency (RF) cavities (resonators tuned to a selected frequency), magnetic fields alternatively focus and de-focus the proton beam in one direction or the other in the transverse plane. The outgoing proton direction is accessible from the momentum direction of the dileptons. The transverse momentum of the dileptons must be sufficiently large to measure the momentum direction of the dileptons precisely, while being small enough not to be in the background (with inclusive and dissociative events).

With the installation for Run 3 of the Muon Forward Tracker (MFT), a new high resolution Si-tracking detector installed in front of the muon spectrometer, the resolution is expected to increase significantly (less than 100 µm in spatial resolution) [24], which may help in measuring the angular asymmetries of the lepton pair.

5.2 Cross sections for J/ψ photoproduction off protons

As we saw in section 1.4.3, the measurement of J/ψ photoproduction, in an elastic or dissociative process, presents complementary interests to unveil the proton structure and, in particular, the behavior of gluons at low Bjorken-x.

The exclusive J/ψ photoproduction allows for the study of the gluon distribution in protons, since its cross section scales with the square of the gluon PDF in the target proton, according to LO QCD calculations[1] [26]. At high $W_{\gamma p}$ energies, a reduction in the growth rate of the exclusive J/ψ photoproduction cross section would indicate that non-linear terms must be taken into account in QCD calculations. These non-linearities are expressed as gluon recombinations which tame the growth of gluon distributions, and are commonly referred to as gluon saturation [27] (see section 1.3.2).

On the other hand, J/ψ diffractive photoproduction off protons with proton dissociation is a scattering event that produces a single J/ψ vector meson and, separated by a rapidity gap, remnants of the dissociated proton. In a LO pQCD calculation, this process is a direct measurement of the fluctuations of the initial state configurations of the target proton [28–30]. These fluctuations should evolve in the center-of-mass energy of the virtual photon-proton scattering, $W_{\gamma p}$. At sufficiently large energies, in the CGC framework, the gluon saturation at small x would result in the so-called black disc limit where event-by-event fluctuations are suppressed. Several models exist where the cross section of dissociative J/ψ photoproduction could either continue rising at high $W_{\gamma p}$ [29] or vanish [30].

Moreover, measuring the ratio of the dissociative and exclusive cross sections provide another powerful tool to study gluon saturation, since it is expected to vanish at high energies, owing to the onset of gluon saturation at sufficiently small x [29–31].

This section presents the computation of cross sections, then it introduces several previous measurements and theoretical predictions. The measurements presented here are then compared with previous ones and the aforementioned predictions. Finally, results are discussed with limitations of the measurements and possible enhancements in the future.

5.2.1 Calculation of cross sections

The cross sections corresponding to exclusive and dissociative J/ψ photoproduction off protons are obtained using

$$\frac{\mathrm{d}\sigma}{\mathrm{d}y}(\mathrm{p}+\mathrm{Pb}\to\mathrm{p}+\mathrm{Pb}+\mathrm{J}/\psi) = \frac{N_{\mathrm{J}/\psi}}{(A\times E)_{\mathrm{J}/\psi}\cdot\mathcal{L}\cdot\epsilon_{\mathrm{veto}}\cdot BR\cdot\Delta y} \tag{5.7}$$

where $N_{\mathrm{J}/\psi}$ is the number of reconstructed exclusive or dissociative J/ψ in the dimuon decay channel, $(A\times E)_{\mathrm{J}/\psi}$ is the factor of acceptance and reconstruction efficiency in the corresponding rapidity bin studied and for $2.5 < M_{\mu\mu} < 3.5$ GeV/c^2, and $BR = (5.961 \pm 0.033)\%$ is the branching ratio for the J/ψ decay into a muon pair [32].

In order to compare these measurements to existing ones, we refer to the interaction system γp rather than p–Pb. The cross section $\mathrm{d}\sigma/\mathrm{d}y(\mathrm{p}+\mathrm{Pb}\to\mathrm{p}+\mathrm{Pb}+\mathrm{J}/\psi)$ is related to the γp cross

[1] Recent studies at NLO [25] however show that one might be sensitive to both gluon and quark PDFs instead.

section $\sigma(\gamma + \mathrm{p} \to \mathrm{J}/\psi + \mathrm{p}/X)$ through the photon flux $k\,\mathrm{d}n/\mathrm{d}k$:

$$\frac{\mathrm{d}\sigma}{\mathrm{d}y}(\mathrm{p} + \mathrm{Pb} \to \mathrm{p}/X + \mathrm{Pb} + \mathrm{J}/\psi) = k\frac{\mathrm{d}n}{\mathrm{d}k}\sigma(\gamma + \mathrm{p} \to \mathrm{J}/\psi + \mathrm{p}/X) \tag{5.8}$$

where p/X is either the outgoing proton that remained intact or that dissociated, and k is the photon energy, determined by the J/ψ mass and rapidity: $k = (1/2)M_{\mathrm{J}/\psi}\exp(-y)$. The photon flux is calculated using STARlight, as described in section 4.4.2.

The cross sections $\sigma^{\mathrm{exc}}_{\mathrm{J}/\psi} \equiv \sigma(\gamma + \mathrm{p} \to \mathrm{J}/\psi + \mathrm{p})$ and $\sigma^{\mathrm{diss}}_{\mathrm{J}/\psi} \equiv \sigma(\gamma + \mathrm{p} \to \mathrm{J}/\psi + X)$ are listed in table 5.2, along with the average of the $\gamma\mathrm{p}$ center-of-mass energy weighted by the product of the photon spectrum and the cross section $\sigma(\gamma\mathrm{p})$ from STARlight, $\langle W_{\gamma\mathrm{p}}\rangle$.

Rapidity range	$W_{\gamma\mathrm{p}}$ range (GeV)	$\langle W_{\gamma\mathrm{p}}\rangle$ (GeV)	$\sigma^{\mathrm{exc}}_{\mathrm{J}/\psi}$ (nb)	$\sigma^{\mathrm{diss}}_{\mathrm{J}/\psi}$ (nb)
$2.50 < y < 4.00$	$27 < W_{\gamma\mathrm{p}} < 57$	39.9	$40.4 \pm 2.9 \pm 2.5$	$51.8 \pm 2.8 \pm 7.2$
$2.50 < y < 3.25$	$39 < W_{\gamma\mathrm{p}} < 57$	47.7	$48.5 \pm 4.2 \pm 3.1$	$59.3 \pm 4.2 \pm 8.4$
$3.25 < y < 4.00$	$27 < W_{\gamma\mathrm{p}} < 39$	32.8	$33.7 \pm 1.7 \pm 2.5$	$43.8 \pm 3.1 \pm 6.3$

Table 5.2: Cross sections for exclusive and dissociative J/ψ photoproduction off protons in $\gamma\mathrm{p}$ interactions. The corresponding J/ψ photoproduction cross sections in bins of $W_{\gamma\mathrm{p}}$ are also presented.

Both cross sections $\sigma^{\mathrm{diss}}_{\mathrm{J}/\psi}$ and $\sigma^{\mathrm{exc}}_{\mathrm{J}/\psi}$ rise with $W_{\gamma\mathrm{p}}$ and are of similar size.

The measurements for the ratio of dissociative to exclusive J/ψ photoproduction cross sections, $\sigma^{\mathrm{diss}}_{\mathrm{J}/\psi}/\sigma^{\mathrm{exc}}_{\mathrm{J}/\psi}$, are given in table 5.3.

Rapidity range	$W_{\gamma\mathrm{p}}$ range (GeV)	$\langle W_{\gamma\mathrm{p}}\rangle$ (GeV)	$\sigma^{\mathrm{diss}}_{\mathrm{J}/\psi}/\sigma^{\mathrm{exc}}_{\mathrm{J}/\psi}$
$2.50 < y < 4.00$	$27 < W_{\gamma\mathrm{p}} < 57$	39.9	$1.27 \pm 0.15 \pm 0.10$
$2.50 < y < 3.25$	$39 < W_{\gamma\mathrm{p}} < 57$	47.7	$1.21 \pm 0.18 \pm 0.10$
$3.25 < y < 4.00$	$27 < W_{\gamma\mathrm{p}} < 39$	32.8	$1.29 \pm 0.23 \pm 0.11$

Table 5.3: Ratio of dissociative to exclusive J/ψ photoproduction cross sections in ultra-peripheral p–Pb collisions at $\sqrt{s_{\mathrm{NN}}} = 8.16$ TeV. The first errors are the statistical uncertainties, and the second errors are the systematic uncertainties.

The two cross sections $\sigma^{\mathrm{diss}}_{\mathrm{J}/\psi}$ and $\sigma^{\mathrm{exc}}_{\mathrm{J}/\psi}$ are of similar sizes since their ratio is close to 1. In the studied $W_{\gamma\mathrm{p}}$ range, the black disk regime of saturated gluons, which would manifest as a strong reduction of the ratio, is not achieved.

5.2.2 Previous measurements of J/ψ photoproduction

Fixed target experiments E401, E516 and E687 at Fermilab

In the 1980's and 1990's, several fixed target experiments have measured the exclusive J/ψ photoproduction off protons at low $W_{\gamma\mathrm{p}}$, notably E401 [33], E516 [34] and E687 [35] at Fermilab. They used a high energy photon beam, with energies ranging from 60 to 300 GeV, to interact with the detector material and detect recoil protons target fragments. The J/ψ is then measured

in either its e^+e^- or $\mu^+\mu^-$ decay channel, and the measured $W_{\gamma p}$ energies ranged from $\sim$ 13 GeV to $\sim$ 30 GeV.

H1 and ZEUS at HERA

The first measurements of J/ψ photoproduction in a collider experiment were carried with beams of protons and electrons (e^-p), positrons (e^+p), protons (pp) or anti-protons ($p\bar{p}$). The ZEUS experiment measured the exclusive J/ψ photoproduction in the process $\gamma + p \to J/\psi + p$, using beams of positrons and protons (e^+p) [36], at center-of-mass energies of the γp system of $20 < W_{\gamma p} < 290$ GeV. The J/ψ mesons were reconstructed both in their dielectron and dimuon channels. They measured the J/ψ photoproduction cross section as a function of $W_{\gamma p}$, and observed a steep rise of the cross section $\sigma(\gamma p \to J/\psi p)$ with increasing $W_{\gamma p}$.

The H1 experiment also measured the exclusive J/ψ photoproduction off protons, in electron-proton collisions at HERA. The energy range probed by H1 was firstly $40 < W_{\gamma p} < 305$ GeV and a more precise measurement was performed at $25 < W_{\gamma p} < 110$ GeV [37, 38]. The J/ψ mesons were also reconstructed both in their dielectron and dimuon channels. In addition to the exclusive J/ψ photoproduction, the proton-dissociative photoproduction was measured, where the proton dissociates to a system of remnants X of mass $M_p < M_X < 10$ GeV where M_p is the proton mass [38].

ALICE at the LHC

ALICE measured the exclusive J/ψ photoproduction in p–Pb at $\sqrt{s_{NN}} = 5.02$ TeV [39, 40], at forward, backward, semi-forward, and semi-backward rapidity, and at mid-rapidity, covering an energy range $21 < W_{\gamma p} < 952$ GeV. At mid-rapidity ($-2.5 < y < 2.7$), the J/ψ mesons are reconstructed in their e^+e^- and $\mu^+\mu^-$ decay channels, corresponding to an energy in the γp center-of-mass in the interval $40 < W_{\gamma p} < 550$ GeV. At forward and backward rapidity ($2.5 < y < 4.0$ and $-4.0 < y < 2.5$ respectively), they are reconstructed in the dimuon decay channel in an analysis similar to the one presented here, where the forward and backward configurations are obtained by switching the directions of the proton and lead beams. The corresponding energy ranges achieved were $21 < W_{\gamma p} < 45$ GeV ($4 \times 10^{-3} < x < 2 \times 10^{-2}$) and $577 < W_{\gamma p} < 952$ GeV ($1 \times 10^{-5} < x < 3 \times 10^{-5}$). Finally, the semi-forward (semi-backward) rapidity regions correspond to one muon detected in the central barrel of ALICE at mid-rapidity, and one in the muon spectrometer at forward (backward) rapidity.

LHCb at the LHC

LHCb measured the exclusive J/ψ photoproduction cross sections in pp collisions, at $\sqrt{s_{NN}}$ = 7 TeV [41, 42] and 13 TeV [43]. The 13 TeV LHCb data allow reaching center-of-mass energies $W_{\gamma p}$ of almost 2 TeV. The J/ψ mesons are reconstructed via the dimuon decays in the pseudo-rapidity range $2.0 < \eta < 4.5$. However, since a symmetric collision system is used, each of the protons may act as a photon source or as a target and the data suffer from the intrinsic impossibility of identifying the photon emitter and the photon target. Consequently, the rapidity of the J/ψ may have positive or negative sign in each event, leading to an ambiguous determination of the energy $W_{\gamma p}$. The low-energy (W^-) and high-energy components (W^+) are present in the data together, and each of the two contributions was extracted in a model-dependent approach by postulating the power law results from H1 for the other. Moreover, the uncertainty in the

hadronic survival probability in pp collisions is much larger than in p–Pb collisions, and samples of pp collisions can contain a contamination of J/ψ production through Odderon-Pomeron fusion [44, 45].

5.2.3 Description of some theoretical models of J/ψ photoproduction

The JMRT model

The JMRT group [46, 47] (S.P. Jones, A.D. Martin, M.G. Ryskin and T. Teubner) provided two calculations based on pQCD : the first one is a LO calculation, while the second one includes contributions which mimic effects expected from the dominant NLO corrections.

Let us recall the cross section corresponding to LO at zero momentum transfer, $t = 0$, at the vertex of the proton [26]:

$$\left.\frac{\mathrm{d}\sigma}{\mathrm{d}t}(\gamma \mathrm{p} \to \mathrm{J}/\psi \mathrm{p})\right|_{t=0} = \frac{\Gamma_{ee} M_{\mathrm{J}/\psi}^3 \pi^3}{48\alpha} \left[\frac{\alpha_s(\bar{Q}^2)}{\bar{Q}^4}(xg(x,\bar{Q}^2)\right]^2 \left(1 + \frac{Q^2}{M_{\mathrm{J}/\psi}}\right) \tag{5.9}$$

with

$$\bar{Q}^2 = (Q^2 + M_{\mathrm{J}/\psi}^2)/4 \text{ and } x = (Q^2 + M_{\mathrm{J}/\psi}^2)/(W_{\gamma\mathrm{p}}^2 + Q^2) \tag{5.10}$$

where Q^2 is the virtuality of the photon, Γ_{ee} is the width of the dielectron decay, $M_{\mathrm{J}/\psi}$ is the rest mass of the J/ψ, α_s is the strong coupling constant, $xg(x, Q^2)$ is the gluon PDF, and $W_{\gamma\mathrm{p}}$ is the center-of-mass energy of the photon-proton system.

At LO, the following simple formula is used:

$$xg(x,\mu^2) = Nx^{-\lambda} \text{ and } \lambda = a + b\ln(\mu^2/0.45\ \mathrm{GeV}^2) \tag{5.11}$$

where N, a and b are free parameters determined by a non-linear χ^2 fit to the exclusive J/ψ data from HERA and LHCb (Run 1).

For the calculation including the dominant NLO effects, the gluon PDF uses a parametrization which explicitly includes the double logarithmic factor coming from the summation of the leading $(\alpha_s \ln(1/x) \ln \mu^2)^n$ contributions to account for the effect of the running of α_s in the DGLAP evolution (section 1.3.1) :

$$xg(x,\mu^2) = Nx^{-a}(\mu^2)^b \exp(\sqrt{16N_c/\beta_0 \ln(1/x)\ln(G)}) \text{ with } G = \frac{\ln(\mu^2/\Lambda_{\mathrm{QCD}}^2)}{\ln(Q_0^2/\Lambda_{\mathrm{QCD}}^2)} \tag{5.12}$$

where $N_c = 3$ is the number of colors and Q_0 is the infrared scale taken as $Q_0 = 1$ GeV. Again, N, a, and b are free parameters determined by a non-linear χ^2 fit to the exclusive J/ψ data from HERA and LHCb (Run 1).

Both LO and NLO calculations result in a deviation of the energy-dependence cross section from a simple power-law shape at high $W_{\gamma\mathrm{p}}$.

The CCT model

The CCT model [30], named after J. Cepila, J.G. Contreras and J. D. Takaki, is based on the color dipole approach (see section 1.4.2 for an introduction).

According to the color dipole model, the photon fluctuates into a quark-antiquark pair, which then interacts with the target with the cross section of the color dipole σ_{dip} and finally the dipole forms a vector meson.

The cross section of the interaction of the color dipole and the target σ_{dip} incorporates a term $T(\vec{b})$ which describes the profile of the proton in the plane of the impact parameters $\vec{b}$ and includes the quantum fluctuations of the proton from one interaction to another. The proton profile is defined as the sum of N_{hs} regions with high gluon density [48, 49], called *hot spots*. Each hot spot has a Gaussian profile:

$$T(\vec{b}) = \frac{1}{N_{hs}} \sum_{i=1}^{N_{hs}} T_{hs}(\vec{b} - \vec{b_i}) \text{ with } T_{hs}(\vec{b} - \vec{b_i}) = \frac{1}{2\pi B_{hs}} e^{-\frac{(\vec{b}-\vec{b_i})^2}{2B_{hs}}} \tag{5.13}$$

where each $\vec{b_i}$ is obtained from a two-dimensional Gaussian distribution centered at $(0, 0)$ and with a width B_p. The number of hot spots N_{hs} increases with the number of gluons available for the next interaction

$$N_{hs}(x) = p_0 x^{p_1}(1 + p_2\sqrt{x}) \tag{5.14}$$

where the parameters p_0, p_1 and p_2 are obtained from a fit to the dissociative J/ψ photoproduction measured by H1. Thus the number of hot spots increases with decreasing x. This hallmark of the theory implements the assumption that at a given scale Q^2, as the energy increases, the number of gluons available for interaction increases. This feature of the model implies an indirect dependence of the profile of the proton $T(\vec{b})$ on the energy.

Moreover, the model predicts that for $W_{\gamma p} \approx 500$ GeV, the dissociative cross section J/ψ reaches a maximum and then decreases sharply with energy, while the ratio of dissociative to exclusive cross sections vanishes at high $W_{\gamma p}$ where the gluon saturation regime is expected.

The MS model

The model calculated by H. Mäntysaari and B. Schenke (MS) [50] is based on the perturbative JIMWLK (Jalilian-Marian-Iancu-McLerran-Weigert-Leonidov-Kovner) evolution equation [51–54] (see section 1.3.2), with initial parameters constrained to fits to H1 data starting from $x \sim 10^{-3}$. The profile of the proton is modeled with a sum of three randomly positioned hot spots, each of them modeled with a Gaussian function. Parameters fitted to H1 data are the width of such Gaussian functions and another parameter describing how far from each other they are sampled on average.

As a result of the JIMWLK evolution, the proton becomes smoother on long-length scales, which is expected since the emission of more gluons would wash out the initial hot spot structure. This also results in a decreasing ratio of dissociative to exclusive cross sections with $W_{\gamma p}$, while the dissociative cross section increases with increasing $W_{\gamma p}$.

5.2.4 Discussion of the results

Exclusive J/ψ photoproduction

Figure 5.5 shows the new ALICE measurements for the exclusive J/ψ photoproduction cross section $\sigma(\gamma + \mathrm{p} \rightarrow \mathrm{J}/\psi + \mathrm{p})$ as a function of $W_{\gamma\mathrm{p}}$, covering the range $27 < W_{\gamma\mathrm{p}} < 57$ GeV. Comparisons to previous measurements and to the theoretical models described above are also shown.

Both LO and NLO JMRT calculations have been fitted to the same data (HERA and LHCb Run 1 measurements) and their energy dependence is rather similar, so only the NLO version is shown. ALICE measurements at $\sqrt{s_{\mathrm{NN}}} = 5.02$ TeV and this new measurement at $\sqrt{s_{\mathrm{NN}}} = 8.16$ TeV support their extracted gluon distribution up to $x \sim 2 \times 10^{-5}$, however the calculation uses parametrizations for the gluon distribution determined by the experimental data. The CCT model seems to under-estimate the cross sections at high $W_{\gamma\mathrm{p}}$, though it remains in reasonable agreement with the data.

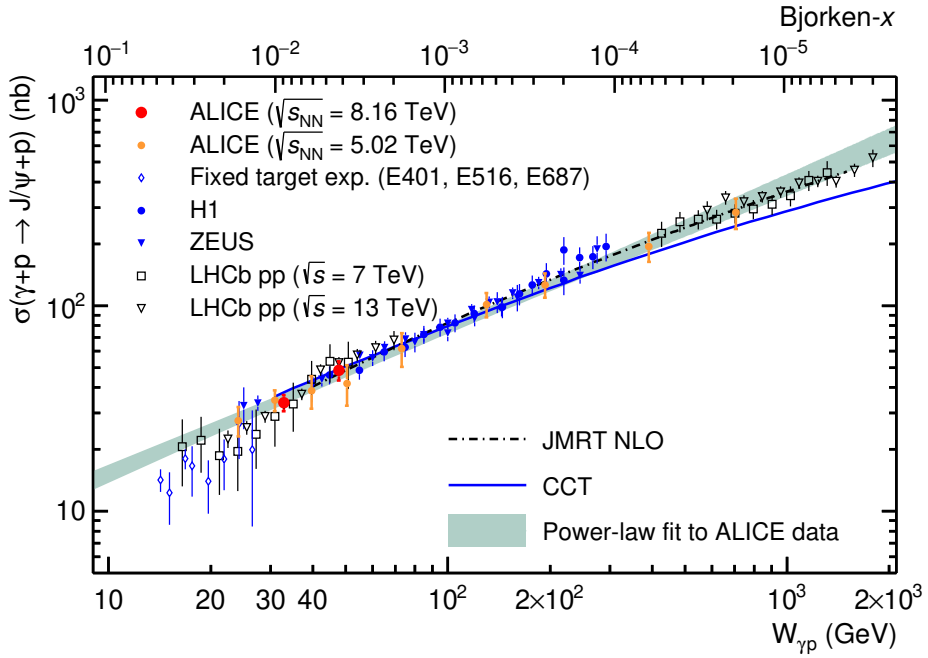

Figure 5.5: Exclusive J/ψ photoproduction cross section off protons measured as a function of the center-of-mass energy of the photon–proton system $W_{\gamma\mathrm{p}}$ by ALICE and compared to previous measurements and to next-to-leading-order JMRT and CCT models. The power law fit to ALICE data is also shown. The uncertainties are the quadratic sum of the statistical and systematic uncertainties. The upper horizontal axis is marked in values of the Bjorken-x, which is given as $x = (M_{\mathrm{J}/\psi}/W_{\gamma\mathrm{p}})^2$.

For HERA energies, the gluon distribution at low Bjorken-x is well described by a power law in x [55], and the gluon density at the leading order is parametrized as [56]

$$xg(\mu, Q^2) \propto x^{-\lambda} \tag{5.15}$$

where λ a parameter to be determined from the data. The skewness effects[2] are neglected in

[2]In the interaction, the two exchanged gluons carry different fractions $x - \xi$ and $x + \xi$ where ξ is the

the present formula. As discussed in section 1.4.3, $\sigma(W_{\gamma p})$ is proportional to the square of the gluon PDF in the proton [26]. This implies that the cross section $\sigma(W_{\gamma p})$ will also follow a power law. Hence, the elastic cross section of $\gamma p \rightarrow J/\psi p$ is parametrized by the empirical power law proportionality

$$\sigma(W_{\gamma p}) = N \left(\frac{W_{\gamma p}}{W_0} \right)^{\delta} \tag{5.16}$$

When extrapolated to lower x values, the equation 5.15 shows an increase of the number of gluons with decreasing momentum fraction, until the expected saturation regime is reached, taming the fast growth of the gluon density. Hence, the onset of gluon saturation would present itself by a deflection from equation 5.15 and consequently the elastic photoproduction cross section would move into a lower value of the δ parameter in the power law dependency.

A χ^2-fit of a power law function $N(W_{\gamma p}/W_0)^{\delta}$ is performed to the full set of ALICE data, combining data at $\sqrt{s_{NN}} = 5.02$ TeV and $\sqrt{s_{NN}} = 8.16$ TeV, with $W_0 = 90.0$ GeV as was done before in HERA analyses [38] and in previous ALICE measurements [40]. The fit uses the quadratic sum of statistical and systematical errors, treating the systematical errors as uncorrelated. The parameters obtained by the fit are $N = 71.6 \pm 3.6$ nb and $\delta = 0.70 \pm 0.04$ with a correlation of $+0.16$ between both parameters. The quality of the fit is χ^2/ndf = 1.62 for 9 degrees of freedom. The value of the exponent δ is the same as in previous ALICE measurements at $\sqrt{s_{NN}} = 5.02$ TeV considering forward, semi-forward and mid-rapidity data [40], thus the new ALICE measurements at $\sqrt{s_{NN}} = 8.16$ TeV validate previous results. The H1 and ZEUS collaborations measurements, performed over an energy range $W_{\gamma p}$ that encompasses the new ALICE measurements, are also shown in the same figure. They found $\delta = 0.67 \pm 0.03$ (stat. + syst.) [36–38], which is compatible with the value measured by ALICE.

The ALICE measurements at $\sqrt{s_{NN}} = 5.02$ TeV at the highest energies and LHCb measurements show no deviation from a power law to about $W_{\gamma p} \sim 2$ TeV, where the gluon distribution is probed down to $x \sim 3 \times 10^{-6}$. Therefore, no change in gluon behavior in this energy range is observed. However, LHCb results are model-dependent, and new precise data at high energies with a clearly identified photon emitter could provide more conclusive statements.

Dissociative J/ψ photoproduction

Figure 5.6 shows the new measurements for the dissociative J/ψ photoproduction cross section $\sigma(\gamma + p \rightarrow J/\psi + X)$ as a function of $W_{\gamma p}$, covering the range $27 < W_{\gamma p} < 57$ GeV. Previous measurements by H1 [38] are also shown at similar energies, with which ALICE measurements are in good agreement. In addition, the CCT model, discussed in the previous section, is shown. It describes correctly the energy evolution of the dissociative cross section both for H1 and ALICE measurements, and predicts that the cross section will reach a maximum at $W_{\gamma p} \simeq 500$ GeV, then turn around and decrease for higher energies. This behavior is produced by the hot spots saturating the proton area.

skewness parameter. See reference [21] for a precise definition of the skewness.

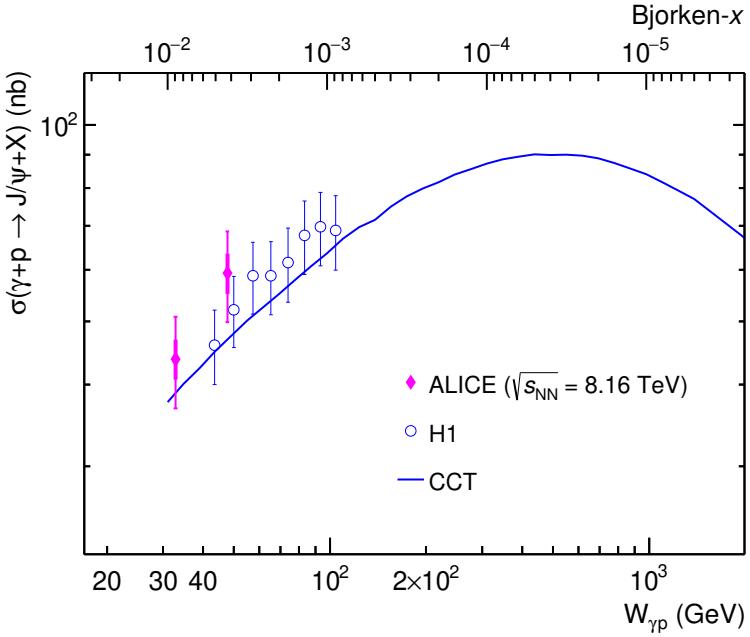

Figure 5.6: Dissociative J/ψ photoproduction cross section off protons measured by ALICE and compared to H1 data. Comparison to CCT model [30] is shown. For ALICE data points, the thick line represents the statistical error while the thin line is the sum in quadrature of statistical and systematic uncertainties.

Ratio of dissociative to exclusive J/ψ photoproduction

The measurements for the ratio of dissociative to exclusive J/ψ photoproduction cross sections, $\sigma(\gamma + p \to J/\psi + X)/\sigma(\gamma + p \to J/\psi + p)$, are shown in figure 5.7 as a function of $W_{\gamma p}$, together with the measurements by H1 [38] at similar energies. Two models are compared with the measurements: the CCT and MS models, described in section 5.2.3. In the framework of these models, the exclusive cross section is sensitive to the average interaction of the color dipole $q\bar{q}$ with the proton, and the dissociative cross section is sensitive to the fluctuations in the $q\bar{q}$-proton interaction between the different color field configurations of the proton. At high $W_{\gamma p}$ where the gluon saturation regime is expected, both models predict that the ratio of dissociative to exclusive cross sections vanishes.

5.2.5 Discussion and outlook

The t-slope dependence of the exclusive J/ψ cross section was measured by H1, using the relation $t \approx -p_T^2$ valid for collider kinematics and with an unfolding procedure that includes detector efficiency corrections and migration effects [38]. As explained in the first chapter, section 1.4.3, the t slope is of great interest because it directly measures the size of the proton. The trajectories of charged particles are measured in H1 with a transverse momentum resolution of $\sigma(p_T)/p_T \approx 0.2\%$. As shown in section 4.2.1, in the ALICE muon spectrometer, the invariant mass resolution of dimuons is about 72 MeV/c^2 at the J/ψ peak mass region, hence a relative mass resolution of $\sigma(M_{\mu\mu})/M_{\mu\mu} \approx 2.3\%$. The dimuon p_T resolution Δp_T is related to the mass

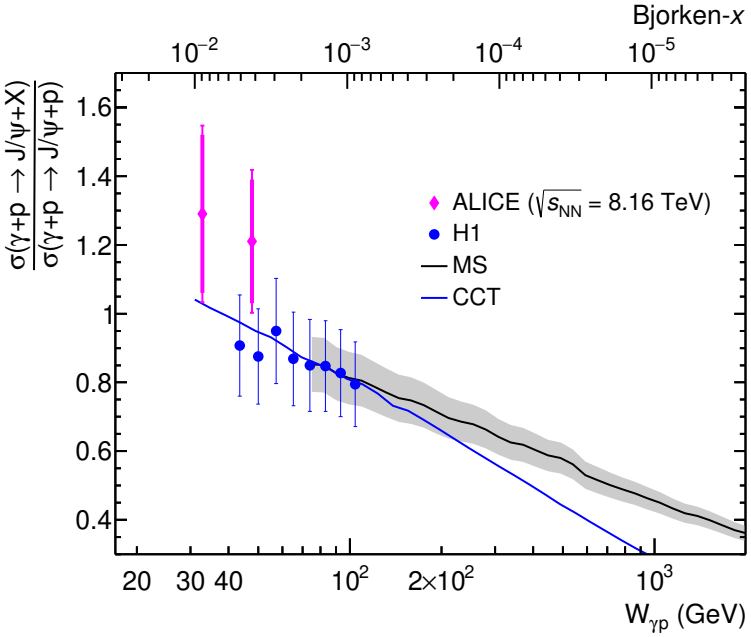

Figure 5.7: Ratio of dissociative to exclusive J/ψ photoproduction cross sections as measured by ALICE and compared to H1 measurements. For ALICE data points, the thick line represents the statistical error while the thin line is the sum in quadrature of statistical and systematic uncertainties. The experimental uncertainties for H1 data are computed assuming completely independent uncertainties for the exclusive and dissociative cross sections. The measurements are compared to the CCT model [30] and a model calculated by H. Mäntysaari and B. Schenke (MS) [50].

resolution via the relation

$$\Delta p_{\mathrm{T}} = \Delta M_{\mu\mu}/\sqrt{2} \tag{5.17}$$

so the relative resolution of $M_{\mu\mu}$ and p_{T} is the same and $\sigma(p_{\mathrm{T}})/p_{\mathrm{T}} \approx 2.3\%$ in the ALICE muon spectrometer. Due to this modest p_{T} resolution, notably due to the fact that the ALICE detector was designed to measure muons from heavy ion collisions behind a thick absorber, clean measurements of the t slope could not be achieved. On the other hand, this measurement is possible at mid-rapidity in the central barrel of ALICE where the resolution is much better and was performed in Pb–Pb UPCs [57].

The complementary measurement at backward rapidity (Pb–p), in which the orientation of the proton and lead beams are reversed, is still in progress. This configuration corresponds to large center-of-mass energies in the photon-proton system, $W_{\gamma\mathrm{p}}$, ranging up to $\sim$ 1500 GeV, and could be sensitive to gluon saturation. Moreover, the energy range probed is similar to the measurements performed by LHCb in pp collisions with Run 1 and Run 2 data. Since their results are model-dependent, a comparison with measurements which unambiguously identify the photon source is of great interest. Unfortunately, it is not yet clear if this measurement is feasible, since the trigger used in this data set requires different vetoes as in the present analysis and veto efficiencies might differ.

The Run 3 data, which is planned to start this year, should make it possible to greatly increase the luminosity and further significantly increase the accessible $W_{\gamma\mathrm{p}}$ energies [58]. During Run 3 in p–Pb UPCs, 260,000 J/ψ are expected to be produced with a photon from the lead scat-

tering off the proton in the forward region of ALICE, i.e., in the muon spectrometer coverage, for a net luminosity of 1000 nb^{-1}.

5.3 Summary

This chapter presented measurements performed using ALICE data from Run 2 at $\sqrt{s_{\text{NN}}} = 8.16$ TeV. First, the measurement of exclusive dimuon production in two-photon interactions was presented in the previously unexplored invariant mass range from 1.0 to 2.5 GeV/c^2. The results were compared with LO QED calculations from STARlight, and agree within 3 σ. In a second part, the J/ψ measurement was discussed. The exclusive process was compared to previous measurements of the same kind and to models. The ALICE measurements are consistent with a power-law dependence $\sigma(\gamma\text{p} \to \text{J}/\psi p) \sim W^{\delta}_{\gamma\text{p}}$, with $\delta = 0.70 \pm 0.04$, thus indicating no significant change in the behavior of this cross section between HERA and LHC energies. The dissociative process, performed for the first time at the LHC, is compared to H1 measurements and to models as well. This measurement is a proof of concept that other measurements of dissociative processes could be performed in the future, with the data from the LHC Run 3 and Run 4 where a large increase on the number of recorded events is expected [58].

Bibliography

[1] Wangmei Zha and Zebo Tang. Discovery of higher-order quantum electrodynamics effect for the vacuum pair production. *JHEP*, 08:083, 2021. doi: 10.1007/JHEP08(2021)083. URL https://doi.org/10.1007/JHEP08(2021)083.

[2] K. Hencken, E. A. Kuraev, and V. Serbo. Exclusive and inclusive muon pair production in collisions of relativistic nuclei. *Phys. Rev. C*, 75:034903, 2007. doi: 10.1103/PhysRevC.75.034903.

[3] A. J. Baltz. Higher Order QED Calculation of Ultrarelativistic Heavy Ion Production of mu+ mu- Pairs. *Phys. Rev. C*, 80:034901, 2009. doi: 10.1103/PhysRevC.80.034901.

[4] A. J. Baltz. The Physics of Ultraperipheral Collisions at the LHC. *Phys. Rept.*, 458:1–171, 2008. doi: 10.1016/j.physrep.2007.12.001.

[5] Mark Strikman, Ramona Vogt, and Sebastian N. White. Probing small x parton densities in ultraperipheral AA and pA collisions at the LHC. *Phys. Rev. Lett.*, 96:082001, 2006. doi: 10.1103/PhysRevLett.96.082001.

[6] E. Abbas et al. Charmonium and e^+e^- pair photoproduction at mid-rapidity in ultra-peripheral Pb–Pb collisions at $\sqrt{s_{\rm NN}} = 2.76$ TeV. *Eur. Phys. J. C*, 73(11):2617, 2013. doi: 10.1140/epjc/s10052-013-2617-1.

[7] Albert M Sirunyan et al. Observation of Forward Neutron Multiplicity Dependence of Dimuon Acoplanarity in Ultraperipheral Pb–Pb Collisions at $\sqrt{s_{\rm NN}} = 5.02$ TeV. *Phys. Rev. Lett.*, 127(12):122001, 2021. doi: 10.1103/PhysRevLett.127.122001.

[8] Morad Aaboud et al. Observation of centrality-dependent acoplanarity for muon pairs produced via two-photon scattering in Pb+Pb collisions at $\sqrt{s_{\rm NN}} = 5.02$ TeV with the ATLAS detector. *Phys. Rev. Lett.*, 121(21):212301, 2018. doi: 10.1103/PhysRevLett.121.212301.

[9] Measurement of non-exclusive dimuon pairs produced via $\gamma\gamma$ scattering in Pb+Pb collisions at $\sqrt{s_{\rm NN}} = 5.02$ TeV with the ATLAS detector. 11 2019.

[10] S. Afanasiev et al. Photoproduction of J/ψ and of high mass e^+e^- in ultra-peripheral Au+Au collisions at $\sqrt{s_{\rm NN}} = 200$ GeV . *Phys. Lett. B*, 679:321–329, 2009. doi: 10.1016/j.physletb.2009.07.061.

[11] J. Adams et al. Production of e^+e^- pairs accompanied by nuclear dissociation in ultra-peripheral heavy ion collision. *Phys. Rev. C*, 70:031902, 2004. doi: 10.1103/PhysRevC.70.031902.

[12] Jaroslav Adam et al. Measurement of e^+e^- Momentum and Angular Distributions from Linearly Polarized Photon Collisions. *Phys. Rev. Lett.*, 127(5):052302, 2021. doi: 10.1103/PhysRevLett.127.052302.

[13] Jaroslav Adam et al. Low-p_T e^+e^- pair production in Au+Au collisions at $\sqrt{s_{NN}}$ = 200 GeV and U+U collisions at $\sqrt{s_{NN}}$ = 193 GeV at STAR. *Phys. Rev. Lett.*, 121(13):132301, 2018. doi: 10.1103/PhysRevLett.121.132301.

[14] Georges Aad et al. Exclusive dimuon production in ultraperipheral Pb+Pb collisions at $\sqrt{s_{\mathrm{NN}}} = 5.02$ TeV with ATLAS. 11 2020.

[15] Dielectron production at midrapidity at low transverse momentum in peripheral and semi-peripheral Pb−Pb collisions at $\sqrt{s_{\mathrm{NN}}} = 5.02$ TeV. 4 2022.

[16] C. F. von Weizsacker. Radiation emitted in collisions of very fast electrons. *Z. Phys.*, 88: 612–625, 1934. doi: 10.1007/BF01333110.

[17] E. J. Williams. Correlation of certain collision problems with radiation theory. *Kong. Dan. Vid. Sel. Mat. Fys. Med.*, 13N4(4):1–50, 1935.

[18] Spencer R. Klein. e+ e- pair production from 10-GeV to 10-ZeV. *Radiat. Phys. Chem.*, 75: 696–711, 2006. doi: 10.1016/j.radphyschem.2005.09.005.

[19] Spencer Klein and Joakim Nystrand. Exclusive vector meson production in relativistic heavy ion collisions. *Phys. Rev.*, C60:014903, 1999. doi: 10.1103/PhysRevC.60.014903.

[20] Spencer R. Klein, Joakim Nystrand, Janet Seger, Yuri Gorbunov, and Joey Butterworth. STARlight: A Monte Carlo simulation program for ultra-peripheral collisions of relativistic ions. *Comput. Phys. Commun.*, 212:258–268, 2017. doi: 10.1016/j.cpc.2016.10.016.

[21] B. Pire, L. Szymanowski, and J. Wagner. Can one measure timelike Compton scattering at LHC? *Phys. Rev. D*, 79:014010, 2009. doi: 10.1103/PhysRevD.79.014010.

[22] Edgar R. Berger, M. Diehl, and B. Pire. Time - like Compton scattering: Exclusive photoproduction of lepton pairs. *Eur. Phys. J. C*, 23:675–689, 2002. doi: 10.1007/s100520200917.

[23] P. Chatagnon et al. First Measurement of Timelike Compton Scattering. *Phys. Rev. Lett.*, 127(26):262501, 2021. doi: 10.1103/PhysRevLett.127.262501.

[24] Technical Design Report for the Muon Forward Tracker. Technical report, Jan 2015. URL https://cds.cern.ch/record/1981898.

[25] Kari J. Eskola, Christopher A. Flett, Vadim Guzey, Topi Löytäinen, and Hannu Paukkunen. Exclusive J/ψ photoproduction in ultraperipheral Pb+Pb collisions at the LHC to next-to-leading order perturbative QCD. 3 2022.

[26] M. G. Ryskin. Diffractive J/ψ electroproduction in LLA QCD. *Z. Phys.*, C57:89–92, 1993. doi: 10.1007/BF01555742.

[27] Astrid Morreale and Farid Salazar. Mining for Gluon Saturation at Colliders. *Universe*, 7 (8):312, 2021. doi: 10.3390/universe7080312.

[28] Hannu I. Miettinen and Jon Pumplin. Diffraction Scattering and the Parton Structure of Hadrons. *Phys. Rev. D*, 18:1696, 1978. doi: 10.1103/PhysRevD.18.1696.

[29] Heikki Mäntysaari. Review of proton and nuclear shape fluctuations at high energy. *Rept. Prog. Phys.*, 83(8):082201, 2020. doi: 10.1088/1361-6633/aba347.

[30] J. Cepila, J. G. Contreras, and J. D. Tapia Takaki. Energy dependence of dissociative J/ψ photoproduction as a signature of gluon saturation at the LHC. *Phys. Lett.*, B766:186–191, 2017. doi: 10.1016/j.physletb.2016.12.063.

[31] D. Bendova, J. Cepila, and J. G. Contreras. Dissociative production of vector mesons at electron-ion colliders. *Phys. Rev. D*, 99(3):034025, 2019. doi: 10.1103/PhysRevD.99.034025.

[32] P. A. Zyla et al. Review of Particle Physics. *PTEP*, 2020(8):083C01, 2020. doi: 10.1093/ptep/ptaa104.

[33] Morris E. Binkley et al. J/ψ Photoproduction from 60 GeV/c to 300 GeV/c. *Phys. Rev. Lett.*, 48:73, 1982. doi: 10.1103/PhysRevLett.48.73.

[34] Bruce Hayes Denby. *Inelastic and Elastic Photoproduction of* J/ψ *(3097)*. PhD thesis, UC, Santa Barbara, 1983.

[35] P. L. Frabetti et al. A Measurement of elastic J/ψ photoproduction cross-section at fermilab E687. *Phys. Lett. B*, 316:197–206, 1993. doi: 10.1016/0370-2693(93)90679-C.

[36] S. Chekanov et al. Exclusive photoproduction of J / ψ mesons at HERA. *Eur. Phys. J. C*, 24:345–360, 2002. doi: 10.1007/s10052-002-0953-7.

[37] A. Aktas et al. Elastic J/ψ production at HERA. *Eur. Phys. J. C*, 46:585–603, 2006. doi: 10.1140/epjc/s2006-02519-5.

[38] C. Alexa et al. Elastic and Proton-Dissociative Photoproduction of J/ψ Mesons at HERA. *The European Physical Journal C*, 73(6):2466, 2013. doi: 10.1140/epjc/s10052-013-2466-y. URL https://doi.org/10.1140/epjc/s10052-013-2466-y.

[39] Betty Abelev et al. Exclusive J/ψ photoproduction off protons in ultra-peripheral p-Pb collisions at $\sqrt{s_{\rm NN}} = 5.02$ TeV. *Phys. Rev. Lett.*, 113(23):232504, 2014. doi: 10.1103/PhysRevLett.113.232504.

[40] Shreyasi Acharya et al. Energy dependence of exclusive J/ψ photoproduction off protons in ultra-peripheral p–Pb collisions at $\sqrt{s_{\rm NN}} = 5.02$ TeV. *Eur. Phys. J. C*, 79(5):402, 2019. doi: 10.1140/epjc/s10052-019-6816-2.

[41] Roel Aaij et al. Updated measurements of exclusive J/ψ and ψ(2S) production cross-sections in pp collisions at $\sqrt{s} = 7$ TeV. *J. Phys. G*, 41:055002, 2014. doi: 10.1088/0954-3899/41/5/055002.

[42] R Aaij et al. Exclusive J/ψ and ψ(2S) production in pp collisions at $\sqrt{s} = 7$ TeV. *J. Phys. G*, 40:045001, 2013. doi: 10.1088/0954-3899/40/4/045001.

[43] Roel Aaij et al. Central exclusive production of J/ψ and $\psi(2S)$ mesons in pp collisions at $\sqrt{s} = 13$ TeV. *JHEP*, 10:167, 2018. doi: 10.1007/JHEP10(2018)167.

[44] T. Aaltonen et al. Observation of exclusive charmonium production and $\gamma+\gamma$ to $\mu^+\mu^-$ in $p\bar{p}$ collisions at $\sqrt{s} = 1.96$ TeV. *Phys. Rev. Lett.*, 102:242001, 2009. doi: 10.1103/PhysRevLett.102.242001.

[45] Alec J. Schramm and Daniel H. Reeves. Production of η mesons in double pomeron exchange. *Phys. Rev. D*, 55:7312–7314, 1997. doi: 10.1103/PhysRevD.55.7312.

[46] S. P. Jones, A. D. Martin, M. G. Ryskin, and T. Teubner. Probes of the small-x gluon via exclusive J/ψ and Υ production at HERA and the LHC. *JHEP*, 11:085, 2013. doi: 10.1007/JHEP11(2013)085.

[47] S. P. Jones, A. D. Martin, M. G. Ryskin, and T. Teubner. Exclusive J/ψ production at the LHC in the k_T factorization approach. *J. Phys. G*, 44(3):03LT01, 2017. doi: 10.1088/1361-6471/aa56ea.

[48] Heikki Mäntysaari and Björn Schenke. Evidence of strong proton shape fluctuations from incoherent diffraction. *Phys. Rev. Lett.*, 117(5):052301, 2016. doi: 10.1103/PhysRevLett.117.052301.

[49] Heikki Mäntysaari and Björn Schenke. Revealing proton shape fluctuations with incoherent diffraction at high energy. *Phys. Rev. D*, 94(3):034042, 2016. doi: 10.1103/PhysRevD.94.034042.

[50] Heikki Mäntysaari and Björn Schenke. Confronting impact parameter dependent JIMWLK evolution with HERA data. *Phys. Rev. D*, 98(3):034013, 2018. doi: 10.1103/PhysRevD.98.034013.

[51] Jamal Jalilian-Marian, Alex Kovner, Larry D. McLerran, and Heribert Weigert. The Intrinsic glue distribution at very small x. *Phys. Rev. D*, 55:5414–5428, 1997. doi: 10.1103/PhysRevD.55.5414.

[52] Jamal Jalilian-Marian, Alex Kovner, Andrei Leonidov, and Heribert Weigert. The BFKL equation from the Wilson renormalization group. *Nucl. Phys. B*, 504:415–431, 1997. doi: 10.1016/S0550-3213(97)00440-9.

[53] Jamal Jalilian-Marian, Alex Kovner, Andrei Leonidov, and Heribert Weigert. The Wilson renormalization group for low x physics: Towards the high density regime. *Phys. Rev. D*, 59:014014, 1998. doi: 10.1103/PhysRevD.59.014014.

[54] Edmond Iancu and Larry D. McLerran. Saturation and universality in QCD at small x. *Phys. Lett. B*, 510:145–154, 2001. doi: 10.1016/S0370-2693(01)00526-3.

[55] F. D. Aaron et al. Combined Measurement and QCD Analysis of the Inclusive e+- p Scattering Cross Sections at HERA. *JHEP*, 01:109, 2010. doi: 10.1007/JHEP01(2010)109.

[56] A. D. Martin, C. Nockles, Mikhail G. Ryskin, and Thomas Teubner. Small x gluon from exclusive J/psi production. *Phys. Lett. B*, 662:252–258, 2008. doi: 10.1016/j.physletb.2008.02.067.

[57] Shreyasi Acharya et al. First measurement of the $|t|$-dependence of coherent J/ψ photonuclear production. *Phys. Lett. B*, 817:136280, 2021. doi: 10.1016/j.physletb.2021.136280.

[58] Z. Citron et al. Report from Working Group 5: Future physics opportunities for high-density QCD at the LHC with heavy-ion and proton beams. *CERN Yellow Rep. Monogr.*, 7:1159–1410, 2019. doi: 10.23731/CYRM-2019-007.1159.

Part II

Development and characterization of a novel structure of micro-pattern gaseous detector reducing ion backflow

Chapter 6

Micro-Pattern Gaseous Detectors as TPC readout systems

Contents

6.1 Time Projection Chambers 140
6.1.1 Operating principle of a Time Projection Chamber 140
6.1.2 Drift and diffusion of particles in the gas of a TPC 141
6.1.3 TPC readout systems and space charge effect 143
6.2 MPGDs as TPC readout systems 144
6.2.1 Electron avalanche in a strong field region 145
6.2.2 MicroMEGAS detectors 145
6.2.3 Gas Electron Multiplier 146
6.2.4 Combinations of MicroMEGAS and GEM detectors 147
6.3 Producing events in a MPGD structure 149
6.3.1 Gas choice 149
6.3.2 Interactions of X-rays in gas and escape peak 149
6.4 Summary 151
Bibliography 152

To understand the behavior of matter at very high energies, particle accelerators have been built. Accelerators can be used in fixed target mode or as colliders, smashing nuclei against each other. Today, the LHC and the RHIC are two of the largest colliders in operation. Several experiments, such as the ALICE experiment at the LHC, which was discussed in the first part of this thesis, bring together a set of detectors that allow the reconstruction of particles produced during collisions. They use a Time Projection Chamber (TPC) as their main particle detection tool [1–3]. Many other experiments of collider physics use TPCs: for example the T2K [4], STAR [5] or sPHENIX [6, 7] experiments. A TPC allows a three-dimensional reconstruction of a charged particle trajectory via the application of a combination of electric and magnetic fields. The active detection volume is contained in the chamber, and the reconstruction of tracks is done via TPC readout systems. There exists many types, and their characteristics and operation are determined by the specifications of the TPC.

This chapter is primarily dedicated to the presentation of the operation of TPCs. Then, the chapter presents Micro-Pattern gaseous detectors (MPGDs), which are suitable detectors for TPC readout. In particular, we focus on two examples of MPGD, namely MICRO MEsh GAseous Structure (MicroMEGAS) and Gas Electron Multiplier (GEM) detectors, and the development of a new type of MPGD which uses these two different structures. The new MPGD structure is the object of study in this part of the thesis. Finally, we discuss the choice of gas in the detector and explain how events are produced using a ^{55}Fe source.

6.1 Time Projection Chambers

6.1.1 Operating principle of a Time Projection Chamber

A Time Projection Chamber (TPC) is a type of particle detector that aims to perform a three-dimensional reconstruction of a charged particle trajectory with a combination of electric and magnetic fields. Its sensitive volume, i.e., the volume in which activity can be detected, is a chamber filled with gas and sometimes liquid. Its invention at the Lawrence Berkeley Laboratory by David R. Nygren, an American physicist, dates back to 1974 [8]. Today, TPCs are still widely used in many particle physics experiments, such as ALICE [1–3], sPHENIX [6, 7], STAR [5] or T2K [4].

In its original design, which remains the most commonly used in experiments at colliders, the TPC is a cylindrical chamber with readout systems as end plates, as represented in figure 6.1 at left. It is the case, for example, of the TPCs of the ALICE or sPHENIX experiments: the chamber is divided in two along its length by means of a central disc which is a high voltage electrode that establishes an electric field between the center and end plates.

The operating principle of a TPC is as follows: a charged particle traversing the chamber collides with the atoms of the gas of the sensitive volume and thus ionizes them along its trajectory. Due to the application of electric fields in the TPC, the ionized electrons drift towards the closest anode, while the ions drift towards the cathode. This situation is represented in figure 6.1 at right. At the anode, the readout systems record the position of the ionized electrons in the transverse plane. The longitudinal coordinate z, i.e. the depth of the primary ionization in the TPC, is obtained by calculating the drift time between the passage of the incident particle and the arrival of the electrons at the readout system. Thus, the longitudinal position is obtained by temporal projection. Moreover, a magnetic field is usually applied along the length of the cylinder in order to measure the momentum of the tracks.

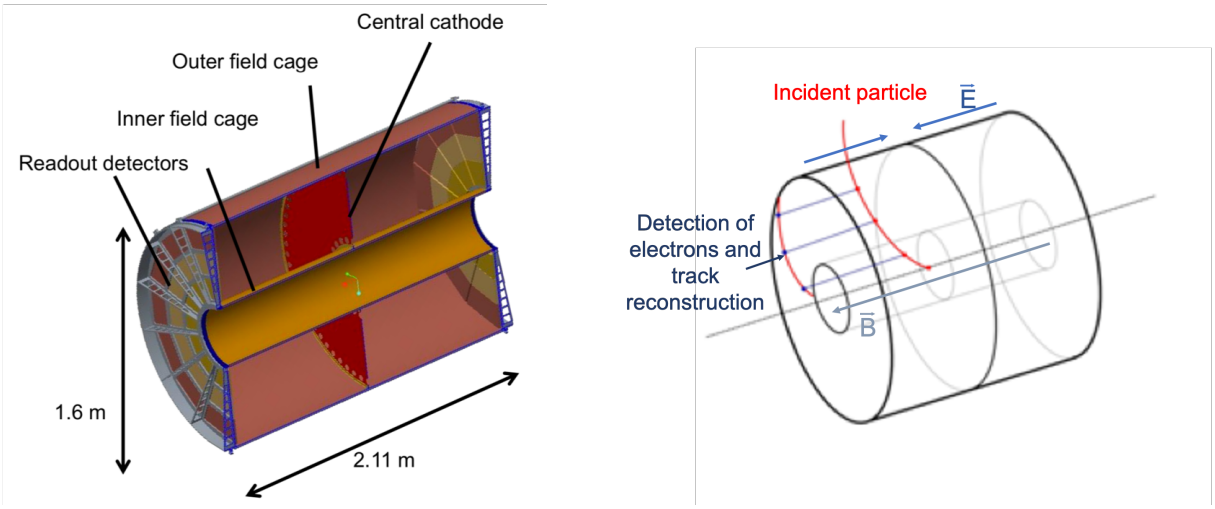

Figure 6.1: Left: representation of a cylindrical TPC with a cathode plane in the middle and two anode planes containing the readout systems. Right: representation of the detection of the track of a particle traversing the TPC.

Thus, the TPC can be used to:

- Reconstruct the trajectory of particles, for which the three-dimensional position is obtained using the readout systems (in the transverse plane) and the drift time of ionization electrons (for the coordinate z).
- Measure charged particles momentum, via the application of a magnetic field which curves their trajectory.
- Identify particles by measuring their ionization energy loss in the volume, i.e., the number of charges collected in the readout systems.

A detailed discussion of the features of TPCs and a review can be found in references [9, 10].

6.1.2 Drift and diffusion of particles in the gas of a TPC

TPCs are constrained on the one hand by the fact that the electrons from primary ionizations must be evacuated quickly, so as to minimize the dead time of the TPC[1], and on the other hand by the spatial resolution requirements. The first constraint imposes the use of intense electric fields - in the ALICE and sPHENIX experiments the drift field is fixed to 400 V/cm - while the second requires limiting the diffusion of ionized charges in the gas.

Drift properties of electrons

The electrons drift under the action of the electric field $\vec{E}$ and the magnetic field $\vec{B}$ with instantaneous velocity $\vec{v}$ given by Langevin's equation:

$$m\frac{\mathrm{d}\vec{v}}{\mathrm{d}t} = e\vec{E} + e\vec{v}\times\vec{B} + \vec{Q}(t) \tag{6.1}$$

[1]The dead time of a detector is defined as the time during which it cannot be exploited because it is already busy recording a signal.

where m is the mass of the electron, e is its charge and $\vec{Q}(t) = -K\vec{v}(t)$ describes the average friction force due to diffusion with gas molecules.

Let τ be the collision time. The steady state is reached when $\dfrac{d\vec{v}}{dt} = 0$. This condition defines the drift velocity $\vec{v}_D$ of electrons:

$$e(\vec{E} + \vec{v}_D \times \vec{B}) - \frac{m}{\tau}\vec{v}_D = 0 \tag{6.2}$$

assuming that the average friction is of Stokes-type, $\vec{Q}(t) = -\dfrac{m}{\tau}\vec{v_D}$.

Therefore, the drift velocity of electrons in gas is given by:

$$\vec{v}_D = \frac{e\tau}{m}\vec{E} + \omega\tau(\vec{v}_D \times \vec{B}) = \mu_-\vec{E} + \omega\tau(\vec{v}_D \times \vec{B}) \tag{6.3}$$

with Larmor frequency $\omega = \dfrac{eB}{m}$ and where $\mu_- \equiv \dfrac{e\tau}{m}$ is the electron mobility.

Drift properties of ions

The motion of ions is dictated by two contributions: one due to thermal effects which is isotropic, and the second is due to the electric field $\vec{E}$. The average speed of ions in all directions due to thermal effects can be described by:

$$\langle v \rangle = \sqrt{\frac{8k_BT}{\pi M}} \tag{6.4}$$

where k_B is the Boltzmann constant, T is the gas temperature, and M the ion mass.

The velocity of ions due to the electric field is described by the term $\vec{u}_e$. Assuming an instantaneous ion velocity due to electric field $u_e = 0$ at $t = 0$ and a typical collision time τ, then directly prior to collision u_e becomes

$$\vec{u}_e = \frac{e\vec{E}}{M} \cdot \tau \tag{6.5}$$

and the drift velocity of ion becomes

$$\vec{v}_D = \langle \vec{u}_e \rangle = \frac{1}{2}\vec{u}_e = \frac{e\vec{E}}{2M}\tau = \mu_+\vec{E} \tag{6.6}$$

where $\mu_+ \equiv \dfrac{e\tau}{2M}$ is the ion mobility.

When comparing electron mobility to ion mobility, one finds that $\mu_+ \ll \mu_-$ since $M \gg m$.

Diffusion of charges in gas

After a time t corresponding to $n = t/\tau$ collisions, charges are spread in a cloud. The dispersion of the cloud is given by

$$\sigma(t) = \sqrt{2Dt} \tag{6.7}$$

where D is the diffusion coefficient such as

$$D = \langle v \rangle \lambda \tag{6.8}$$

with λ the mean free path of electrons / ions in gas and $\langle v \rangle$ the mean thermal velocity.

For $|\vec{E}| = |\vec{B}| = 0$, $\langle v \rangle$ corresponds to the thermal motion of particles in gas and is given in equation 6.4 for ions and electrons. Therefore, the diffusion coefficient is defined by:

$$D_0 = \frac{2}{3\sqrt{\pi}} \frac{1}{P\sigma_0} \sqrt{\frac{(k_B T)^3}{m}} \tag{6.9}$$

This equation points out that the diffusion of particles in gas depends on their mass, and as a consequence ions will diffuse much less in gas than electrons.

However under the application of electromagnetic fields, the thermal motion of an electron becomes negligible. But given the fact that the motion of electrons scales with its inverse mass, as seen in equation 6.3, their diffusion remains much greater than that of ions. The electrons scatter isotropically at the (heavy) gas molecules, hence a greater dispersion.

To summarize

Ions have two important drift properties in gas when submitted to parallel electric and magnetic fields, due to their heavier mass:

1. Ionized gas atoms drift much slower in the chamber volume than electrons.
2. Ions diffuse little in gas, and their trajectory is quasi rectilinear along the longitudinal coordinate z.

6.1.3 TPC readout systems and space charge effect

The first systems used to read out TPCs are Multi-Wire Proportional Chambers (MWPCs), invented in 1968 by Georges Charpak [11]. MWPCs are detectors that consist of a chamber filled with a noble gas, like argon (Ar), inside of which several grids composed of a large number of wires are arranged in parallel, as shown in the figure 6.2. All grids are under high voltage and stacked with alternating cathodes and anodes. When a charged particle passes through

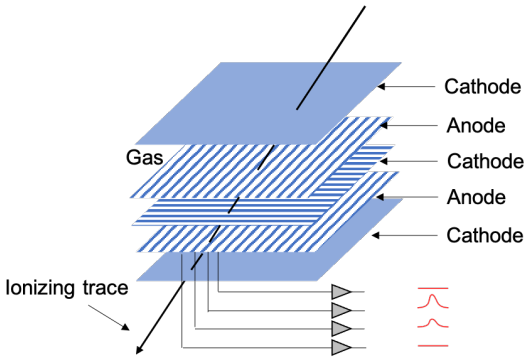

Figure 6.2: Representation of a multi-wire proportional chamber

the chamber, it ionizes the gas along its path. The ionized electrons are then attracted to the anodes and the ions to the cathodes. As the electrons approach the wires, the electric field increases, and electrons are accelerated enough to produce secondary ionizations in a so-called avalanche process. Consequently, the charges produced in the secondary ionizations (mostly the ions which are slower) generate a signal in the form of an electrical pulse on the wires, and the position of the incident particle track can be reconstructed. However, ions created from the

secondary ionizations drift in the opposite direction, which means that they travel up to the drift volume, the TPC itself. The fraction of ions that migrate back to the drift volume is called the Ion Backflow (IBF), and is of order 1 for MWPCs. This phenomenon is known as space charge [12, 13] and results in a local electric field distortion. As discussed in section 6.1.2, the electric and magnetic fields are essential components for the accuracy of spatial track reconstruction of a TPC since they define diffusion and trajectories of charges produced along the track of a charged primary particle. Thus, any field distortion induced by space charge affects the path of ionized electrons, displacing around the actual value of the position of a charged particle.

One possible solution to address this problem is to use a gating grid. Studies have been carried out with two meshes, positioned between the detection volume and the amplification stages, which would make it possible to reverse the electric field in the area bounded by these two grids [14]. Thus, ions drifting back towards the TPC volume are efficiently suppressed. However, using a gating grid induces by definition a dead time in the readout detector, and is the main rate limitation to these TPC-based experiments in high energy physics [2, 3, 15].

Therefore, one of the main challenges of readout detectors is to inherently suppress the IBF, so as not to need gating grids and to be able to read TPCs in continuous, untriggered mode. Continuous readout is required in high luminosity experiments, such as the upgrade of ALICE [16]. In Run 3 at the LHC, the ALICE collaboration plans to record high luminosity Pb–Pb collisions, with a maximum drift time of electrons in the TPC of about 100 µs while an average event spacing of 20 µs. This implies recording significant pile-up events, where several interactions occur in a single bunch crossing, so the data taking cannot be operated in a triggered mode.

In order to achieve this challenge, other readout systems have replaced MWPCs, such as MPGDs which are the object of the next section.

6.2 MPGDs as TPC readout systems

A Micro-Pattern gaseous detector (MPGD) is a type of gaseous detector for which the principle of operation is based on the ionization of the detector gas by charged particles passing through. These detectors consist of electrodes with sub-millimetric distances between one another, which allow one to apply very intense electric fields (> 10 kV/cm) inside the detector. The electrons and ions resulting from the gas ionizations then drift in opposite directions. In order to obtain a readable signal, the electrons are then accelerated in a region with a strong electrostatic field: this will create other electron-ion pairs in an avalanche process. The way this strong field region is created differs for each type of MPGD. The main advantages of MPGDs are their count rate capability, time and spatial resolution, granularity, stability, and construction simplicity. Therefore, they are widely used in TPC-based experiments.

This section describes electron avalanches in gas, and gives two examples of MPGD commonly used in association with TPCs: MicroMEGAS and GEM detectors. Then we present a new development of MPGD based on MicroMEGAS and GEM technologies.

6.2.1 Electron avalanche in a strong field region

When electrons drifting in a gas enter an area with a strong electric field, they are accelerated, hence their kinetic energy increases and can exceed the ionization energy of the gas. This typically happens for electric fields of the order of 10 kV/cm in argon-isobutane mixtures. The electrons then have enough kinetic energy for two processes to be possible, namely ionization and excitation.

- High energetic electrons can ionize the gas. The new electrons created by direct ionization will in turn be accelerated and give rise to a multiplication chain of electrons which in turn gain enough kinetic energy to ionize or excite the gas atoms.
- Electrons can also excite the gas atoms. The de-excitation energy of all the excited states of argon is greater than the ionization potential of isobutane (w = 10.67 eV). Thus, the excitation of the argon atoms can induce in a second step the ionization of the isobutane atoms: this process is known as Penning transfer [17, 18]. Although the excitation cross sections are generally smaller than the ionization cross sections, indirect ionization by collisional transfer results in a significant increase in the multiplication of electrons in the gas.

In addition, low-energy electrons can be captured other gas atoms in a process called attachment. Consequently, this process slows down the avalanche. However, the attachment process is quite rare in the avalanche, where electrons quickly gain kinetic energy[2]. Therefore, the number of avalanche electrons increases exponentially with the distance. The number of electrons in an avalanche is given by

$$N(x) = N(x_0) \cdot \exp\left(\int_{x_0}^{x} \alpha(x)dx\right) \tag{6.10}$$

where x is the longitudinal distance traveled since the start of the avalanche, x_0 is the start point of the avalanche, $N(x_0)$ is the number of primary electrons, and α is the first Townsend coefficient which describes the probability of ionization per unit length and depends on the gas mixture, the temperature, the pressure and the intensity of the electric field.

The gain of the MPGD is defined by

$$\text{Gain} = \frac{N(x_f)}{N(x_0)} = \exp\left(\int_{x_0}^{x_f} \alpha(x)dx\right) \tag{6.11}$$

where x_f is the end point of the avalanche and $N(x_f)$ is the number of electrons after amplification.

This avalanche process is the key to the operation of MPGDs, of which we now present two examples.

6.2.2 MicroMEGAS detectors

The MicroMEGAS (MICRO MEsh GAseous Structure) detector was invented in 1996 by I. Giomataris [19]. In MicroMEGAS detectors, a few-tens-of-µm-thick metallic micro-mesh separates the low-field drift region from the high-field amplification region. The movement of

[2]Attachment plays a much bigger role during the drift of primary ionization charges than in the avalanche process.

charges created during the amplification (mainly ions) induces a signal on the readout electrodes, from which the position in the readout plane is obtained (see figure 6.3).

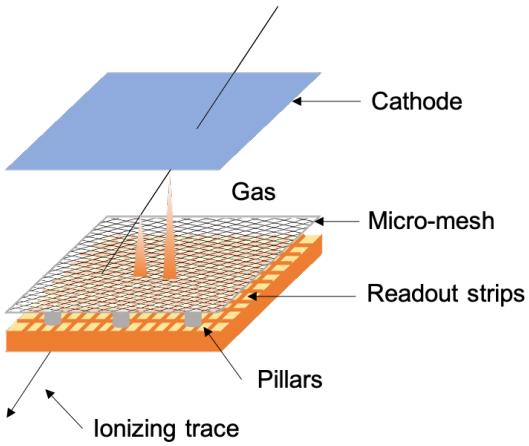

Figure 6.3: Representation of a MicroMEGAS detector.

The amplification region is usually around a hundred-µm wide and the electric field there is within the range of 10 to 50 kV/cm, while the drift region is a gap where the electric field is of the order of a few hundreds of V/cm. When MicroMEGAS detectors are used in combination with a TPC, the TPC itself constitutes the drift region. Due to the electric field gradient between these two regions, the field lines are compressed in the vicinity of the micro-mesh holes (see figure 6.4 at left). A funnel effect then occurs: an electron which comes from the drift zone and approaches the micro-mesh is then sucked into the holes towards the amplification zone, as shown in figure 6.4 in the middle. In this area where the electric field is much stronger, the electron gains enough kinetic energy to produce an avalanche process, as explained in section 6.2.1. Due to the transverse diffusion of electrons in the gas, they disperse as if to form a cone, with a dispersion of the order of 100 µm at the readout plane. On the other hand, the ions, more massive, diffuse very little in the gas as discussed in section 6.1.2 and drift upwards along the field lines, towards the micro-mesh (see figure 6.4 at right). Most are collected by the micro-mesh, yet some can drift back towards the drift volume.

The MicroMEGAS technology tested in this thesis are built using the bulking process [20]. First, a photo-resistive film with a thickness of the size of the desired amplification gap is added on the base material and laminated. Second, a woven mesh which is stretched and glued on a frame is positioned on the film where it is subsequently encapsulated. Third, the film and the mesh are laminated together, at a high temperature, forming a single object. Finally, the photoresistive material is etched by a photolithographic method, using a mask to produce the pillars.

6.2.3 Gas Electron Multiplier

Gas Electron Multipliers (GEMs) were invented in 1997 at CERN by physicist Fabio Sauli [21]. The GEM is made of a 50-µm-thick insulating foil with copper-coated surfaces, typically 2 - 5 µm thick, perforated in a regular pattern of double-conical holes (see figure 6.5). The avalanche process takes place in the holes of the GEM, where the electric field is much more intense than in the drift region, as shown in figure 6.6. As it passes through the GEM, the electron undergoes

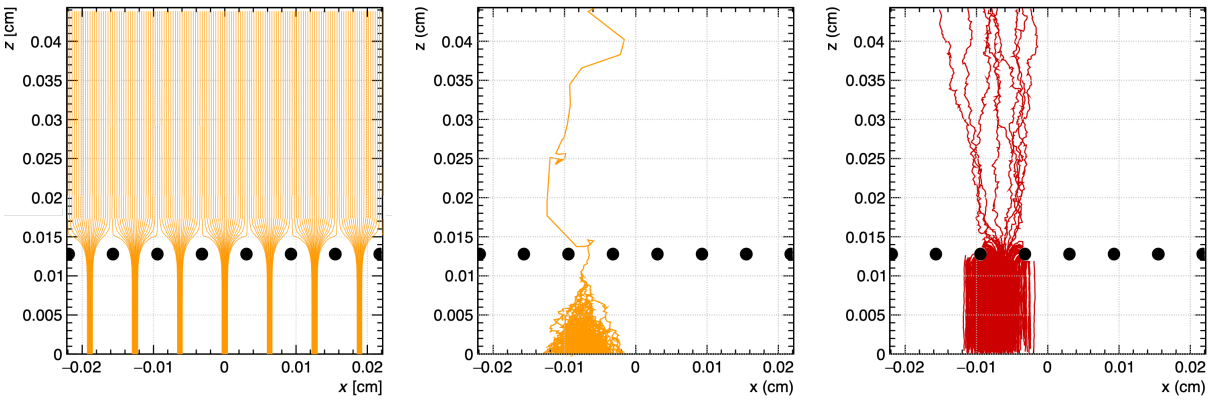

Figure 6.4: Simulations made with Garfield ++ for a MicroMEGAS configuration with a 128-µm-wide amplification gap. Left: electric field lines from a set of starting points at the top of the detector (field lines that starts from the mesh are not drawn); middle: representation of an electronic avalanche; right: trajectories of the ions from the same avalanche. In this specific example, 2.7% of the ions are not stopped by the micro-mesh.

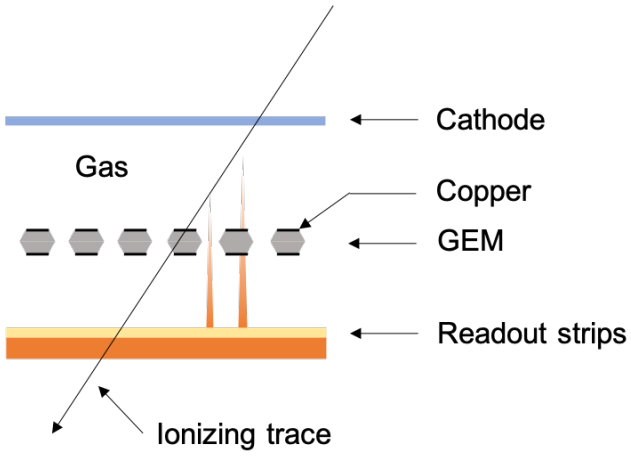

Figure 6.5: Representation of a GEM detector.

the funnel effect and multiplies. But only a fraction of these electrons will succeed in coming out of the holes of the GEM, depending on the ratio of the field inside the GEM holes and the transfer field below the GEM: the more intense the transfer field is - without entering a regime of avalanche multiplication, the better the electrons will succeed in escaping. Most of the ions created in the avalanche are collected on the top side of the GEM foil due to the field gradient.

6.2.4 Combinations of MicroMEGAS and GEM detectors

MicroMEGAS and GEM detectors have demonstrated very good performance in terms of spatial resolution (< 50 µm) and energy resolution to equip TPCs as reading systems [1, 4]. Moreover, they can record high rate signals, and they are simple to manufacture and robust.

However, the performances in terms of IBF of these two technologies, extensively studied in the past [14, 22–27], do not satisfy current TPC requirements when used alone. TPCs are usually

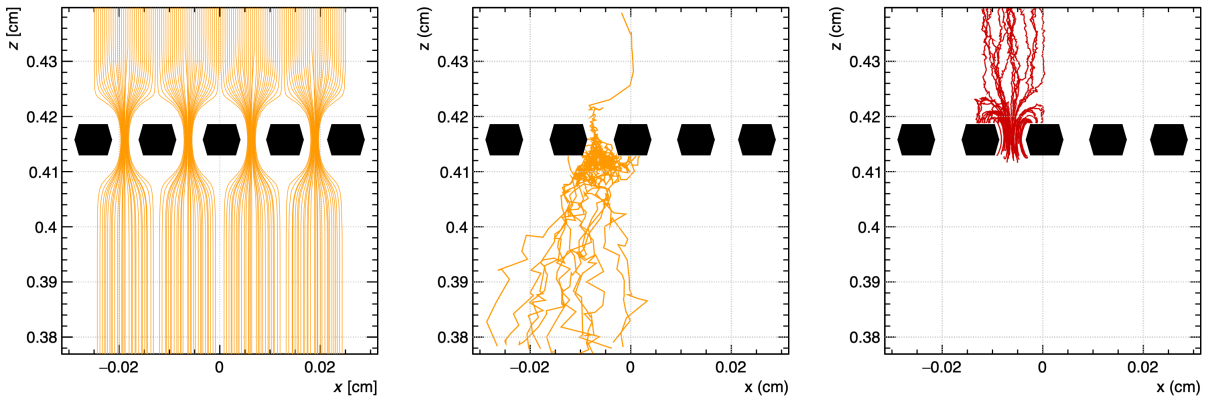

Figure 6.6: Simulations made with Garfield++ for a GEM configuration. On the left, the electric field lines are drawn from a set of starting points at top of the detector. In the middle, an electron avalanche is represented, and on the right, the trajectories of the ions. Most of the secondary ions are stopped by the GEM, and a certain proportion of the ions pass through (in this example: 12.7%).

operated with an effective gain of the readout detectors of about 2000, and with IBF values lower than 0.3% [1–3, 6, 7], motivated by the need to have an important signal amplification without polluting the TPC with a high space charge.

Therefore, other solutions consist in using these technologies in combination. One proposed solution is based on a system of two GEMs and a MicroMEGAS detector [28]. Another one is based on the use of a double-mesh [29–31]. Another one consists in using quadruple GEM detectors [26, 27], where four GEMs are stacked together: this is the solution chosen by the ALICE and sPHENIX experiments [1–3, 6, 7].

Another unexplored idea, which is the subject of the study presented here, is a solution combining a MicroMEGAS detector and an ensemble of a micro-mesh bulked on top of a GEM. This new detector is represented in figure 6.7: an amplification mesh lies 128 µm above the readout plane, a GEM foil a few millimeters above, and a micro-mesh is bulked on the GEM with a few-hundred-µm gap. In the following, this new geometry will be referred to as MMGEM.

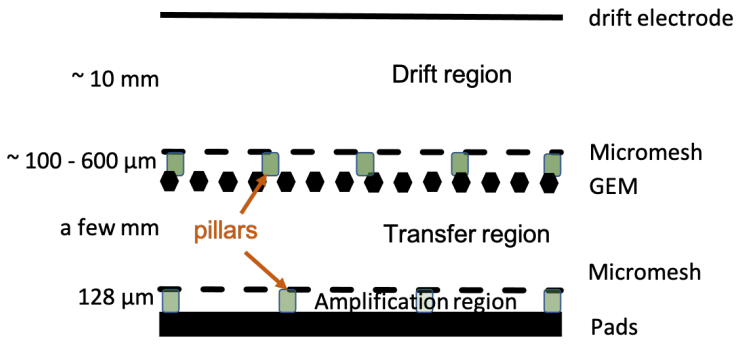

Figure 6.7: Representation of the new MPGD structure proposed.

Such a structure has never been studied in the past. With the future construction of high luminosity facilities such as the Electron Ion Collider (EIC) [32] and the International Linear Collider (ILC) [33], TPCs are good candidates to constitute the main tracking detection instru-

ment. This new MPGD structure is part of the research of optimizing TPC readout detectors for future particle physics experiments in view of possible industrialization.

6.3 Producing events in a MPGD structure

In order to study this new MPGD structure, one needs to choose a gas as the sensitive volume of the detector, and create signals in the detector to understand its behavior. In this section, the choice of gas is discussed. Then we talk about the characterization of the detector by means of an iron source which sends 5.9 keV photons in the detector, inducing measurable signals.

6.3.1 Gas choice

A TPC-based experiment has specific requirements concerning the gas mixture to be used. In particular, high precision data taking requires a gas with low transverse diffusion (as discussed in section 6.1.2), low sensitivity to external parameters (temperature, pressure), and high ionization rates. In the case of high-rate experiments, it is necessary to have a rapid evacuation of the ions in order to limit the space charge effect in the TPC. The reference [34] nicely details the ideal features of a gas mixture for use in a TPC.

Noble gases match most of the requirements. In particular argon and neon gases are favored, as they are affordable (they are respectively the 3rd and 5th most common gas in the atmosphere) and of reasonable density. Argon is denser than air with ρ = 1.784 g/l and neon lighter with ρ = 0.900 g/l. Denser gases are not preferred as they lead to significant multiple scatterings.

During the avalanche process, the atoms in the gas can either be excited or ionized (see section 6.2.1). In the case of excitation, atoms fall back into their ground state by emitting photons, and both neon and argon are transparent to their own light. If the photons hit an electrode, they are likely to extract an electron, which initiates another delayed amplification avalanche, resulting in an unstable gain of the gas. Therefore, noble gases need to be used in association with at least one quencher, which is a gas able to absorb these feedback photons because of their numerous levels of excitations, rotations and vibrations. This stabilizes the operation of the detector and limits the development of delayed avalanche processes. Isobutane, carbon dioxide and methane can be used as possible quenchers.

Studies presented in reference [35] show that the use of the gas mixture composed of 95% of argon with 5% of isobutane maximizes the energy resolution. This gas is well adapted for the detection of X-rays between 1-10 keV, providing a very good energy resolution and gains up to 2×10^4. Therefore, this gas mixture was chosen for both simulations and tests in the laboratory.

6.3.2 Interactions of X-rays in gas and escape peak

In order to characterize MPGDs, the most commonly used source is an X-ray source. The source used in the tests presented in the following chapters is an iron ^{55}Fe source, which emits mostly photons at 5.9 keV, though other energy rays exist - the ^{55}Fe source also has an energy ray at K_β = 6.4 keV. An incoming X-ray photon of energy $h\nu$ can ionize an atom of the gas, releasing a free energy electron $E = h\nu - E_b$ where E_b is the binding energy of the electron. This energetic electron subsequently creates a cloud of electrons by collision with neighboring gas atoms.

As for the newly created ion, it is then in an excited state if the electron ejected by the incoming X-ray was located in an inner atomic layer since the electron left a vacant place. An electron from a higher energy layer can then fill this place, and by doing so, it loses energy. This energy has two possible outcomes.

- In the first case, this energy is transmitted to an atomic electron which is then ejected from the atom with the energy E_b: this is the Auger electron emission. Therefore, all the energy of the incoming photon is transferred to electrons, and the average number of electron-ion pairs created is given by $\bar{N} = h\nu/w$, where w is the mean ionization energy of the gas (w = 25.85 eV for argon-isobutane (95/5)). Thus, with an incoming X-ray of energy 5.9 keV, there are on average $\bar{N} \approx 228$ electron-ion pairs created.
- In the second case, this energy is released in the form of a photon emission: it is X-fluorescence. The fluorescence photon escapes the detecting volume and its energy is lost. For argon, and with $h\nu > 3.2$ keV, there is a 14% probability to have the emission of a 2.96 keV photon by argon K fluorescence [36]. This missing energy leads to a parent argon escape peak in the signal at 2.9 keV for an incoming 5.9 keV X-ray photon (see figure 6.8).

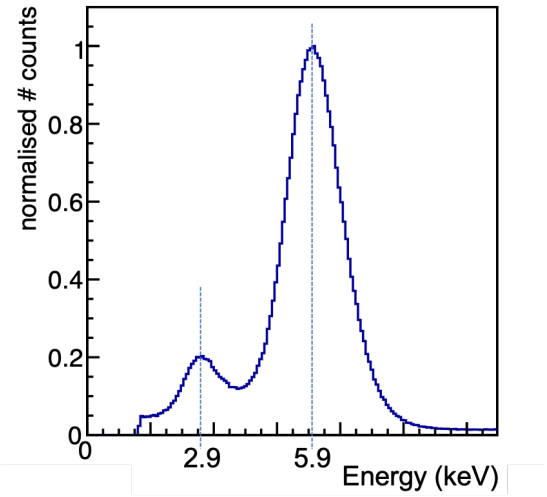

Figure 6.8: Energy spectrum generated by 5.9 keV photons in argon-isobutane (95/5). This spectrum is obtained from laboratory measurements on a bulk MicroMEGAS [20] using a ^{55}Fe source.

6.4 Summary

TPCs are present in many particle experiments. With the future construction of high luminosity facilities such as the Electron Ion Collider (EIC) [32] and the International Linear Collider (ILC) [33], TPCs are good candidates to constitute the main tracking detection instrument: a TPC has the advantage of providing enough measurement points for a robust pattern recognition and small material budget. Thus, optimizing their readout detectors is becoming a major focus for the future of particle physics experiments. One of the main issues with MPGDs, very commonly associated with TPCs as readout systems, is the IBF which results in the space charge effect inside the chamber, inducing local field distortions and therefore affecting the spatial resolution of TPCs. This study concerns a new structure of MPGD, which combines MicroMEGAS and GEMs, and which aims to inherently suppress the IBF.

In order to characterize and comprehend the behavior of signals in this structure, simulations have been set up and are the subject of the next chapter.

Bibliography

[1] J. Adolfsson et al. The upgrade of the ALICE TPC with GEMs and continuous readout. *JINST*, 16(03):P03022, 2021. doi: 10.1088/1748-0221/16/03/P03022.

[2] G. Dellacasa et al. ALICE: Technical design report of the time projection chamber. 1 2000.

[3] J. Alme et al. The ALICE TPC, a large 3-dimensional tracking device with fast readout for ultra-high multiplicity events. *Nucl. Instrum. Meth. A*, 622:316–367, 2010. doi: 10.1016/j.nima.2010.04.042.

[4] N. Abgrall et al. Time Projection Chambers for the T2K Near Detectors. *Nucl. Instrum. Meth. A*, 637:25–46, 2011. doi: 10.1016/j.nima.2011.02.036.

[5] M. Anderson et al. The Star time projection chamber: A Unique tool for studying high multiplicity events at RHIC. *Nucl. Instrum. Meth. A*, 499:659–678, 2003. doi: 10.1016/S0168-9002(02)01964-2.

[6] Klaus Dehmelt. The sPHENIX TPC Project. *PoS*, MPGD2017:044, 2019. doi: 10.22323/1.322.0044.

[7] Henry Klest. Overview and design of the sPHENIX TPC. *J. Phys. Conf. Ser.*, 1498:012025, 2020. doi: 10.1088/1742-6596/1498/1/012025.

[8] D. R. Nygren. The Time Projection Chamber: A New 4 pi Detector for Charged Particles. *eConf*, C740805:58, 1974.

[9] W. Blum and Gigi Rolandi. *Particle detection with drift chambers*. 12 1993. ISBN 978-3-540-56425-6.

[10] H. J. Hilke. Time projection chambers. *Rept. Prog. Phys.*, 73:116201, 2010. doi: 10.1088/0034-4885/73/11/116201.

[11] Georges Charpak, R. Bouclier, T. Bressani, J. Favier, and C. Zupancic. The Use of Multiwire Proportional Counters to Select and Localize Charged Particles. *Nucl. Instrum. Meth.*, 62:262–268, 1968. doi: 10.1016/0029-554X(68)90371-6.

[12] F. V. Böhmer, M. Ball, S. Dorheim, C. Höppner, B. Ketzer, I. Konorov, S. Neubert, S. Paul, J. Rauch, and M. Vandenbroucke. Simulation of Space-Charge Effects in an Ungated GEM-based TPC. *Nucl. Instrum. Meth. A*, 719:101–108, 2013. doi: 10.1016/j.nima.2013.04.020.

[13] Ernst Hellbär. Reconstruction in ALICE and calibration of TPC space-charge distortions in Run 3. *PoS*, LHCP2021:023, 2021. doi: 10.22323/1.397.0023.

[14] Deb Sankar Bhattacharya et al. Experimental and numerical simulation of a TPC like set up for the measurement of ion backflow. 10 2017.

[15] Shuai Wang. MWPC Prototyping and Testing for STAR Inner TPC Upgrade. *Int. J. Mod. Phys. Conf. Ser.*, 46:1860079, 2018. doi: 10.1142/S2010194518600790.

[16] Z. Citron et al. Report from Working Group 5: Future physics opportunities for high-density QCD at the LHC with heavy-ion and proton beams. *CERN Yellow Rep. Monogr.*, 7: 1159–1410, 2019. doi: 10.23731/CYRM-2019-007.1159.

[17] F. Penning. Über den einfluß sehr geringer beimischungen auf die zündspannung der edelgase. *Zeitschrift für Physik 46*, 335, 1928.

[18] F.M. Penning. The starting potential of the glow discharge in neon argon mixtures between large parallel plates: II. Discussion of the ionisation and excitation by electrons and metastable atoms. *Physica*, 1(7):1028–1044, 1934. ISSN 0031-8914. doi: https://doi.org/10.1016/S0031-8914(34)80298-4. URL https://www.sciencedirect.com/science/article/pii/S0031891434802984.

[19] Y. Giomataris, P. Rebourgeard, J. P. Robert, and Georges Charpak. MICROMEGAS: A High granularity position sensitive gaseous detector for high particle flux environments. *Nucl. Instrum. Meth. A*, 376:29–35, 1996. doi: 10.1016/0168-9002(96)00175-1.

[20] I. Giomataris, R. De Oliveira, S. Andriamonje, S. Aune, G. Charpak, P. Colas, G. Fanourakis, E. Ferrer, A. Giganon, Ph. Rebourgeard, and P. Salin. Micromegas in a bulk. *Nuclear Instruments and Methods in Physics Research Section A: Accelerators, Spectrometers, Detectors and Associated Equipment*, 560(2):405–408, 2006. ISSN 0168-9002. doi: https://doi.org/10.1016/j.nima.2005.12.222. URL https://www.sciencedirect.com/science/article/pii/S0168900205026501.

[21] F. Sauli. GEM: A new concept for electron amplification in gas detectors. *Nucl. Instrum. Meth. A*, 386:531–534, 1997. doi: 10.1016/S0168-9002(96)01172-2.

[22] P. Colas, I. Giomataris, and V. Lepeltier. Ion backflow in the Micromegas TPC for the future linear collider. *Nucl. Instrum. Meth. A*, 535:226–230, 2004. doi: 10.1016/j.nima.2004.07.274.

[23] Purba Bhattacharya, Deb Sankar Bhattacharya, Supratik Mukhopadhyay, Sudeb Bhattacharya, Nayana Majumdar, Sandip Sarkar, Paul Colas, and David Attie. Investigation of Ion Backflow in Bulk Micromegas Detectors. *JINST*, 10(09):P09017, 2015. doi: 10.1088/1748-0221/2015/9/P09017.

[24] F. Jeanneau, M. Kebbiri, and V. Lepeltier. Ion back-flow gating in a micromegas device. *Nuclear Instruments and Methods in Physics Research Section A: Accelerators, Spectrometers, Detectors and Associated Equipment*, 623:94–96, 2010. doi: 10.1016/j.nima.2010.02.159. URL http://hal.in2p3.fr/in2p3-00464017.

[25] J. Va'vra and T. Sumiyoshi. Ion Feedback Suppression Using Inclined MCP Holes in a Single-MCP+Micromegas+Pads Detector. *Nucl. Instrum. Meth. A*, 553:76–84, 2005. doi: 10.1016/j.nima.2005.08.047.

[26] Senta V. Greene, Julia Velkovska, Brandon Blankenship, Michael Z. Reynolds, and Sourav Tarafdar. Effective gain and Ion Back Flow study of triple and quadruple gem detector. 11 2020.

[27] Sourav Tarafdar, Senta V. Greene, Julia Velkovska, Brandon Blankenship, and Michael Z. Reynolds. Reduction of ion back flow using a quadruple GEM detector with various gas mixtures. 10 2021.

[28] S. Aiola, R. J. Ehlers, S. Gu, J. W. Harris, R. Majka, J. D. Mulligan, M. Oliver, J. Schambach, and N. Smirnov. Combination of two Gas Electron Multipliers and a Micromegas as gain elements for a time projection chamber. *Nucl. Instrum. Meth. A*, 834:149–157, 2016. doi: 10.1016/j.nima.2016.08.007.

[29] Zhiyong Zhang, Binbin Qi, Chengming Liu, Jianxin Feng, Jianbei Liu, Ming Shao, Yi Zhou, Daojin Hong, You Lv, Guofeng Song, Xu Wang, and Wenhao You. A high-gain, low ion-backflow double micro-mesh gaseous structure for single electron detection. *Nuclear Instruments and Methods in Physics Research A*, 889:78–82, May 2018. doi: 10.1016/j.nima.2018.02.006.

[30] Zhiyong Zhang, Binbin Qi, Ming Shao, Jianxin Feng, Xu Wang, Chengming Liu, Jianbei Liu, Yi Zhou, Daojin Hong, You Lv, Guofeng Song, and Wenhao You. Study on the double micro-mesh gaseous structure (DMM) as a photon detector. *Nuclear Instruments and Methods in Physics Research A*, 952:161978, February 2020. doi: 10.1016/j.nima.2019.03.033.

[31] Binbin Qi, Kunyu Liang, Zhiyong Zhang, Jianxin Feng, Jianbei Liu, Ming Shao, and Yi Zhou. Optimization of the double micro-mesh gaseous structure (DMM) for low ion-backflow applications. *Nuclear Instruments and Methods in Physics Research A*, 976:164282, October 2020. doi: 10.1016/j.nima.2020.164282.

[32] Ferdinand Willeke. Electron Ion Collider Conceptual Design Report 2021. 2 2021. doi: 10.2172/1765663.

[33] Halina Abramowicz et al. International Large Detector: Interim Design Report. 3 2020.

[34] Rob Veenhof. Choosing a gas mixture for the ALICE TPC. 5 2003.

[35] F. J. Iguaz et al. New developments in Micromegas Microbulk detectors. *Phys. Procedia*, 37:448–455, 2012. doi: 10.1016/j.phpro.2012.02.392.

[36] Takeshi Watanabe, H. W. Schnopper, and F. N. Cirillo. K X-Ray Fluorescence Yield of Argon. *Phys. Rev.*, 127:2055–2057, Sep 1962. doi: 10.1103/PhysRev.127.2055. URL https://link.aps.org/doi/10.1103/PhysRev.127.2055.

Chapter 7

Simulation of Micro-Pattern Gaseous Detectors

Contents

7.1 Numerical tools 156
7.1.1 Generation of electric field maps with COMSOL Multiphysics . 156
7.1.2 Generating events with Garfield++ software 158
7.2 Definition of the observables in the simulation 159
7.2.1 Gain 159
7.2.2 Ion Backflow 159
7.2.3 Transparency 160
7.3 Models simulated 160
7.3.1 Single-stage MicroMEGAS 160
7.3.2 MicroMEGAS and a GEM 162
7.3.3 MicroMEGAS and a micro-mesh bulked on a GEM (MMGEM) 163
7.4 Simulation results on MMGEM detectors 164
7.4.1 Gain and transparency of each electrode 166
7.4.2 Ion stopping power of each electrode 166
7.4.3 Other results 167
7.5 Summary 168
Bibliography 169

In order to build a detector with the best possible performance, simulations are carried out on different geometric configurations of detectors. The goal is to understand the behavior of electrons and ions in the avalanche processes depending on both the geometric and field configurations and therefore design a detector with optimal performances in terms of gain (required to be about 2000) and IBF ($< 0.3\%$), as needed in the ALICE and sPHENIX experiments [1–5]. The structures tested combine micro-meshes and GEMs with different spaces between the elements and different geometric specifications for each.

In this chapter, we first introduce the numerical tools used before describing the method to obtain the gain and the IBF in the simulations, then we focus on the different simulated models. Finally, we discuss the results obtained with the simulation of the new type of MPGD proposed for construction and testing.

7.1 Numerical tools

The simulations are performed following a two-step procedure.

1. Three-dimensional electric field maps in the detector are built using the COMSOL Multiphysics® software. In order to optimize the duration of computation and computer memory, the built geometry is a single volume element (referred to as *pattern*) which is a parallelepiped with a square base. The square has the size of the mesh pitch or twice its size, corresponding to a very small portion of detector in the (x, y) plane defined by the plane parallel to the anode and cathode.

2. The electric field maps obtained in the pattern volume are exported into Garfield++ simulation framework [6], where they are mirrored in order to produce an infinite detector in the (x, y) plane. Within this framework, 5.9 keV photons are simulated. They convert to electrons which subsequently produce avalanches.

7.1.1 Generation of electric field maps with COMSOL Multiphysics

COMSOL Multiphysics® calculates precisely the electric field in a structure built by the user with a method based on finite element analysis.

In the case of a micro-mesh placed 128 µm above the anode plane, two intersecting wires are constructed, as shown in figure 7.1, at z = 128 µm where z is the height in the detector. The wires have a length of the pitch size and the two resulting crossing wires constitute the single *pattern*. A parallelepiped of the same width and depth as the wires is built, with a height from z = 0 to z = 5 mm. The last step in building the geometry consists of subtracting the two wires from the parallelepiped: the resulting volume corresponds to the detector sensitive volume filled with gas. The electrodes are defined by surfaces: for the micro-mesh, it is that of the wires, for the anode - or the pads, it is the lower surface of the parallelepiped, and for the cathode - or the drift electrode - it is the top surface of the parallelepiped.

The procedure is repeated with more complicated structures, involving an additional GEM and sometimes another mesh. In the example shown figure 7.1, the combination of a GEM and a micro-mesh with a 128-µm gap has been built above a micro-mesh which is 128-µm above the anode plane. Both micro-meshes have a pitch of 63 µm and a wire diameter of 18 µm. The GEM has a pitch of 126 µm, it is 60-µm thick, it inner diameter is 50 µm and its outer diameter is 70

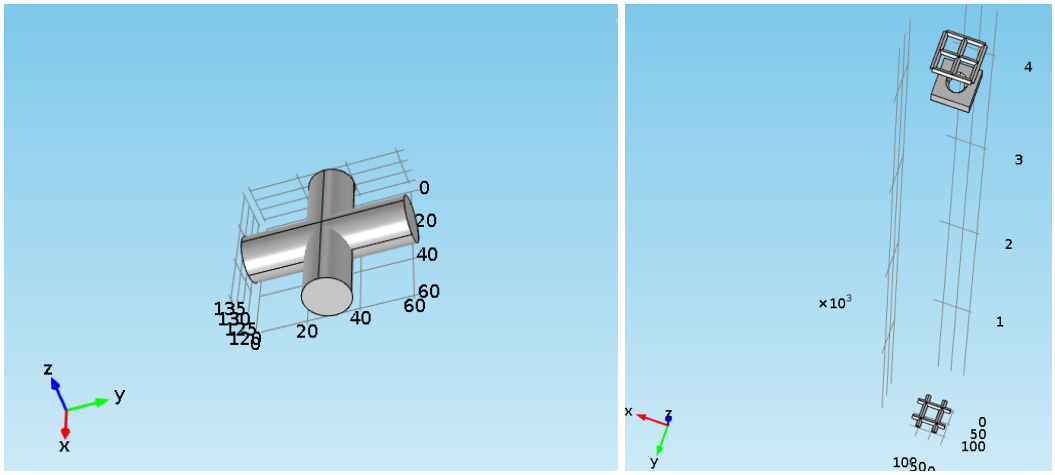

Figure 7.1: Screenshots of COMSOL Multiphysics® software interface. Left: construction of two wires to model the mesh with a simple pattern. Right: Construction of a micro-mesh and a GEM on top of another micro-mesh.

µm. The GEM is located 4 mm above the bottom micro-mesh. The resulting parallelepiped has a square base of side 126 µm, corresponding to twice the pitch of the meshes and once that of the GEM.

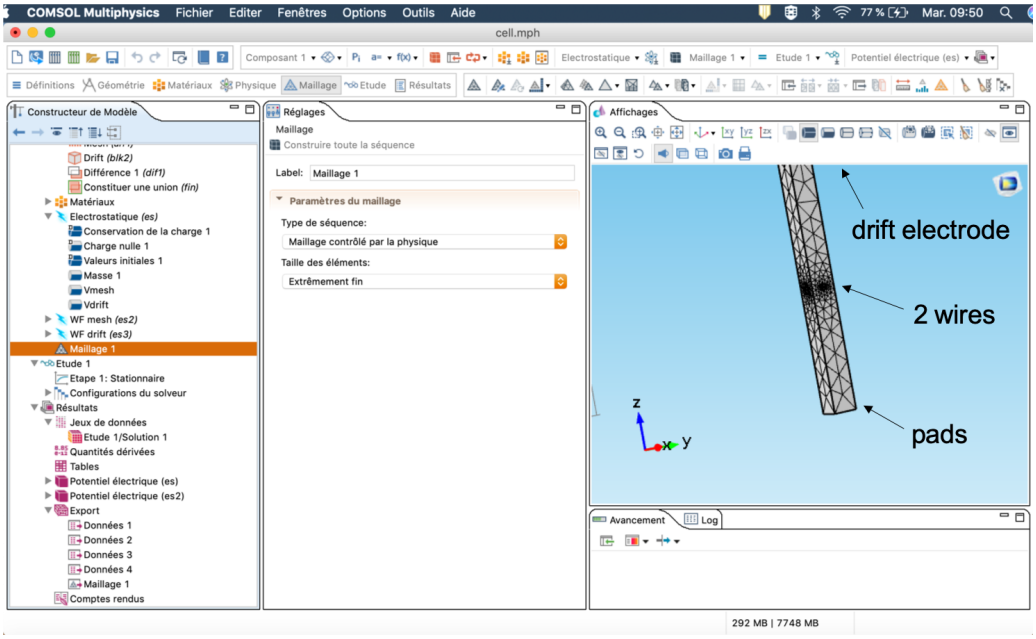

Figure 7.2: Screenshot of COMSOL Multiphysics® software interface, zooming in on the lower part of the constructed parallelepiped, with its mesh which defines the points at which the electric potential is calculated. This example illustrates the modeling of a simple MicroMEGAS.

Then, a fine *mesh network* is built by the software (see figure 7.2). The mesh network corresponds to a tetrahedral distribution of vertices, and the spaces between the vertices are controlled by the structure of the built element. Finally, the electric potential is computed at each

vertex based on the electrostatic field module provided by the software (see figure 7.3) and based on the electric potential values given to each electrode.

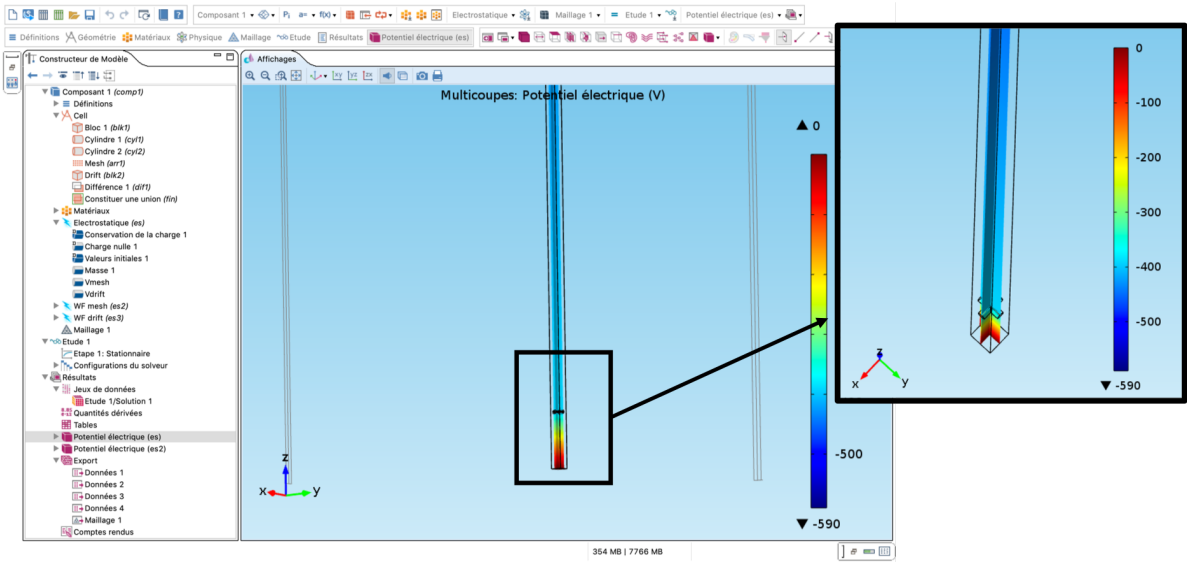

Figure 7.3: Screenshot of the COMSOL Multiphysics software®, zooming in on the lower part of the constructed parallelepiped, after the calculation of the electric potential maps in 3D. This example illustrates the modeling of a simple MicroMEGAS.

7.1.2 Generating events with Garfield++ software

The electric field maps obtained using COMSOL Multiphysics® software are exported into Garfield++ simulation framework [6]. Garfield++ is a toolkit for the detailed simulation of detectors which use gases or semiconductors as sensitive medium. In our case, the gas associated with the volume of the simulated detector is an argon based gas mixture: 95% argon (Ar) + 5% isobutane (iC_4H_{10}).

In order to reproduce a detector with a fairly large detection space, a Garfield++ option allows to mirror the electric field map in 3D in order to have an infinite detector in x and y.

Photons with an incoming energy of 2.9 keV, 5.9 keV and 6.4 keV are generated in order to mimic the escape peak of argon, and the two energy rays of a ^{55}Fe source. Then, they are converted into electrons by photoelectric effect in the drift region. For this calculation, Garfield++ estimates the primary ionization due to photon track using HEED [7, 8]. Transport properties are computed with Magboltz [9, 10], also implemented in Garfield++ toolkit.

The Penning transfer rate r_p is a parameter which needs to be tuned in the simulation framework. This parameter was determined in reference [11] by comparing the simulations with Magboltz 10.1 [9, 10] to their measurements, and they obtained $r_p = 0.321 \pm 0.003$ in argon-isobutane (95/5). Thus, the value for the Penning transfer rate is fixed to $r_p = 0.321$ in the simulation.

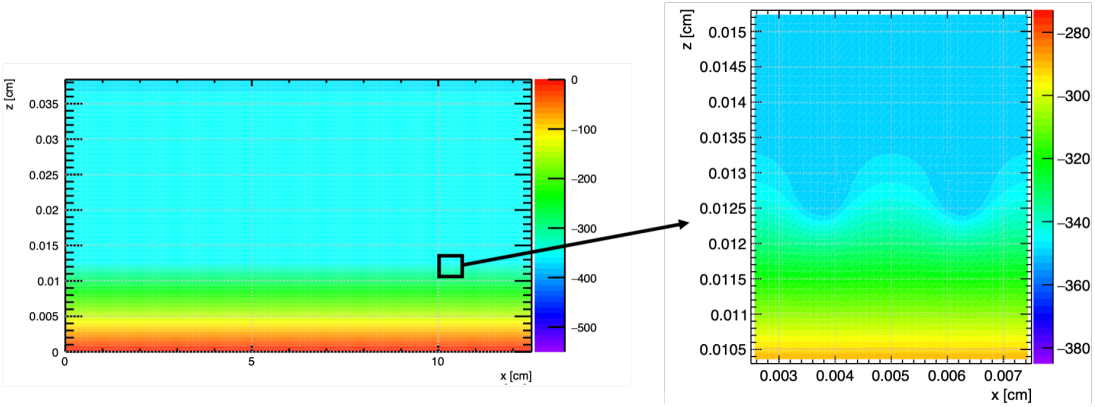

Figure 7.4: Simulation of the electric potential of a MicroMEGAS detector with a µm amplification gap for the following voltages on the micro-mesh and on the drift at z = 5mm from the bottom plane: V_{mesh} = -360V, V_{drift} = -560V.

7.2 Definition of the observables in the simulation

7.2.1 Gain

For each event, that is for each photon converting into the drift space, the gain is estimated by the number of secondary electrons which arrive at the bottom of the detector, on the anode, then normalized by the expected number of primary electrons in the gas mixture. The number of primary electrons is computed as the ratio of the energy of the incoming photon, 5.9 keV, and the ionization potential of the gas mixture. The spectrum resulting from this normalized number of electrons shows a large peak associated with the 5.9 keV photon energy, fitted with a Gaussian function to extract the gain, standard deviation (σ) and full width half maximum (FWHM) defined by:

$$\text{FWHM} = 2 \times \sqrt{2 \ln 2}\sigma,$$

and a peak associated with the 2.9 keV escape peak of 5.9 keV photons in argon (see section 6.3.2). The gain of the detector is obtained by the mean value of the gaussian fit. The associated uncertainty is the statistical error on the parameter as given by the fit procedure (see figures 7.5, 7.8, 7.10).

7.2.2 Ion Backflow

The IBF is estimated for each event according to the expression:

$$\text{IBF} = \frac{N^{\text{ions}}_{\text{drift}}}{N^{\text{ions}}_{\text{total}}}$$

where $N^{\text{ions}}_{\text{total}}$ is the number of ion charges induced on the mesh, and $N^{\text{ions}}_{\text{drift}}$ is the number of ion charges induced on the drift electrode. IBF values are then fitted with a gaussian function (see for example figure 7.5 at right). The average IBF is given by the central value of the gaussian function, given with its statistical uncertainty.

7.2.3 Transparency

The total transparency of the detector is defined by the proportion of electrons starting in the drift space for which the generated amplification electrons reach the anode. Similarly, the electronic transparency of each electrode is defined by the proportion of electrons for which the initial z coordinate (corresponding to the height in the detector, where $z = 0$ is the position of the anode) is above the electrode of interest, and the final z coordinate is below. In the following, the micro-meshes are labeled by their central z position, whereas "GEM down" denotes the lower limit on the z position of the GEM, and "GEM up" denotes its upper limit.

Given the fact that each electrode has an intrinsic transparency and gain, one cannot only use the product of the different transparencies to recover the full transparency of the detector. One must take into account the fact that the gain of each electrode increases its probability to let electrons pass through. Therefore, the full transparency of the detector and the individual electrode transparencies are quantities computed separately in the simulation.

7.3 Models simulated

Several models of detectors have been simulated with different geometries in order to choose the optimal configuration which can both reduce the ion backflow and improve the resolution while satisfying several constraints.

- The total gain must be of the order of 2000, in order to match standard TPC requirements.
- The drift time of primary particles has to be small in order to avoid pile-up events, and the transverse diffusion must be of the order of 1 mm (see for example the requirements for the ALICE experiment [3]). The electric field applied in a TPC is generally of the order of a few hundreds of V/cm to meet these two requirements. Therefore, the electric field in the drift region - which must be the same as in the TPC - is arbitrarily set at $\sim$ 400 V/cm.

7.3.1 Single-stage MicroMEGAS

The first simulated model consists of a micro-mesh with a pitch of 63 µm and a wire diameter of 18 µm (45/18, where 45 µm is the size of the hole side), and a drift electrode modeled by a plane. Geometric parameters of the electrodes are summarized in table 7.1.

electrode	position	parameters
drift electrode	z = 5 mm	plane in x, y
micro-mesh	z = 128 µm	pitch = 63 µm, wire diameter = 18 µm, hole size = 45 µm
pads	z = 0	plane in x, y

Table 7.1: Geometric parameters of the MicroMEGAS model.

Given the constraint on the drift electric field, the simulation predicts ion backflow values between 2 and 3% for gains from 2000 to 3000. An example is shown in figure 7.5. For each

photon that converts in the detector, the IBF histogram is filled with the fraction of ions that drift back into the drift zone. In this example, the electronic transparency of the micro-mesh is of 95%.

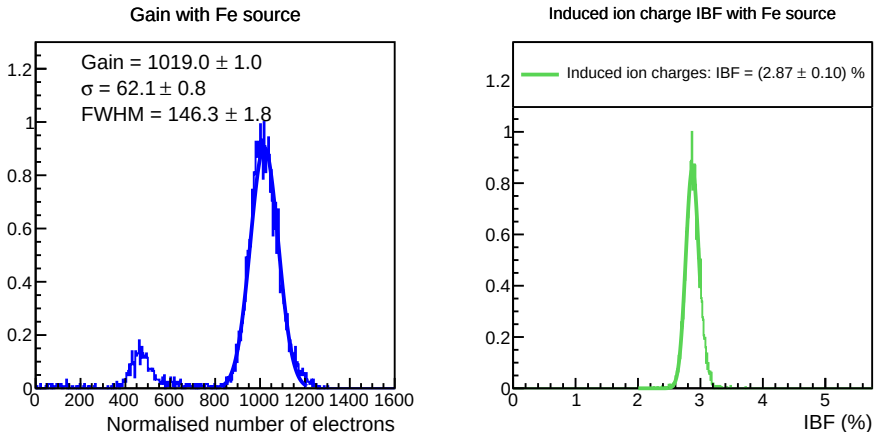

Figure 7.5: Left: simulated spectrum produced by a ^{55}Fe source in a MicroMEGAS detector. The x axis gives the number of electrons per initial photon ionisation. Right: IBF histogram. In this example, the field ratio is 73, E_{amp} = 30 kV/cm, E_{drift} = 410 V/cm.

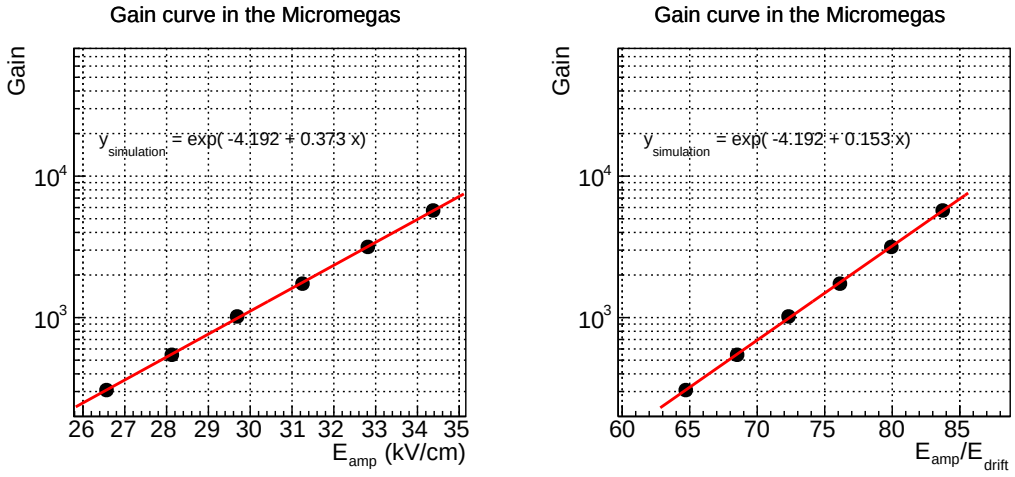

Figure 7.6: Gain curve for a MicroMEGAS obtained with Garfield++ simulations.

The gain and IBF curves of the MicroMEGAS are shown figures 7.6 and 7.7, along with the IBF. The curve is produced by keeping the electric field in the drift region constant at 400 V/cm while increasing the electric field in the amplification region. While the gain increases exponentially with the amplification field, as expected from the discussion in section 6.2.1, the IBF decreases very smoothly and remains above 2%, which is a factor 10 higher than the goal.

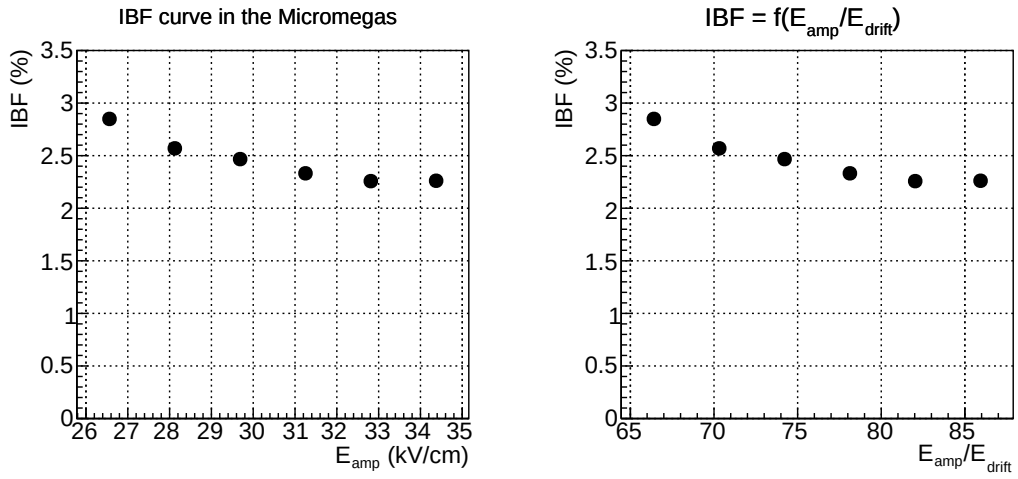

Figure 7.7: IBF curve for a MicroMEGAS obtained with Garfield++ simulations.

7.3.2 MicroMEGAS and a GEM

The addition of a GEM above the micro-mesh has been implemented, the objective being to stop back flowing ions. The geometric parameters of this model are given in table 7.2. The geometry of the GEM simulated is not exactly the same as the one used in the laboratory tests presented in the next chapter. In the simulation, the pitch of the GEM is 126 µm instead of 140 µm in the detector. This pitch was chosen in the simulation in order to have a pattern with only one GEM hole and two pitches for the micro-mesh, in order to optimize the computation time of the electric field maps.

electrode	**position**	**parameters**
drift electrode	z = 7 mm	plane in x, y
GEM	z = 4.128 mm to 4.188 mm	pitch = 126 µm, hole inner diameter = 50 µm, outer diameter = 70 µm
micro-mesh	z = 128 µm	pitch = 63 µm, wire diameter = 18 µm, hole size = 45 µm
pads	z = 0	plane in x, y

Table 7.2: Geometric parameters of a hybrid detector model with a GEM and a MicroMEGAS.

In order to avoid ions flowing back to the drift zone, few ions must be created in the GEM, which would involve operating the GEM at low gain. Doing so dramatically decreases the electronic transparency of the GEM, which is defined by the ability of the GEM to let electrons pass: the smaller the gain, the worse the transparency for a given drift field. Losing transparency leads to a degradation of the local energy resolution due to a loss of primary electrons: a compromise must therefore be found to keep the gain in the GEM low enough while maximizing its transparency. An example is given in figure 7.8. The degradation in energy resolution

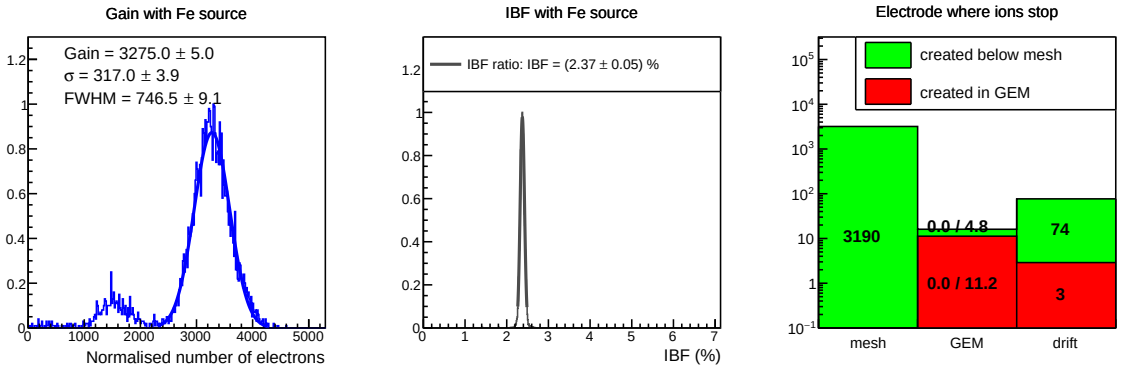

Figure 7.8: Left: simulated iron spectrum of a hybrid MicroMEGAS and GEM detector. Middle: IBF histogram. Right: histogram showing the number of ions that were stopped at each electrode, depending on where they were created. For the GEM, the first number corresponds to the number of ions stopped at the bottom, while the second is for the top. For this specific example, the electric fields are: below the MicroMEGAS, E_{amp} = 27 kV/cm, between the MicroMEGAS and the GEM E_{transfer} = 400V/cm, inside the GEM E_{GEM} = 33 kV/cm, and above the GEM in the drift region E_{drift} = 430 V/cm.

compared to the previous model is explained by the electronic transparency of the GEM, which is about 63% for the electrical configuration simulated here, while it is 95% for a micro-mesh. 97.6% of the ions created under the micro-mesh are stopped by it, 0.2% are stopped by the GEM and 2.3% arrive in the drift space. According to the simulations, this is the same proportion as in the case of a simple MicroMEGAS without the addition of a GEM: the latter therefore does not seem capable of effectively stopping the ions. In addition, 21% of the ions created in the GEM travel to the drift electrode, resulting in an overall high IBF.

However, the GEM can be useful as a pre-amplification stage, as it multiplies electrons, thus the gain in the bottom micro-mesh can be reduced to keep the overall detector gain around 2000. Due to the diffusion of electrons in gas, several stochastically spaced avalanches are produced in the final amplification stage, which increases the spatial resolution in the readout plane.

7.3.3 MicroMEGAS and a micro-mesh bulked on a GEM (MMGEM)

In order to overcome the poor efficiency of the GEM in stopping ions, a micro-mesh is added above the GEM using the bulk technique (see section 6.2.2). The set of a micro-mesh placed above a GEM with a gap of only a few µm has never been studied before and constitutes the main object of the study presented here. The new detector geometry, represented in figure 7.9 and presented in section 6.2.4, is referred to as MMGEM.

The micro-mesh inherently has a good electronic transparency even while keeping its gain quite low. According to the simulations, the micro-mesh can be operated at a gain of 10 with an electronic transparency of about 75%. However, it is necessary that the top micro-mesh amplifies the electrons enough to compensate for those that are lost at the GEM below. An example of an avalanche is shown in figure 7.9. In this example, the electrons are amplified by a factor ~ 50 under the top micro-mesh, but only a fraction of them reach the GEM holes. There, the electrons are amplified again by a factor ~ 30, and only few of them escape the GEM holes

to drift to the bottom micro-mesh. Finally, most of the electrons multiply in the amplification space of the bottom micro-mesh. Several models were tested with a gap of 128, 256 and 660 µm between the GEM and the micro-mesh, which corresponds to the amplification zone of the top micro-mesh.

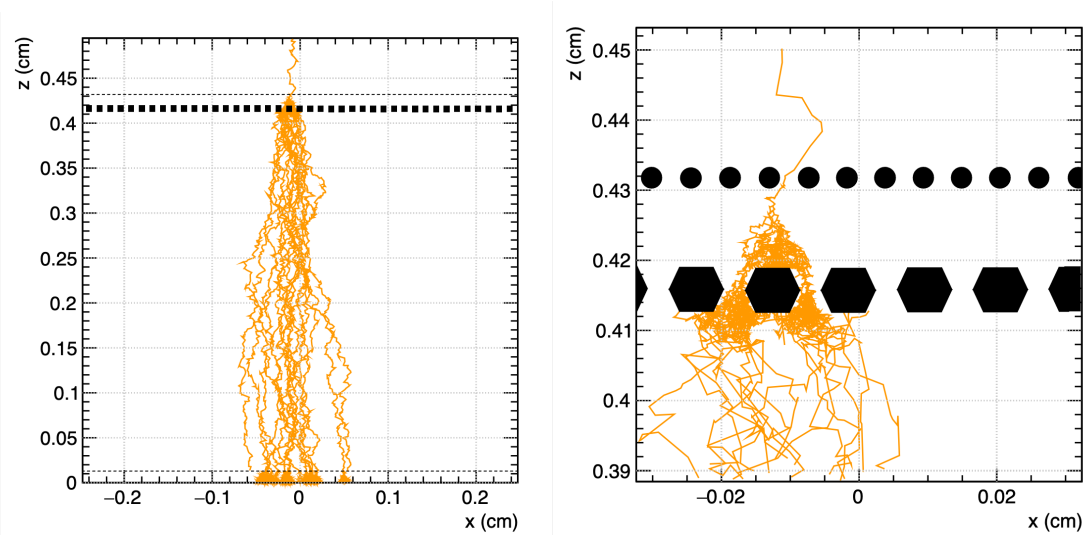

Figure 7.9: On the left, an electronic avalanche is shown in the configuration of a micro-mesh and a set of GEM and micro-mesh. On the right, a zoom is made on the pre-amplification region. In this model, the gap between the GEM and the top-micro-mesh is 128 µm.

7.4 Simulation results on MMGEM detectors

Exhaustive studies have been carried out to understand the mechanisms involved in the avalanche process and IBF of MMGEM detectors. In particular, the aim of these studies is to measure the gain and electronic transparency of each electrode, as well as their ability to stop feedback ions. One geometry tested in described in table 7.3. Figure 7.10 shows results for the geometric configuration given in table 7.3. This section describes several aspects tested in the simulation for MMGEM detectors.

electrode	position	parameters
drift electrode	z = 7 mm	plane in x, y
top micro-mesh	z = 4.316 mm	pitch = 63 µm, wire diameter = 18 µm, hole size = 45 µm
GEM	z = 4.128 mm to 4.188 mm	pitch = 126 µm, hole inner diameter = 50 µm, outer diameter = 70 µm
bottom micro-mesh	z = 128 µm	pitch = 63 µm, wire diameter = 18 µm, hole size = 45 µm
pads	z = 0	plane in x, y

Table 7.3: Geometric parameters of one MMGEM detector simulated.

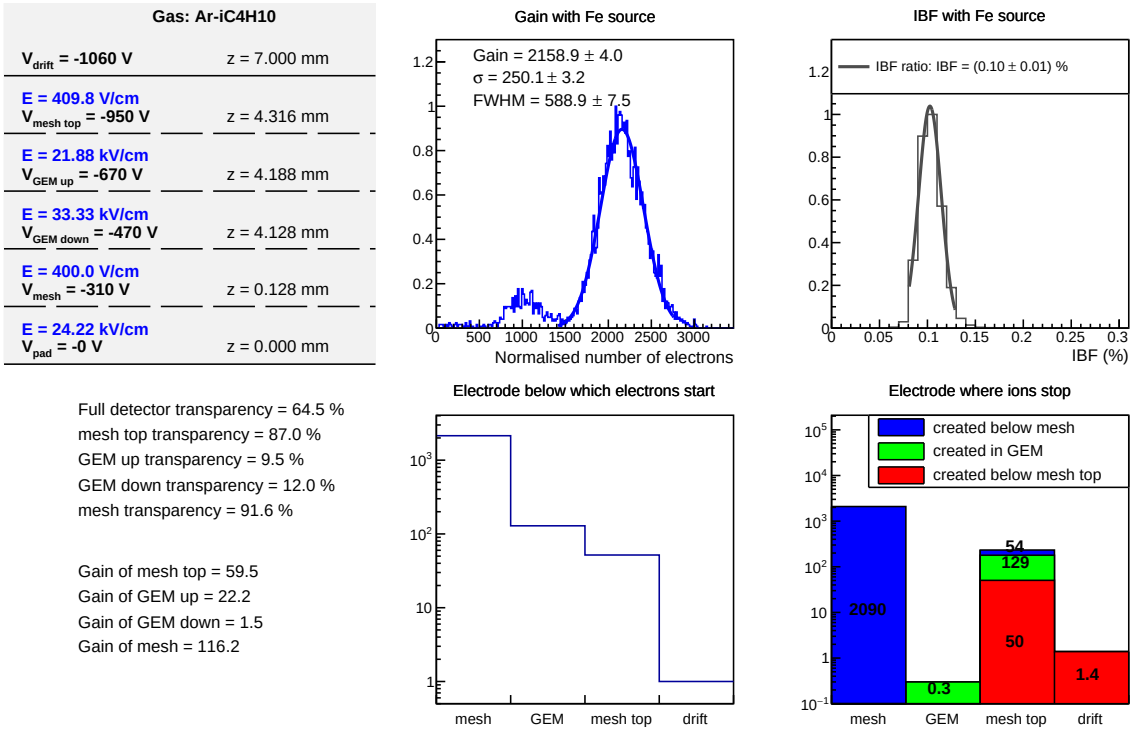

Figure 7.10: Top left: a representation of the electrical and geometric configuration of the detector; top middle: gain spectrum obtained with an iron source; top right: histogram of IBF; bottom left: calculation of the gain and transparency of the electrodes, bottom middle: the average number of electrons created at each stage of amplification per event; at the bottom right, the average number of ions that stop at each electrode per event.

7.4.1 Gain and transparency of each electrode

To obtain the gain of each electrode, the initial z position of electrons is used, since it defines as which stage they were created. Indeed, the gain of each electrode is given by

$$\text{Electrode gain} = \frac{N_{\text{created}}}{N_{\text{above}} \times \text{Electrode transparency}}$$

where N_{created} denotes the number of electrons created under the electrode in question, and N_{above} is the number of electrons present above, deduced by iteration.

The number of electrons created at each amplification stage N_{created} per event is also drawn at the middle bottom of the figure. The number of electrons created below "GEM up" and "GEM down" are summed up since these all come from the amplification of the GEM.

Given the transparencies and gains for each electrode, one can recover the average gain by multiplying the intrinsic gains and transparencies at each stage:

$$\text{Total gain} = (\text{G} \times \text{Tr})_{\text{mesh top}} \times (\text{G} \times \text{Tr})_{\text{GEM up}} \times (\text{G} \times \text{Tr})_{\text{GEM down}} \times (\text{G} \times \text{Tr})_{\text{mesh down}},$$

where $(\text{G} \times \text{Tr})$ denotes the product of gain and transparency of each electrode.

In the example given figure 7.10,

$$\text{Total gain} = (65.3 \times 0.857) \times (41.4 \times 0.114) \times (1.7 \times 0.142) \times (51.8 \times 0.777) = 2566$$

As a comparison, the gain obtained with the spectrum at top middle of the figure is 2159 with an energy resolution σ of 250. Therefore, the calculation of the overall gain expected using the intrinsic gains and transparencies of each electrode is 1.6 σ away from the actual value, which is reasonable.

7.4.2 Ion stopping power of each electrode

Finally, we are interested in the ion stopping power of each electrode, according to the stage at which they were created (see for example the bottom right of figure 7.10). This reveals the ionic transparency of each electrode. The contributions of the ions created below "GEM up" and "GEM down" are summed up.

The figure 7.10 at bottom right indicates that:

- The GEM is not effective at stopping ions. Only 0.3 on average are stopped there, among the $\sim$ 2300 ions created in the GEM or below, under the bottom micro-mesh.
- The top micro-mesh however seems to solve this issue: more than 99% of ions created in the GEM (129 in $\sim$ 130) are stopped there. In addition, the 3% (54 out of 2144) of ions created under the bottom micro-mesh and which have passed through it are stopped by the top micro-mesh.
- The only ions which reach the drift electrode come from the amplification under the top micro-mesh: as for a single micro-mesh, about 3% of them drift back. In this example, for an avalanche created by a single electron, this corresponds to between 1 and 2 ions in the drift zone for a gain of $\sim$ 2200.

7.4.3 Other results

Other geometric models were simulated, with the same bottom micro-mesh and GEM as given in table 7.3. Different gaps between the GEM and the top micro-mesh were simulated. Finally, the top micro-mesh is either 45/18 or 70/30.

Some results for these different models are presented table 7.4. The number N_i of feedback ions per primary electron corresponds to the product of the gain and the IBF. The electric fields are the same for each detector model everywhere else than under the top mesh where the field has been adapted in order to keep a total gain of the order of 2000. These electric fields are given in table 7.5.

gap	**top mesh specifications**	**transparency**	**total gain**	**resolution** $= \frac{\sigma}{\text{gain}}$	**IBF**	N_i
128 µm	45/18	70.8%	2555	9.9%	0.12%	3
128 µm	70/30	73.7%	1879	10.6%	0.21%	4
256 µm	45/18	66.0%	1995	9.7%	0.21%	4
660 µm	45/18	57.8%	2198	10.0%	0.68%	15

Table 7.4: Examples of simulation results with different gaps between the GEM and top micro-mesh. The electric fields are fixed in the bottom micro-mesh and in the GEM, while the potential differences between the GEM and the top micro-mesh are adapted so as to keep a gain of around 2000. The first column corresponds to the gap between the GEM and the top micro-mesh. The last column, N_i, is the number of feedback ions per e^- resulting from the first ionization.

gap between the GEM and top micro-mesh	**top mesh specifications**	$E_{\text{mesh top}}$	E_{drift}
128 µm	45/18	20 kV/cm	410 V/cm
128 µm	70/30	20 kV/cm	410 V/cm
256 µm	45/18	14 kV/cm	390 V/cm
660 µm	45/18	10 kV/cm	390 V/cm

Table 7.5: Electric field configurations corresponding to the results presented table 7.4. The field below the bottom micro-mesh, in the transfer region and inside the GEM are fixed: E_{amp} = 20 kV/cm, E_{transfer} = 500 V/cm and E_{GEM} = 33 kV/cm.

Even if the electronic transparency with the mesh 70/30 is higher, the gain of this mesh is lower than for a 45/18 mesh. In addition, according to table 7.4, the mesh 70/30 stops half as many ions as the 45/18 mesh.

Table 7.4 shows that all the simulated models allows us to reach IBF values lower than 0.7% with gains of about 2000. For models using a gap smaller than 256 µm, the IBF is even smaller than 0.3%, hence the new structure appears very promising.

7.5 Summary

Simulations are carried out first on simple detector models using a MicroMEGAS only, then electrodes are added step by step. The GEM appears inefficient in stopping ions, however, it is used as a pre-amplification stage that scatters the avalanche, resulting in a better spatial reconstruction in the readout plane. Several MMGEM models are simulated and appear very promising in terms of energy resolution and of IBF for gains of about 2000.

As a consequence, two prototypes were built at the Commissariat à l'Énergie Atomique et aux Énergies Alternatives (CEA). Measurements on these two prototypes are presented in the next chapter.

Bibliography

[1] J. Adolfsson et al. The upgrade of the ALICE TPC with GEMs and continuous readout. *JINST*, 16(03):P03022, 2021. doi: 10.1088/1748-0221/16/03/P03022.

[2] G. Dellacasa et al. ALICE: Technical design report of the time projection chamber. 1 2000.

[3] J. Alme et al. The ALICE TPC, a large 3-dimensional tracking device with fast readout for ultra-high multiplicity events. *Nucl. Instrum. Meth. A*, 622:316–367, 2010. doi: 10.1016/j.nima.2010.04.042.

[4] Klaus Dehmelt. The sPHENIX TPC Project. *PoS*, MPGD2017:044, 2019. doi: 10.22323/1.322.0044.

[5] Henry Klest. Overview and design of the sPHENIX TPC. *J. Phys. Conf. Ser.*, 1498:012025, 2020. doi: 10.1088/1742-6596/1498/1/012025.

[6] H. Schindler and R. Veenhof. Garfield++ – Simulation of tracking Detectors. URL http://cern.ch/garfieldpp.

[7] I. Smirnov. Interactions of particles with gases. URL http://cern.ch/heed.

[8] I. B. Smirnov. Modeling of ionization produced by fast charged particles in gases. *Nucl. Instrum. Meth. A*, 554:474–493, 2005. doi: 10.1016/j.nima.2005.08.064.

[9] S. Biagi. Magboltz - Transport of electrons in Gas Mixture. URL http://cern.ch/magboltz.

[10] S. F. Biagi. Monte Carlo simulation of electron drift and diffusion in counting gases under the influence of electric and magnetic fields. *Nucl. Instrum. Meth. A*, 421(1-2):234–240, 1999. doi: 10.1016/S0168-9002(98)01233-9.

[11] T. Zerguerras et al. Understanding avalanches in a Micromegas from single-electron response measurement. *Nucl. Instrum. Meth. A*, 772:76–82, 2015. doi: 10.1016/j.nima.2014.11.014.

Chapter 8

Measurements

Contents

8.1 Description of the setup 172

8.1.1 Detector construction 172

8.1.2 Setup configuration 172

8.1.3 Measuring ion backflow with currents 174

8.2 Measurements with the 660-µm-gap detector 176

8.2.1 Study of the bottom micro-mesh 176

8.2.2 Study of the GEM 179

8.2.3 Study of the top micro-mesh 186

8.2.4 Gain after amplification at all stages 187

8.3 Measurements with the 128-µm-gap detector 192

8.3.1 Study of the top micro-mesh alone 192

8.3.2 Gain after amplification at all stages 194

8.4 Contamination on the drift electrode 197

8.5 Summary 199

Bibliography 200

The numerical studies presented in the previous chapter suggest which detector geometry could be the most optimal to reduce the ion backflow while keeping a reasonable energy resolution. Two prototypes were produced and tested. The first one has a gap of 660 µm between the GEM and the top micro-mesh, while the second one has a smaller gap of 128 µm. This chapter presents the characterization studies of these prototypes. First, the setup common to the two detectors used to make the measurements is introduced. Then we present the analysis of the 660-µm-gap detector to understand the amplification mechanisms involved in each electrode and the study of the 128-µm-gap detector. Finally, a complementary study is performed to evaluate systematic errors in our measurements.

8.1 Description of the setup

8.1.1 Detector construction

Each prototype has an active area $\sim 12 \times 12$ cm^2. The detectors have 256 strips on the anode plane with a 500 µm pitch, that can be read using the DREAM electronics [1, 2].

The bottom micro-meshes are mounted in the detectors using the bulk technology [3] at the DEDIP MPGD workshop. All micro-meshes are woven wire mesh made of stainless steel (see photos figure 8.1). The GEMs are produced at CERN. The GEM Polyimide foil is perforated by photo-lithographic processing, forming a dense, regular pattern of double-conical holes. The holes have an inner diameter of 50 µm, an outer diameter of 70 µm, and a pitch of 140 µm. Finally, the top micro-meshes are assembled on the GEMs using the bulking method. The gaps between the GEM and the top micro-mesh vary for the two prototypes. Table 8.1 gives the values of the gaps, along with other design parameters.

	model 1	**model 2**
gap between the GEM and top micro-mesh	660 µm	128 µm
top micro-mesh specifications	45/18	70/30
GEM specifications	inner diameter = 50 µm outer diameter = 70 µm pitch = 140 µm	
bottom micro-mesh specifications	45/18	

Table 8.1: Geometric parameters of prototypes tested in the laboratory. For the micro-meshes specifications, the numbers indicate the size of a side of the square hole / wire diameter in µm.

The ensemble of the top micro-mesh bulked on the GEM and the drift electrode are separated by pillars and then screwed to fix the structure. They are movable by hand when opening the detector, so electrodes can be interchanged with ease.

8.1.2 Setup configuration

Measurements are carried out using a ^{55}Fe source of 300 MBq. The ^{55}Fe decays into manganese by electron capture emitting 5.9 keV (K_α) and 6.4 keV (K_β) characteristic X-rays and the photons then convert to electrons inside the detector by photo-electric effect with gas atoms. The

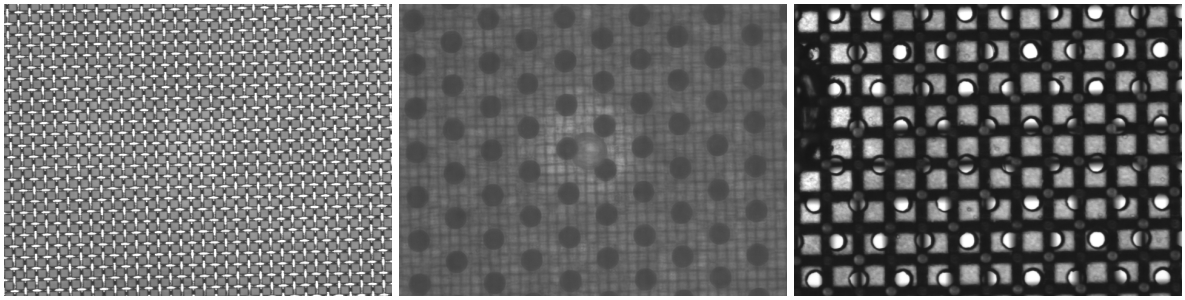

Figure 8.1: Left: picture of the top micro-mesh (45/18); middle: picture of the micro-mesh (45/18) on top of the GEM with 660 µm gap (plots are 120 µm thick); right: picture of the micro-mesh (70/30) on top of the GEM with 128 µm gap.

detector is placed in a Faraday cage to reduce electronic background noise, and the gas mixture injected is argon with 5% isobutane. A sketch of the experimental setup is shown in figure 8.2.

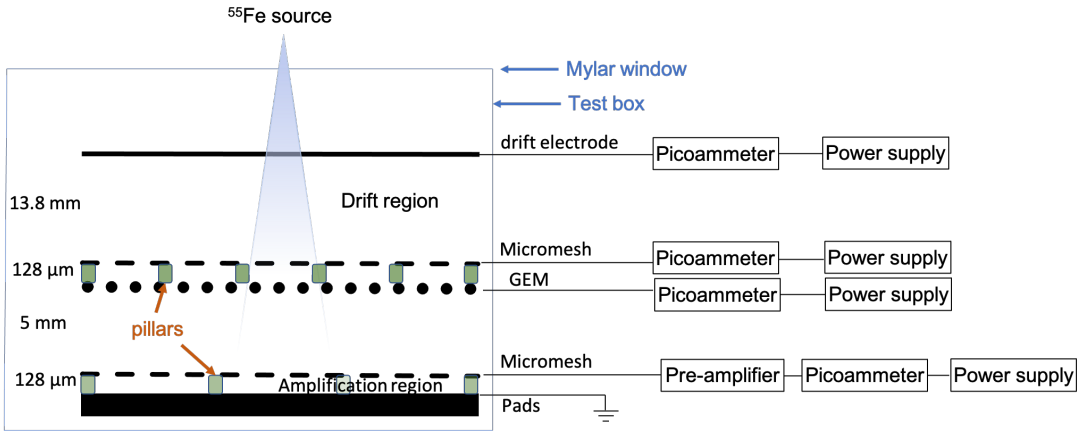

Figure 8.2: Schematic diagram of experimental setup for ion backflow measurement.

The anode (pads) is grounded, and all other electrodes are biased with negative high voltages provided by the CAEN model N471A power supply.

In order to recover the energy deposited in the detector by the photons, the currents at the output of the micro-mesh are integrated and amplified by first passing through a pre-amplifier [4] then a chain of electronic amplification (ORTEC group). Spectra are obtained with a MultiChannel Analyzer module [5], which is characterized by a high-speed analog-to-digital converter (100 MHz, 16 bit) with digital pulse height measurement, allows to read up to 8000 data channels and has an input range of 0 to 1 V or 0 to 10 V (software selectable). Finally, they are recorded with DPPMCA software [6].

In order to measure the IBF, electric currents on all the electrodes are measured with a Pico-Logic multi-channel picoammeter [7] and recorded using a custom python acquisition software (see figure 8.4). Currents are recorded for 60 seconds with 100 points per second.

The gas mixture injected in the detector, argon-isobutane (95/5), is premixed in a bottle and circulates to the detector through PCV tubes with a flow rate of 3 to 5 L/h.

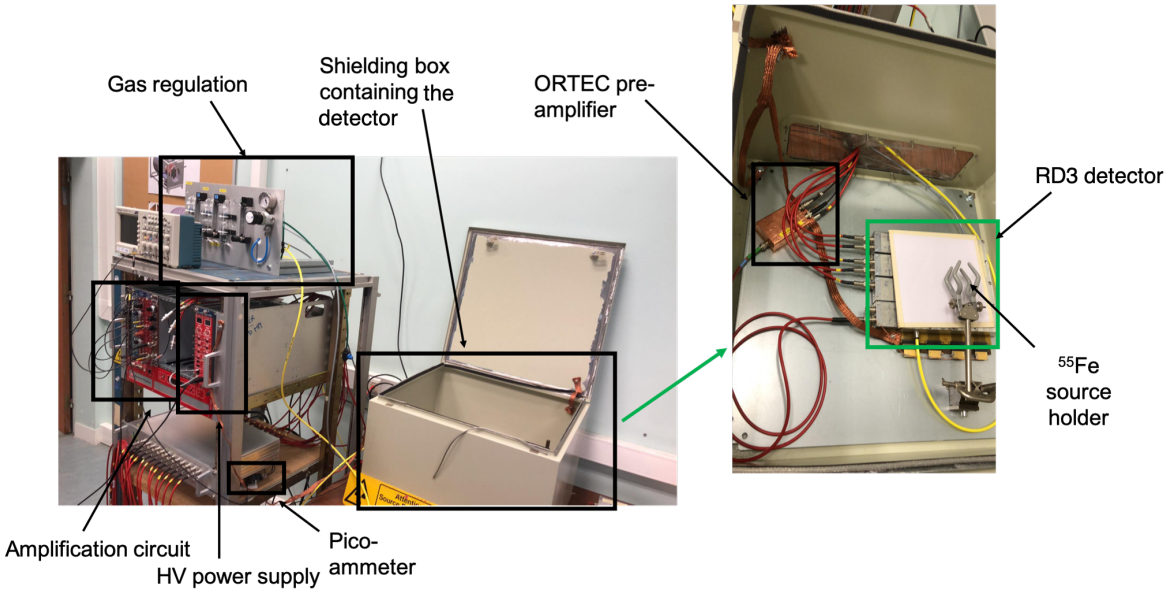

Figure 8.3: View of experimental setup.

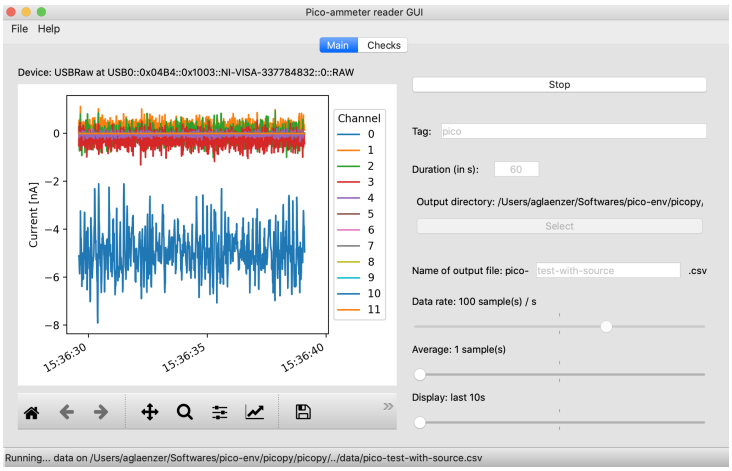

Figure 8.4: Screenshot of the python window designed to monitor currents measurements.

8.1.3 Measuring ion backflow with currents

In section 7.2.2, the IBF was defined as :

$$\text{IBF} = \frac{N_{\text{ions}}^{\text{back}}}{N_{\text{ions}}^{\text{total}}} \tag{8.1}$$

where $N_{\text{ions}}^{\text{back}}$ is the number of ions that drifted back to the drift space and $N_{\text{ions}}^{\text{total}}$ is the total number of ions created during the avalanche processes. These two numbers can be estimated by measuring the displacement of the average current on each electrode with (i^{with}) and without (i^{without}) the source, since $i^{\text{with}} - i^{\text{without}} \propto N_{\text{ions}}$. The subtraction of i^{without} is necessary in order to measure the effect of the iron source only. The average currents, i_d^{with} and i_d^{without} on the drift electrode, and i_m^{with} and i_m^{without} on the bottom micro-mesh, are estimated by fitting a Gaussian function to the recorded current (see figure 8.5).

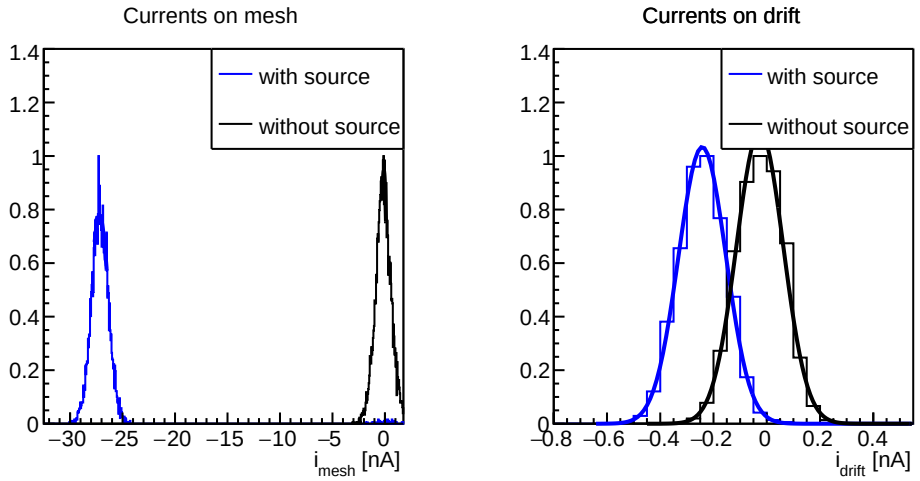

Figure 8.5: Blue curves represent measurements of currents with the source, while the black curves are the data taken without the iron source. A Gaussian function is fitted to the data, and the mean value of the current is taken to be the mean of the Gaussian.

However, the ions present in the drift region are those that drifted back after the amplification ($N_{\text{ions}}^{\text{back}}$), and one from the first ionisation ($N_{\text{ions}}^{\text{primary}}$). Hence,

$$(i_d^{\text{with}} - i_d^{\text{without}}) \propto (N_{\text{ions}}^{\text{back}} + N_{\text{ions}}^{\text{primary}}) \tag{8.2}$$

Therefore,

$$\text{IBF} = \frac{N_{\text{ions}}^{\text{back}}}{N_{\text{ions}}^{\text{total}}} = \frac{N_{\text{ions}}^{\text{back}} + N_{\text{ions}}^{\text{primary}}}{N_{\text{ions}}^{\text{total}}} - \frac{N_{\text{ions}}^{\text{primary}}}{N_{\text{ions}}^{\text{total}}} \tag{8.3}$$

Since $\dfrac{N_{\text{ions}}^{\text{primary}}}{N_{\text{ions}}^{\text{total}}} \equiv \dfrac{1}{\text{Gain}}$,

$$\boxed{\text{IBF} = \frac{i_d^{\text{with}} - i_d^{\text{without}}}{i_m^{\text{with}} - i_m^{\text{without}}} - \frac{1}{\text{Gain}}} \tag{8.4}$$

In order to compute the uncertainty on the IBF (ΔIBF), let A and B be such as

$$\begin{cases} A = i_d^{\text{with}} - i_d^{\text{without}} \\ B = i_m^{\text{with}} - i_m^{\text{without}} \end{cases}$$

So

$$\begin{cases} (\Delta A)^2 = (\Delta i_d^{\text{with}})^2 + (\Delta i_d^{\text{without}})^2 \\ (\Delta B)^2 = (\Delta i_m^{\text{with}})^2 + (\Delta i_m^{\text{without}})^2 \end{cases}$$

The uncertainty on the IBF is then given by:

$$\Delta\text{IBF} = \sqrt{\left(\Delta\frac{A}{B}\right)^2 + \left(\Delta\frac{1}{\text{Gain}}\right)^2} \tag{8.5}$$

$$\text{with} \begin{cases} \left(\Delta\frac{A}{B}\right)^2 = \left(\frac{A}{B}\right)^2 \times \left[\left(\frac{\Delta A}{A}\right)^2 + \left(\frac{\Delta B}{B}\right)^2\right] \\ \left(\Delta\frac{1}{\text{Gain}}\right)^2 = \left(\frac{1}{\text{Gain}}\right)^2 \times \left(\frac{\Delta\text{Gain}}{\text{Gain}}\right)^2 \end{cases}$$

where ΔGain is the statistical uncertainty on the gain.

Finally,

$$\Delta\text{IBF} = \left[\left(\frac{i_d^{\text{with}} - i_d^{\text{without}}}{i_m^{\text{with}} - i_m^{\text{without}}}\right)^2 \times \left(\frac{(\Delta i_d^{\text{with}})^2 + (\Delta i_d^{\text{without}})^2}{(i_d^{\text{with}} - i_d^{\text{without}})^2} + \frac{(\Delta i_m^{\text{with}})^2 + (\Delta i_m^{\text{without}})^2}{(i_m^{\text{with}} - i_m^{\text{without}})^2}\right) + \frac{(\Delta\text{Gain})^2}{(\text{Gain})^4}\right]^{1/2} \quad (8.6)$$

8.2 Measurements with the 660-µm-gap detector

The first prototype manufactured at IRFU / DEDIP (CEA) has a gap between the GEM and the bulked micro-mesh of 660 µm, and the top micro-mesh has 45 µm hole size and 18 µm in wire diameter (45/18). This section presents the performance of this detector by characterizing each amplification stage.

8.2.1 Study of the bottom micro-mesh

First, the MicroMEGAS alone is characterized. In order to simplify the measurements, the bulked micro-mesh and GEM assembly is placed at the top of the detector, and the drift electrode is inserted above the mesh (see figure 8.6). In order to prevent events where the photon would convert above the drift electrode, the voltage on the GEM and top mesh is kept slightly higher than that of the drift: the electrons resulting from ionizations above the drift electrode would then go in the other direction.

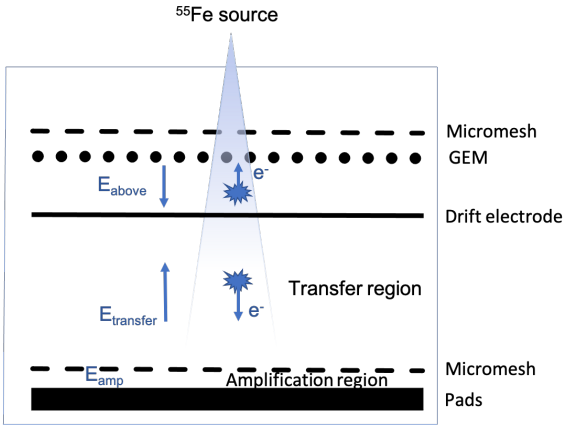

Figure 8.6: Configuration of the detector to study the bottom micro-mesh.

Amplification curve

The goal is to characterize the amplification of the micro-mesh when the amplification field is increased. Thus, the transfer field (E_{transfer}) - between the bottom micro-mesh and the drift electrode, see figure 8.6 - is set at 400 V/cm for all measurements while the amplification field (E_{amp}) under the bottom micro-mesh is increased.

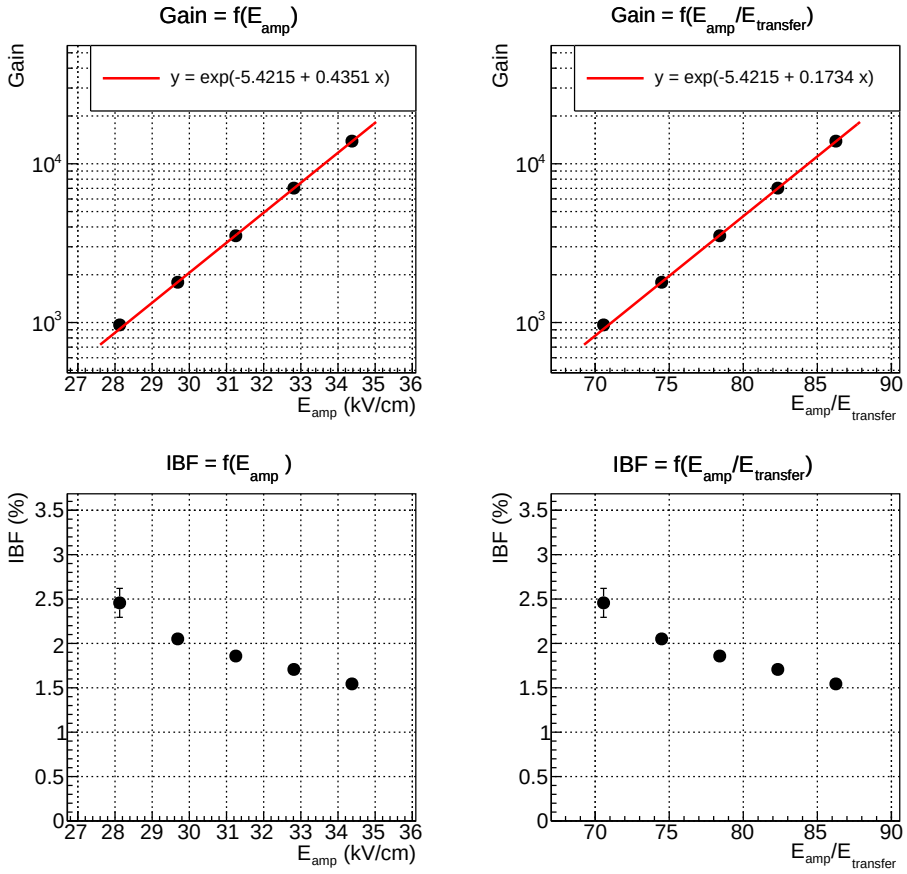

Figure 8.7: Top: gain curve of the bottom micro-mesh as a function of the amplification field E_{amp} (left) and the field ratio $E_{\text{amp}}/E_{\text{transfer}}$ (right). Bottom: same for the IBF.

Transparency

In a second step, the transparency of the mesh is studied. It consists in evaluating the capacity of the micro-mesh to let electrons pass for a given amplification field E_{amp} - and therefore a fixed gain - when varying the transfer field E_{transfer}. The transparency is obtained by assuming that it reaches the level of 100% at its maximum. All transparency values shown in figure 8.8 at top correspond to the measured gain normalized with the maximum gain, where full transparency is expected.

When the ratio of the electric fields in the amplification gap and in the transfer region ($E_{\text{amp}}/E_{\text{transfer}}$) increases, the electronic transparency of the micro-mesh improves. However, as the electric field in the transfer region becomes lower, the chances for ions and electrons to recombine grow, and less electrons are collected. Consequently, the gain of the detector decreases. Therefore, the gain appears to be constant between two threshold values determining

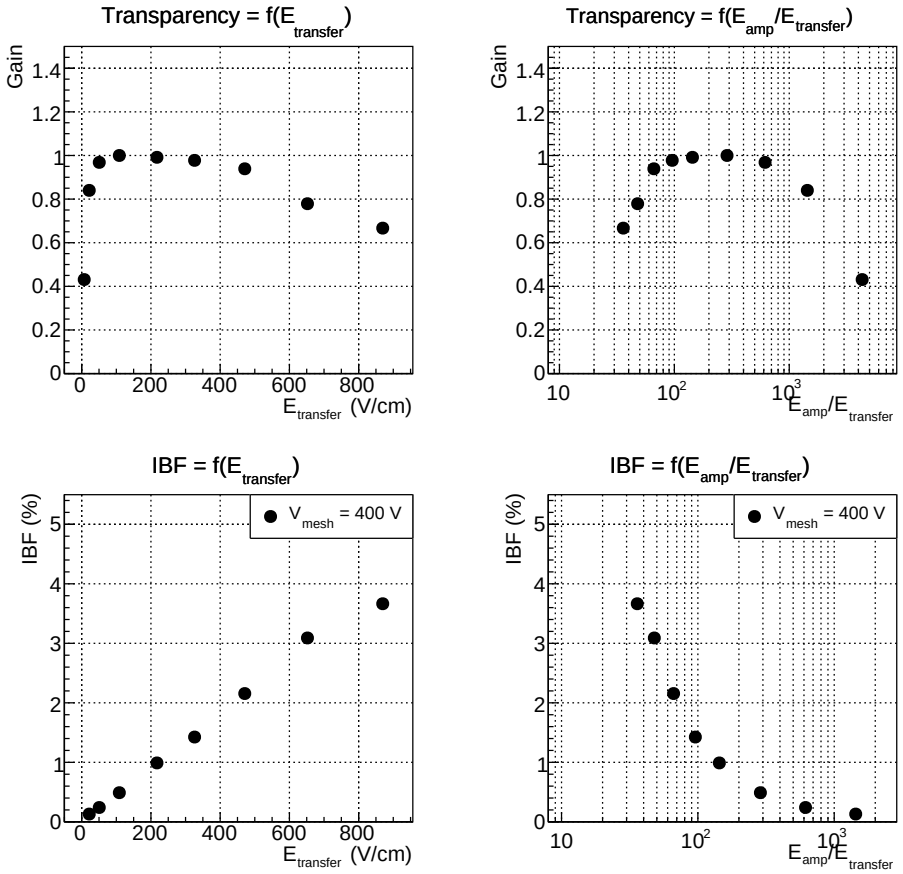

Figure 8.8: Top (bottom) transparency (IBF) of the bottom micro-mesh as function of the transfer field E_{transfer} (left) and the field ratio $E_{\text{amp}}/E_{\text{transfer}}$ (right).

recombination for high ratios $E_{\text{amp}}/E_{\text{transfer}}$ and primary electrons absorbed in the micro-mesh for low ratios $E_{\text{amp}}/E_{\text{transfer}}$. This transparency plateau displays the optimal configurations for the operation of the bottom micro-mesh.

On the other hand, IBF values seem to increase linearly with E_{transfer} (see figure 8.8 at bottom). The ionic transparency, defined as the capacity of micro-mesh to let ions pass though, appears to scale linearly with $E_{\text{transfer}}/E_{\text{amp}}$, implying that a low transfer field is required to operate the detector with a low IBF from the bottom micro-mesh.

8.2.2 Study of the GEM

The detector is now reassembled according to the configuration shown in figure 8.9. Since we want to study the GEM, events of interest are the photons that convert into electrons in the region between the GEM and the top micro-mesh (represented by the brown object). Photons can also convert in the drift region or the transfer region. The voltage applied on the drift electrode is slightly higher than on the top micro-mesh so that electrons created from ionizations in the drift region would drift upwards. On the other hand, photons converting in the transfer region (green object) are more likely to occur since the transfer region is 11 times larger than the region between the GEM and the top micro-mesh. These events are considered a contamination since they are not amplified in the GEM.

In addition, pile-up events - at least two photons that were recorded at the same time - are likely to occur in the transfer region, where the rate of events is the largest. Details about pile-up studies are given in appendix H.1.

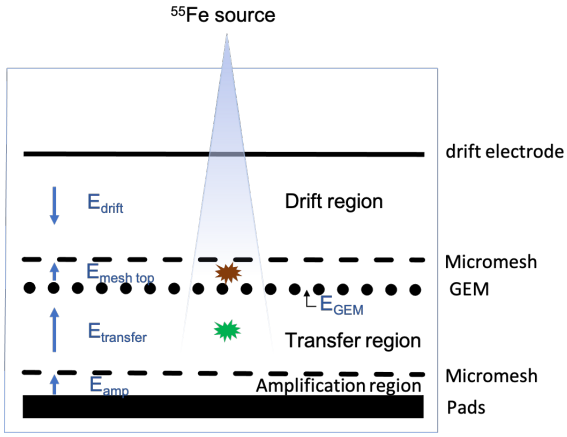

Figure 8.9: Representation of the detector with the electric field configuration used to study the GEM.

When studying the GEM, the IBF is estimated by replacing the current i_d in the equations (8.4) and (8.6) by the current recorded on the top mesh $i_{\text{mesh top}}$. The IBF is impacted by all the photons which converted in the transfer zone. Thus, to understand the capacity of the GEM to stop the ions, it is necessary to look at the measurements in parallel with those of figure 8.8.

Extraction of electrons from the GEM

The first characteristic studied is the extraction of electrons from the GEM, that is, the proportion of electrons in the GEM which manage to leave it. Indeed, the electrons encounter at the exit of the GEM a much less intense electric field and can then be trapped in the GEM by following the field lines, as can be seen in the simulations (figure 7.9). For this purpose, the detector is in a configuration for which the gains of the bottom micro-mesh and of the GEM are fixed. The field $E_{\text{mesh top}}$ is arbitrarily fixed at 300 V/cm, so that the field ratio - $E_{\text{GEM}}/E_{\text{mesh top}} \sim 130$ - would maximize the GEM transparency (see in the following figure 8.16), and the transfer field E_{transfer} is changed.

The gain in the bottom micro-mesh is approximately 3500: the higher the gain, the higher the average current on the drift electrode with the source, and the more precise the measurements of the IBF. It is preferable to increase the gain of the bottom micro-mesh instead of that

of the GEM since electrons created below the bottom micro-mesh can be stopped either by the micro-mesh itself or the GEM, hence a lower IBF. Figure 8.10 shows an example of a ^{55}Fe spectrum. The contributions to the gain of the different amplification regions are fitted with Gaussian functions.

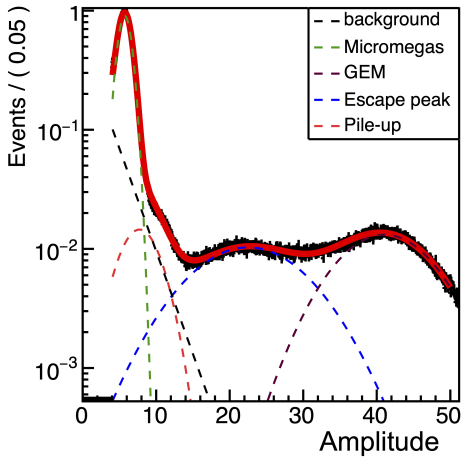

Figure 8.10: The peak of the photons which convert in the transfer zone is shown in green. Pile-up events from the transfer region are shown in red. Events of interest above the GEM are only visible on logarithmic scale, given their low rate compared to that of the transfer region. The iron escape peak is drawn in blue.

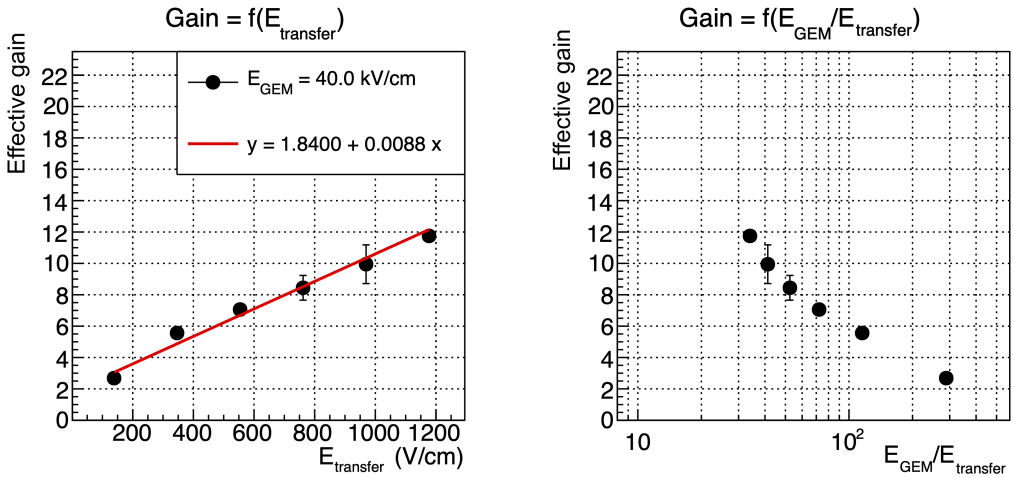

Figure 8.11: Extraction of electrons from the GEM as a function of the transfer field E_{transfer} (left) and the field ratio $E_{\text{GEM}}/E_{\text{transfer}}$ (right).

The gain of the GEM is convoluted with its electron extraction efficiency and its electron transparency. This quantity is obtained by dividing the mean of the GEM peak (brown curve in the figure 8.10) with the mean of the bottom micro-mesh peak (green curve that accounts for events represented with the green object in figure 8.9). The measurements are shown in figure 8.11 as a function of the transfer field E_{transfer} and of the field ratio $E_{\text{GEM}}/E_{\text{transfer}}$. It appears that the proportion of extracted electrons scales linearly with E_{transfer}, hence a linear fit is performed. The behavior of the extracted electrons is similar to the ionic transparency of the

bottom micro-mesh (see figure 8.8). The probability of a charge entering a lower field region to escape depends linearly on this low field.

The following analysis consists in deconvoluting the proportion of electrons extracted from the GEM from the two other components (intrinsic gain and transparency). Let P_e be the proportion of electrons extracted, Tr the transparency of the GEM, and G_i its intrinsic gain. It is assumed that Tr depends only on $E_{\text{GEM}}/E_{\text{mesh top}}$, P_e only on the field ratio $x = E_{\text{GEM}}/E_{\text{transfer}}$ and G_i only on E_{GEM}. The goal is to estimate the evolution of electron extraction $P_e(x)$. The fit to the data (figure 8.11) gives the following equation with two unknowns $G_i(E_{\text{GEM}})$ and $Tr(E_{\text{GEM}}/E_{\text{mesh top}})$ (fixed since E_{GEM} and $E_{\text{mesh top}}$ are fixed).

$$G_i(E_{\text{GEM}}) \times P_e(x) \times Tr(E_{\text{GEM}}/E_{\text{mesh top}}) = \alpha_1 + \beta_1 \times E_{\text{transfer}} \tag{8.7}$$

$$= \alpha_1 + \frac{\beta_1}{(E_{\text{GEM}}/E_{\text{transfer}})} \times E_{\text{GEM}} \tag{8.8}$$

$$= \alpha_1 + \frac{\beta_1}{x} \times E_{\text{GEM}} \tag{8.9}$$

with α_1 = 1.840 and β_1 = 0.0088 [V/cm]$^{-1}$, $E_{\text{mesh top}}$ = 303.0 V/cm and E_{GEM} = 40 kV/cm.

From equation 8.9, one obtains

$$\boxed{P_e(x) = \frac{1}{A}\left(\alpha_1 + \frac{\beta_1}{x} \times [E_{\text{GEM}} = 40 \text{ kV/cm}]\right) \text{ with } x = E_{\text{GEM}}/E_{\text{transfer}}} \tag{8.10}$$

where $A = G_i(E_{\text{GEM}}) \times Tr(E_{\text{GEM}}/E_{\text{mesh top}})$ is a factor constrained using simulations. Let us take the figure 7.10: for $x_0 = E_{\text{GEM}}/E_{\text{transfer}}$ = 83.33, the extraction of electrons from the GEM corresponds to $P_e^{\text{sim}}(x_0 = 83.33)$ = 12.0%. Thus,

$$A = \left(\alpha_1 + \frac{\beta_1}{x_0} \times E_{\text{GEM}}\right) / P_e^{\text{sim}}(x_0) \tag{8.11}$$

$$A = 50.1 \tag{8.12}$$

Finally, the parameterization of the proportion of electrons extracted from the GEM given by equation 8.10 is shown in figure 8.12.

The measurements of IBF are presented in figure 8.13. The measurements on the bottom micro-mesh only (figure 8.8) are also shown in red on the same figure for comparison. When E_{transfer} increases, the ionic transparency of the bottom micro-mesh increases as well. Hence, the GEM "sees" more ions moving up towards it. By comparing the two sets of measurements, it appears that the IBF increases less quickly with a GEM than in a simple MicroMEGAS configuration, which suggests that the GEM is successful at stopping ions. However, the overall IBF still increases, implying that the GEM does not stop enough ions to compensate for the IBF of the bottom micro-mesh.

Gain curve of the GEM

In order to measure the gain of the GEM, the field of the GEM is increased, at fixed transfer field E_{transfer} and fixed gain of the bottom micro-mesh $G_{\text{mesh down}}$ = 460. The fields in the transfer

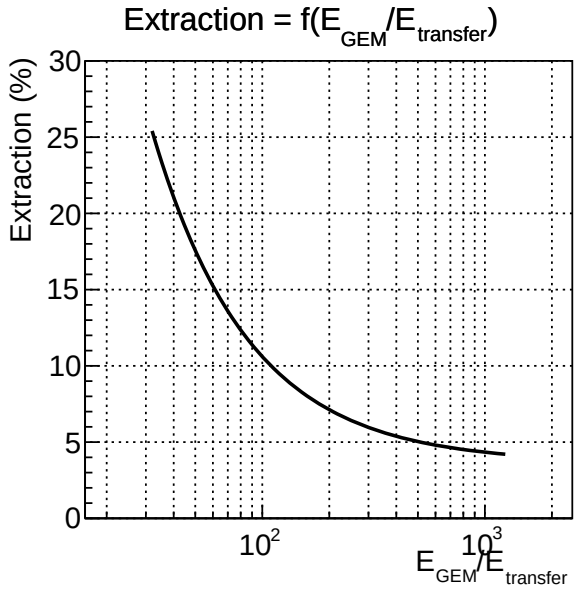

Figure 8.12: Parametrizations of the proportion of electrons extracted as a function of $E_{\text{GEM}}/E_{\text{transfer}}$.

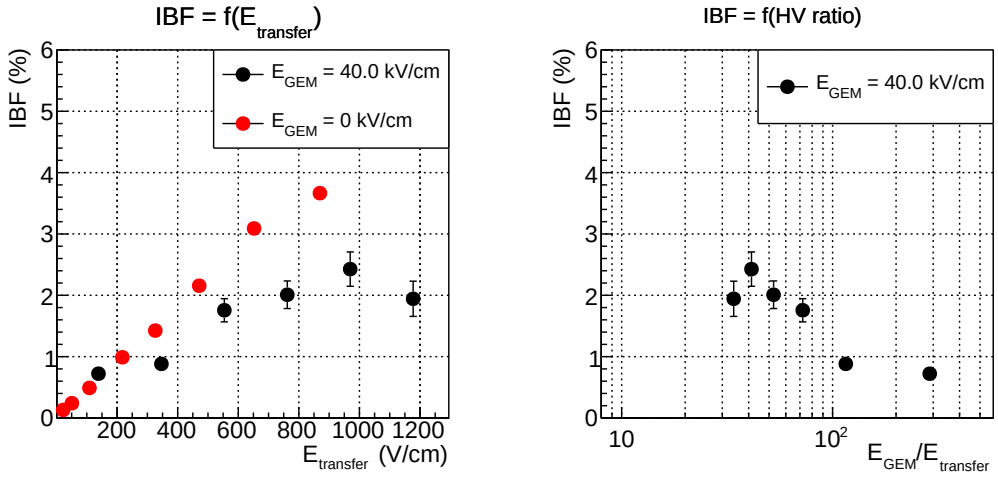

Figure 8.13: Ion backflow measurements as a function of the transfer field (left) and of the field ratio between the GEM and the transfer zone (right). The red points come from figure 8.8, and represent the measurements in single-stage MicroMEGAS configuration. The black markers represent the measurements of IBF when the top micro-mesh is used as a drift electrode, and the gain in the GEM is fixed.

region E_{transfer} = 485 V/cm and below the bottom micro-mesh $E_{\text{amp}} \approx 27$ kV/cm were chosen in order to maximize simultaneously the transparency of the micro-mesh $Tr_{\text{mesh down}} \approx 0.9$ (according to figure 8.8) and the extraction of electrons from the GEM, while keeping a total gain $< 10^4$ after amplification in the GEM. The field between the top micro-mesh and the GEM $E_{\text{mesh top}}$ = 306 V/cm is fixed and chosen so that the ratio $E_{\text{GEM}}/E_{\text{mesh top}}$ is high enough to maximize the transparency of the GEM (see figure 8.16). In the measured E_{GEM} interval, the ratio $E_{\text{GEM}}/E_{\text{mesh top}}$ ranges from 113 to 147, so according to the figure 8.16, $Tr(E_{\text{GEM}}/E_{\text{mesh top}}) \approx$

0.4.

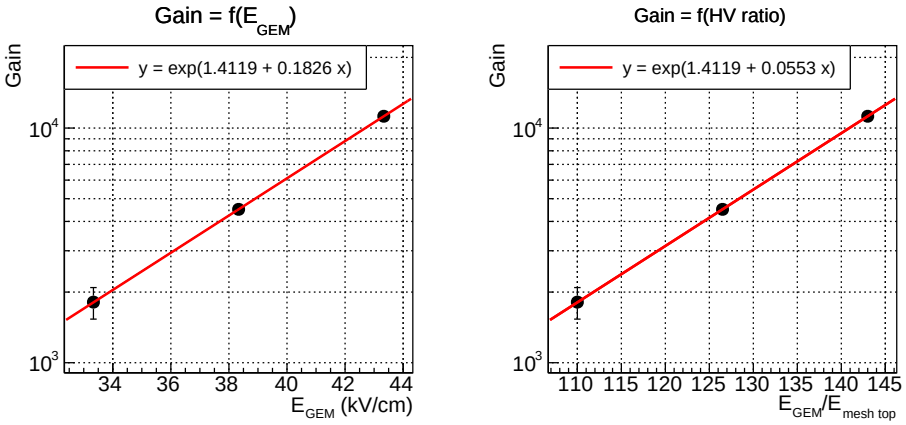

Figure 8.14: Gain curve of the GEM as a function of the electric field E_{GEM} (left) and of the field ratio $E_{\text{GEM}}/E_{\text{mesh top}}$ (right). Here the gain of the bottom micro-mesh is fixed at 460, its electronic transparency is fixed at 90%.

Figure 8.14 shows the gain measurements, where the gain obtained is actually the product of:

- the electron extraction coefficient of the GEM
- the gain of the GEM
- the electronic transparency of the GEM
- the gain of the bottom micro-mesh
- the electronic transparency of the bottom micro-mesh

The following analysis consists in separating the intrinsic gain of the GEM and all other factors, using the measurements presented in figure 8.14 and equation 8.10. The fit to the data (figure 8.14) give

$$\begin{aligned} G_i(E_{\text{GEM}}) \times P_e(E_{\text{GEM}}/E_{\text{transfer}}) \times Tr(E_{\text{GEM}}/E_{\text{mesh top}}) \times G_{\text{mesh down}} \times Tr_{\text{mesh down}} \\ = \exp(\alpha_2 + \beta_2 \times E_{\text{GEM}}) \end{aligned} \tag{8.13}$$

where $\alpha_2 = 1.4119$ and $\beta_2 = 0.1826$ [kV/cm]$^{-1}$. $P_e(E_{\text{GEM}}/E_{\text{transfer}})$ is given by equation 8.10 and all other gain and transparency factors are fixed.

Hence

$$\boxed{G_i(E_{\text{GEM}}) = \frac{\exp(\alpha_2 + \beta_2 \times E_{\text{GEM}})}{P_e(E_{\text{GEM}}/[E_{\text{transfer}} = 485 \text{ V/cm}]) \times Tr \times G_{\text{mesh down}} \times Tr_{\text{mesh down}}}} \tag{8.14}$$

The parameterization of the intrinsic gain of the GEM given by equation 8.14 is shown in figure 8.15.

Transparency of the GEM

The last subject of study concerning the GEM is its transparency, that is to say its capacity to let through the electrons arriving from above depending on the field between the GEM and

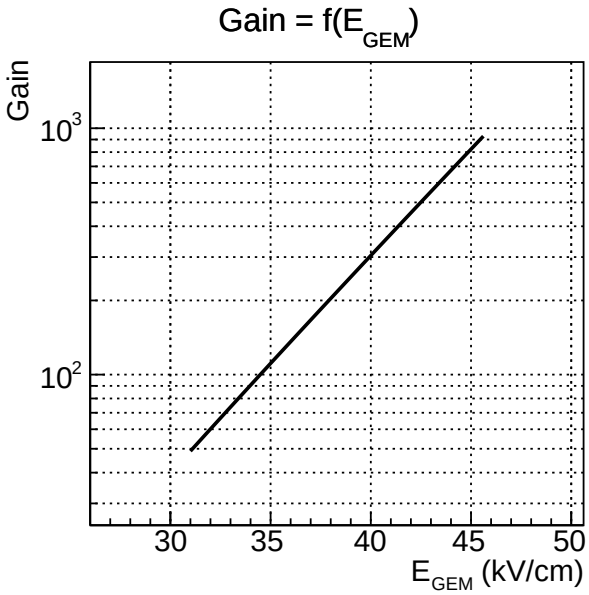

Figure 8.15: Parametrizations of the intrinsic gain of the GEM as a function of E_{GEM}.

the top micro-mesh $E_{\text{mesh top}}$. Besides $E_{\text{mesh top}}$ which is increased, all electric fields are fixed: $E_{\text{amp}} \approx 31$ kV/cm, $E_{\text{transfer}} \approx 700$ V/cm, and $E_{\text{GEM}} \approx 40$ kV/cm. These field choices are justified by the fact that the overall gain has to be high ($\sim 10^4$) in order to have a precise measurement of the IBF. In this electric field configuration, the gain in the bottom micro-mesh is ~ 3000 (figure 8.7), its transparency is $\sim 70\%$ (figure 8.8), the proportion of extracted electrons from the GEM is $\sim 17\%$ (figure 8.12) and the gain of the GEM is ~ 300. Combining these expectations, the overall gain with the bottom micro-mesh and the GEM should be of the order of 9×10^4.

For each value of $E_{\text{mesh top}}$, we are interested in the gain indicated by the peak of the GEM (in brown figure 8.10), then all these values are normalized such that the electronic transparency is equal to the optical transparency for the lowest value of $E_{\text{EM}}/E_{\text{mesh top}}$. The optical transparency of the GEM is estimated as the ratio of the surface of the hole (using its outer diameter) and the surface of a pattern:

$$\text{GEM optical transparency} = \frac{\pi \times (\text{outer diameter})^2/4}{(\text{pitch})^2} \approx 0.20 \tag{8.15}$$

The measurements are shown in figure 8.16. The shape appears very different compared to the measurements of transparency of the bottom micro-mesh in figure 8.8. However, $E_{\text{amp}}/E_{\text{transfer}}$ in figure 8.8 ranges from 30 to 4×10^3 whereas in this study $E_{\text{GEM}}/E_{\text{mesh top}}$ ranges from 7 to 10^2. Within this range, the same effect is observed as for the bottom micro-mesh: the funnel effect increases, and so does the transparency. However, the field $E_{\text{mesh top}}$ is never low enough to make recombination of electrons with ions possible in the zone between the GEM and the top micro-mesh. In fact, $E_{\text{mesh top}}$ has to be high enough to eventually attract electrons coming from the drift zone, requiring a field ratio $E_{\text{mesh top}}/E_{\text{drift}}$ with the constraint $E_{\text{drift}} = 400$ V/cm.

The IBF is shown in figure 8.16 at bottom. The ionic transparency of the GEM increases with $E_{\text{mesh top}}$, before going down again. This decrease is probably due to the fact that as the electronic transparency of the GEM decreases, the only events that contribute to the IBF are those for which the photons have converted in the transfer zone.

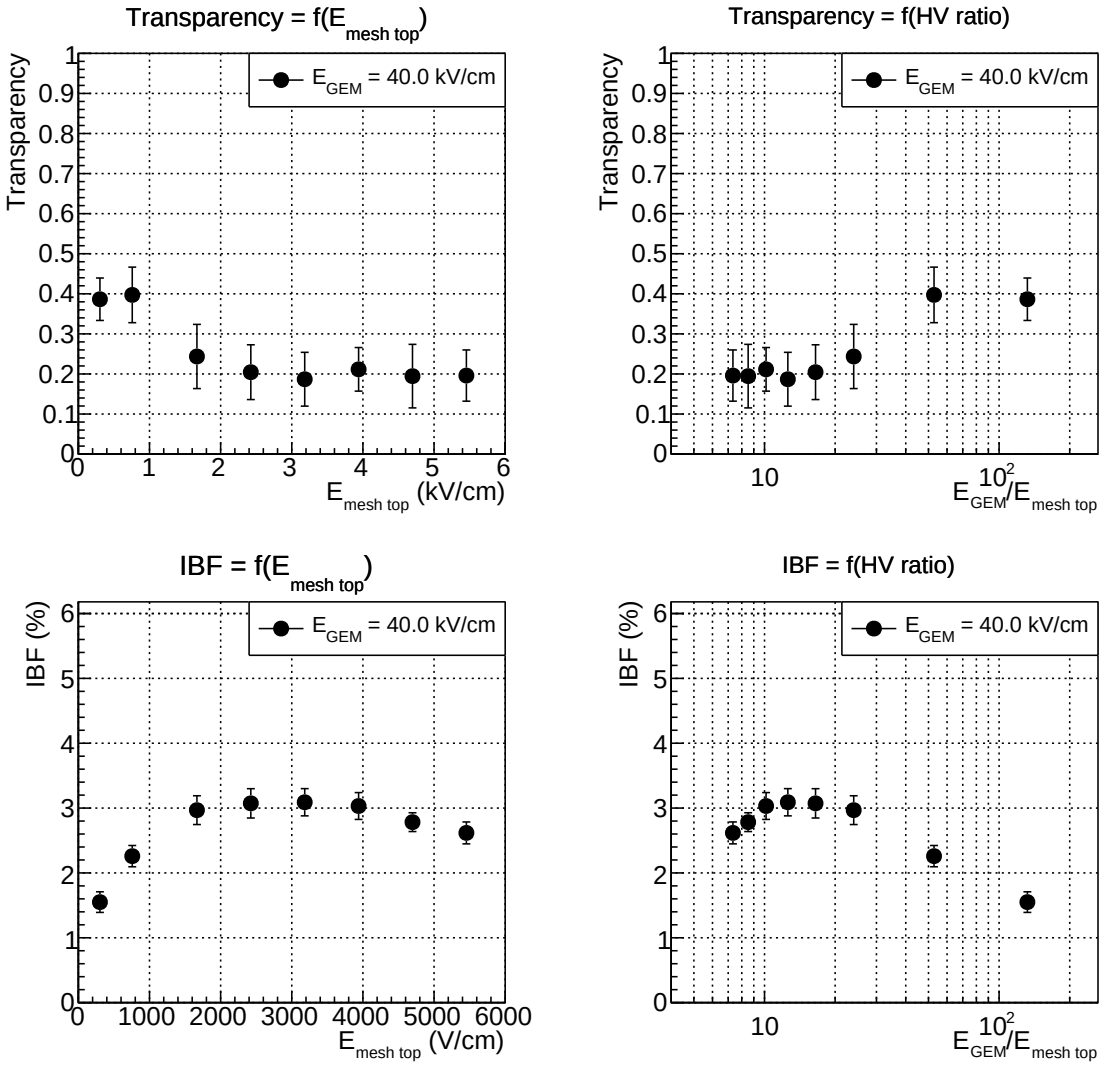

Figure 8.16: Top: evolution of the electronic transparency of GEM as a function of $E_{\text{mesh top}}$ (left) and of the field ratio (right). Bottom: same for the IBF.

Summary of previous measurements

The previous measurements indicate that:

- Figure 8.16 : transparency of GEM and IBF are better for a strong field ratio $E_{\text{GEM}}/E_{\text{mesh top}}$, around 10^2.
- Figures 8.11 et 8.13 : electron extraction and IBF are better for $E_{\text{GEM}}/E_{\text{transfer}} \sim 100 - 200$.
- Figure 8.8 : the transparency of the bottom micro-mesh and the IBF are better for $E_{\text{amp}}/E_{\text{transfer}} \sim 10^2 - 10^3$.

The gain in the bottom micro-mesh and therefore E_{amp} must be adapted so as to satisfy the constraint of keeping the gain around 2000. By combining all these constraints, we choose: E_{drift} = 400 V/cm, E_{GEM} = 40 kV/cm, and E_{transfer} = 300 V/cm.

8.2.3 Study of the top micro-mesh

This part is dedicated to the characterization of the top micro-mesh. The events of interest are those for which the photon converted in the drift region (gray object in the figure 8.17). Although events coming from the lower zones (see figure 8.9) can be observed, photons converting in the drift zone represent the majority of the statistics due to the geometry of the detector: the drift zone is 11 mm high, compared to 7 mm for the transfer zone and 660 µm between the GEM and the top micro-mesh. In addition, photons coming from the source interact rapidly with the detector gas, therefore mainly in the upper part of the detector.

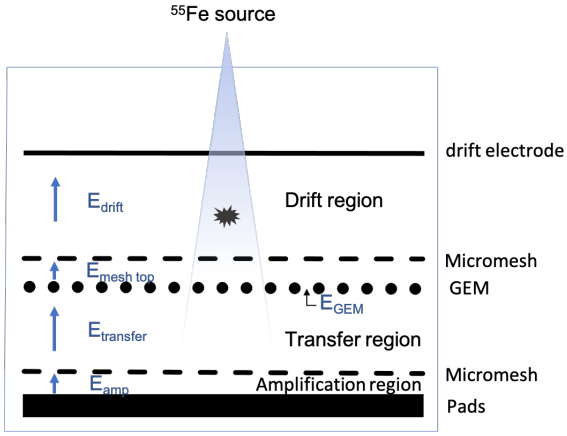

Figure 8.17: Representation of the detector with the electric field configuration used to study the top micro-mesh, with $E_{\text{drift}} = 400$ V/cm.

Transparency

In order to evaluate the top micro-mesh transparency, the measurements described to obtain the transparency of the GEM are repeated but this time by applying an electric field in the drift region $E_{\text{drift}} = 400$ V/cm.

The transparency of the top mesh is defined by the ratio of the total gain of the detector (represented by the gray object) and that of the GEM and bottom micro-mesh (brown object in figure 8.9), knowing that multiplication of electrons under the top micro-mesh is not expected, the electric field being too weak there.

Gain measurements are shown in figure 8.18. The total gain of the detector first increases with $E_{\text{mesh top}}$, indicating an improvement of the top mesh transparency. Then a plateau is reached, implying that the better mesh top transparency is compensated by the worse GEM transparency. This effect is clearly visible in the bottom plots of figure 8.18, and in figure 8.16 for the transparency of the GEM. Finally, for $E_{\text{mesh top}} > 4.5$ kV/cm, the total gain rises steeply, suggesting that the electric field is high enough for amplification electrons to be created.

Figure 8.19 shows the IBF measurements. Values below 0.3% are achieved, although the total gain of the detector is about 6000, much higher than the 2000 imposed by standard TPC requirements. The IBF decreases significantly with E_{transfer}, showing that the top micro-mesh is effective at stopping ions, compared to the GEM which allows about 3% of ions to drift upwards according to figure 8.16 for the same field range.

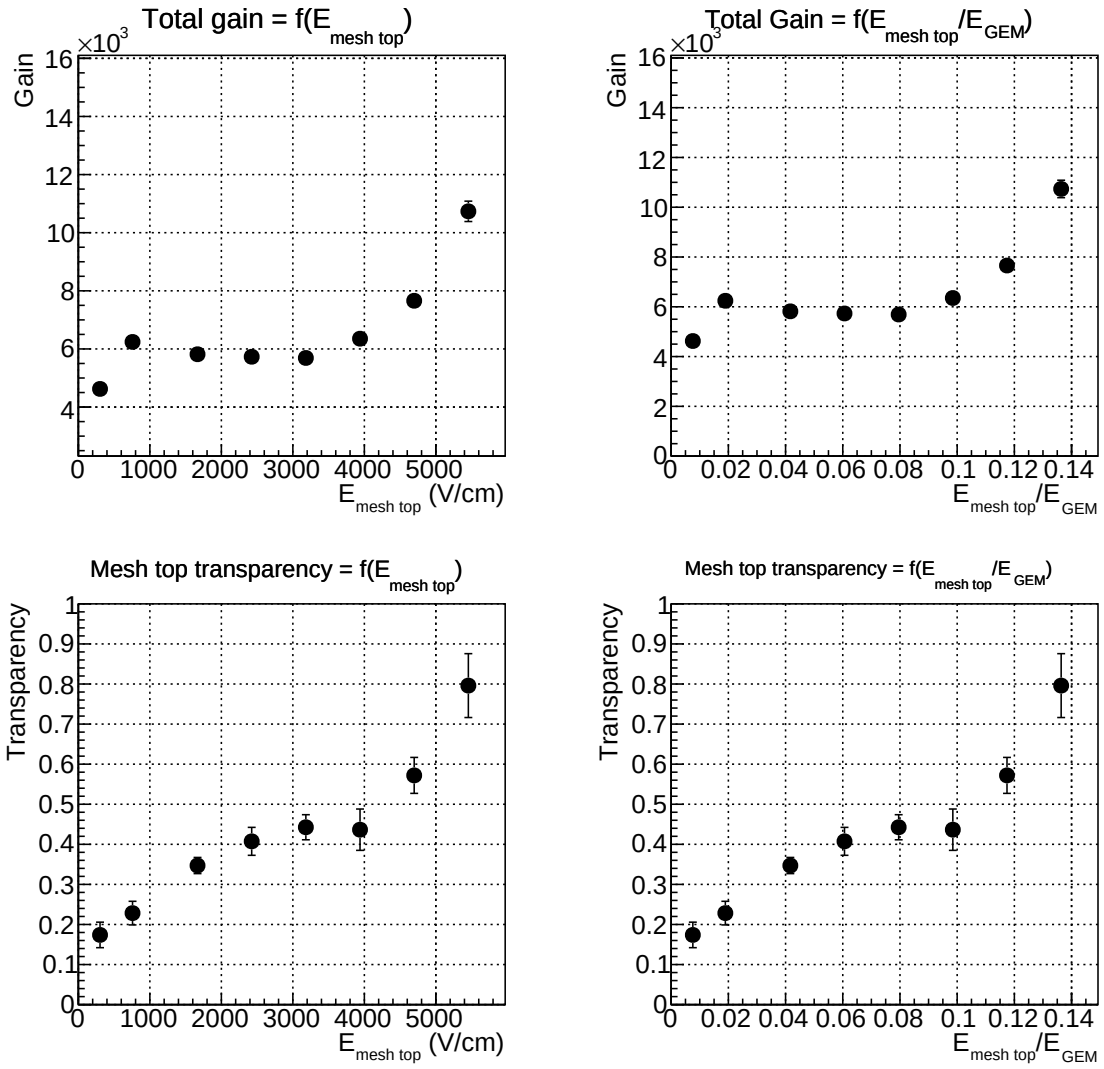

Figure 8.18: Top: total gain with a collimated source as a function of the field $E_{\text{mesh top}}$ (left) and the field ratio $E_{\text{mesh top}}/E_{\text{GEM}}$. Bottom: transparency of the top micro-mesh as a function of the field $E_{\text{mesh top}}$ (left) and the field ratio $E_{\text{mesh top}}/E_{\text{GEM}}$. It is obtained as a ratio of the total gain displayed above and the gain of the GEM with the same electric field configuration.

8.2.4 Gain after amplification at all stages

The total gain of the detector is now studied. To obtain a better energy resolution, the source is collimated for the gain measurements using a copper plate pierced with a hole of 1 mm in diameter and placed between the iron source and the detector. This permits to avoid being impacted by possible inhomogeneities of the electric fields due to deformations or non uniformity of the mesh. However, in order to measure precisely the IBF, intense currents provided by a high event rate are favored. As a consequence, the source is not collimated for IBF measurements. A study presented in appendix I shows that IBF values should not be affected by whether the source is collimated or not. The IBF and its uncertainty are estimated according to the equations 8.4 and 8.6.

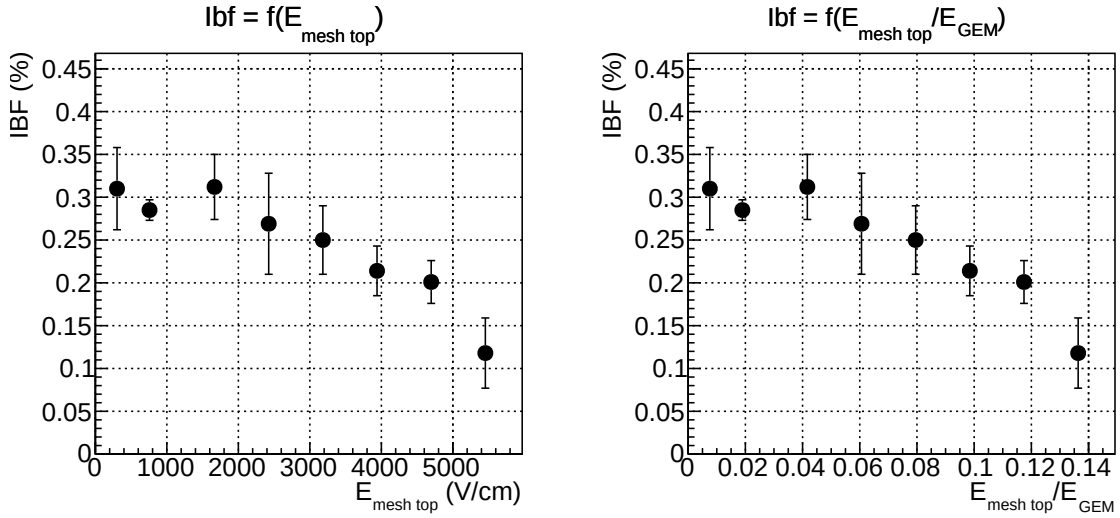

Figure 8.19: IBF of the top micro-mesh as a function of the field $E_{\text{mesh top}}$ (left) and the field ratio $E_{\text{mesh top}}/E_{\text{GEM}}$.

The total gain of the detector corresponds to the product of:

- the gain of the top micro-mesh
- the electronic transparency of the top micro-mesh
- the electron extraction coefficient of the GEM
- the gain of the GEM
- the electronic transparency of the GEM
- the gain of the bottom micro-mesh
- the electronic transparency of the bottom micro-mesh.

Its value is given by the position of the peak of the 5.9 keV energy ray (see figure 8.20). The energy resolution of the detector is given by the standard deviation σ of the gaussian function that models the total amplification.

The energy spectrum of photons from an iron source in argon-isobutane (95/5) depicted in figure 8.20 displays three main contributions. One corresponds to the escape peak at 2.9 keV, and the two others correspond to the K_α (5.9 keV) and K_β (6.4 keV) lines of the ^{55}Fe source. Three Gaussian functions are used to fit the data, where the mean μ_{K_α} of the Gaussian function corresponding to the K_α line is determined by the position of the maximum, and the ratios of the two other lines and the mean of the μ_{K_α} ray are fixed: $\mu_{K_{\text{escape}}}/\mu_{K_\alpha} = 0.4915$ and $\mu_{K_\beta}/\mu_{K_\alpha} = 1.102$.

Two set of measurements are performed.

- A first set of measurements followed the prescriptions given at the end of section 8.2.2, namely: E_{amp} = 31 kV/cm, E_{transfer} = 350 V/cm, E_{GEM} was set at three different values between 30 and 37 kV/cm, E_{drift} = 400 V/cm, and $E_{\text{mesh top}}$ is increased. These measurements are shown in figure 8.21.

- A second set of measurements is done with the following field constraints: E_{amp} = 30 kV/cm, E_{transfer} = 300 V/cm, E_{GEM} = 40 kV/cm, E_{drift} = 400 V/cm, and $E_{\text{mesh top}}$ is increased. They are shown in figure 8.22.

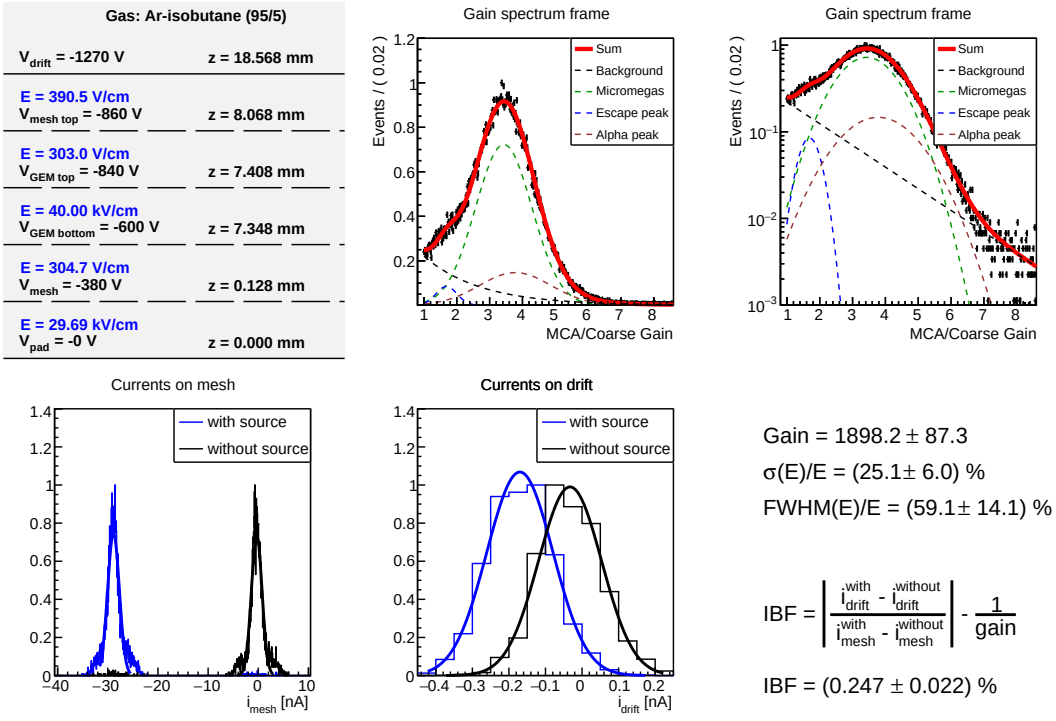

Figure 8.20: Example of measurement with at top left: the electric field configuration of the detector, top middle: spectrum obtained with an iron source, top right: same spectrum in log scale, bottom left: currents read on the bottom micro-mesh, bottom middle: currents read on the drift electrode, bottom right: calculation of gain and IBF.

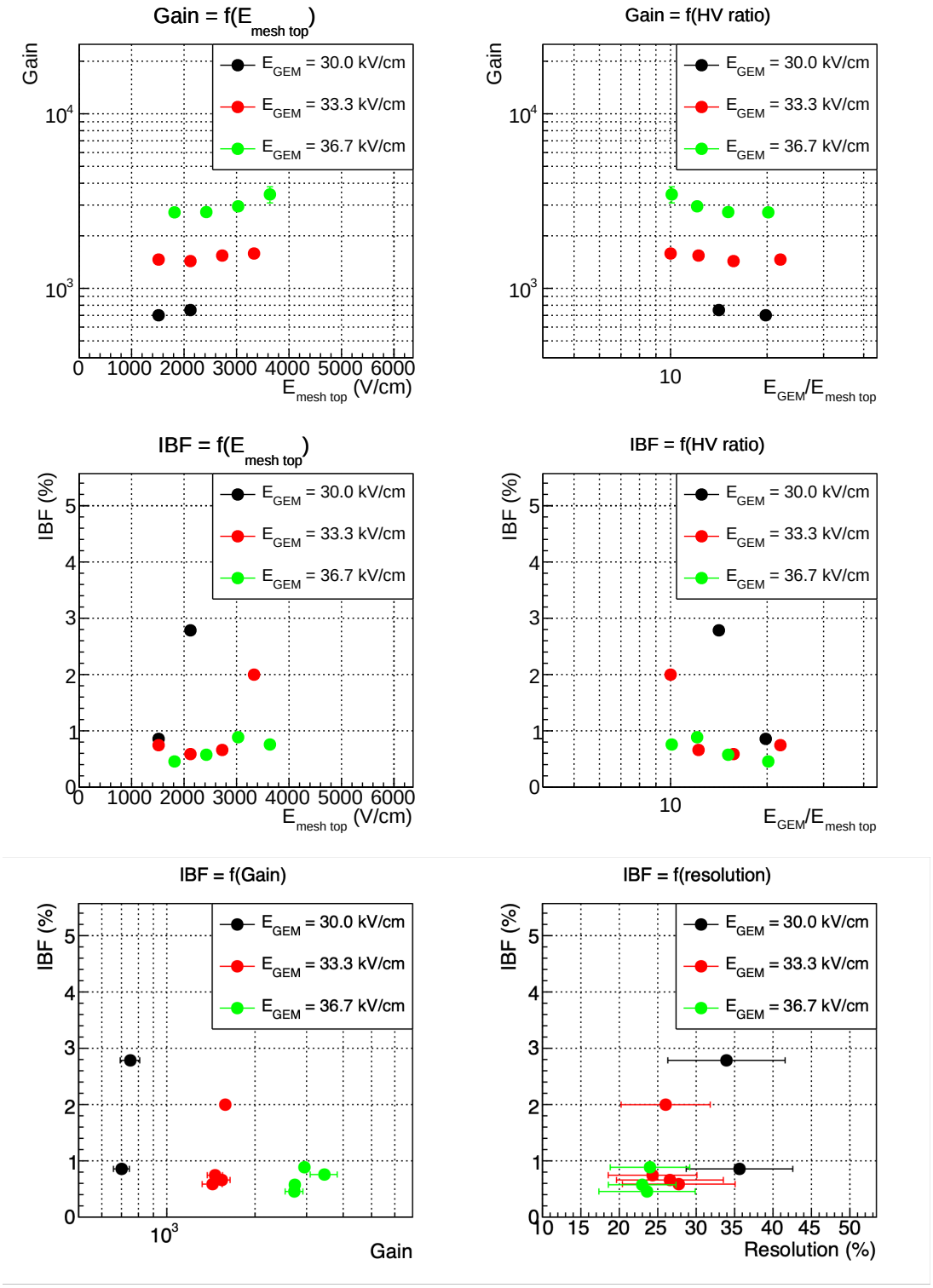

Figure 8.21: Top / middle: Gain curve of the detector/ IBF as a function of the gain (left) and the energy resolution (right) for three different values of E_{GEM}. Bottom: IBF as a function of the gain (left) and the energy resolution (right) for three different values of E_{GEM}. These measurements are performed using the 660-µm-gap detector.

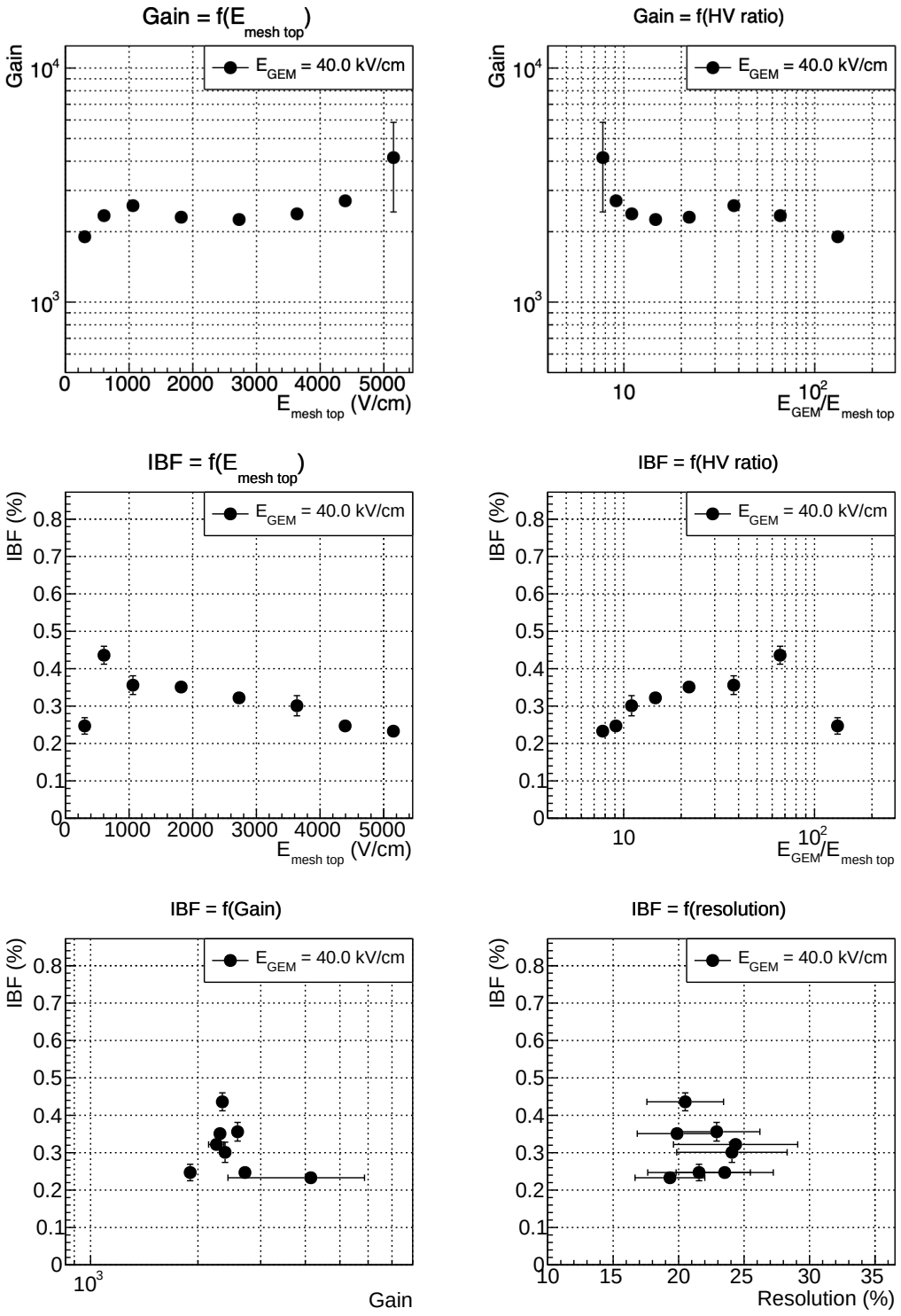

Figure 8.22: Top / middle: Gain curve of the detector/ IBF as a function of the gain (left) and the energy resolution (right). Bottom: IBF as a function of the gain (left) and the energy resolution (right). These measurements are performed using the 660-µm-gap detector.

As explained when studying the transparency of the top micro-mesh, the flat curves representing the total gain as a function of $E_{\text{mesh top}}$ or as a function of the field ratio $E_{\text{GEM}}/E_{\text{mesh top}}$ show that the increase in the transparency of the mesh top is compensated by the poor transparency of the GEM. Within this range of $E_{\text{GEM}}/E_{\text{mesh top}}$, the IBF measured with the first set of data appears almost constant, while it seems to increase in the second set of data, except for the lowest $E_{\text{mesh top}}$ point. This point corresponds to the region of $E_{\text{GEM}}/E_{\text{mesh top}}$ where the GEM effectively stops ions, according to previous measurements presented in figure 8.16. For the other points, the decrease of IBF with $E_{\text{mesh top}}$ is expected, since the field lines are more contracted in the vicinity of the mesh holes and it is harder for ions to escape. The first set of data spans a narrower $E_{\text{GEM}}/E_{\text{mesh top}}$ range, which explains why the IBF appears constant. Finally, the gain and IBF do not show a strong correlation when $E_{\text{mesh top}}$ is increased. However, one can see with the first set of data that the lower the field in the GEM E_{GEM} (hence the lower the ratio $E_{\text{GEM}}/E_{\text{mesh top}}$), the higher the IBF, which is consistent with the plot at middle right of figure 8.22.

8.3 Measurements with the 128-µm-gap detector

Since the gap between the GEM and the top micro-mesh is only 128 µm, it is improbable to see photons converting into electrons in this space. Thus, all the studies presented in the previous section concerning the bottom micro-mesh and the GEM are assumed valid for the study of this second detector. This section only presents the study of the top micro-mesh, which differs in dimensions from that of the first detector. The top micro-mesh has dimensions of 70 µm in hole size and 30 µm in diameter, unlike the bottom micro-mesh which has dimensions 45/18. Then, the total gain of the detector is characterized.

8.3.1 Study of the top micro-mesh alone

The method is the same as presented at the beginning of section 8.2.1, with the difference that the preamplifier is positioned on the top micro-mesh, and all the other electrodes than that of the top micro-mesh and drift are grounded.

Gain curve

The amplification field is increased, and the drift field is set at 400 V/cm. The gain and IBF curves are therefore obtained in figures 8.23 and 8.24.

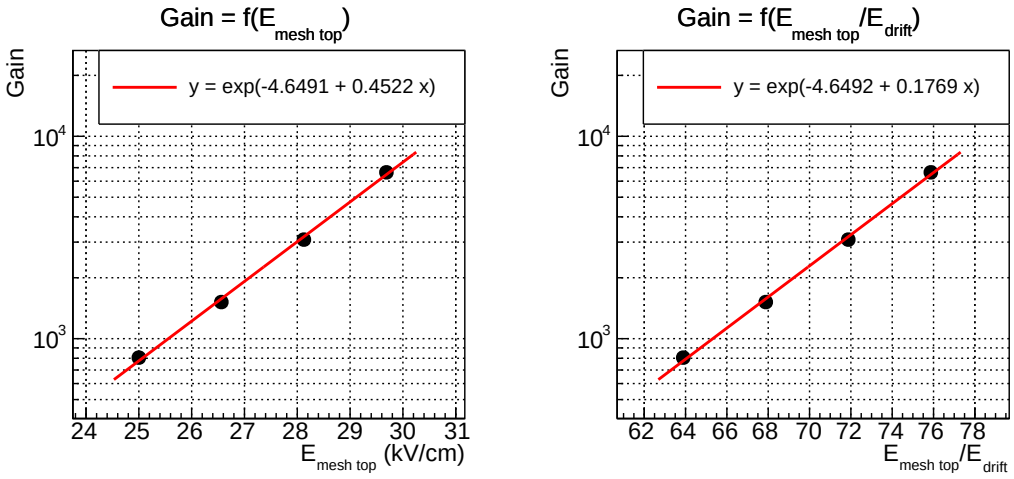

Figure 8.23: Gain curve of the top micro-mesh (70/30) as a function of the amplification field (left) and the field ratio (right).

As this micro-mesh has a much broader opening than that of the bottom of the detector, the IBF is much larger for the same electric field configuration (see figure 8.7). The gain instead is larger by a factor 3. Besides these differences with the bottom micro-mesh, the shapes of gain and IBF obtained display the same behavior as discussed in section 8.2.1.

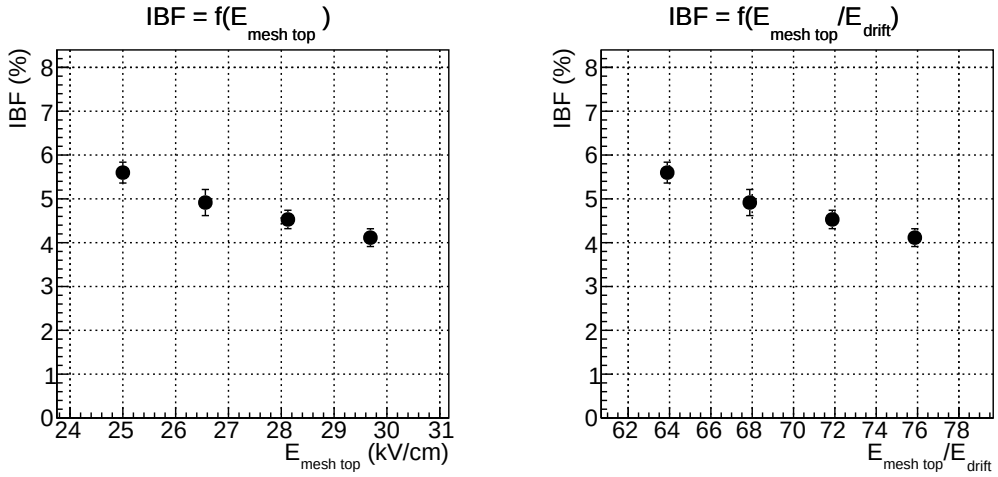

Figure 8.24: IBF curve of the top micro-mesh (70/30) as a function of the amplification field (left) and the field ratio (right).

Transparency

The amplification field is now fixed - and so is the gain - and the drift field is changed. The observations described at the end of section 8.2.1 are valid here, although IBF values are twice larger for the top micro-mesh (70/30) than for the bottom micro-mesh (45/18) for same E_{drift} values. Measurements are shown in figures 8.25 and 8.26.

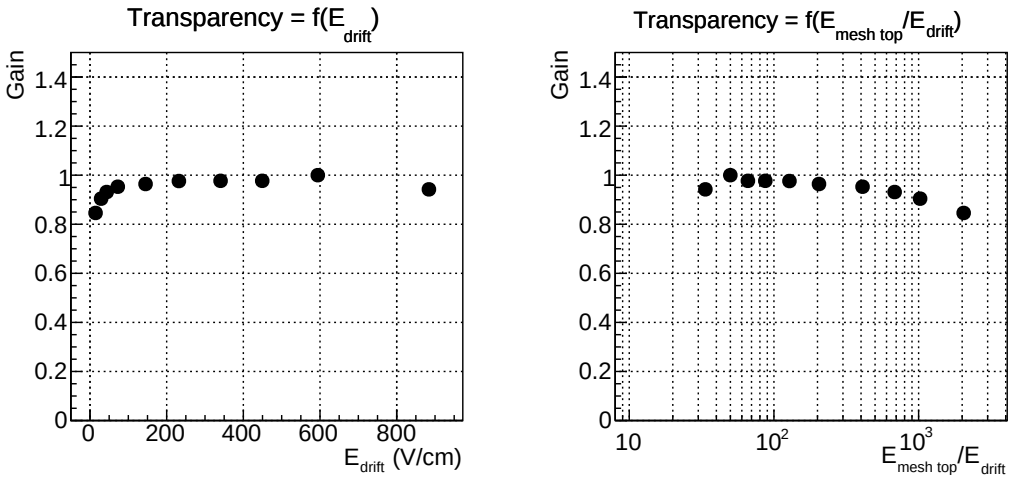

Figure 8.25: Transparency of the bottom micro-mesh as function of the transfer field (left) and the field ratio (right).

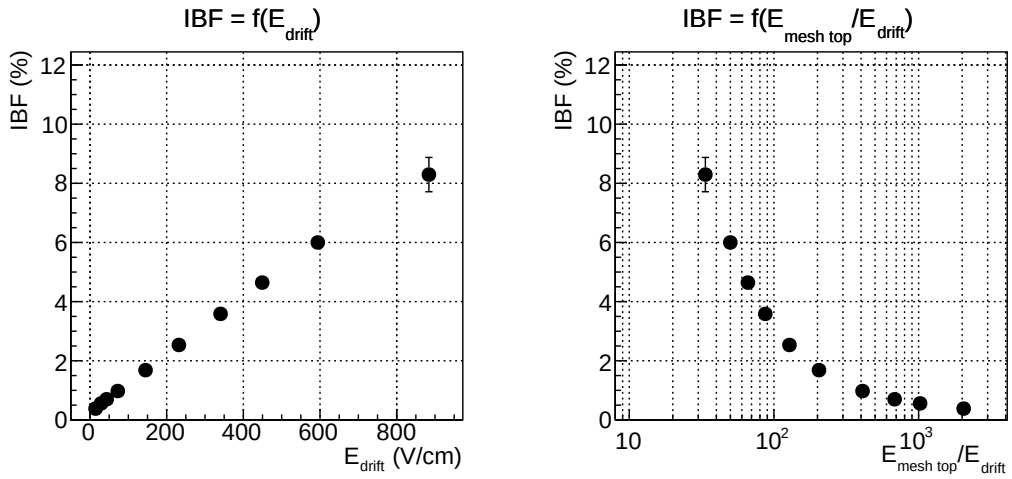

Figure 8.26: IBF as function of the transfer field (left) and the field ratio (right).

8.3.2 Gain after amplification at all stages

Similarly to section 8.2.4, the total gain of the detector is studied. Two sets of measurements are performed.

- A first set of measurements followed the prescriptions given at the end of section 8.2.2, namely: E_{amp} = 25 kV/cm, E_{transfer} = 460 V/cm, E_{GEM} took three different values between 30 and 37 kV/cm, E_{drift} = 400 V/cm, and $E_{\text{mesh top}}$ is increased. These measurements are given in figure 8.27.
- A second set of measurements has been performed, with the following field constraints: E_{amp} = 25 kV/cm, E_{transfer} = 440 V/cm then 670 V/cm, E_{GEM} = 33 kV/cm, E_{drift} = 400 V/cm, and $E_{\text{mesh top}}$ is increased. These measurements are presented in figure 8.28.

Unlike the 660-µm-gap detector, amplification occurs below the top micro-mesh. Therefore, in both figures, the gain increases exponentially with $E_{\text{mesh top}}$ and keeping a total detector gain

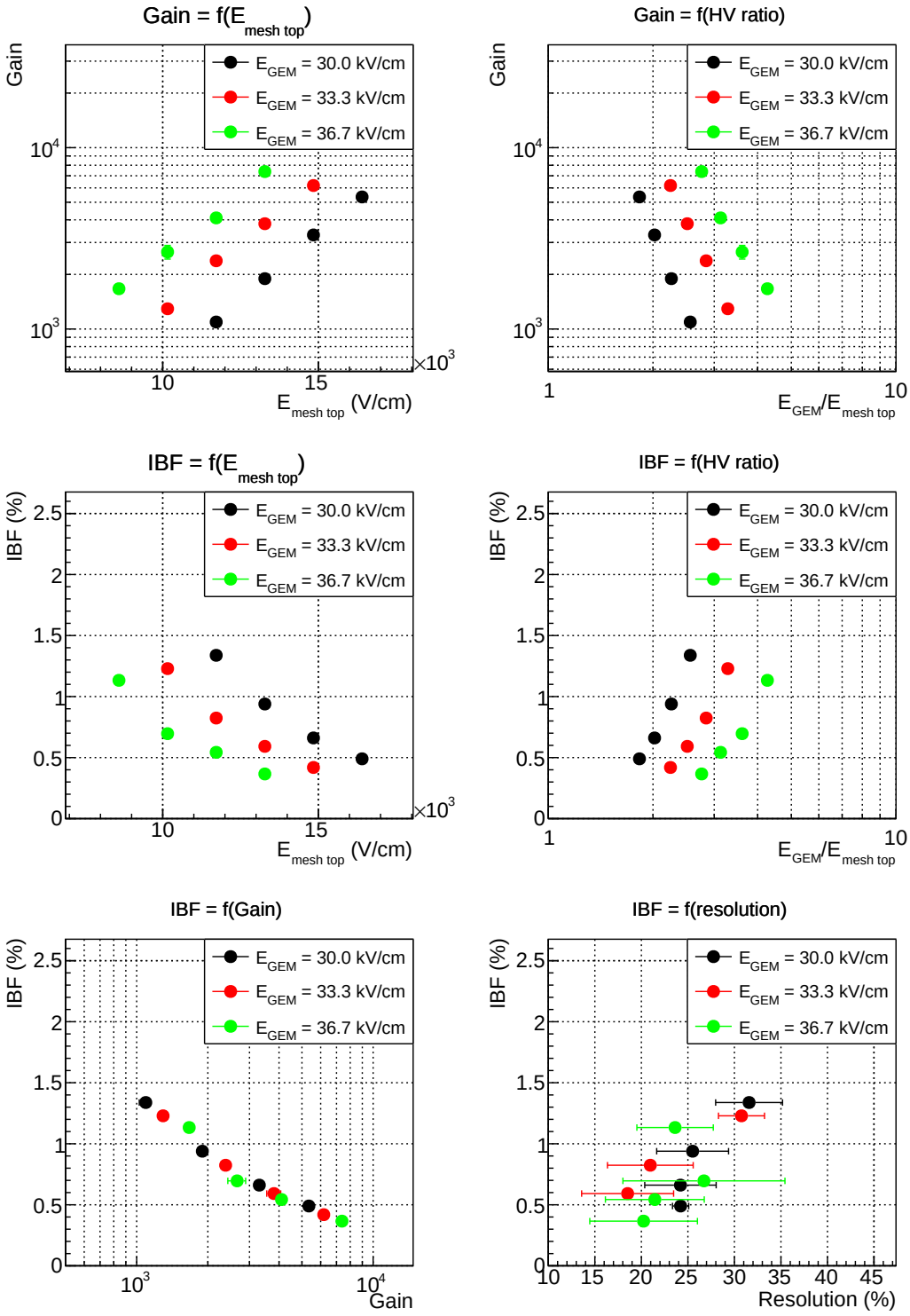

Figure 8.27: Top / middle: Gain curve of the detector/ IBF as a function of the gain (left) and the energy resolution (right). Bottom: IBF as a function of the gain (left) and the energy resolution (right). These measurements are performed using the 128-µm-gap detector.

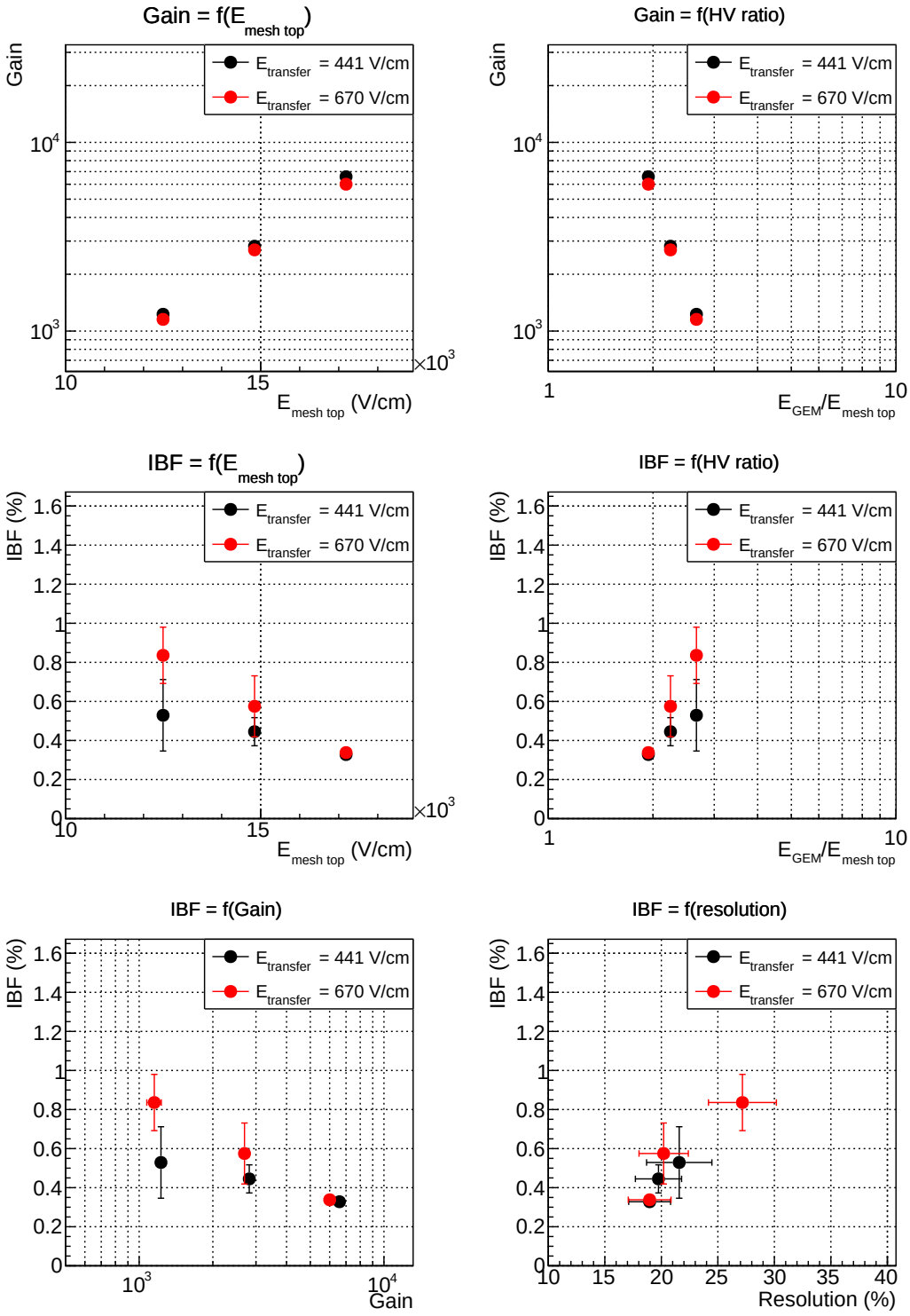

Figure 8.28: Top / middle: Gain curve of the detector/ IBF as a function of the gain (left) and the energy resolution (right). Bottom: IBF as a function of the gain (left) and the energy resolution (right). These measurements are performed using the 128-µm-gap detector.

around 2000 greatly restricts the possible field configurations. Figure 8.27 at top also displays the exponential increase in gain when E_{GEM} is increased.

Low IBF values are achieved when E_{GEM} is the lowest (figure 8.27) and when E_{transfer} is the lowest (figure 8.28). Since the intrinsic ion transparency of the mesh (70/30) is worse than that to the first detector, the overall IBF reaches higher values, especially for low values of the ratio $E_{\text{mesh top}}/E_{\text{drift}}$ - corresponding to low values of $E_{\text{mesh top}}$: since the ion transparency is directly correlated to this ratio and the opening of the mesh is larger, the top micro-mesh is less efficient at stopping ions.

Finally, figure 8.27 at bottom shows an exponential decrease of the IBF with the gain, which follows the same tendency independently of the field E_{GEM}. Figure 8.28 however indicates that although changing E_{transfer} has a small impact on the gain, it significantly changes the IBF due to the increasing ionic transparency of the bottom micro-mesh with E_{transfer}. There is no clear correlation between the IBF and resolution on both figures.

8.4 Contamination on the drift electrode

Some photons are likely to convert to electrons inside the detector above the drift electrode. The ions resulting from these ionizations drift towards the drift electrode on which they induce a current, i_d^{conta}, contaminating the measurement. This results in an overestimation of the IBF. The study presented here consists in evaluating the systematic error induced by these events on the measurement of the IBF in the 660-µm-gap detector. In order to do so, one of the measurements presented in section 8.2.4 is reproduced. The one for which the electric potential is the highest on the drift electrode in absolute value is chosen: this measurement is the one for which the contamination effect should be the strongest, since the electric field near the drift electrode is the most intense there.

V_{mesh}	$V_{\text{GEM bot}}$	$V_{\text{GEM up}}$	$V_{\text{mesh top}}$	V_{drift}
-380 V	-600 V	-840 V	-1180 V	-1590 V

Table 8.2: Electrical configuration of the detector for a particular measurement of the ion backflow. The currents are measured with and without the source.

In order to measure the contamination current without measuring events taking place in the drift zone, the detector is in the electrical configuration represented in figure 8.29. In this electric configuration, $V_{\text{mesh}} = -400$ V, $V_{\text{GEM bot}} = -1400$ V, $V_{\text{GEM up}} = -1400$ V, $V_{\text{mesh top}} = -1590$ V, $V_{\text{drift}} = -1590$ V. The electric field in the drift zone is null, and the electric potential of the electrodes under the top micro-mesh is gradually reduced so as to avoid sparks. Thus, only events from above the drift electrode are selected. The induced current is then measured with the iron source positioned in the same place as for the previous measurement, and the contamination current is given by:

$$i_d^{\text{conta}} = i_d^{\text{conta with}} - i_d^{\text{conta without}} \tag{8.16}$$

Thus, the current induced by the IBF on the drift electrode actually corresponds to $(i_d^{\text{with}} - i_d^{\text{without}}) - i_d^{\text{conta}}$ and not only $i_d^{\text{with}} - i_d^{\text{without}}$. Therefore, the ion back flow should be defined as

$$\text{IBF} = \frac{i_d^{\text{with}} - i_d^{\text{without}} - i_d^{\text{conta}}}{i_m^{\text{with}} - i_m^{\text{without}}} - \frac{1}{\text{Gain}} \tag{8.17}$$

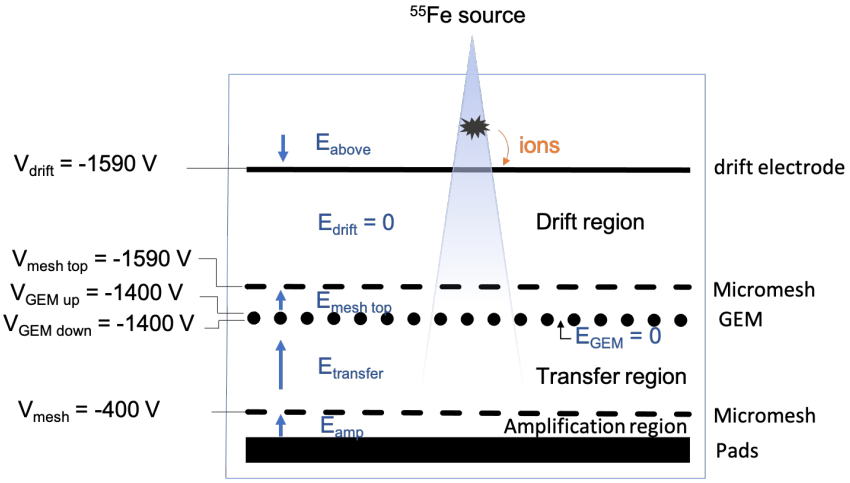

Figure 8.29: Electrical setup of the detector to assess contamination from ionizations that take place above the drift electrode. The measurement is made with the source of iron.

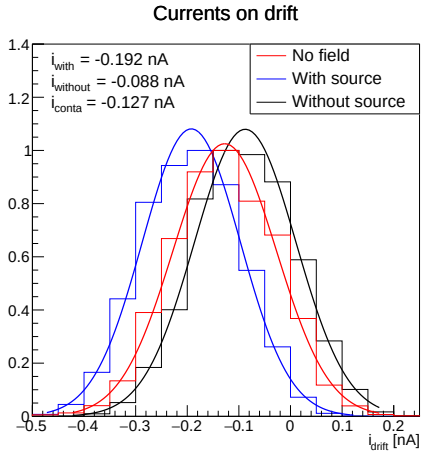

Figure 8.30: Currents read on the drift electrode with 250 seconds of data acquisition, when the detector is in the electrical configuration according to the table 8.2 without the source (black curve), with the source (curve blue), and in the electrical configuration given in figure 8.29 with the source (red curve).

instead of equation 8.4, where $i_d^{\text{conta}} = i_d^{\text{conta with}} - i_d^{\text{conta without}}$ should be the same quantity for all measurements, provided that the source is placed at the exact same position. The measurements of currents are given is table 8.3.

Assuming that the contribution of ions from the first ionisation to the IBF - the term $1/\text{Gain}$ in equations 8.4 and 8.17 - is negligible (for a gain of 2000, it is 0.05%), IBF measurements can be up to 60% overestimated.

However, given the fact that the source position changed for each measurement, the value i_d^{conta} = -0.039 nA cannot be subtracted as a constant contamination current from the current read on the drift.

A complementary study conducted with simulations is presented in appendix H.2 in order to estimate the bias induced by events taking place outside the drift region on IBF measure-

i_d^{with}	-0.192 nA
i_d^{without}	-0.088 nA
$i_d^{\text{no conta}} = i_d^{\text{with}} - i_d^{\text{without}}$	-0.104 nA
$i_d^{\text{conta}} = i_d^{\text{conta with}} - i_d^{\text{conta without}}$	-0.127 nA - (-0.088 nA) = -0.039 nA
$\lvert i_d^{\text{no conta}} - i_d^{\text{conta}} \rvert$	0.065 nA
$\frac{\lvert i_d^{\text{no conta}} \rvert}{\lvert i_d^{\text{no conta}} - i_d^{\text{conta}} \rvert}$	1.60

Table 8.3: Average values of the currents measured on the drift.

ments. This study shows that the IBF measurement could be overestimated by 34% due to contamination from ions coming from above the drift electrode in the 660-µm-gap detector, and 26% in the 128-µm-gap detector. In addition, the contamination from events coming from the transfer region can induce an underestimation of up to 10% on the ion backflow in the 660-µm-gap detector, and up to 2% in the 128-µm-gap detector.

8.5 Summary

Two prototype detectors have been tested and fully characterized. The behavior of each electrode and its role in the amplification process in terms of intrinsic gain, transparency, and ion stopping power has been carefully studied. Finally, contamination currents induced by photons converting outside the drift region are studied and taken as a systematic uncertainty in the measurements. The following chapter discusses the accuracy of the simulations by comparing them with the prototypes tested in the laboratory. We also discuss the improvement of the MMGEM detector compared to simpler geometric configurations tested.

Bibliography

[1] C. Flouzat et al. Dream: A 64-channel front-end chip with analogue trigger latency buffer for the Micromegas tracker of the CLAS12 experiment, 2014.

[2] D. Attie et al. The readout system for the Clas12 Micromegas vertex tracker. In *19th Real Time Conference*, 2014. doi: 10.1109/RTC.2014.7097517.

[3] Y. Giomataris, P. Rebourgeard, J. P. Robert, and Georges Charpak. MICROMEGAS: A High granularity position sensitive gaseous detector for high particle flux environments. *Nucl. Instrum. Meth. A*, 376:29–35, 1996. doi: 10.1016/0168-9002(96)00175-1.

[4] Ortec 142C pre-amplifier. https://www.ortec-online.com/-/media/ametekortec/manuals/142abc-mnl.pdf.

[5] MCA8000D specifications by Amptek. https://www.amptek.com/-/media/ametekamptek/documents/products/mca-8000d-digital-multichannel-analyzer-specifications.pdf?dmc=1&la=en&revision=8a383ad0-454e-40d6-9bd7-04748889d667.

[6] DPPMCA Display & Acquisition Software. https://www.amptek.com/software/dp5-digital-pulse-processor-software/dppmca-display-acquisition-software.

[7] A. Utrobicic, M. Kovacic, F. Erhardt, N. Poljak, and M. Planinic. A floating multi-channel picoammeter for micropattern gaseous detector current monitoring. *Nucl. Instrum. Meth. A*, 801:21–26, 2015. doi: 10.1016/j.nima.2015.08.021.

Chapter 9

Comparison of measurements with simulations and other detector configurations

Contents

9.1 Comparison of laboratory tests with simulations 202

9.1.1 Single-stage MicroMEGAS detectors 202

9.1.2 Hybrid MicroMEGAS and GEM detectors 203

9.1.3 MMGEM detectors 204

9.1.4 Discussion on the comparison of the measurements and simulations 210

9.2 Comparison of MMGEM models with other geometric configurations 211

9.2.1 Single-stage MicroMEGAS and double-stage MicroMEGAS and GEM detectors 211

9.2.2 ALICE quadruple GEM detector 212

9.3 Summary 213

Bibliography 215

In this chapter, the measurements made on the two prototype detectors are compared with the simulations in terms of gain and IBF to help understand the amplification mechanisms involved in each electrode. The comparison is also made with other structures to assess the improvements brought by MMGEM detectors compared to what already exists.

In the first section, we compare the measurements with the simulations for different structures: first simply for a MicroMEGAS detector, then a MicroMEGAS with a GEM (hybrid structure), and finally the MMGEM structures. Then we discuss why simulations and data differ and the possible improvements of the MMGEM detectors setup. In the second section, we put the measurements with the MMGEM structures in parallel with other structures: the MicroMEGAS single-stage structures, the hybrid structures, and the quadruple GEM detectors of ALICE.

9.1 Comparison of laboratory tests with simulations

The models tested in the simulations, as introduced in chapter 7, reproduce the geometry of the detectors tested in the laboratory (chapter 8). Besides the geometry, other input parameters that correspond to real laboratory test conditions define the simulations. These input parameters include the gas and the Penning transfer coefficient, as described in section 7.1.2. We compare the different geometry structure detectors one by one.

9.1.1 Single-stage MicroMEGAS detectors

Two models of MicroMEGAS have been simulated: the first one with a 45/18 micro-mesh, and the second one with a 70/30 micro-mesh, both with an amplification gap of 128 µm. The first one is compared with the measurements of the bottom micro-mesh presented in section 8.2.1 in figure 9.1, and the second one with the measurements of the top micro-mesh presented in section 8.3.1 in figure 9.2.

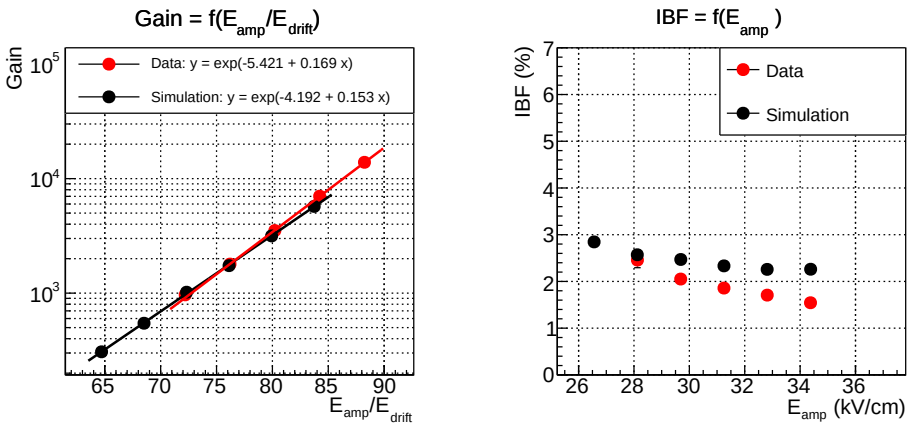

Figure 9.1: Left: gain curve of the bottom micro-mesh as a function of the field ratio, fitted with an exponential. Right: same for the IBF.

The simulation reproduces with good accuracy the micro-mesh 45/18 in terms of gain, although the gain slope is higher in the data than in the simulation. The IBF seems to be well described in the simulation for low amplification fields E_{amp}, but deviates from the data up to

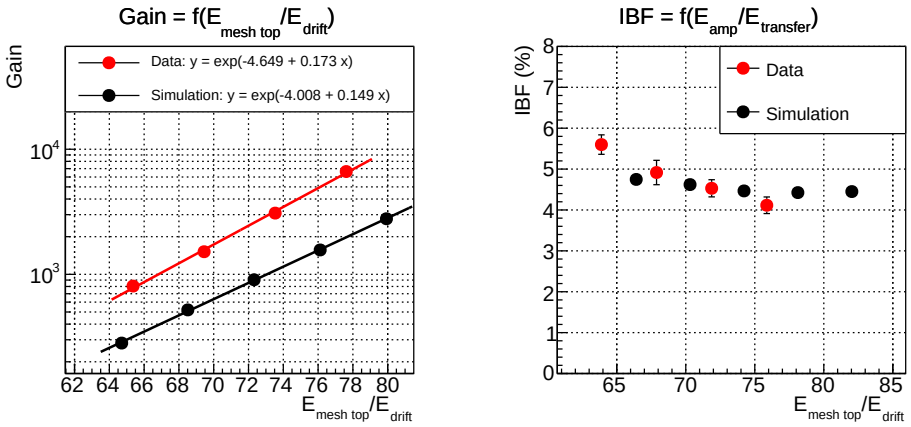

Figure 9.2: Left: gain curve of the bottom micro-mesh as a function of the field ratio, fitted with an exponential. Right: same for the IBF.

30% for the highest amplification field. The gain obtained with the simulation of the micro-mesh 70/30 instead is lower by a factor of 2.5 and again, the gain slope is lower. However, the IBF obtained from the data and simulation match well.

9.1.2 Hybrid MicroMEGAS and GEM detectors

Simulations are carried out on a hybrid configuration made up of a micro-mesh and a GEM, presented in section 7.3.2, for 4 electric field values in the GEM E_{GEM}. The fields below and above are kept constant: $E_{\text{transfer}} = 400\,\text{V/cm}$, and $E_{\text{drift}} \simeq 400\,\text{V/cm}$. The gains of the GEM and

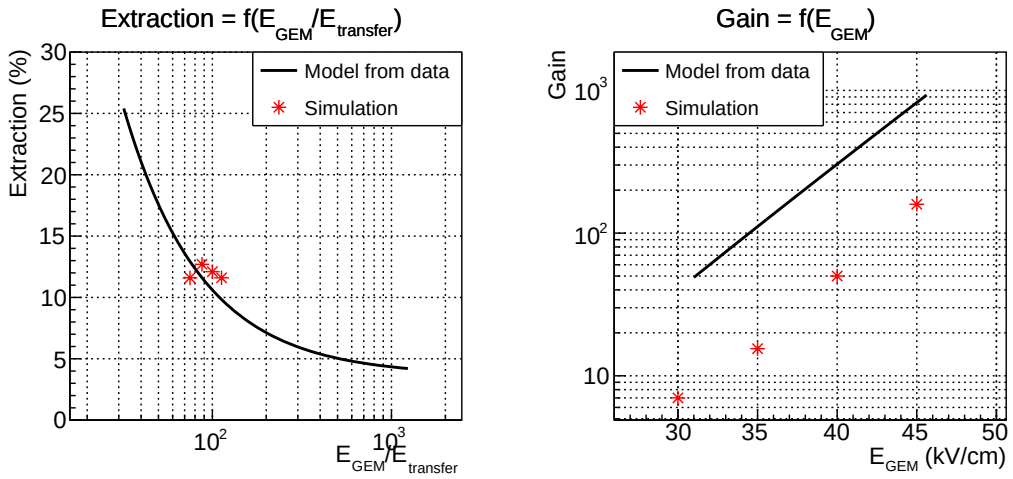

Figure 9.3: Comparison of the proportion of electrons extracted and of the intrinsic gain of the GEM obtained with simulations and a parametrization of the data.

the proportions of electrons extracted are obtained for these 4 points to be compared with the parametrizations obtained from the data and drawn in figures 8.12 and 8.15. The comparison is shown in figure 9.3.

The gain obtained with the simulations is lower by a factor of 3. The values of proportion of electrons extracted agree within 20% in the data and in the simulation. However, when com-

puting a parametrization of the proportion of electrons extracted with $E_{\text{GEM}}/E_{\text{transfer}}$ from the data, a bias was introduced since the simulation was used to fix the A factor in equation 8.10.

In addition, the curve of transparency of the GEM is also drawn as a function of $E_{\text{GEM}}/E_{\text{mesh top}}$ in figure 9.4, and superimposed with the curve obtained in figure 8.16 at top.

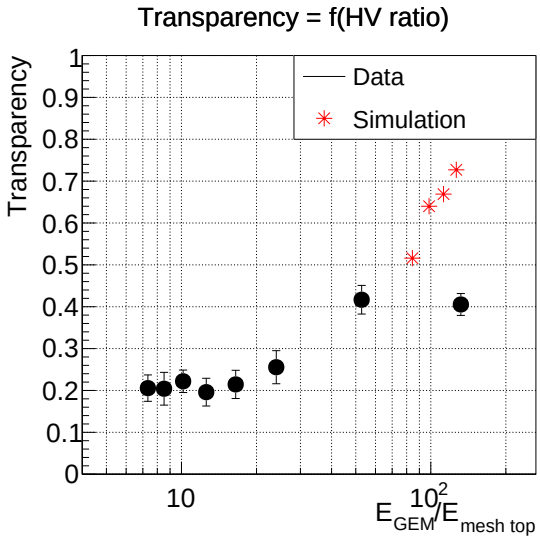

Figure 9.4: Comparison of the GEM transparency obtained with simulations and from the data, as shown in figure 8.16.

In the simulation, the curve is obtained by varying E_{GEM} as described above, while in the measurements, E_{GEM} was fixed and $E_{\text{mesh top}}$ was changed, allowing to span a wide range in $E_{\text{GEM}}/E_{\text{mesh top}}$. The simulation predict a steep increase of the GEM transparency with the field ratio, which is not observed in the measurements with the 660-µm-gap prototype. Given the fact that the geometry of the GEM in the simulation and in the prototype is not the same, the optical transparency of the GEM differs, as discussed in section 9.1.4.

9.1.3 MMGEM detectors

In order to compare the results of the measurements on the two MMGEM detectors with simulations, we examine two significant examples. For these examples, the electric configurations are the same in the simulation and in the laboratory.

660-µm-gap model

Figure 9.5 shows a laboratory measurement and figure 9.6 shows the corresponding simulation for the same electric field configuration.

In the simulation, the gain (460 ± 3) is lower by a factor of 6 compared to the measurement in the laboratory (2778 ± 159). The possible reasons for this difference are discussed in section 9.1.4. The energy resolution obtained in the simulation, $\sigma(E)/E$, is about 29%. This value is similar to the (26 ± 7)% obtained in the data, and could be explained by the low detector transparency (11.5%) according to simulations. This value of detector transparency is mainly due to the fact that the transparencies of the top micro-mesh and the GEM do not exceed 36%.

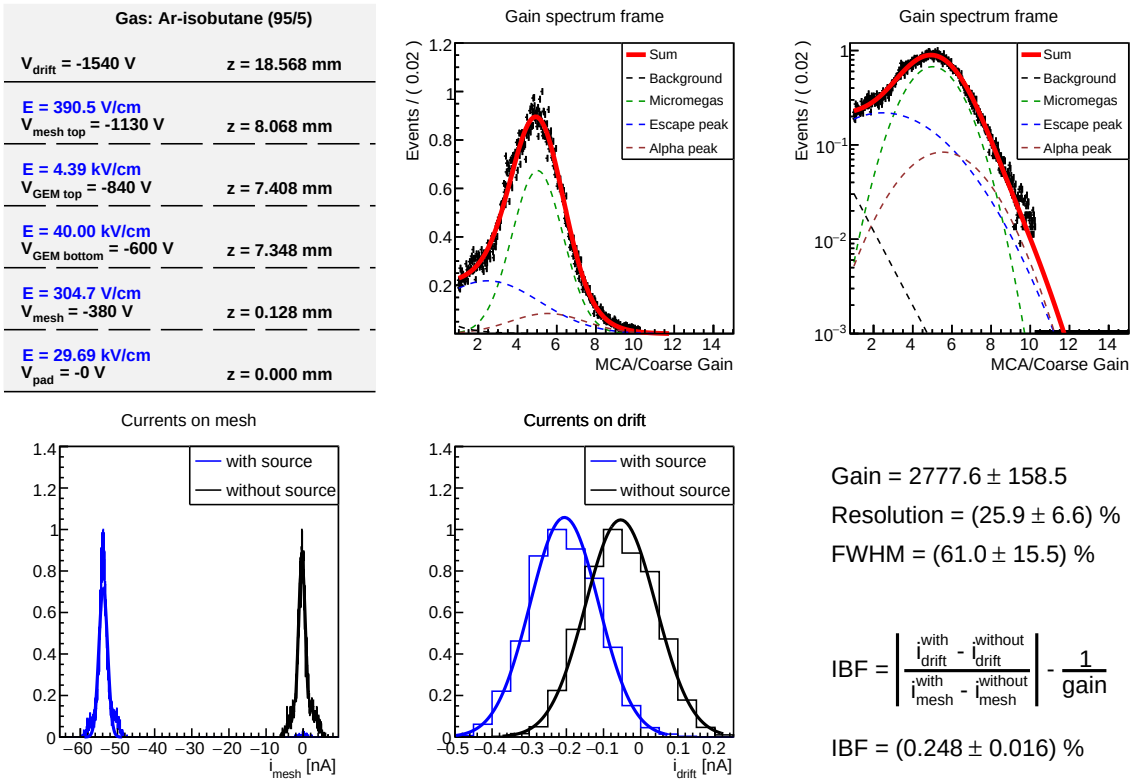

Figure 9.5: Measurement with at top left: the electric field configuration of the detector, top middle: gain spectrum obtained with an iron source, top right: same spectrum in log scale, bottom left: currents read on the bottom micro-mesh, bottom middle: currents read on the drift electrode, bottom right: calculation of gain and IBF.

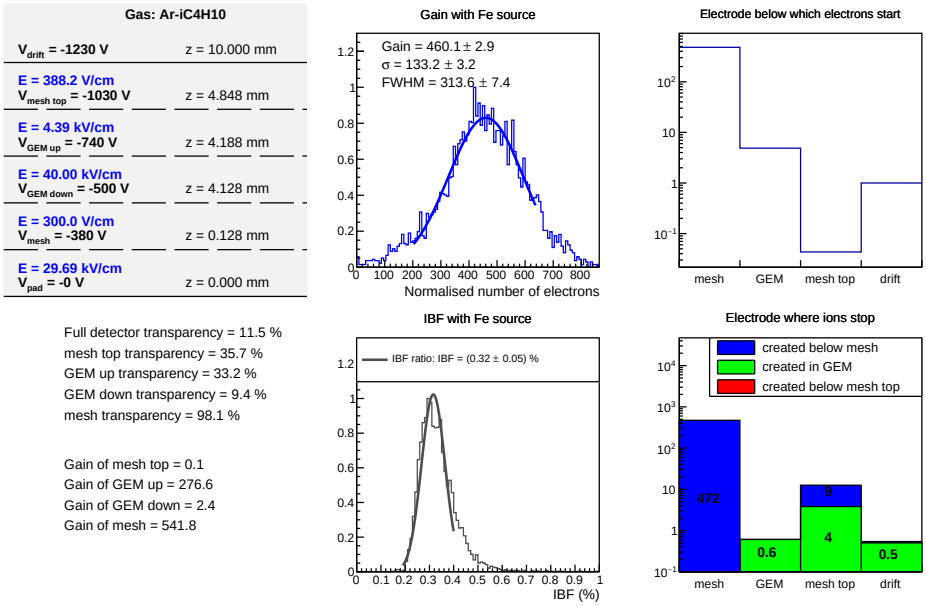

Figure 9.6: Simulation with at top left: the electric field configuration of the detector; top middle: gain spectrum obtained with an iron source; top right: average numbers of electrons created at each stage of amplification per event; bottom left: calculation of the gain and transparency of the electrodes; bottom middle: histogram of the IBF; bottom right: average number of ions that stop at each electrode per event.

Since there is no amplification below the top micro-mesh, the transparencies of these electrodes are multiplied and lead to a decrease in energy resolution.

The IBF is (0.25 ± 0.02)% in the data measurement and (0.32 ± 0.05)% in the simulation. These values are compatible within statistical uncertainties. According to the simulation, there is no amplification below the top micro-mesh. The ions that reach the drift electrode are created in the GEM.

128-µm-gap model

Figure 9.7 shows a laboratory measurement and figure 9.8 shows the corresponding simulation for the same electric field configuration.

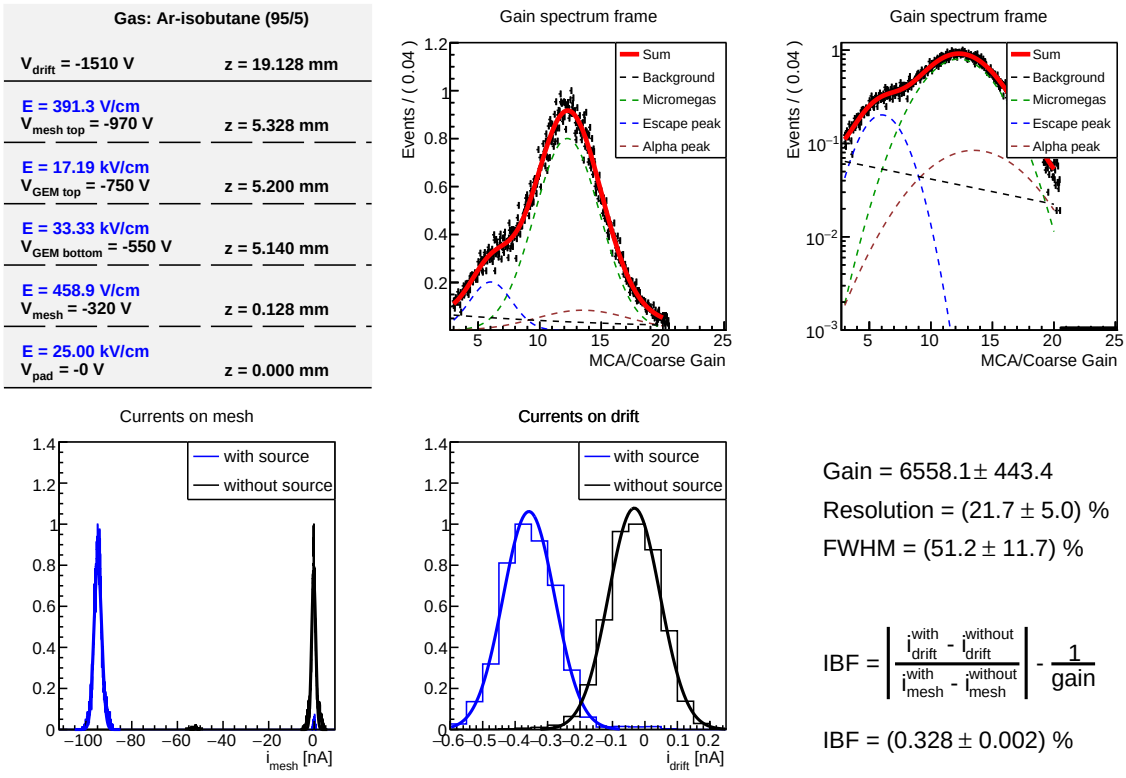

Figure 9.7: Measurement with at top left: the electric field configuration of the detector, top middle: spectrum obtained with an iron source, top right: same spectrum in log scale, bottom left: currents read on the bottom micro-mesh, bottom middle: currents read on the drift electrode, bottom right: calculation of gain and IBF.

In the simulation, the gain (601 ± 2) is lower by a factor 11 compared to the measurement in the laboratory (6558 ± 443). The energy resolution obtained in the simulation, $\sigma(E)/E$, is about 13%, which is much better that the energy resolution of (22 ± 5)% actually measured in the laboratory. The possible reasons for the differences of gain and energy resolution are discussed in section 9.1.4.

The IBF is (0.33 ± 0.00)% in the data measurement and (0.23 ± 0.03)% in the simulation, which is 40% lower. According to the simulation, the ions which reach the drift electrode are

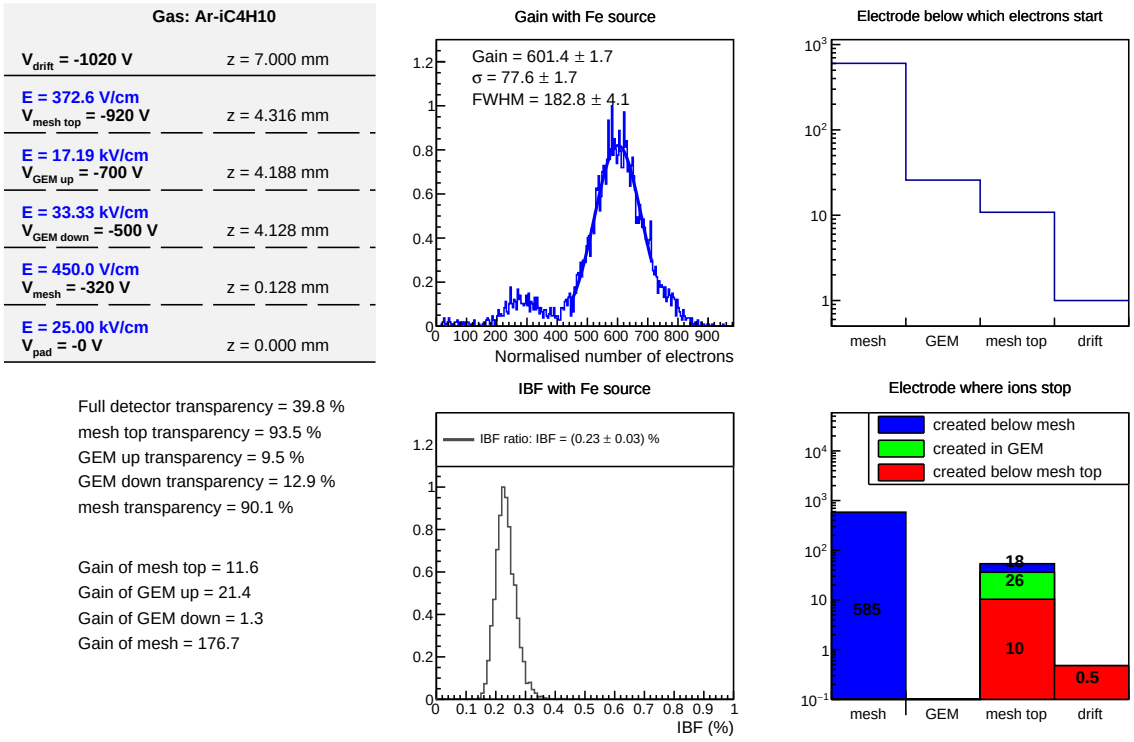

Figure 9.8: Simulation with at top left: the electric field configuration of the detector; top middle: gain spectrum obtained with an iron source; top right: average numbers of electrons created at each stage of amplification per event; bottom left: calculation of the gain and transparency of the electrodes; bottom middle: histogram of the IBF; bottom right: average number of ions that stop at each electrode per event.

those created below mesh top only: the top micro-mesh effectively stops the ions created in the amplification stages below.

9.1.4 Discussion on the comparison of the measurements and simulations

Simulations and measurements in the laboratory show sometimes large discrepancies. There can be many reasons for these differences.

- The Penning coefficient, which greatly impacts the final gain, is entered manually into the simulation, and it is not known with good precision. Simulations have been carried out with the Penning transfer rate $r_p = 0.48$ for single-stage MicroMEGAS configurations, and the gain was found to be at least three times higher than for $r_p = 0.321$ used in the simulations presented (see appendix J for details of this study). In particular, the higher r_p, the higher the gain slope. Given the fact that for both micro-meshes 45/18 and 70/30 the gain slope in the simulation is lower than for measurements (see figures 9.1 and 9.2), the r_p provided by the reference [1] in argon-isobutane (95/5) might be too low. However, the same study presented in appendix J shows that the Penning transfer rate has a little impact on the IBF.

- Secondly, in the laboratory, the micro-mesh is likely to flatten down when the amplification field is strong as a consequence of the electromagnetic force. The amplification gap is then reduced, which can alter the final gain and the energy resolution.

- The IBF measured in the laboratory is not known with as much certainty as in simulations: in the laboratory, not all events originate from the drift region. The events considered as contamination for the measurements are those for which the photon converts above the drift electrode, and those which convert in the transfer region (the proportion of events taking place in the spaces of amplification being negligible). This contamination is explained in more detail in the appendix H.2.1. Events that take place above the drift electrode are expected to bias the ion backflow measurement by overestimating it, (also shown in section 8.4), while events that take place in the transfer region are expected to bias the ion backflow measurement by undervaluing it.

- The geometry of the GEM in the simulations and in the detector was not exactly the same: in the simulation, the pitch of the GEM is 126 µm instead of 140 µm in the detector, as explained in section 7.3.2. This pitch was defined in the simulation to optimize the computation time of the electric field maps. On the other hand, the double-conical holes have the same geometries. The optical transparency of the GEM is therefore not the same. According to equation 8.15, the optical transparency of the GEM tested in the laboratory is 20%, whereas it is 24% in the simulation, which represents a 20% difference.

- The geometry of the micro-meshes differs in the sense that in the detector, the micro-meshes are woven - the wires cross each other by passing alternately over and under and are crushed at the crossings, while the wires cross each other in the same plane in the simulation. The electric field can thus be locally altered around the wires.

- The simulations give in general a much better resolution in energy than in laboratory measurements, for the reasons mentioned above. As shown in figure 7.5, where the resolution is 6%, the measurement for the same field configuration is about 20%. An example is given in the appendix I, showing that a better resolution can be achieved by collimating the source.

A possible improvement of the setup would consist in using an X-ray gun, which would allow targeting the drift region only, and therefore cleaner IBF measurements, free from the contamination currents explained in the section 8.4 and in the appendix H.2.

The simulations could also be improved by getting closer to reality: for example, by simulating woven micro-meshes, as they are in reality, or by building electric field maps while respecting the geometric configurations of each electrode. However, this would imply constructing several patterns of each electrode, since the pitches are not multiple from each other, which requires a very long computation time and generates very memory-consuming files.

9.2 Comparison of MMGEM models with other geometric configurations

9.2.1 Single-stage MicroMEGAS and double-stage MicroMEGAS and GEM detectors

The measurements performed on the two prototype detectors are compared to those taken in the single-stage MicroMEGAS configuration and in the hybrid configuration with a micro-mesh and a GEM.

In this latter configuration however, the measured IBF does not correspond to the true IBF, induced by events from just above the GEM, since the signal is dominated by events from the transfer region. Looking at figure 7.8 at right, if one takes into account only ions created below the micro-mesh - which correspond to events taking place in the transfer region - the average IBF should correspond to $\text{IBF}^{\text{transfer}}$ = 74/(74+5+3190) = 2.26%. However, the average IBF for events taking place in the gap between the GEM and the top micro-mesh corresponds to IBF^{gap} = (3+74)/(3+74+5+11+3190) = 2.35%. According to table H.3, the fraction of photons f_γ^{gap} that convert in the detector and generate a signal in the gap above the GEM is 1.4%, and the fraction of photons $f_\gamma^{\text{transfer}}$ that generate a signal in the transfer region is 11.4%. Therefore, the measured IBF should correspond to

$$\text{IBF}^{\text{meas}} = P_\gamma^{\text{gap}} \times \text{IBF}^{\text{gap}} + P_\gamma^{\text{transfer}} \times \text{IBF}^{\text{transfer}} \tag{9.1}$$

where P_γ^{gap} and $P_\gamma^{\text{transfer}}$ are the fractions of photons of interest, in the gap between the top micro-mesh or in the transfer region, that converted in one or the other of these two regions. Therefore,

$$P_\gamma^{\text{gap}} = \frac{f_\gamma^{\text{gap}}}{f_\gamma^{\text{gap}} + f_\gamma^{\text{transfer}}} \text{ and } P_\gamma^{\text{transfer}} = \frac{f_\gamma^{\text{transfer}}}{f_\gamma^{\text{gap}} + f_\gamma^{\text{transfer}}}$$

and

$$\text{IBF}^{\text{meas}} = \frac{1.4}{1.4+11.4} \times 2.35\% + \frac{11.4}{1.4+11.4} \times 2.26\% \tag{9.2}$$

$$\text{IBF}^{\text{meas}} = 2.27\% \tag{9.3}$$

However, figure 7.8 (middle) indicates the IBF obtained in this example is $(2.37 \pm 0.05)\%$. When taking into account events where the photons convert in the transfer region in the computation of IBF (IBF^{meas}), the value obtained is 4% underestimated compared to the real value obtained with events converting above the GEM only. Therefore, IBF measurements presented for this

configuration (labeled Micro-mesh + GEM) should be taken as a lower estimate.

All the measurements are presented in figure 9.9.

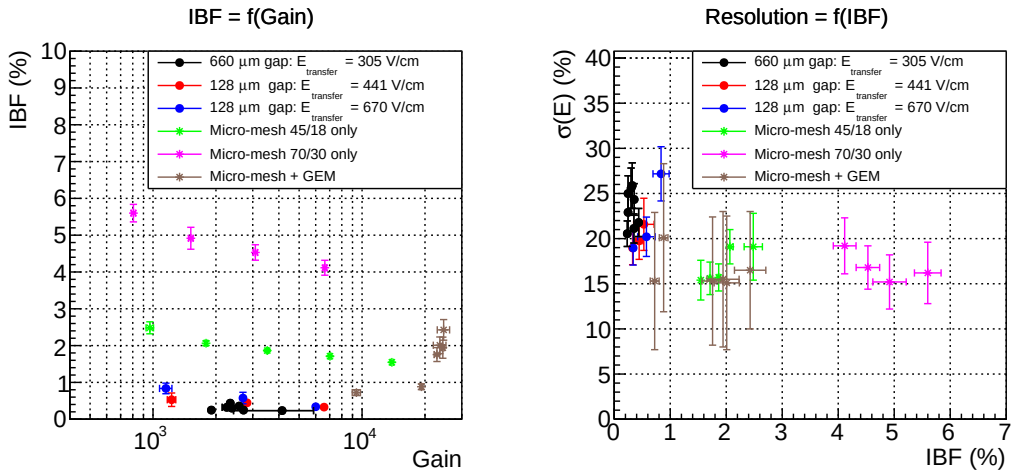

Figure 9.9: Left: measurements of IBF as a function of gain. Right: energy resolution as a function of IBF, for all configurations tested in the laboratory. The 660-µm-gap MMGEM detector is shown with black markers, the 128-µm-gap MMGEM detector with red and blue markers (for two E_{transfer} values, the single-stage MicroMEGAS with a micro-mesh 45/18 in green, the single-stage MicroMEGAS with a micro-mesh 70/30 in magenta, and the hybrid detector with a MicroMEGAS and a GEM in brown.

The MMGEM models show a clear improvement in terms of IBF compared to MicroMEGAS and hybrid models. However, the energy resolution is worse for the MMGEM models: with the 45/18 micro-mesh, energy resolutions are of the order of 15%, whereas they are of the order of 20% to 25% for the MMGEM models.

9.2.2 ALICE quadruple GEM detector

Secondly, these measurements are compared to the quadruple GEM detector used in the ALICE experiment at CERN [2, 3]. They utilize a quadruple GEM system in which the foils in layer 1 and 4 have a standard hole pitch (Standard, 140 µm), whereas the foils in layer 2 and 3 have a hole pitch that is two times larger (Large Pitch, 280 µm) [4]. This arrangement allows to block ions efficiently by employing asymmetric transfer fields and foils with low optical transparency. In this configuration, the electric fields are chosen such that most of the gain comes from the GEMs at lower levels, thus allowing the ions to be blocked more efficiently. On the other hand, the electric fields are constrained by the electron transmission which must be as good as possible in order to obtain good energy resolution.

Figure 9.10 on the left-hand side, taken from [4], illustrates IBF and energy resolution measurements for different combinations of ΔU_{GEM1} and ΔU_{GEM2}, and at different ratios $\Delta U_{\text{GEM3}}/\Delta U_{\text{GEM4}}$. The measurements are obtained using an X-ray gun which sent 5.9 keV photons into the detector. The gas used in the detector is a gas mixture of Ne-CO_2-N_2 (90/10/5).

The measurements taken for MMGEM detectors are drawn in figure 9.10 on the right-hand side.

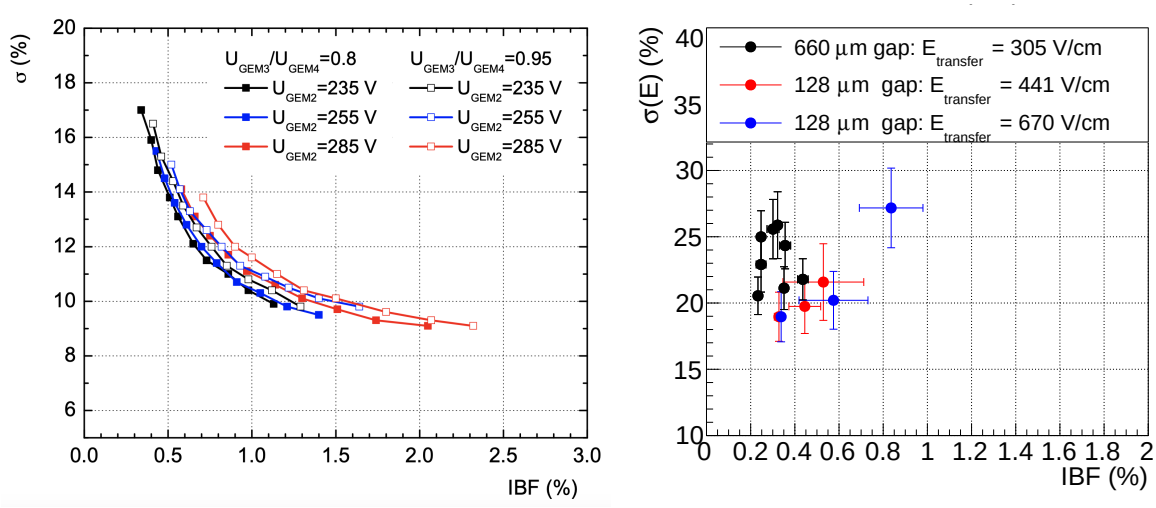

Figure 9.10: Left: Correlation between ion backflow and energy resolution at 5.9 keV in a quadruple GEM in Ne-CO_2-N_2 (90/10/5) for various settings of ΔU_{GEM2}. The voltage on GEM1 increases for a given setting between 225 and 315 V from left to right. The voltages on GEM3 and GEM4 are adjusted to achieve a total effective gain of 2000, while keeping their ratio fixed. The transfer and induction fields are 4, 2, 0.1 and 4 kV/cm, respectively. Right: Correlation between ion backflow and energy resolution at 5.9 keV in the MMGEM detector configuration. The electric field below the top micro-mesh is increased, while all other electric fields remain constant. The 660-µm-gap detector has a gain kept constant at 2000, while the gain in the 128-µm-gap detector increases from 1000 to 6000.

MMGEM detectors achieve lower IBF values, scaling down to 0.2%, but higher energy resolutions $\sigma(E)/E$. As the gas used in the quadruple GEM detectors of ALICE, Ne-CO_2-N_2 (90/10/5), and in the MMGEM detectors, argon-isobutane (95/5), are different, simulations presented in appendix K show that when adapting the electric fields to reach the same gain in the detectors, the IBF remains unchanged. Therefore, the gas used in the detector is not responsible for the better IBF performance of the MMGEM detectors. According to the same study, the resolution however is expected to be 4% better in argon-isobutane (95/5) than in Ne-CO_2-N_2 (90/10/5).

9.3 Summary

Simulations carried out with Garfield++ [5] and presented in chapter 7 clearly show the efficiency of each electrode in stopping the ions, and make it possible to discern how to reconcile a good electronic transmission with a low IBF for gain values of the order of 2000. The simulations carried out initially with the MMGEM geometry promised good performances in terms of energy resolution and IBF. However, major differences are observed between laboratory measurements and simulations, as shown in section 9.1. In particular, the gain measured in the simulations is a factor of 2 to 10 below the measurements made in the laboratories for the same models in the same configuration of electric fields. Many reasons could explain these differences, such as the choice of the Penning transfer rate in the simulation, the imprecision on IBF measurement due to contamination events, or the geometry differences between simulations

and real prototypes.

The new MMGEM models are compared with the single MicroMEGAS configuration and the MicroMEGAS and GEM hybrid configuration, and show a reduction in IBF by a factor of 10.

The MMGEM models are also compared with the ALICE quadruple GEM, and can achieve lower IBF. On the other hand, the energy resolution is 25 to 60% less good while keeping an IBF smaller than 0.5%.

Bibliography

[1] T. Zerguerras et al. Understanding avalanches in a Micromegas from single-electron response measurement. *Nucl. Instrum. Meth. A*, 772:76–82, 2015. doi: 10.1016/j.nima.2014.11.014.

[2] J. Adolfsson et al. The upgrade of the ALICE TPC with GEMs and continuous readout. *JINST*, 16(03):P03022, 2021. doi: 10.1088/1748-0221/16/03/P03022.

[3] G. Dellacasa et al. ALICE: Technical design report of the time projection chamber. 1 2000.

[4] Christian Lippmann. Upgrade of the ALICE Time Projection Chamber. 3 2014.

[5] H. Schindler and R. Veenhof. Garfield++ – Simulation of tracking Detectors. URL http://cern.ch/garfieldpp.

Part III

Appendices - ALICE

Appendix A

Computation of the center-of-mass energy in the γp system

The Feynman diagram for the exclusive J/ψ photoproduction at LO is shown in figure A.1.

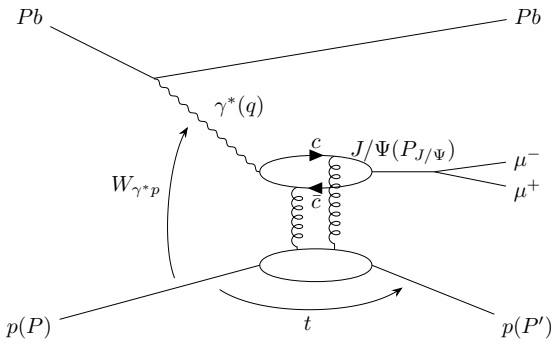

Figure A.1

Since the energy is conserved, the following relation holds:

$$W^2_{\gamma \mathrm{p}} = (q + P)^2 = (P_{\mathrm{J}/\psi} + P')^2 \tag{A.1}$$

where q, $P_{\mathrm{J}/\psi}$, P and P' are the quadri-momenta of the virtual photon, the J/ψ, the incoming proton and the outgoing proton respectively, in the laboratory frame. $P_{\mathrm{J}/\psi}$ and P' are defined as:

$$P_{\mathrm{J}/\psi} = \begin{pmatrix} E_{\mathrm{J}/\psi} \\ \vec{p}_{\mathrm{J}/\psi} \end{pmatrix} \quad \text{and} \quad P' = \begin{pmatrix} E'_p \\ \vec{p}'_p \end{pmatrix} \tag{A.2}$$

where the energy and momentum of the outgoing proton are to first order equal to the ones of the incoming proton $E'_p = E_p$ and $\vec{p}'_p = \vec{p}_p$.

Then,

$$\begin{aligned} W^2_{\gamma p} &= (P_{\mathrm{J}/\psi} + P')^2 && \text{(A.3)} \\ &= (E_p + E_{\mathrm{J}/\psi})^2 - (\vec{p}_p + \vec{p}_{\mathrm{J}/\psi})^2 && \text{(A.4)} \\ &= E_p^2 + 2E_p E_{\mathrm{J}/\psi} + E^2_{\mathrm{J}/\psi} - p_p^2 - p^2_{\mathrm{J}/\psi} - 2p_p p_z && \text{(A.5)} \\ & && \text{(A.6)} \end{aligned}$$

where $p_p = |\vec{p}_p|$ and $p_{\mathrm{J}/\psi} = |\vec{p}_{\mathrm{J}/\psi}|$, and p_z is longitudinal momentum of the J/ψ. The last line uses the fact that the proton goes in the longitudinal direction.

Since in the high energy limit $p_p \simeq E_p$,

$$W^2_{\gamma p} = 2E_p E_{\mathrm{J}/\psi} + E^2_{\mathrm{J}/\psi} - p^2_{\mathrm{J}/\psi} - 2E_p p_z \tag{A.7}$$

$$= 2E_p(E_{\mathrm{J}/\psi} - p_z) + E^2_{\mathrm{J}/\psi} - p^2_{\mathrm{J}/\psi} \tag{A.8}$$

and using $E^2_{\mathrm{J}/\psi} - p^2_{\mathrm{J}/\psi} = M^2_{\mathrm{J}/\psi}$

$$W^2_{\gamma p} = 2E_p(E_{\mathrm{J}/\psi} - p_z) + M^2_{\mathrm{J}/\psi} \tag{A.9}$$

In the high energy limit, all particle masses are assumed negligible, so $M_{\mathrm{J}/\psi} \ll E_{\mathrm{J}/\psi}$ and $M_{\mathrm{J}/\psi} \ll E_p$, therefore

$$W^2_{\gamma p} = 2E_p(E_{\mathrm{J}/\psi} - p_z) \tag{A.10}$$

Let us now find an expression of $E_{\mathrm{J}/\psi}$ as a function of the rapidity y of the J/ψ. The rapidity of the J/ψ is reads

$$y = \frac{1}{2}\ln\left(\frac{E + p_z}{E - p_z}\right) \tag{A.11}$$

$$= \frac{1}{2}\ln\left(\frac{E^2 - p_z^2}{(E - p_z)^2}\right) \tag{A.12}$$

$$= \frac{1}{2}\ln\left(\frac{M^2_{\mathrm{J}/\psi} + p^2_{\mathrm{T}}}{(E - p_z)^2}\right) \tag{A.13}$$

$$\tag{A.14}$$

where E is the simplified notation of the energy of the J/ψ, and p_{T} its transverse momentum.

Assuming $t \to 0$ and using $t = -p^2_{\mathrm{T}}$,

$$y = \frac{1}{2}\ln\left(\frac{M^2_{\mathrm{J}/\psi}}{(E - p_z)^2}\right) \tag{A.15}$$

hence

$$E_{\mathrm{J}/\psi} - p_z = M_{\mathrm{J}/\psi} e^{-y} \tag{A.16}$$

Injecting the formula (A.16) in equation (A.10), the expression of $W^2_{\gamma\mathrm{p}}$ becomes

$$\boxed{W^2_{\gamma\mathrm{p}} = 2E_p M_{\mathrm{J}/\psi} e^{-y}} \tag{A.17}$$

Appendix B

Studies on V0C detector

B.1 Traces of dissociative J/ψ photoproduction in V0C

In order to assess if signals of J/ψ photoproduction off protons with proton dissociation can leave a signal in the V0C detector, studies have been conducted using RAPGAP 3.3 event generator [1]. The RAPGAP software uses DIFFVM, which is a MC generator that was widely used by the H1 collaboration for studies of diffractive vector meson production.

The simulated process is a positron-proton collision, with the following requirements as input:

- The basic partonic subprocess selected is the interaction of an electron with a quark $eq \rightarrow e'q'$ following the quark parton model (QPM) - in the implementation in RAPGAP only QPM type events can be generated.
- The proton dissociates.
- The gluon density of the pomeron is given according to the Nikolaev Zakharov model [2].
- The pomeron density is given according to the Nikolaev Zakharov model [2].
- The initial momentum of the proton and of the positron have been fixed to match the center-of-mass energy of our data set, namely p_p = 6500 GeV and p_e = -2510 GeV.
- The limits of the inelasticity[1] have been chosen in order to match the ALICE muon spectrometer acceptance, namely y_{min} = 0.00001 and y_{max} = 0.00006.

[1]The inelasticity is defined by $y = (P.q)/(P.l)$ where P is the initial proton four vector, $q = l - l'$ is the four vector of the virtual photon with l (l') the four vectors of the initial (scattered) electron.

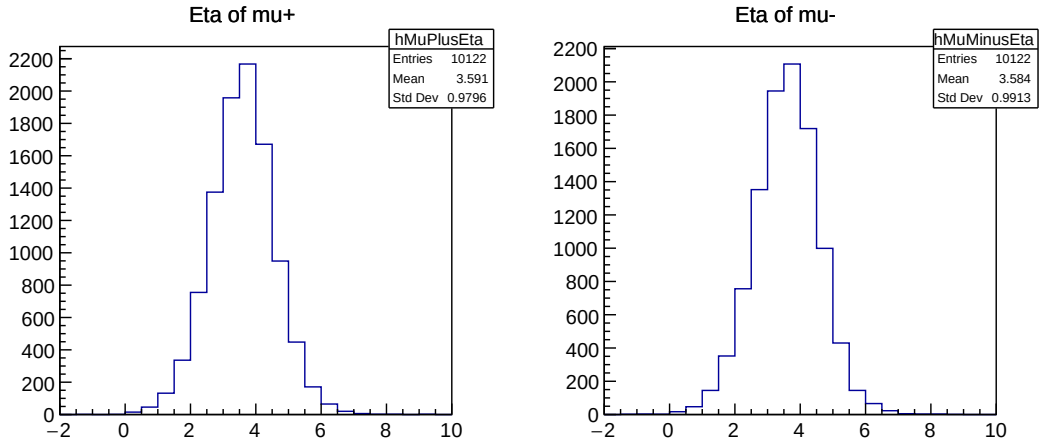

Figure B.1: Distribution of the pseudo-rapidity of both muons resulting from the J/ψ decay.

10122 events are produced with the configuration described above. The distribution of the pseudorapidities η of both muons from the J/ψ are shown in figure B.1. Among these 10122 events, 2530 J/ψ mesons decay in two muons which are both in the muon spectrometer acceptance, with $2.5 < \eta < 4.0$[2].

For these 2530 events, the pseudorapidity η of each track per event other than the tracks of muons resulting from the J/ψ decay is recorded in order to check if it falls into the V0C geometrical acceptance. The number of tracks per event, for which the pseudorapidity falls into the V0C, are shown in figure B.2.

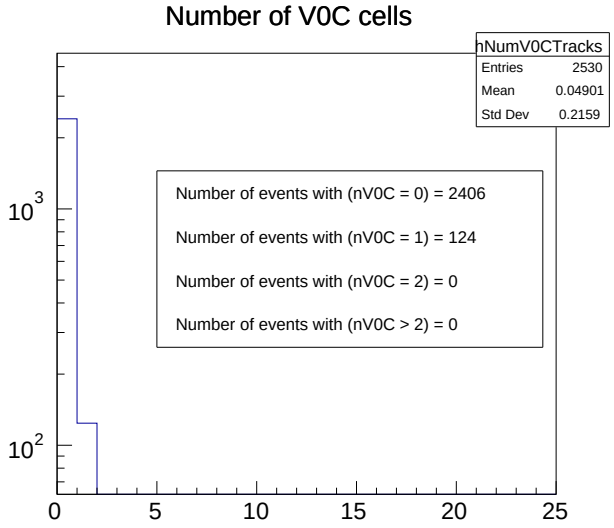

Figure B.2: Number of particles per event in the acceptance of V0C.

According to RAPGAP, no dissociative event appears to have more than one produced particle in the geometrical acceptance of V0C. This observation shows that the analysis cut

[2]In this study with RAPGAP, the convention for the pseudorapidity is the reverse of the one used in ALICE.

applied on V0C - to restrict the number of fired cells to the number of matched cells with a muon with a tolerance of two additional cells - should not reject dissociative J/ψ events.

B.2 V0C matching

B.2.1 Cut on V0C cells

In order to reconstruct a J/ψ signal, or a signal from the $\gamma\gamma \to \mu^+\mu^-$ process, two muons must be reconstructed in the muon spectrometer. A "good" muon, defined as in section 3.2.1, with well defined η and φ coordinates with respect to the ALICE reference system, is associated with a signal in V0C with the following procedure. The V0C is made of four concentric rings, each divided in eight sectors in azimuth. V0C coordinates thus correspond to a maximum of thirty two possible combinations of (η, φ) identifiers. When the (η, φ) coordinates of a muon correspond to a fired V0C cell, it is considered "matched" to it. In the following, the number of matched muons to a V0C cell will be referred to as "nMatched".

Figure B.3 shows the number of events contained in the sample and in the restricted mass range $2.8 < M_{\mu\mu} < 3.3$ GeV/c^2, using the exclusive selection (left), the standard selection (in the middle), and the subtraction of the last two (on the right), by varying the cutoff on V0C cells. The number of events contained in the exclusion selection sample stabilizes when the number of fired V0C cells is smaller than the number of matched muons with a tolerance of two additional cells. However, the number of events in standard mid selection, which contain exclusive and inclusive events, does not appear to stabilize and the difference between the standard and the exclusive selection is interpreted as a growing inclusive contamination.

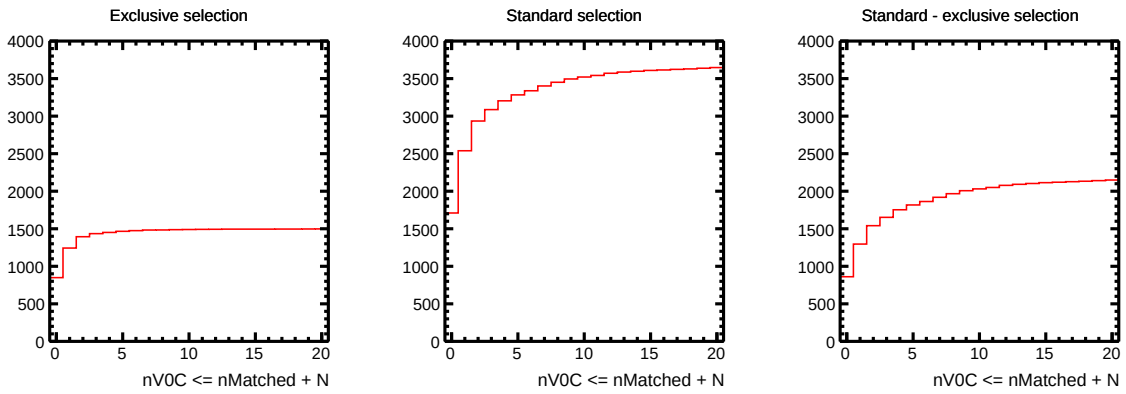

Figure B.3: The number of raw candidates between $2.8 < M_{\mu\mu} < 3.3$ GeV/c^2 for the exclusive selection (left), the standard selection (middle), and the subtraction of these two (right), depending on the number of fired V0C cells nV0C $\leq$ nMatched + N, where N varies between 0 and 20.

In order to better understand the behavior of the standard selection sample when increasing the number of fired V0C cells accepted, the two-dimensional fit as described in section 4.2.4 is repeated by varying the condition on V0C. The data is selected in the usual invariant mass range, $2.5 < M_{\mu\mu} < 3.5$ GeV/c^2. The raw yields of each contribution in the data are extracted and given in table B.1. Then again, the number of events corresponding to the exclusive two-photon interactions, $N_{\gamma\gamma}^{\text{exc}}$, as well as the number of events corresponding to the exclusive J/ψ

photoproduction, $N^{\text{exc}}_{\text{J}/\psi}$, become stable for nV0C $<$ nMatched $+2$, while the numbers of events corresponding to the inclusive components ($N^{\text{inc}}_{\gamma\gamma}$ and $N^{\text{diss}}_{\text{J}/\psi}$) keep increasing with nV0C.

V0C cut	$N^{\text{exc}}_{\gamma\gamma}$	$N^{\text{inc}}_{\gamma\gamma}$	$N^{\text{exc}}_{\text{J}/\psi}$	$N^{\text{diss}}_{\text{J}/\psi}$	$R = \frac{N^{\text{diss}}_{\text{J}/\psi}}{N^{\text{exc}}_{\text{J}/\psi}}$
nV0C $\leq$ nMatched + 0	120	165	729	817	1.121
nV0C $\leq$ nMatched + 1	221	202	1083	1231	1.137
nV0C $\leq$ nMatched + 2	246	225	1180	1515	1.284
nV0C $\leq$ nMatched + 3	248	246	1211	1622	1.339
nV0C $\leq$ nMatched + 4	251	261	1209	1724	1.426
nV0C $\leq$ nMatched + 5	250	271	1221	1788	1.464

Table B.1

The interpretation of these numbers is as follows : other bona fide interactions during the same collision can occur, and leave a signal in one or two V0C cell. Moreover, events with at least two additional fired V0C cells can be interpreted as the production of a J/ψ and several other particles in inclusive photoproduction or hadronic production with a low number of produced particles in peripheral collisions that may have survived the selection. Since the p_{T} shape of exclusive J/ψ is fixed in the two-dimensional fit, the contamination of inclusive J/ψ when increasing the tolerance on nV0C is assumed to be included in the dissociative component.

Therefore, the veto nV0C $\leq$ nMatched + 2 corresponds to the threshold for which exclusive events are selected without significant loss, while increasing nV0C would let the number of inclusive events grow.

B.2.2 Systematic uncertainties induced by the V0C cut

In order to evaluate the systematic uncertainty induced by the contamination of inclusive events on the raw numbers extracted when varying the V0C cut, the following study is presented.

Systematic uncertainties on J/ψ events

The data that passed the standard selection and nV0C $\leq$ nMatched + 0 is not expected to contain a significant inclusive contamination, since this is the most stringent cut. Therefore, the ratio $N_{\text{dissociative J}/\psi}/N_{\text{exclusive J}/\psi}$ using this selection should be the closest to reality under the assumption that the cut nV0C $\leq$ nMatched + 0 fully rejects inclusive events and that the V0C cut does not impact dissociative events as studied with RAPGAP in section B.1. This ratio is taken from table B.1:

$$\left(\frac{N^{\text{diss}}_{\text{J}/\psi}}{N^{\text{exc}}_{\text{J}/\psi}}\right)^{\text{nV0C}\leq\text{nMatched}+0} = 1.121 \tag{B.1}$$

.

Since the number of exclusive J/ψ stabilizes for nV0C $\leq$ nMatched + 2, the number of exclusive J/ψ is taken to be

$$N^{\text{exc}}_{\text{J}/\psi} = 1180 \tag{B.2}$$

from table B.1.

The number of expected dissociative J/ψ can thus be estimated as

$$(N_{J/\psi}^{\text{diss}})^{\text{expected}} = \left(\frac{N_{J/\psi}^{\text{diss}}}{N_{J/\psi}^{\text{exc}}}\right)^{\text{nV0C}\leq\text{nMatched}+0} \times N_{J/\psi}^{\text{exc}} \tag{B.3}$$

$$= 1180 \times 1.121 \tag{B.4}$$

$$= 1323 \tag{B.5}$$

Hence, the systematic error of the number on dissociative J/ψ can be estimated as the difference between the extracted number in table B.1, $(N_{J/\psi}^{\text{diss}})^{\text{extracted}} = 1515$ with nV0C $\leq$ nMatched + 2, and the expected number:

$$\frac{\Delta N_{J/\psi}^{\text{diss}}}{N_{J/\psi}^{\text{diss}}} = \frac{(N_{J/\psi}^{\text{diss}})^{\text{extracted}} - (N_{J/\psi}^{\text{diss}})^{\text{expected}}}{(N_{J/\psi}^{\text{diss}})^{\text{extracted}}} \tag{B.6}$$

$$= \frac{1515 - 1323}{1515} \tag{B.7}$$

$$= 13\% \tag{B.8}$$

On the other hand, the systematic error on the number of exclusive J/ψ is estimated as the difference between the number taken from table B.1 with nV0C $\leq$ nMatched + 2 ($N_{J/\psi}^{\text{exc}} = 1180$), and the number extracted with the looser cut nV0C $\leq$ nMatched + 3, $(N_{J/\psi}^{\text{exc}})^{\text{nV0C}\leq\text{nMatched}+3} = 1211$. Hence the relative systematic uncertainty induced by the cut on V0C is estimated as:

$$\frac{\Delta N_{J/\psi}^{\text{exc}}}{N_{J/\psi}^{\text{exc}}} = \frac{|(N_{J/\psi}^{\text{exc}})^{\text{nV0C}\leq\text{nMatched}+3} - N_{J/\psi}^{\text{exc}}|}{N_{J/\psi}^{\text{exc}}} = 2.6\% \tag{B.9}$$

Finally, the systematic error on the ratio of the numbers of dissociative and exclusive J/ψ, denoted $R = N_{J/\psi}^{\text{diss}}/N_{J/\psi}^{\text{exc}}$, is estimated as the difference between the ratio taken from table B.1 with nV0C $\leq$ nMatched +2 ($R = 1.284$), and the number extracted with the looser cut nV0C $\leq$ nMatched + 3, $R^{\text{nV0C}\leq\text{nMatched}+3} = 1.339$. Hence the relative systematic uncertainty induced on the ratio by the cut on V0C is estimated as:

$$\frac{\Delta R}{R} = \frac{|R^{\text{nV0C}\leq\text{nMatched}+3} - R|}{R} = 4.3\% \tag{B.10}$$

Systematic uncertainties on $\gamma\gamma \to \mu^+\mu^-$ events

A similar study has been conducted for the dimuon continuum in the invariant mass range $1.0 < M_{\mu\mu} < 2.5$ GeV/c^2. The number of exclusive $\gamma\gamma \to \mu^+\mu^-$ events are obtained following the procedure described in section 4.1 while changing the condition on V0C cut, and they are given in table B.2. Similarly as for the case of exclusive J/ψ events, the systematic error of the number on exclusive $\gamma\gamma \to \mu^+\mu^-$ events is estimated as the difference between the number extracted in table B.2 with nV0C $\leq$ nMatched + 2, $N_{\gamma\gamma}^{\text{exc}}$, corresponding to the usual selection, and the number extracted with nV0C $\leq$ nMatched + 3, $(N_{\gamma\gamma}^{\text{exc}})^{\text{nV0C}\leq\text{nMatched}+3}$. The relative uncertainties are then computed as

$$\frac{\Delta N_{\gamma\gamma}^{\text{exc}}}{N_{\gamma\gamma}^{\text{exc}}} = \frac{|(N_{\gamma\gamma}^{\text{exc}})^{\text{nV0C}\leq\text{nMatched}+3} - N_{\gamma\gamma}^{\text{exc}}|}{N_{\gamma\gamma}^{\text{exc}}}, \tag{B.11}$$

and they are given in table B.2 for each studied mass range.

Mass interval [GeV/c^2]	$(1.0, 1.5)$	$(1.5, 2.0)$	$(2.0, 2.5)$
nV0C $\leq$ nMatched + 0	367	243	110
nV0C $\leq$ nMatched + 1	522	370	178
nV0C $\leq$ nMatched + 2	590	411	189
nV0C $\leq$ nMatched + 3	597	418	190
nV0C $\leq$ nMatched + 4	597	422	190
nV0C $\leq$ nMatched + 5	599	424	191
Uncertainty value	**1.2%**	**1.7%**	**0.5%**

Table B.2: Number of exclusive $\gamma\gamma \to \mu^+\mu^-$ events extracted from the data depending on the V0C cut and the mass range.

Bibliography

[1] Hannes Jung. Hard diffractive scattering in high-energy e p collisions and the Monte Carlo generator RAPGAP. *Comput. Phys. Commun.*, 86:147–161, 1995. doi: 10.1016/0010-4655(94)00150-Z.

[2] Nikolai Nikolaev and Bronislav G. Zakharov. Pomeron structure function and diffraction dissociation of virtual photons in perturbative QCD. *Z. Phys. C*, 53:331–346, 1992. doi: 10.1007/BF01597573.

Appendix C

Pile-up correction

The trigger used in the analysis, as described in section 3.1.2, rejects events with a signal in ADA or V0A detectors. However, these vetoes can be activated in good UPC events by signals coming from another interaction, a phenomenon known as pile-up. In addition, pile-up can also occur due to the vetoes applied at the selection level when requiring no activity in the Pb-side of the event as described in section 3.2.2. Therefore, using vetoes might suppress events of interest, and the raw numbers extracted from the signal must be corrected for this effect. The pile-up correction factor ϵ_{veto} is defined by the probability that the events are rejected properly, when they do not contain an event of interest i.e. when they are not mistakenly rejected because of pile-up. This probability depends on the average number of inelastic hadronic collisions per bunch crossing, denoted μ, which is stored in the OCDB files for each run.

The probability of a given event being rejected by pile-up is computed in each run using events triggered by a MB trigger, for which the events are triggered at the expected time when potentially colliding bunches cross the nominal IP of ALICE. As the pile-up we are interested in originates in relatively empty events, being mainly produced by electromagnetic interactions, events with little activity are selected, the goal being to determine the probability of observing the signal that would veto the event. For the case of p–Pb collisions the emptiness requirement is fulfilled by events that match the following requirements:

- there is no signal in ZNC,
- there are less than 3 tracklets in the SPD,
- V0C and ADC trigger input elements have not been fired,
- the event is not classified as "beam–beam" interaction by the ADC and V0C detectors.

Then, the pile-up probability is computed as

$$p(\mu) = \frac{N_{\text{pile-up}}}{N_{\text{selected}}} \tag{C.1}$$

where N_{selected} is the number of events that fulfil the emptiness requirements, and $N_{\text{pile-up}}$ is the number of events which fulfil either one of the following conditions:

- there is a signal in ZNA
- V0C trigger input elements have been fired
- ADC trigger input elements have been fired
- the event is classified as a "beam–beam" interaction by the V0A detector,
- the event is classified as a "beam–beam" interaction by the ADA detector.

Figure C.1 shows the pile-up behavior as a function of μ for the p–Pb data samples when the

line is forced to pass through (0,0). The total pile-up is computed using the fit to evaluate the expected probability for each run and then taking the average over all runs using the luminosity of each run as a weight. Most of the pile-up rejection (0.037) comes from V0A.

The same analysis is repeated by varying the conditions of the analysis; for example, lifting the constraint of the fit line crossing $(0, 0)$, changing the definition of emptiness by requiring no tracklets, or changing the time-windows for the definition of signal in ZN. The results varied from 0.0372 to 0.0406, therefore the pile-up is considered to be $p = 0.039 \pm 0.002$ and the correction to the cross section to account for the losses is:

$$\epsilon_{\text{veto}} = 1 - p = 0.961 \pm 0.002. \tag{C.2}$$

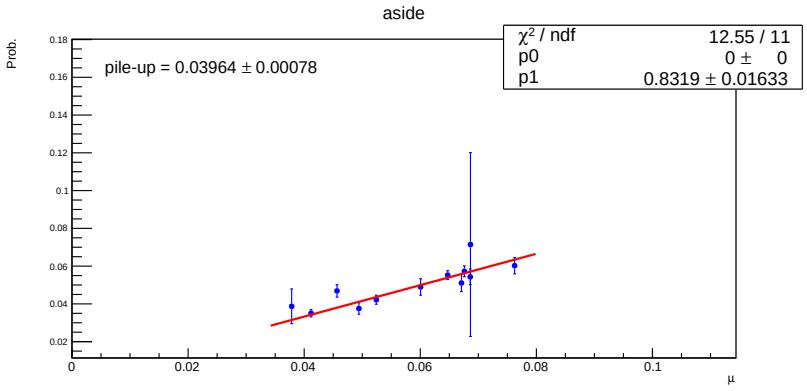

Figure C.1: Pile-up behaviour in the p–Pb period with the intercept fixed to zero

Appendix D

Empirical functions to describe the data

D.1 Landau distribution

The Landau distribution is a probability density function given by:

$$f(x) = \frac{1}{\pi\sigma} \int_0^\infty e^{-t} \cos\left(t\left(\frac{x-\mu}{\sigma}\right) + \frac{2t}{\pi}\log\left(\frac{t}{\sigma}\right)\right) dt \tag{D.1}$$

where $\mu \in (-\infty, \infty)$ is the location parameter, and $\sigma \in (0, \infty)$ is the scale parameter.

D.2 Double-sided Crystal Ball function

The double-sided crystal ball function has the following seven parameters: a normalisation factor N, two Gaussian core parameters (mean μ and width σ), and four tail parameters (α_1, n_1, α_2, n_2). The function is defined as:

$$f(x) = N \cdot \begin{cases} \exp\left(-\frac{(x-\mu)^2}{2\sigma^2}\right) & \text{if } -\alpha_2 < \frac{x-\mu}{\sigma} < \alpha_1 \\ A \cdot \left(B - \frac{x-\mu}{\sigma}\right) & \text{if } \frac{x-\mu}{\sigma} \leq -\alpha_1 \\ C \cdot \left(D + \frac{x-\mu}{\sigma}\right) & \text{if } \frac{x-\mu}{\sigma} \geq \alpha_2 \end{cases} \tag{D.2}$$

with $A = \left(\frac{n_1}{|\alpha_1|}\right)^{n_1} \cdot \exp\left(-\frac{|\alpha_1|^2}{2}\right)$, $B = \frac{n_1}{|\alpha_1|} - |\alpha_1|$, $C = \left(\frac{n_2}{|\alpha_2|}\right)^{n_2} \cdot \exp\left(-\frac{|\alpha_2|^2}{2}\right)$, and $D = \frac{n_2}{|\alpha_2|} - |\alpha_2|$.

Appendix E

Estimation of the number of J/ψ events in γPb interactions

In this section, a computation of the expected number of J/ψ produced off Pb nuclei is presented, based on the measurement from reference [1]. As a first step, the J/ψ photoproduction is examined in Pb–Pb, before later specialising the exercise to the p–Pb case. The measured differential cross section in Pb–Pb is a mixture of two components, as either of the Pb nuclei may have emitted the γ. Since muons are always detected on the same side, and given the centre-of-mass energy of the γPb system as in equation E.1:

$$W^2_{\gamma Pb} = 2E_{\mathrm{Pb}} M_{\mathrm{J}/\psi} e^{-y} \,, \tag{E.1}$$

where E_{Pb} is the energy per nucleon carried by Pb nuclei, the high energy configuration is the one where the γ-emitter is the Pb nucleus going in the direction of the muon spectrometer, and for the low energy configuration the γ-emitter Pb nucleus is going in the opposite direction. It is then possible to separate the cross sections as in equation E.2:

$$\frac{d\sigma}{dy}^{\text{meas}} = \frac{d\sigma}{dy}^{\text{low W}} + \frac{d\sigma}{dy}^{\text{high W}} \,. \tag{E.2}$$

In p–Pb collisions, exclusive J/ψ photoproduction off proton targets dominate, but a contamination of coherent J/ψ photoproduction off Pb targets has to be accounted for. As the Pb nuclei go in the opposite direction of the muon spectrometer, the component of interest in equation E.2 is the low energy one.

Equation E.2 can be manipulated as shown in equation E.3:

$$\frac{d\sigma}{dy}^{W_1} = \frac{d\sigma}{dy}^{\text{meas}} \Bigg/ \left[1 + \left(\frac{d\sigma}{dy}^{W_2} \Big/ \frac{d\sigma}{dy}^{W1}\right)\right] \,, \tag{E.3}$$

where the ratio $\left(\frac{d\sigma}{dy}^{W_2} \Big/ \frac{d\sigma}{dy}^{W_1}\right)$ is obtained with an analysis using STARlight event generator, and W_1 and W_2 can interchangeably refer to either the low and high energy solutions.

In the coherent J/ψ Pb–Pb UPC analysis [1] the coherent J/ψ photoproduction cross sections are obtained as in equation E.4:

$$\frac{d\sigma^{\text{meas}}_{\mathrm{J}/\psi}}{dy} = \frac{N_{\mathrm{J}/\psi}}{(1 + f_I + f_D) \cdot \epsilon(\mathrm{J}/\psi) \cdot BR(\mathrm{J}/\psi \to \mu\mu) \epsilon_{\text{veto}} \cdot L_{\text{int}} \cdot \Delta y} \,, \tag{E.4}$$

where $f_D = N(\text{feed-down J}/\psi)/N(\text{primary J}/\psi) = 0.055 \pm 0.004$ is the feed down due to the decay of the $\psi(2S)$ taken from reference [1], $f_I = N(\text{incoh J}/\psi)/N(\text{coh J}/\psi) = 0.055 \pm 0.001$ is the incoherent fraction with a hard p_T cut at 0.25 GeV$/c$ taken from reference [1], and $\epsilon_{\text{veto}} = 0.95$ is the correction factor for veto efficiency.

In the case of the present p–Pb analysis, the terms of equation E.4 are adapted: $\epsilon_{\text{veto}} = 0.96$ (see appendix C), $f_I = 0$ since there is no contribution from incoherent events, and the photon flux has to be renormalised since it is the proton to emit the photon instead of lead nuclei as in the case of a Pb–Pb analysis.

As a consequence, it is possible to compute for p–Pb the number of expected coherent J$/\psi$ obtained by the interaction of the proton-emitted photon with the Pb nucleus going towards the A side of the ALICE detector. The formalism is shown in the following equation E.5, where $\left(k\frac{dn}{dk}\right)^W_{\text{p}}$ and $\left(k\frac{dn}{dk}\right)^W_{\text{Pb}}$ are the photon fluxes at the chosen energy W considering a proton in p–Pb and a Pb ion in Pb–Pb as the source of the photon flux respectively:

$$N^{\text{coh}}_{\text{J}/\psi,W} = \frac{d\sigma}{dy}^W \cdot (1 + f_D) \cdot (A \times E) \cdot L_{\text{int}} \cdot BR(\text{J}/\psi \to \mu\mu) \cdot \Delta y \cdot \frac{\left(k\frac{dn}{dk}\right)^W_{\text{p}}}{\left(k\frac{dn}{dk}\right)^W_{\text{Pb}}} \tag{E.5}$$

with the acceptance - efficiency factor $A \times E$ and the luminosity L_{int} specifically computed for this analysis in p–Pb. The term $(d\sigma/dy)^W$ is obtained following equation E.3, where the differential cross sections ratio is obtained by computing each differential cross section with the STARlight event generator for the two low and high energy solutions, which are given in table E.1. The photon fluxes are also computed with STARlight and are shown in table E.2 and E.3 for a Pb γ-source and a proton γ-source, respectively.

Rapidity range	$\frac{d\sigma}{dy}^{\text{low W}}$ (nb)	$\frac{d\sigma}{dy}^{\text{high W}}$ (nb)
$2.50 < y < 4.00$	2560 ± 8	465 ± 1
$2.50 < y < 3.25$	2851 ± 11	744 ± 3
$3.25 < y < 4.00$	2268 ± 10	186 ± 1

Table E.1: Differential cross sections computed with STARlight with their statistical uncertainties for the low and high energy solutions.

Rapidity range	$\left(k\frac{dn}{dk}\right)^{\text{low W}}$	$\left(k\frac{dn}{dk}\right)^{\text{high W}}$
$2.50 < y < 4.00$	$1.88 \cdot 10^2$	6.08
$3.25 < y < 4.00$	$2.00 \cdot 10^2$	2.19
$2.50 < y < 3.25$	$1.77 \cdot 10^2$	10.2

Table E.2: Photon flux computed with Starlight for Pb–Pb collisions.

Rapidity range	$\left(k\frac{dn}{dk}\right)_{\text{low W}}$	$\left(k\frac{dn}{dk}\right)_{\text{high W}}$
$2.50 < y < 4.00$	0.00572	0.0356
$3.25 < y < 4.00$	0.00417	0.0373
$2.50 < y < 3.25$	0.00727	0.0338

Table E.3: Photon flux computed with Starlight for p–Pb collisions.

Using the coherent J/ψ photoproduction cross sections presented in the coherent J/ψ paper in Pb–Pb by the ALICE Collaboration [1], it is finally possible to compute the expected number of remaining coherent J/ψ events in p–Pb which are a background to the extraction of the exclusive J/ψ raw signal. The calculated numbers are shown in table E.4, along with the numbers predicted by STARlight simulations.

Rapidity range	$N^{\gamma\mathrm{Pb}}_{\mathrm{J}/\psi}$ (computed)	$N^{\gamma\mathrm{Pb}}_{\mathrm{J}/\psi}$ (STARlight)
$2.50 < y < 4.00$	56	57
$2.50 < y < 3.25$	33	32
$3.25 < y < 4.00$	25	25

Table E.4: Expected number of remaining coherent J/ψ production in $\gamma\mathrm{Pb}$ interaction in the data sample according to the calculation, and compared with predictions from STARlight simulations.

Bibliography

[1] Shreyasi Acharya et al. Coherent J/ψ photoproduction at forward rapidity in ultra-peripheral Pb-Pb collisions at $\sqrt{s_{\mathrm{NN}}} = 5.02$ TeV. *Phys. Lett. B*, 798:134926, 2019. doi: 10.1016/j.physletb.2019.134926.

Appendix F

Contamination from ϕ production at low mass in the continuum

Since exclusive $\gamma\gamma \to \mu^+\mu^-$ production is measured at low mass between $1.0 < M_{\mu\mu} < 1.5$ GeV/c^2, a few events of ϕ production decaying to dimuons might contaminate the sample, given the mass of the ϕ meson $M_\phi = 1019.461 \pm 0.016$ MeV [1].

The number of expected ϕ mesons decaying to dimuons in the sample can be estimated as:

$$N_\phi = \sigma(\phi \to \mu^+\mu^-) \times (A \times E)_{1.0<M_{\mu\mu}<1.5} \times \frac{N_{J/\psi}}{\sigma(J/\psi \to \mu^+\mu^-) \times (A \times E)_{J/\psi}} \tag{F.1}$$

$$N_\phi = \sigma(\phi \to K^+K^-) \times \frac{BR(\phi \to \mu^+\mu^-)}{BR(\phi \to K^+K^-)} \times (A \times E)_{1.0<M_{\mu\mu}<1.5} \times \frac{N_{J/\psi}}{\sigma(J/\psi \to \mu^+\mu^-) \times (A \times E)_{J/\psi}} \tag{F.2}$$

where $(A \times E)_{1.0<M_{\mu\mu}<1.5}$ and $(A \times E)_{J/\psi}$ are the acceptance - efficiency factors for the full rapidity range taken from tables 4.8 and 4.9 respectively, the cross sections $\sigma(\phi \to K^+K^-) = 870$ μb and $\sigma(J/\psi \to \mu^+\mu^-) = 6.2$ μb are taken from [2], and the branching ratios $BR(\phi \to K^+K^-) = (48.9 \pm 0.5)\%$ and $BR(\phi \to \mu^+\mu^-) = (2.87 \pm 0.19) \times 10^{-4}$ are taken from [1].

When summing up the numbers of exclusive and dissociative J/ψ candidates in the standard selection sample and in the full rapidity range (see table 4.6), the total number of J/ψ events is estimated to be $N_{J/\psi} \sim 2700$. Therefore, the expected number of ϕ mesons in the data is firstly estimated to be

$$N_\phi = 19. \tag{F.3}$$

If one considers that the mass peak of ϕ mesons is distributed as a gaussian function centered around M_ϕ, then only half of this number should be measured in the mass region $1.0 < M_{\mu\mu} < 1.5$ GeV/c^2.

According to table 4.1, in these mass and rapidity ranges, the numer of extracted exclusive $\gamma\gamma \to \mu^+\mu^-$ events is $N_{\gamma\gamma}$ = 618.

Therefore, the contamination from ϕ mesons should result in an uncertainty of

$$\frac{\Delta N_{\gamma\gamma}}{N_{\gamma\gamma}} = \frac{19/2}{618} = 1.5\%$$

in the number of exclusive $\gamma\gamma \to \mu^+\mu^-$ events at low mass.

Bibliography

[1] P. A. Zyla et al. Review of Particle Physics. *PTEP*, 2020(8):083C01, 2020. doi: 10.1093/ptep/ptaa104.

[2] Z. Citron et al. Future physics opportunities for high-density QCD at the LHC with heavy-ion and proton beams. In *HL/HE-LHC Workshop: Workshop on the Physics of HL-LHC, and Perspectives at HE-LHC Geneva, Switzerland, June 18-20, 2018*, 2018.

Appendix G

Computation of the expected number of $\psi(2S) \rightarrow \mu^+\mu^-$ from the feed-down factor

The number of $J/\psi \rightarrow \mu^+\mu^-$ events is given by

$$N^{J/\psi\rightarrow\mu\mu} = \frac{N^{\text{candidates}}}{1 + f_D} \tag{G.1}$$

where $N^{\text{candidates}}$ is the number of J/ψ candidates. Hence

$$N^{\text{candidates}} = N^{J/\psi\rightarrow\mu\mu} + f_D \times N^{J/\psi\rightarrow\mu\mu} \tag{G.2}$$

The feed-down factor is defined as in section 4.4.1 by

$$f_D = \frac{\sigma(\Psi(2s))BR(\psi(2S) \rightarrow J/\psi + X) \times (A \times \epsilon)^{\psi(2S)\rightarrow J/\psi+X}}{\sigma(J/\psi) \times (A \times \epsilon)^{J/\psi\rightarrow\mu\mu}} \tag{G.3}$$

and can also be defined as

$$f_D = \frac{N(\psi(2S) \rightarrow J/\psi + X)}{N^{J/\psi}} \tag{G.4}$$

$$f_D = \frac{N(\psi(2S) \rightarrow J/\psi + X) \times BR(J/\psi \rightarrow \mu\mu)}{N^{J/\psi\rightarrow\mu\mu}} \tag{G.5}$$

Using equations G.2 and G.5,

$$N^{\text{candidates}} = N^{J/\psi\rightarrow\mu\mu} + N(\psi(2S) \rightarrow J/\psi + X) \times BR(J/\psi \rightarrow \mu\mu) \tag{G.6}$$

Moreover,

$$N(\psi(2S) \rightarrow \mu\mu) = N(\Psi(2s)) \times BR((\psi(2S) \rightarrow \mu\mu) \times (A \times \epsilon)^{\Psi(2s)\rightarrow\mu\mu} \tag{G.7}$$

and

$$N(\psi(2S) \rightarrow J/\psi + X) = N(\Psi(2s)) \times BR((\psi(2S) \rightarrow J/\psi + X) \times (A \times \epsilon)^{\Psi(2s)\rightarrow J/\psi+X} \tag{G.8}$$

From equation G.8 one obtains

$$N(\Psi(2s)) = \frac{N(\psi(2S) \rightarrow J/\psi + X)}{BR(\psi(2S) \rightarrow J/\psi + X) \times (A \times \epsilon)^{\Psi(2s)\rightarrow J/\psi+X}} \tag{G.9}$$

We inject equation G.9 in equation G.8.

$$N(\psi(2\mathrm{S}) \to \mu\mu) = N(\psi(2\mathrm{S}) \to \mathrm{J}/\psi + X) \times \frac{BR(\psi(2\mathrm{S}) \to \mu\mu)}{BR(\psi(2\mathrm{S}) \to \mathrm{J}/\psi + X)} \times \frac{(A \times \epsilon)^{\Psi(2s)\to\mu\mu}}{(A \times \epsilon)^{\Psi(2s)\to \mathrm{J}/\psi + X}} \tag{G.10}$$

We use equations G.1 and G.3 to express $N(\psi(2\mathrm{S}) \to \mathrm{J}/\psi + X)$ as a function of $N^{\text{candidates}}$, f_D and $BR(\mathrm{J}/\psi \to \mu\mu)$.

$$N(\psi(2\mathrm{S}) \to \mathrm{J}/\psi + X) = \frac{f_D \times N^{\mathrm{J}/\psi\to\mu\mu}}{BR(\mathrm{J}/\psi \to \mu\mu)} \tag{G.11}$$

$$= \frac{f_D}{1 + f_D} \times \frac{N^{\text{candidates}}}{BR(\mathrm{J}/\psi \to \mu\mu)} \tag{G.12}$$

Finally,

$$\boxed{N(\psi(2\mathrm{S}) \to \mu\mu) = \frac{f_D}{1 + f_D} \times \frac{N^{\text{candidates}}}{BR(\mathrm{J}/\psi \to \mu\mu)} \times \frac{BR(\psi(2\mathrm{S}) \to \mu\mu)}{BR(\psi(2\mathrm{S}) \to \mathrm{J}/\psi + X)} \times \frac{(A \times \epsilon)^{\Psi(2s)\to\mu\mu}}{(A \times \epsilon)^{\Psi(2s)\to \mathrm{J}/\psi + X}}} \tag{G.13}$$

G.1 Numerical application

The feed-down correction factors and $A \times E$ factors are calculated in section 4.4.1 and given in table 4.10. We use f_D = 9%, $(A \times \epsilon)^{\mathrm{J}/\psi \text{ from } \Psi(2s)}$ = 19%, and $(A \times \epsilon)^{\mathrm{J}/\psi\to\mu\mu}$ = 19%.

The branching ratios BR are taken from reference [1]:
$BR\Psi(2s) \to \mathrm{J}/\psi + \text{anything})$ = 61.4%
$BR(\Psi(2s) \to \mathrm{J}/\psi + \text{neutrals})$ = 25.4%
$BR(\Psi(2s) \to \mathrm{J}/\psi + \pi^+\pi^-)$ = 34.7%
$BR(\Psi(2s) \to \mathrm{J}/\psi + \pi^0\pi^0)$ = 18.2%
$BR(\Psi(2s) \to \mu\mu)$ = 0.8% $BR(\mathrm{J}/\psi \to \mu\mu)$ = 6.0%

Therefore, with $N^{\text{candidates}} = 2864$ as extracted in figure G.1,

$$\boxed{N(\psi(2\mathrm{S}) \to \mu\mu) = 51} \tag{G.14}$$

This number is twice lower than the one obtained from the one-dimensional fit shown in figure G.1, which yields $N^{\text{extracted}}(\psi(2\mathrm{S}) \to \mu\mu) = 99 \pm 17$. This underestimation remains reasonable given the amount of statistics.

Bibliography

[1] P. A. Zyla et al. Review of Particle Physics. *PTEP*, 2020(8):083C01, 2020. doi: 10.1093/ptep/ptaa104.

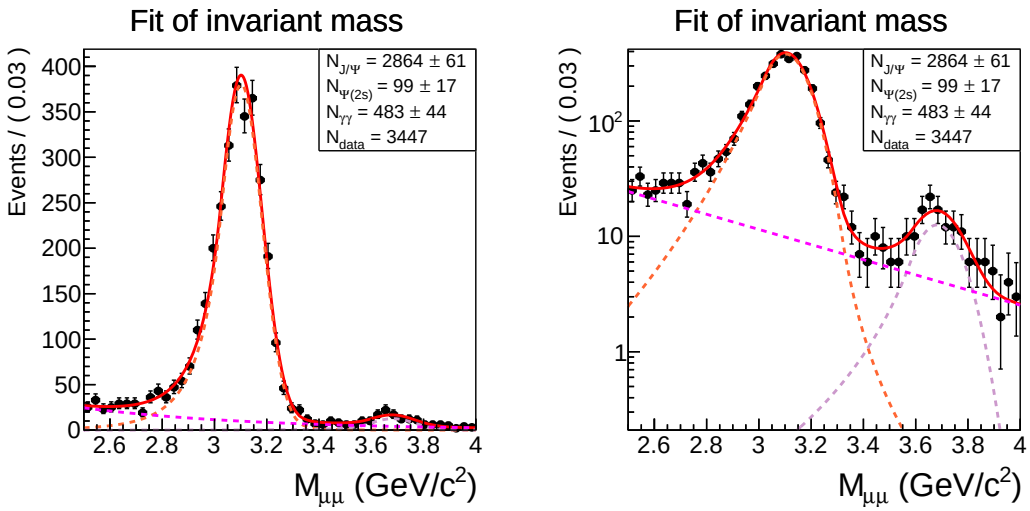

Figure G.1: One-dimensional mass fit, with $2.5 < M_{\mu\mu} < 4.0$ GeV$/c^2$ and using the mid-selection, in linear (left) and log (right) scales fot better visibility.

Part IV

Appendices - MPGD

Appendix H

Interaction of photons in the detector gas

In order to understand the behaviour of photons in gas, in particular argon and air, simulations were carried out using Garfield ++[1] and Magboltz[2]. The study consists in counting the proportion $P_{\gamma}^{\text{gas}}(d)$ of generated photons which are converted into electrons after a given distance of travel d and in a given gas. The results of this study are presented in figure H.1 in air and figure H.2 in Argon-isobutane (95/5), the gas used in the detectors.

The histograms are then fitted with a function of the form

$$y = 1 - \exp(\sigma_{\gamma-X} \times d \times x) \tag{H.1}$$

where $\sigma_{\gamma-X}$ (in cm^2) is the cross section of photons with the medium X which can either be Argon or gas, d (in cm^{-3}) is the density of the medium and x (in cm) the length traversed.

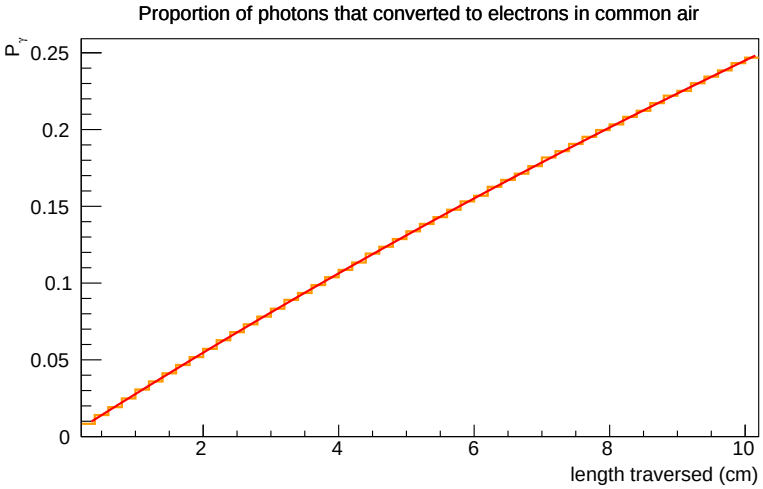

Figure H.1: Proportion of 5.9 keV photons that are converted into electrons in air (78.1% nitrogen, 20.9% oxygen, 0.9% argon and 0.4% carbon dioxide) as a function of the distance traveled.

In the case of argon, the density d is given by:

$$d = 0.95 \times \frac{\rho}{M} \times N_A \tag{H.2}$$

where the factor 0.95 comes from the fact that the gas is composed of 95% of argon, $\rho = 1.784 \times 10^{-3}$ g/cm^3 is the mass density, $M = 39.95$ g/mol is the molar density and $N_A = 6.0221409 \times 10^{23}$ mol^{-1} is the Avogadro number. After fitting the histogram, the cross section of photons with Argon is $\sigma_{\gamma-Ar} = 1.68 \times 10^{-20}$ cm^{-2}.

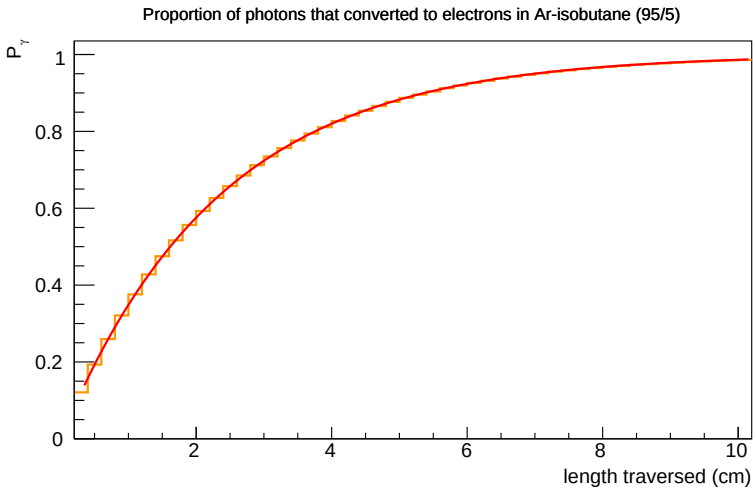

Figure H.2: Proportion of 5.9 keV photons that are converted into electrons in Argon-isobutane (95/5) as a function of the distance traveled.

H.1 Pile-up events in the transfer and drift spaces

The number of events - photons that convert to electrons in the detector - during a given time interval follows a Poissonian distribution of parameter λ, where λ is the mean value:

$$P(X = k) = \frac{\lambda^k}{k!} e^{-\lambda} \tag{H.3}$$

And the probability of at least two events occurring during this time interval, called the pile-up probability, is given by:

$$P(\text{pile-up}) = \frac{P(X > 1)}{P(X > 0)} \tag{H.4}$$

$$= \frac{1 - P(X = 0) - P(X = 1)}{1 - P(X = 0)} \tag{H.5}$$

$$= \frac{1 - e^{-\lambda} - \lambda e^{-\lambda}}{1 - e^{-\lambda}} \tag{H.6}$$

In our case, the average number of events during a time interval that corresponds to the analyzer sampling time is defined by

$$\lambda = \Gamma_{\text{source}} / \Gamma_{\text{analyzer}} \tag{H.7}$$

where $\Gamma_{\text{source}} = f \times \Gamma^0_{\text{source}}$ is the average number of events per unit of time in the considered zone of the detector, Γ^0_{source} corresponds to the radioactivity rate of the iron source, f is the fraction of photons emitted by the radioactive source which are converted in the considered

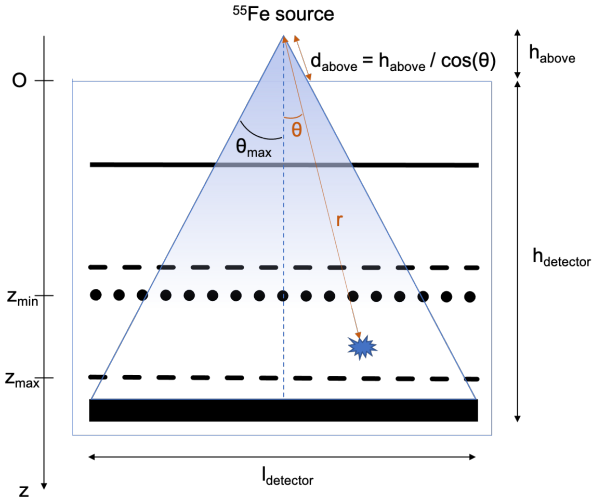

Figure H.3: Schematic representation of the detector.

zone of the detector and Γ_{analyzer} corresponds to the recording frequency of the analyzer. As Γ_{analyzer} and Γ^0_{source} are known parameters, we will now focus on the calculation of the factor f.

Calculation of f

Let us use spherical coordinates, where $r \in [0, +\infty]$ is the radial coordinate, $\theta \in [0, \pi]$ is the angle with the axis z directed downwards, and $\phi \in [0, 2\pi]$ is the rotation in the plane perpendicular to the z axis.

The radiation from the source being isotropic, the probability $P_\gamma(r)$ for a photon to have converted into electrons after a distance crossed r depends only on this distance r. We can therefore write the number of decays in a volume delimited by r, θ and ϕ as follows:

$$\Gamma_{\text{source}}(r, \theta, \phi) = \Gamma^0_{\text{source}} \times \frac{1}{2\pi} \times \frac{1}{\pi} \times \int_0^{\phi} \int_0^{\theta} \int_0^{r} \frac{dP_\gamma(r)}{dr} dr d\theta d\phi \tag{H.8}$$

All photons are converted after an infinite distance, therefore

$$\int_0^{\infty} \frac{dP_\gamma(r)}{dr} dr = 1 \tag{H.9}$$

And the relation $\Gamma_{\text{source}}(r = \infty, \theta = \pi, \phi = 2\pi) = \Gamma^0_{\text{source}}$ is verified.

We are now looking for the fraction f of photons that will convert in the transfer space, between z_{min} and z_{max}, as shown in figure H.3. To be detected, these photons must arrive with an angle $\theta < \theta_{\text{max}}$ such that

$$\tan(\theta_{\text{max}}) = \frac{l_{\text{detector}}/2}{h_{\text{detector}} + h_{\text{above}}} \tag{H.10}$$

In addition, the distance r traveled by the photons to be detected between z_{min} and z_{max} will depend on their angle of arrival θ. Thus, the photons must interact for $r_{\text{min}} < r < r_{\text{max}}$ with:

$$\begin{cases} r_{\text{min}} = z_{\text{min}} / \cos(\theta) \\ r_{\text{max}} = z_{\text{max}} / \cos(\theta) \end{cases}$$

We then obtain:

$$\begin{cases} \Gamma_{\text{source}}(r,\theta,\phi) = f \times \Gamma^0_{\text{source}} \\ \Gamma_{\text{source}}(r,\theta,\phi) = \Gamma^0_{\text{source}} \times \dfrac{1}{2\pi} \times \dfrac{1}{\pi} \times \displaystyle\int_{\phi=0}^{2\pi} \int_{\theta=0}^{\theta_{\max}} \int_{r=r_{\min}(\theta)}^{r_{\max}(\theta)} \dfrac{dP_\gamma(r)}{dr} dr d\theta d\phi \end{cases}$$

Therefore

$$f = \frac{1}{\pi} \times \int_{\theta=0}^{\theta_{\max}} \int_{r=r_{\min}(\theta)}^{r_{\max}(\theta)} \frac{dP_\gamma(r)}{dr} dr d\theta \tag{H.11}$$

f can be in good approximation expressed as follows:

$$f \approx \frac{1}{\pi} \sum_{\theta=0}^{\theta_{\max}} \sum_{r=r_{\min}(\theta)}^{r_{\max}(\theta)} \frac{P_\gamma(r+\Delta r) - P_\gamma(r)}{\Delta r} \Delta r \Delta\theta \tag{H.12}$$

$$f \approx \frac{1}{\pi} \sum_{\theta=0}^{\theta_{\max}} \sum_{r=r_{\min}(\theta)}^{r_{\max}(\theta)} (P_\gamma(r+\Delta r) - P_\gamma(r)) \Delta\theta \tag{H.13}$$

$P_\gamma(r)$ is actually the probability that photons did not convert in the air above the detector, multiplied by the probability that the photons did convert into the detector gas after a distance $z/\cos(\theta)$:

$$P_\gamma(r = (h_{\text{above}} + z)/\cos(\theta)) = (1 - P_\gamma^{\text{air}}(h_{\text{above}}/\cos(\theta))) \times P_\gamma^{\text{Ar-iso}}(z/\cos(\theta)) \tag{H.14}$$

In order to obtain $P_\gamma^{\text{air}}(d)$ and $P_\gamma^{\text{Ar-iso}}(d)$, simulations presented in figure H.1 for photons in the air and figure H.2 for photons in Argon-isobutane (95/5) are used.

The calculation is then performed in C++ by looping on θ by steps of $\theta_{\max}/20$ and looping on r by steps of $(r_{\max} - r_{\min})/20$.

Numerical application

We have Γ^0_{source} = 185 MHz and Γ_{analyzer} = 100 MHz. The detectors studied had the following geometric parameters: l_{detector} = 12 cm, and h_{detector} = 3 cm (see figure H.3).

electrode	**position l**	**position from top $z = h_{\text{detector}} - l$**
top of the detector	3.0 cm	0 cm
drift electrode	18.568 mm	1.143 cm
top micro-mesh	8.068 mm	2.193 cm
GEM	between 7.348 mm and 7.414 mm	between 2.258 cm and 2.265 cm
micro-mesh	128 µm	2.987 cm
pads	0 cm	3 cm

Table H.1: Geometric parameters of the 660-µm-gap model.

The source is positioned at $h_{\text{above}} = 10$ cm above the detector.

In the case of the 660-µm-gap detector, the transfer space is between $z_{\min} = 2.265$ cm and $z_{\max} = 2.987$ cm starting from the top of the detector, and the drift space is between $z_{\min} =$

electrode	**position l**	**position from top $z = h_{\text{detector}} - l$**
top of the detector	3.0 cm	0 cm
drift electrode	19.128 mm	1.087 cm
top micro-mesh	5.328 mm	2.467 cm
GEM	between 5.134 mm and 5.200 mm	between 2.480 cm and 2.487 cm
micro-mesh	128 µm	2.987 cm
pads	0 cm	3 cm

Table H.2: Geometric parameters of the 128-µm-gap model.

1.143 cm and $z_{\text{max}} = 2.193$ cm (see table H.1).

We then obtain:

$$f_{\text{transfer}} = 1.4\%$$
$$f_{\text{drift}} = 3.2\%$$

Thus,

$$\lambda_{\text{transfer}} = \frac{f_{\text{transfer}} \times \Gamma^0_{\text{source}}}{\Gamma_{\text{analyzer}}} = 2.5 \times 10^{-2}$$
$$\lambda_{\text{drift}} = \frac{f_{\text{drift}} \times \Gamma^0_{\text{source}}}{\Gamma_{\text{analyzer}}} = 5.9 \times 10^{-2}$$

and

$$P(\text{pile-up in the transfer space}) = \frac{1 - e^{-\lambda} - \lambda e^{-\lambda}}{1 - e^{-\lambda}}$$

$$P(\text{pile-up in the transfer space}) = 1.2\%.$$
$$P(\text{pile-up in the drift space}) = 2.9\%.$$

In the case of the 128-µm-gap detector, the transfer space is between $z_{\text{min}} = 2.487$ cm and $z_{\text{max}} = 2.987$ cm starting from the top of the detector (see table H.1). The source is positioned at $h_{\text{above}} = 10$ cm above the detector.

We then obtain:

$$f = 1.4\%$$

Thus,

$$\lambda = \frac{f \times \Gamma^0_{\text{source}}}{\Gamma_{\text{analyzer}}} = 2.5 \times 10^{-2}$$

and

$$P(\text{pile-up}) = \frac{1 - e^{-\lambda} - \lambda e^{-\lambda}}{1 - e^{-\lambda}} = 1.2\%.$$

H.2 Contamination induced by events taking place outside the drift region

H.2.1 Distribution of events in the detector

Using the simulation presented in figure H.2 and the geometric parameters of the detectors given in tables H.1 and H.2, one obtains the total proportion of photons $P_\gamma^{\text{detector}}$ converted in one detector, assuming that no photons were converted in the air:

$$P_\gamma^{\text{detector}} = 28.1\%,$$

and the proportion of photons converted in each region of the detectors, presented in tables H.3 and H.4. These proportions are then normalised to the total proportion of photons $P_\gamma^{\text{detector}}$ converted in the detector. This then gives an estimate of where the events come from in the detector, when using a ^{55}Fe source.

Region	Proportion of photons that converted	Normalized proportion of photons
Above the drift electrode	16.3%	58.0%
In the drift region	8.1 %	28.8%
In the gap between the top micro-mesh and the GEM	0.4%	1.4%
In the transfer region	3.2 %	11.4%
In the amplification gap	0.1 %	0.4%

Table H.3: Distribution of photons that converted to electrons in the 660-µm-gap detector.

Region	Proportion of photons that converted	Normalized proportion of photons
Above the drift electrode	15.7%	56.0%
In the drift region	10.1 %	35.9%
In the gap between the top micro-mesh and the GEM	0.1%	0.2%
In the transfer region	2.1 %	7.5%
In the amplification gap	0.1 %	0.4%

Table H.4: Distribution of photons that converted to electrons in the 128-µm-gap detector.

H.2.2 Contribution of these events to the measurements of currents and bias on the IBF

Contamination of events above the drift electrode

The current induced on the drift electrode by the ion backflow should be

$$i_d^{\text{IBF}} \propto P_\gamma^{\text{drift}} \times \text{Gain} \times \text{IBF} \tag{H.15}$$

and the current induced on the drift electrode by events coming from above should be

$$i_d^{\text{conta}} \propto P_\gamma^{\text{above}}, \tag{H.16}$$

where P_γ^{drift} and P_γ^{above} are the proportions of photons that converted in the drift space and above the drift electrode, respectively.

Assuming that the real ion backflow is of the order of 0.3% and that the detector is operated at a gain of 2000, in the 660-µm-gap detector:

$$\frac{i_d^{\text{conta}}}{i_d^{\text{IBF}}} = \frac{P_\gamma^{\text{above}}}{P_\gamma^{\text{drift}} \times \text{Gain} \times \text{IBF}} = \frac{0.580}{0.288 \times 2000 \times 0.003} = 34\%. \tag{H.17}$$

The measurement of ion backflow could be overestimated by 34% due to contamination from ions coming from above the drift electrode. The same calculation with the 128-µm-gap detector gives an overestimation of 26% due to contamination.

Contamination of events in the transfer zone

Moreover, signals from the transfer region may induce an under-evaluation of the ion backflow. These events are not expected to contribute to the current on the drift electrode, since all ions are expected to be stopped by the GEM or top micro-mesh. For example figure 7.10 shows that ions that drift up to the drift electrode were created below mesh top only, hence they result from signals in the drift space. Events from the transfer region however contribute to the current on the bottom micro-mesh. The current read on the bottom micro-mesh can be written as:

$$i_m = i_m^{\text{from drift}} + i_m^{\text{from transfer}} \tag{H.18}$$

with

$$\begin{cases} i_m^{\text{from drift}} \propto \text{Total gain} \times P_\gamma^{\text{drift}} \\ i_m^{\text{from transfer}} \propto \text{Bottom micro-mesh gain} \times P_\gamma^{\text{transfer}} \end{cases} \tag{H.19}$$

Assuming that the detector is operated at a gain of 2000, in the 660-µm-gap detector, and that the bottom micro-mesh has a gain of 500:

$$\frac{i_m^{\text{from transfer}}}{i_m^{\text{from drift}}} = \frac{\text{Bottom micro-mesh gain} \times P_\gamma^{\text{transfer}}}{\text{Total gain} \times P_\gamma^{\text{drift}}} = \frac{500 \times 0.114}{2000 \times 0.288)} = 9.9\%. \tag{H.20}$$

Repeating the same exercise for the 128-µm-gap detector, and assuming that the bottom micro-mesh has a gain of 200:

$$\frac{i_m^{\text{from transfer}}}{i_m^{\text{from drift}}} = \frac{200 \times 0.075}{2000 \times 0.359} = 2.1\%.$$

According to simulations, the contamination of events coming from the transfer region can induce an underestimation of up to 10% on the ion backflow in the 660-µm-gap detector, and up to 2% in the 128-µm-gap detector.

Bibliography

[1] H. Schindler and R. Veenhof. Garfield++ – simulation of tracking detectors. URL http://cern.ch/garfieldpp.

[2] S. Biagi. Magboltz - transport of electrons in gas mixture. URL http://cern.ch/magboltz.

Appendix I

Study of the impact of using a collimated source

Some measurements presented here require a collimator, in order to obtain a better resolution in energy. Indeed, the micro-mesh may not be perfectly horizontal, in particular due to the effects of the electric field which will tend to push the grid down. In this case, the electrons do not have the same amplification space depending on their position, and this affects their multiplication. To overcome this effect, the collimator allows the source to be directed towards a precise point of the detector, where the deformations of the micro-mesh should be negligible. In our case, we used a 1 mm diameter collimator. In addition, the use of the collimator removes a large part of the photons produced by the iron source, and thus suppresses the pile-up events (discussed in appendix H.1).

However, to clearly observe the current differences with and without the source, a large event rate is required. Thus, the currents are always measured without a collimator. As the IBF depends on the gain of the detector, it is necessary to ensure that the gain does not vary with or without a collimator, in order to validate the measurements.

Figure I.1 show an example of a gain measurement without and with a collimator respectively. In the first case, we can observe pile-up events of which the signature is a bump after the 5.9 keV Iron peak. The energy resolution is improved by about 30%, and the average peak value is shifted by about 2%, significantly lower than the energy resolution in all cases.

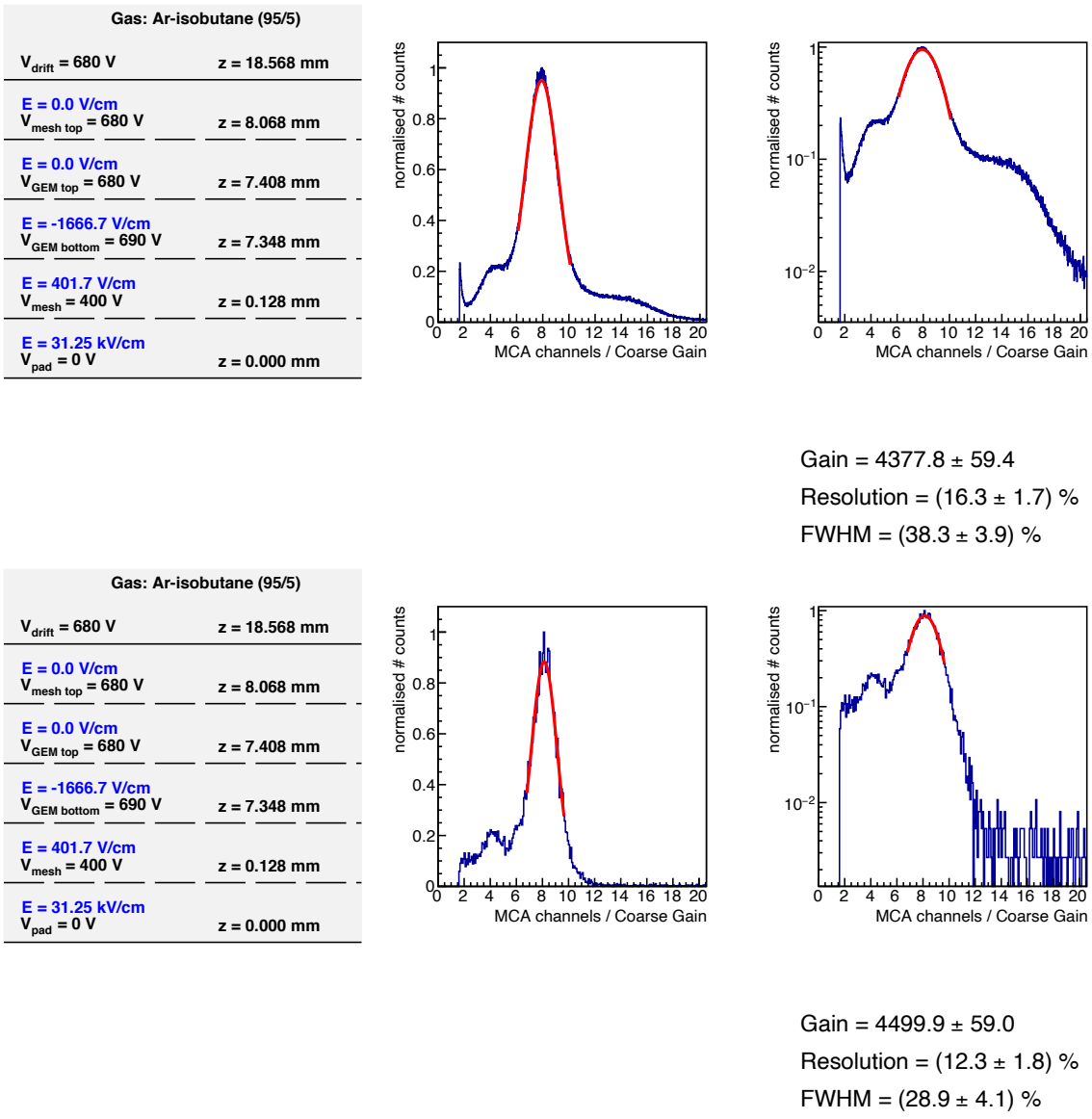

Figure I.1: Example of spectrum without (with) collimation at the top (bottom).

Appendix J

Comparison of two Penning transfer rates

Simulations are carried out on the single-stage MicroMEGAS configuration using a micro-mesh 45/18 in Ar-isobutane (95/5) with a different Penning transfer rate coefficient, $r_p = 0.480$ instead of $r_p = 0.321$ used in the simulation analysis. The comparison of the gain and IBF obtained with the two different input parameters r_p are shown in figure J.1.

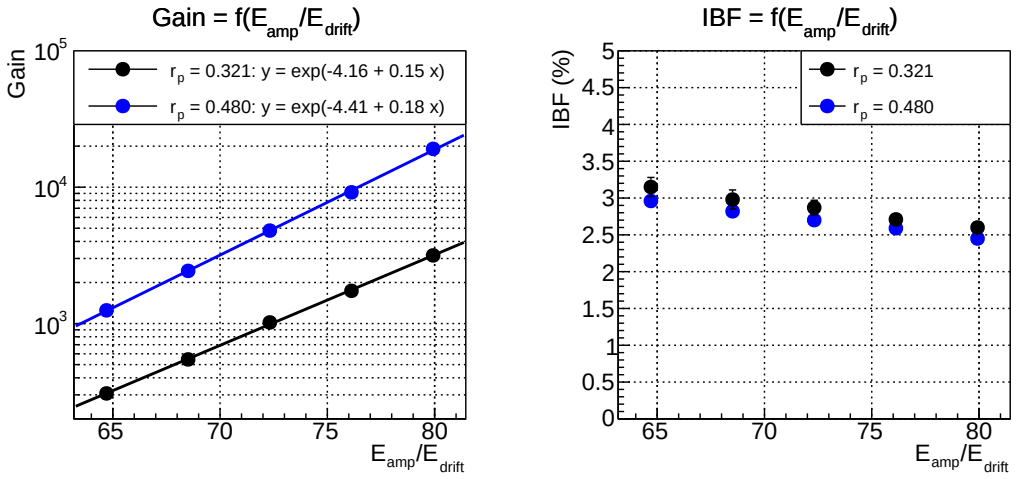

Figure J.1: Comparison of the gain (left) and IBF (right) as a function of $E_{\text{amp}}/E_{\text{drift}}$ for $r_p = 0.321$ (in black) and $r_p = 0.480$ (in blue).

The lower r_p, the lower the gain but also the lower the gain slope with $E_{\text{amp}}/E_{\text{drift}}$. Although the Penning transfer rate has a significant impact of the gain values, the IBF is much less affected. For the same $E_{\text{amp}}/E_{\text{drift}}$, the IBF values vary by 6% at most when comparing the results with different r_p.

Appendix K

Comparison of two gas mixtures with simulations

In order to assess the dependence of the IBF on the gas mixture the same detector and at fixed gain, simulations were carried out using Garfield ++[1] and Magboltz[2].

The two gas mixtures studied are Ar-isobutane (95/5), used as standard gas mixture all along the tests ins simulations and in the laboratory, and Ne-CO_2-N_2 (90/10/5), used by the ALICE experiment [3–5]. In order to achieve equivalent gains, all electric field were multiplied by a factor 1.23 when using the ALICE gas mixture with respect to the standard one. The results of simulations are presented in figures K.1 and K.2.

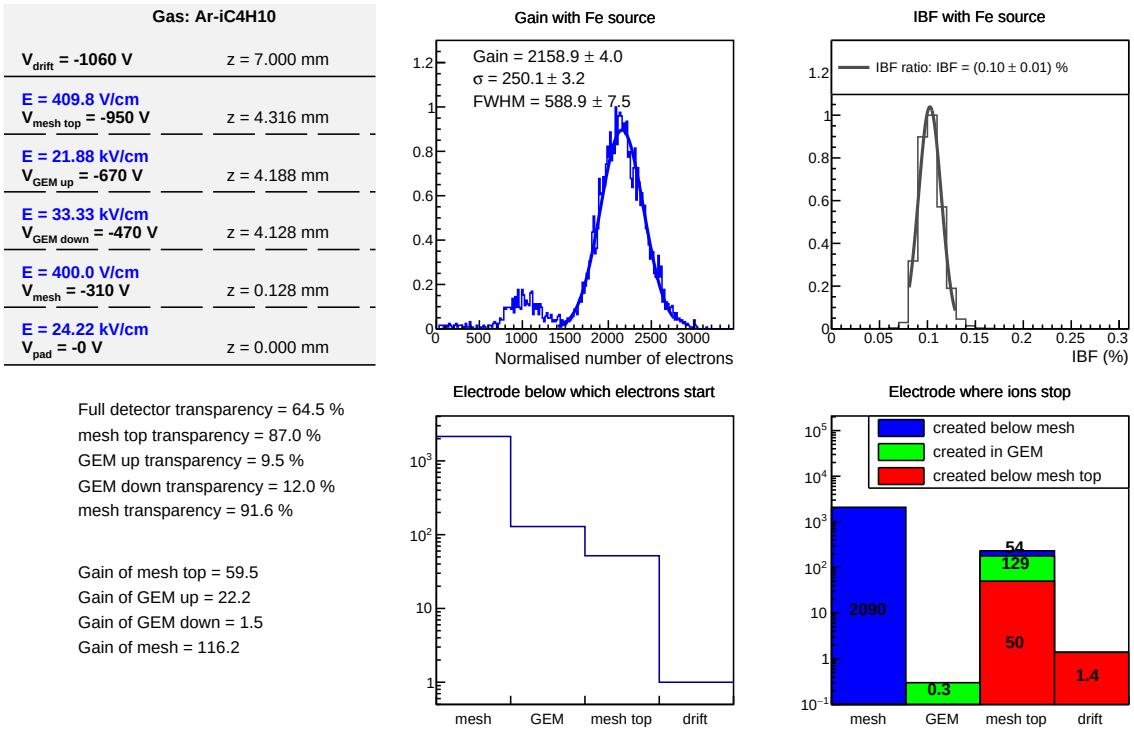

Figure K.1: MMGEM model simulated using the Ar-isobutane (95/5) gas mixture.

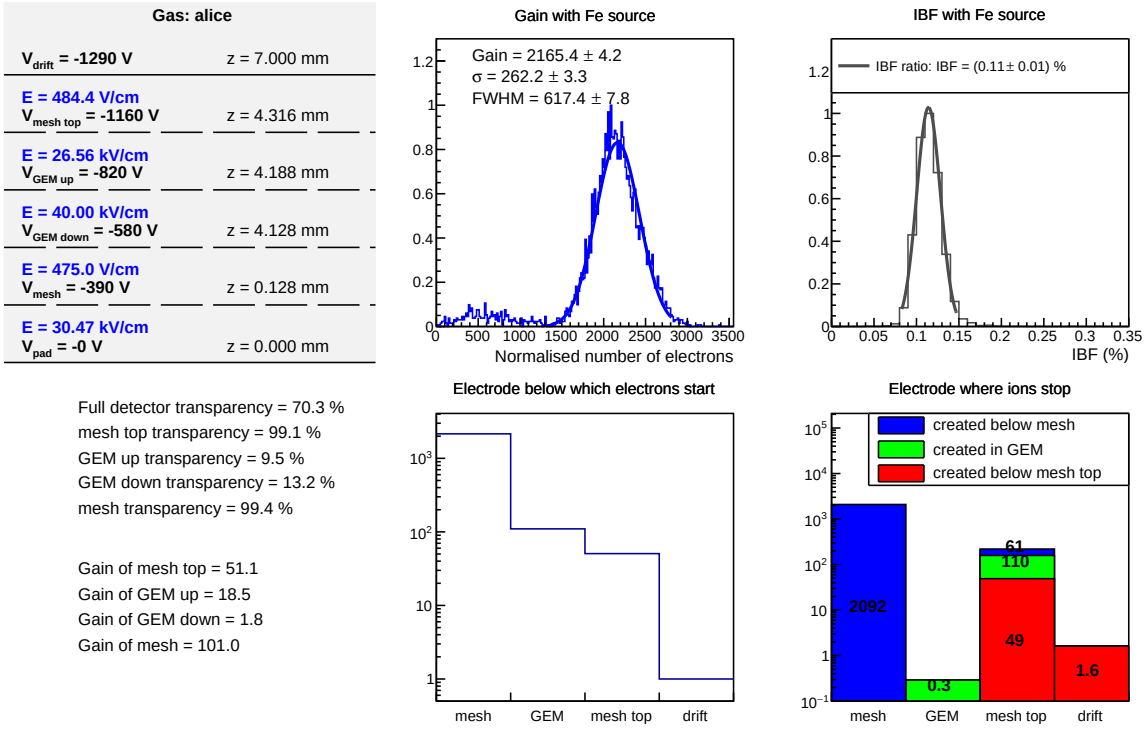

Figure K.2: MMGEM model simulated using the Ne-CO_2-N_2 (90/10/5) gas mixture, as in the ALICE experiment [3–5].

These results demonstrate that for an equivalent gain, the obtained IBF is the same. Moreover, the energy resolution is $\sigma(E)/E$ = 11.6% in Ar-isobutane (95/5) and 12.1% in Ne-CO_2-N_2 (90/10/5), which is a 4% difference.

Bibliography

[1] H. Schindler and R. Veenhof. Garfield++ – simulation of tracking detectors. URL http://cern.ch/garfieldpp.

[2] S. Biagi. Magboltz - transport of electrons in gas mixture. URL http://cern.ch/magboltz.

[3] J. Adolfsson et al. The upgrade of the ALICE TPC with GEMs and continuous readout. *JINST*, 16(03):P03022, 2021. doi: 10.1088/1748-0221/16/03/P03022.

[4] G. Dellacasa et al. ALICE: Technical design report of the time projection chamber. 1 2000.

[5] J. Alme et al. The ALICE TPC, a large 3-dimensional tracking device with fast readout for ultra-high multiplicity events. *Nucl. Instrum. Meth. A*, 622:316–367, 2010. doi: 10.1016/j.nima.2010.04.042.

Part V

Other appendices

Acronyms and glossary

Acronyms

ACORDE ALICE COsmic Ray DEtector. 51, 79

AD Alice Diffractive detector. 51, 54, 70, 73, 74, 79

AOD Analysis Object Data. 63, 64, 70, 265

BH Bethe-Heitler. 119–121

CB2 double-sided crystal-ball function. 93, 94

CGC Color Glass Condensate. 26–29, 122

CTP Central Trigger Processor. 61, 62

DAQ Data AcQuisition system. 61, 62

DDL Detector Data Link. 61

DIS Deep Inelastic Scattering. 17–22, 24, 25, 29, 30, 32, 34

EPA equivalent photon approximation. 31, 117

ESD Event Summary Data. 63, 64, 265

FSR final-state radiation. 117

GDC Global Data Collector. 61

GEM Gas Electron Multiplier. 140, 144, 146–148, 151, 156, 157, 160, 162–164, 166–168, 172, 176, 179–186, 192, 202–204, 207, 210–214, 268–270

GPD Generalized Parton Distribution function. 34, 119–121

HLT High Level Trigger. 61, 62, 265

IBF Ion Backflow. 144, 147, 148, 151, 156, 159, 161, 163, 164, 167, 168, 173–175, 178–181, 184–187, 192, 193, 197–199, 202, 203, 207, 210–214, 251, 253, 255, 256, 268–270

IP Interaction Point. 51, 53–60, 70, 71, 77, 121, 227

ITS Inner Tracking System. 51

LDC Local Data Concentrator. 61

LEIR Low Energy Ion Ring. 48

LHC Large Hadron Collider. 10, 29, 31, 36, 37, 46–50, 53–55, 59, 63, 64, 76, 78, 116, 120, 131, 140, 144, 263, 264, 267

LO Leading Order. 14, 15, 20, 23, 25, 33, 34, 86, 87, 116, 117, 119–122, 125, 127, 131, 219

LTU Local Trigger Unity. 61

MB Minimum Bias. 54, 55, 62, 77–79, 227

MC Monte Carlo. 64, 70, 78, 80, 86, 87, 93–95, 97–99, 102–106, 109, 221

MCH Muon CHambers. 51, 57, 70–72, 108, 109

MFT Muon Forward Tracker. 121

MPGD Micro-Pattern gaseous detector. 140, 144, 145, 149, 151, 156, 172, 268

MTR Muon TRigger. 51, 57, 59, 62, 70, 72, 81, 108, 109

MWPC Multi-Wire Proportional Chamber. 143, 144

NLO Next-to-Leading Order. 14, 15, 20, 24, 25, 28, 34, 86, 117, 121, 122, 125, 127

NNLO Next-to-Next-to-Leading Order. 15, 24

OCDB Offline Condition Data Base. 63, 70, 77–79, 227

PDF Parton Distribution Function. 20–23, 33, 34, 36, 122, 125, 128

PDS Permanent Data Storage. 61

PMT PhotoMultiplier Tube. 53–55

pQCD perturbative Quantum ChromoDynamics. 29, 34, 122, 125

PS Proton Synchrotron. 48

PSB Proton Synchrotron Booster. 48

QCD Quantum ChromoDynamics. 12–16, 18, 20–27, 31, 32, 50, 116, 120, 122

QED Quantum ElectroDynamics. 84, 86, 93, 116–118, 120, 131, 266

QPM quark parton model. 20, 21

RHIC Relativistic Heavy Ion Collider. 29, 116, 140

RPC Resistive Plate Chamber. 59, 60

SC Synchro-Cyclotron. 48

SDD Silicon Drift Detector. 53, 79

SPD Silicon Pixel Detector. 52, 53, 60, 62, 64, 70, 72, 74, 79, 227, 264

SPS Super Proton Synchrotron. 48

SSD Silicon Strip Detector. 53, 79

TCS Timelike Compton Scattering. 119, 120

TDS Transient Data Storage. 61

TPC Time Projection Chamber. 51, 62, 79, 140, 141, 143, 144, 146–149, 151, 160, 186, 268, 270

TRD Transition Radiative Detector. 51, 62

UPC Ultra-Peripheral Collision. 30, 31, 36, 53, 55, 62, 64, 68–70, 72, 86, 105, 116, 119, 130

VdM Van der Meer. 78, 80

ZDC Zero Degree Calorimeter. 51, 53, 54, 62, 64, 70, 73, 79, 104, 264

Glossary

baryon A hadron made up of 3 quarks. 13, 18

Cherenkov Phenomenon producing a flash of light when a charged particle moves in a dielectric medium with a speed greater than the speed of light in this medium (the speed of light in a vacuum always being greater than that of the particle). 53, 55

hadron Composite particle, composed of subatomic particles governed by the strong interaction. 13, 16, 17, 25, 26, 28–31, 34, 68, 117

hadronization Process by which free gluons and quarks assemble into hadrons. 17

lepton Elementary particle of spin 1/2 which is not sensitive to the strong interaction. The lepton family consists of electrons, muons, tauons, respective neutrinos and antiparticles of all these. 11, 12, 56, 68, 116, 117, 119–121

meson A hadron formed with a quark - anti-quark pair. 13, 18, 29–33, 37, 46, 68, 84, 105, 106, 122, 124, 126

pseudorapidity Spatial coordinate commonly used to describe the angle of a particle's track relative to the beam axis. It is defined as $\eta = -\ln\left[\tan\left(\frac{\theta}{2}\right)\right]$. 51, 54, 56, 71, 124, 222

rapidity Dimensionless quantity that measures the relativistic velocity of a particle. It is defined as $y = \operatorname{arctanh}\left(\frac{v}{c}\right) = \frac{1}{2}\ln\left(\frac{1+\frac{v}{c}}{1-\frac{v}{c}}\right)$. 28, 32, 35, 54, 68–72, 84, 86–89, 92–94, 98, 100, 102–108, 116–118, 122, 124, 130

sea quark Virtual quark–antiquark pairs contained in a hadron a long with the valence quarks. Sea quarks form when a gluon of the hadron's color field splits, and they typically annihilate each other within the interior of the hadron plural. 18, 21, 22

valence quark Quarks that determine the quantum numbers of hadrons, they exist for as long as the hadron in which they live. 18, 21, 22

vertex Intersection between lines in a Feynman diagram. 14, 33, 56, 57, 59, 71, 77, 125

Summary in French

Partie 1 : Sonder la structure du proton à l'aide de la photoproduction du J/ψ dans des collisions ultra-relativistes de protons et de noyaux de plomb avec l'expérience ALICE au LHC

Chapitre 1 : Introduction

Le modèle standard des particules, construit au cours du siècle dernier, est capable de décrire la matière ordinaire avec une très grande précision. Ce modèle inclut les particules élémentaires et leurs interactions. L'interaction forte, véhiculée par le gluon, est décrite par la théorie de la chromodynamique quantique (QCD). Elle testée typiquement en sondant le proton, formé de quarks liés entre eux par des gluons. Le proton est le noyau le plus petit et le plus stable (avec une grande durée de vie) qui existe, et c'est une particule chargée, donc facile à accélérer dans des collisionneurs de particules. Grâce aux données fournies par le collisionneur HERA, la structure du proton est bien connue jusqu'à une échelle $x \sim 10^{-4}$, correspondant à la fraction de moment longitudinal porté par les partons (les quarks et les gluons à l'intérieur du proton). Cette variable, appelée Bjorken-x, est inversement propotionnelle à l'énergie de collision entre une particule projectile et le proton cible. Dans le domaine d'énergie sondé par HERA, les fonctions de distribution des partons (PDFs) dans le proton sont bien décrits par des équations perturbatives linéaires. Cependant, les PDFs prédisent une croissance exponentielle de la densité de gluons lorsque x diminue ou que l'énergie augmente, ce qui violerait l'unitarité de la théorie de QCD. Ainsi, on s'attend à ce que les gluons, qui peuvent interagir avec d'autres gluons, puissent se recombiner lorsqu'un régime de *saturation de gluons* est atteint. Ces effets apparaîtraient sous forme de termes non linéaires dans les équations d'évolution des partons qui maîtriseraient la croissance rapide des gluons aux faibles valeurs de Bjorken-x.

La saturation de gluons peut être testée au LHC avec l'expérience ALICE dans des collisions dites ultra-périphériques (UPCs) de protons et de noyaux de plomb (p–Pb). Ce type de collision est caractérisé par un paramètre d'impact, c'est-à-dire la distance entre les deux noyaux dans le plan transverse de la collision, plus grand que la somme des rayons des deux noyaux qui entrent en collision (figure K.3 à gauche). Le noyau de plomb qui possède un fort champ électromagnétique autour de lui sert d'émetteur de photons quasi-réels. Un photon peut alors interagir avec le proton, produisant une particule J/ψ via l'échange de deux gluons du proton.

Deux cas de figure existent. Dans le premier cas, le proton reste intact (figure K.3 à droite). Ce processus, dit exclusif ou cohérent, dépend de la distribution moyenne des gluons sur différentes plages dans Bjorken-x. Dans le deuxième cas, le proton se dissocie. Ce processus, appelé

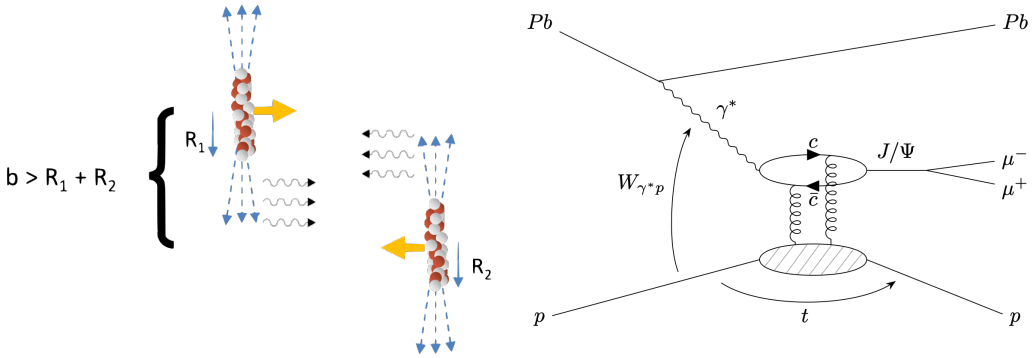

FIGURE K.3 : Gauche : représentation d'une collision ultra-périphérique. Droite : diagramme de Feynman pour la photoproduction exclusive d'un J/ψ dans une collision p–Pb à l'ordre dominant.

dissociatif ou incohérent, est caractérisé par un écart de rapidité entre les particules produites à l'état final. Ce méchanisme de production est sensible aux fluctuations géométriques du proton. Il est prédit que si le régime de saturation de gluons est atteint, le rapport entre les sections efficaces incohérentes et cohérentes devrait s'évanouir.

Chapitre 2 : Description de l'expérience ALICE

ALICE est une expérience dédiée à l'étude des ions lourds alimentée par les faisceaux du LHC situé au CERN. Elle fait partie des quatre expériences les plus importantes par leur taille au LHC, avec ATLAS, CMS, et LHCb. Son programme d'étude inclut des collisions Pb–Pb et Xe–Xe, mais aussi des collisions pp et p–Pb. Le détecteur comprend de nombreux sous-systèmes, dont six seulement sont utilisés dans l'analyse de photoproduction du J/ψ. Le plus important est sans doute le spectromètre à muons dans la région frontale en pseudorapidité $-4,0 < \eta < -2,5$ qui est utilisé pour reconstruire les muons résultant de la désintégration des particules J/ψ. Le spectromètre à muons est consitué de plusieurs chambres de détection de traces potentielles de muons, d'un aimant dipolaire pour courber les trajectoires, ainsi que d'absorbeurs pour filtrer les autres particules produites. D'autres détecteurs sont essentiels afin de s'assurer que le noyau de plomb reste intact et, lorsque le processus exclusif est étudié, que le proton aussi reste intact.

- Le Silicon Pixel Detector (SPD) permet de reconstruire des tracklets (fragments de traces créés à partir de deux points reconstruits dans deux couches de détecteur). Son acceptance est $|\eta| < 1,4$. Il permet de supprimer notamment des événements inclusifs.

- Le Zero Degree Calorimeter (ZDC) est un ensemble de calorimètres hadroniques couvrant la région $6,5 < |\eta| < 8,8$. Il permet d'appliquer un veto sur les événements dans lesquels les noyaux se sont dissociés.

- Le détecteur ALICE Diffractive (AD) est composé de deux ensembles de scintillateurs couvrant les régions $4,8 < \eta < 6,3$ (ADA) et $-7,0 < \eta < -4,9$ (ADC). Il est utilisé comme veto sur les événements dans lesquels les noyaux se sont dissociés. (ADC).

- Le détecteur V0 est un ensemble de deux scintillateurs, couvrant les régions $2,8 < \eta <$

$5,1$ (V0A) et $-3,7 < \eta < -1,7$ (V0C). Il permet aussi d'appliquer un veto sur les événements dans lesquels les noyaux se sont dissociés.

- Le détecteur T0 est un ensemble de deux détecteurs à effet Cherenkov. Ils sont utilisés pour calculer la luminosité associée aux collisions étudiées, enregistrées selon certaines conditions de déclenchement.

Les données sont enregistrées par le système d'acquisition (DAQ) suivant certaines conditions de déclenchement pré-définies. Une sélection dite "en ligne" permet d'effectuer un premier tri, notamment par le High Level Trigger (HLT). Les données brutes suivent ensuite plusieurs étapes de reconstruction, jusqu'à les transformer en fichier Event Summary Data (ESD) ou encore Analysis Object Data (AOD). C'est à partir de ces fichiers que l'analyse peut commencer, grâce au logiciel ALIROOT développé par la collaboration ALICE et qui contient notamment la géométrie des détecteurs d'ALICE. De plus, des simulations sont tournées dans ALIROOT et enregistrées sous forme de fichiers ESD ou AOD. L'analyse peut être envoyée dans la *grid*, un service de contrôle informatique qui permet de paralléliser des tâches et de réduire drastiquement le temps de calcul, étant donné le volume important de données qui sont traitées.

Chapitre 3 : Échantillons de données et sélection des événements

La première étape de l'analyse consiste à sélectionner les données. Une première sélection est faite "en ligne" : il s'agit des conditions de déclenchement qui permettent d'enregistrer les données. Ainsi, l'échantillon de données utilisé pour l'analyse est déterminé par le déclencheur correspondant aux critères suivants :

- au moins un muon avec un faible seuil p_{T} ($\sim 0,5$ GeV/c) est détecté dans les chambres de déclenchement du spectromètre à muon
- aucune activité n'est détectée dans les détecteurs à l'avant V0A et ADA du côté du Pb sortant pour s'assurer que le noyau de plomb reste intact

L'échantillon de données obtenu doit ensuite subir une nouvelle purification. Une sélection dite "hors ligne" est donc effectuée parmi les événements enregistrés afin de garder les événements d'intérêt et supprimer les événements de fond. Deux sélections sont utilisées. La première, appelée sélection standard, vise à sélectionner la production exclusive et dissociative de J/ψ, et permet donc au proton de se dissocier. La seconde, appelée sélection exclusive, est plus restreinte puisque le proton doit rester intact, ce qui est assurant en utilisant les détecteurs du côté du proton sortant comme vetos.

De plus, une étape importante de l'analyse consiste à déterminer la luminosité qui caractérise l'échantillon de données. Cette quantité est essentielle pour normaliser le comptage des événements.

Chapitre 4 : Extraction du signal, corrections et incertitudes

D'autres processus de fond sont susceptibles de survivre dans les données s'ils laissent la même signature dans les détecteurs que les événements de photoproduction de J/ψ. C'est le cas, par exemple, des interactions de deux photons, provenant l'un d'un proton et l'autre d'un noyau de plomb, produisant deux muons selon le processus $\gamma\gamma \to \mu^+\mu^-$. Ces événements sont

distribués de manière continue dans le spectre de masse et constituent un bruit de fond pour la mesure du J/ψ. La section efficace de ce processus est entièrement calculable grâce à la théorie de l'électrodynamique quantique (QED). Ainsi, sa mesure, effectuée ici à basse masse pour $1,0 < M_{\mu\mu} < 2,5$ GeV$/c^2$, permet de tester les calculs de QED.

Le nombre d'événements d'intérêts ($\gamma\gamma \to \mu^+\mu^-$ pour $1,0 < M_{\mu\mu} < 2,5$ GeV$/c^2$ ou J/ψ pour $2,5 < M_{\mu\mu} < 3,5$ GeV$/c^2$) est obtenu par une méthode d'ajustement de fonction. Un modèle est construit, défini par plusieurs composantes, chacune représentant un processus différent qui apparaît dans les données. Dans le cas de la mesure du processus $\gamma\gamma \to \mu^+\mu^-$ à basse masse, seuls deux processus sont modélisés : les productions exclusive et inclusive de dimuons dans des interactions de deux photons. Dans le spectre de masse des dimuons obtenus pour $2,5 < M_{\mu\mu} < 3,5$ GeV$/c^2$, le pic du J/ψ est modélisé par une fonction Crystal Ball à deux côtés, tandis que le fond continu de dimuons est représenté par une exponentielles décroissante. Dans le spectre du moment transverse des dimuons p_{T}, les événements exclusifs et dissociatifs sont modélisés par deux fonctions différentes. Un algorithme de minimisation permet d'ajuster le modèle aux données à partir de la masse et du moment transverse simultanément, et d'extraire l'intégrale de chaque composante (voir figure K.4). Cette intégrale correspond au nombre d'événements extraits.

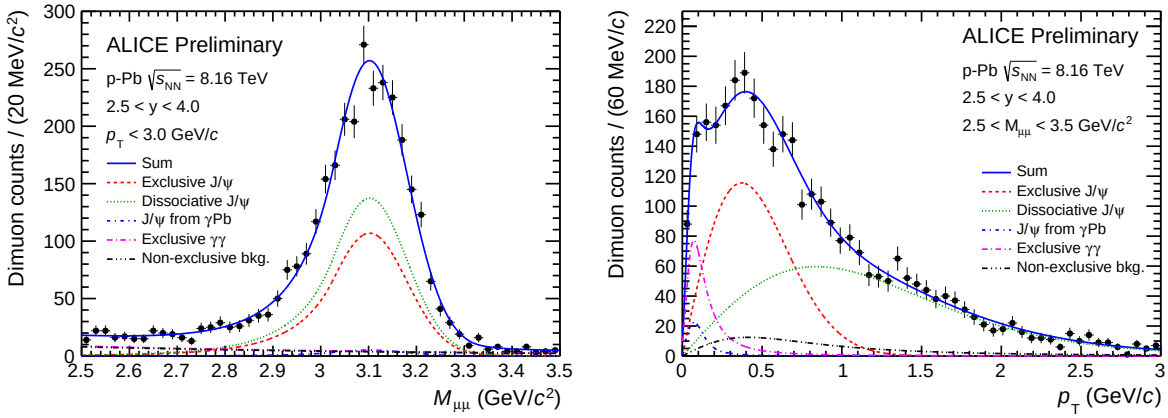

FIGURE K.4 : Projections des ajustements bidimensionnels finaux sur la masse (gauche) et p_{T} (droite) en utilisant la sélection standard.

Les nombres de candidats de chaque catégorie doivent ensuite être corrigés pour tenir compte de plusieurs facteurs. Le premier est le facteur d'acceptance et d'efficacité, obtenu à l'aide des données issues des simulations. Ensuite, le nombre de candidats d'événement de photoproduction du J/ψ doivent être corrigés par le nombre d'événements de photoproduction du $\psi(2S)$, particule cousine du J/ψ mais plus lourde, qui se désintègre en J/ψ.

Toutes ces corrections sont essentielles pour le calcul des sections efficaces.

Finalement, les incertitudes systématiques sont calculées en tenant compte principalement :

- de l'incertitude sur la luminosité
- de l'incertitude sur l'identification d'une vraie paire de muons dans le spectromètre à muons
- de l'incertitude liée à la méthode d'extraction du signal

- des incertitudes liées à la sélection des données

et dans le cas de la mesure du J/ψ

- de l'incertitude liée au flux de photons provenant du noyau de plomb
- de l'incertitude liée à la désintégration de $\psi(2\mathrm{S})$ en J/ψ
- et de l'incertitude sur la fraction de J/ψ qui se désintègrent en paire de muons.

Chapitre 5 : Résultats et comparaison des mesures avec les modèles

Tous les ingrédients étant rassemblés, les sections efficaces sont calculées dans plusieurs gammes de rapidité (et de masse dans le cas de l'extraction du signal $\gamma\gamma \to \mu^+\mu^-$).

La mesure de la production exclusive de dimuons dans les interactions à deux photons est présentée dans la plage de masse invariante précédemment inexplorée de 1,0 à 2,5 GeV/c^2. Les résultats sont comparés avec les calculs du générateur d'événements STARlight basé sur la QED à l'ordre dominant (LO). Des déviations sont observées jusqu'à 3 σ de la mesure. Cependant les incertitudes systématiques mesurées ne permettent pas de mieux contraindre le flux de photons provenant du noyau de plomb.

La mesure de la production exclusive et dissociative du J/ψ est présentée. Le processus exclusif est comparé aux mesures précédentes du même type et aux modèles. Les mesures d'ALICE sont cohérentes avec une dépendance de type loi de puissance $\sigma(\gamma\mathrm{p} \to \mathrm{J}/\psi p) \sim W^{\delta}_{\gamma\mathrm{p}}$, avec $\delta = 0,70 \pm 0,04$, indiquant ainsi qu'il n'y a pas de changement significatif dans le comportement de cette section efficace entre les énergies sondées à HERA et au LHC. Le processus dissociatif, mesuré pour la première fois au LHC, est comparé aux mesures de l'expérience H1 ainsi qu'aux modèles. Cette mesure est une preuve de concept que de nouvelles mesures de processus dissociatifs pourraient être effectuées à l'avenir, avec les données du Run 3 et du Run 4 du LHC où une forte augmentation du nombre d'événements enregistrés est attendue.

Partie 2 : Développement et caractérisation d'une nouvelle structure de détecteur gazeux à micro-motifs réduisant le reflux d'ions

Chapitre 6 : Les détecteurs gazeux à micro-motifs comme systèmes de lecture de TPC

Les chambres à projection temporelle (TPCs) sont utilisées dans de nombreuses expériences de physique des particules, notamment dans ALICE qui fait l'objet de la première partie de cette thèse. Avec la construction future d'installations à haute luminosité telles que le collisionneur électron-ion (EIC) et le collisionneur linéaire international (ILC), les TPCs sont de bons candidats pour constituer le principal instrument de reconstruction de traces de particules. Lorsqu'une particule chargée traverse la TPC, elle ionise le gaz présent dans la chambre le long de sa trajectoire, et les électrons résultants de ces ionisations dérivent vers les plans de lecture sous l'action de champs électriques. La détection de ces électrons permet de reconstruire la trajectoire de la particule initiale. Une TPC a l'avantage de fournir suffisamment de points de mesure pour une reconnaissance robuste d'une trajectoire et peu de matériel. Ainsi, l'optimisation de leurs instruments de lecture devient une préoccupation majeure pour l'avenir des expériences de physique des particules. Les détecteurs gazeux à micro-motifs (MPGDs) sont très communément associés aux TPCs comme systèmes de lecture. Ces systèmes utilisent des champs électriques intenses pour accélérer et multiplier les électrons issus des ionisations d'une particule chargée dans la TPC. Ils sont simple à construire, robustes, et offrent une résolution spatiale de l'ordre de 100 µm. Cependant, lors du processus de multiplication des ionisations dans la zone d'amplification, les ions produits dérivent dans l'autre sens. La plupart sont arrêtés avant de sortir de la zone d'amplification mais certains peuvent atteindre la zone de dérive, c'est-à-dire la TPC elle-même. Cette fraction d'ions est appelé le IBF. Cela entraîne un effet de charge à l'intérieur de la chambre, induisant des distorsions de champ locales et affectant ainsi la résolution spatiale des TPCs.

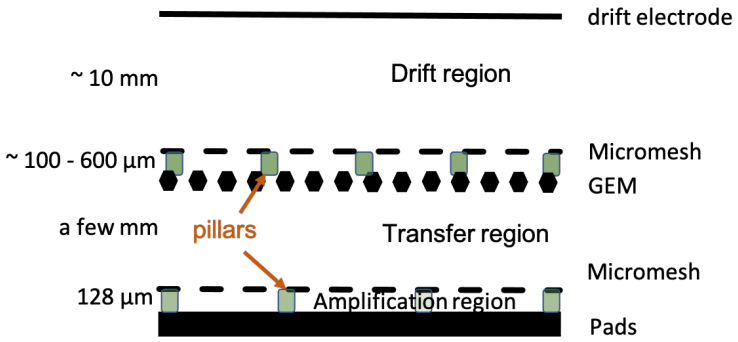

FIGURE K.5 : Représentation de la nouvelle structure de MPGD proposée (MMGEM).

Deux types de MPGD sont étudiés : les détecteurs MicroMEGAS et GEMs. La nouvelle solution proposée consiste à combiner ces deux technologies pour en faire plusieurs étages d'amplification, suivant le schéma montré K.5. Cette solution vise à supprimer intrinsèquement le IBF pour en gardant un gain de l'ordre de 2000, nécessaire pour la bonne opération d'une TPC comme ALICE. Cette nouvelle structure est nommée MMGEM. Le nouveau détecteur est

testé dans la suite dans le mélange de gaz argon-isobutane (95/5) à l'aide du source de fer ^{55}Fe qui envoie principalement des photons à 5.9 keV.

Chapitre 7

Afin de concevoir la bonne géometrie de détecteur (espaces entre les différentes électrodes, caractéristiques géométriques des micro-meshes), des simulations sont faites en deux étapes.

La première consiste à générer des cartes de champ électrique en trois dimensions, à l'aide du logiciel COMSOL Multiphysics®. Ce logociel permet de construire une structure, lui assigner des électrodes sous forme de surfaces, et leur donner un potentiel électrique. Un maillage tétraédrique est construit automatiquement dans le volume obtenu, et le potentiel électrique est calculé à chaque sommet de ce maillage.

Dans un second temps, le logiciel Garfield++ permet de simuler des photons comme s'ils étaient envoyés par une source de fer ^{55}Fe, et de générer des avalanches d'électrons dans le volume sensible du détecteur constitué d'argon-isobutane (95/5).

Les simulations sont d'abord effectuées sur des modèles de détecteurs simples utilisant uniquement un MicroMEGAS, puis des électrodes sont ajoutées étape par étape. La GEM semble inefficace pour arrêter les ions, cependant, elle est utilisée comme un étage de pré-amplification qui disperse l'avalanche, ce qui permet une meilleure reconstruction spatiale dans le plan de lecture situé à l'anode. Plusieurs modèles MMGEM sont simulés et semblent très prometteurs en termes de résolution énergétique et d'IBF pour des gains d'environ 2000.

Chapitre 8

Deux prototypes de détecteurs ont été testés et entièrement caractérisés à l'IRFU, au CEA. Les deux se distinguent par les dimensions de la micro-mesh du haut, et l'espace entre cette micro-mesh et la GEM. Le comportement de chaque électrode et son rôle dans le processus d'amplification en termes de gain intrinsèque, de transparence et de capacité à stopper les ions a été soigneusement étudié. Le gain du détecteur est obtenu par l'analyse du spectre de la source de fer, en normalisant par le nombre d'électrons primaires crées lors de la conversion de photons en électrons. La transparence est définie comme la capacité d'une électrode à laisser passer les électrons, et doit en général être déconvoluée du gain pour être mesurée. L'IBF est obtenu en divisant le déplacement de courant sur la dérive avec et sans la source avec le déplacement de courant sur la micro-mesh d'amplification du bas. Enfin, les courants de contamination induits par les photons convertis en dehors de la région de dérive sont étudiés et considérés comme une incertitude systématique dans les mesures d'IBF.

Chapitre 9

Le chapitre suivant discute de la précision des simulations en les comparant aux prototypes testés en laboratoire. Nous discutons également de l'amélioration du détecteur MMGEM par rapport aux configurations géométriques plus simples testées.

Les mesures obtenus sur les modèles MicroMEGAS simple, combinant une MicroMEGAS et une GEM, et finalement sur le modèle MMGEM, sont comparées aux simulations. Des différences importantes sont observées, notamment en terme de gain. Ces différences peuvent être dûes à de nombreux facteurs, notamment au coefficient de Penning défini par l'utilisateur dans les simulations Garfield++, ou par le fait que les simulations ne reproduisent pas de manière suffisamment réaliste la vraie géometrie du détecteur testé.

Ensuite, les différentes configurations sont comparées entre elles. Les nouveaux modèles MMGEM ont été comparés à la configuration unique MicroMEGAS et à la configuration hybride MicroMEGAS et GEM, et montrent une réduction des IBF par un facteur de 10. Le détecteur avec un écart de 660 µm permet d'obtenir des valeurs de IBF de l'ordre de 0.2% pour des gains de 2000, et le détecteur avec un écart de 128 µm donne des valeurs de IBF aussi basses que $\sim$ 0.3% pour des gains d'environ 6000.

Les modèles MMGEM ont également été comparés aux GEM quadruples utilisées comme sytème de lecture pour la TPC d'ALICE, et permettent d'obtenir des IBF plus faibles. En revanche, la résolution énergétique est de 25 à 60% moins bonne tout en conservant un IBF inférieur à 0,5%.

université PARIS-SACLAY

ÉCOLE DOCTORALE
Particules, hadrons, énergie et noyau : instrumentation, imagerie, cosmos et simulation (PHENIICS)

Titre : Cartographier le proton via la photoproduction du J/ψ avec ALICE et développement d'une nouvelle structure de détecteur de particules gazeux
Mots clés : Structure du proton, Saturation de gluons, Chambre à projection temporelle, GEM, Micromegas, Retour d'ions

Résumé : Depuis les années 60, les expériences ont montré que le proton est un élément composite, fait de quarks liés entre eux par des gluons, médiateurs de l'interaction forte. Le comportement des gluons soulève des questions, en particulier, on s'attend à ce que ceux-ci se recombinent lorsque leur densité devient critique. Ce phénomène, appelé saturation de gluons, peut être testé au LHC dans des collisions dites "ultra-périphériques" de noyaux de plomb et de protons. Le noyau de plomb sert de source de photons, qui viennent sonder l'intérieur du proton. Une signature possible de cette interaction est la production d'une particule, le J/ψ, dont les mécanismes de production dépendent directement de la densité des gluons.

La seconde partie de cette thèse est dédiée au développement d'un nouveau type de détecteur gazeux, qui combine des détecteurs Micromegas et des GEMs. Ces deux technologies permettent d'amplifier le signal via la création d'avalanches d'ionisations. L'enjeu est de capturer les ions des avalanches, car ils pourraient induire une dégradation de la résolution spatiale du détecteur.

Title: Mapping the proton using J/ψ photoproduction with ALICE and development of a novel structure of gaseous particle detector
Keywords: Proton structure, Gluon saturation, Time projection chamber, GEM, Micromegas, Ion backflow

Abstract: Since the 1960s, experiments have shown that the proton is a composite element, made up of quarks bound together by gluons, mediators of the strong interaction. The behavior of gluons raises questions, in particular, they are expected to recombine when their density becomes critical. This phenomenon, called gluon saturation, can be tested at the LHC in so-called "ultra-peripheral" collisions of lead nuclei and protons. The lead nucleus serves as a source of photons, which probe the interior of the proton. A possible signature of this interaction is the production of a particle, the J/ψ, whose production mechanisms depend directly on the density of the gluons.

The second part of this thesis is dedicated to the development of a new type of gaseous detector, which combines Micromegas detectors and GEMs. These two technologies make it possible to amplify the signal via the creation of avalanches of ionizations. The challenge is to capture the ions from the avalanches, because they could induce a degradation of the spatial resolution of the detector.